

The image features four pairs of overlapping sine waves, each pair in a different color: cyan and yellow, magenta and purple, cyan and yellow, and magenta and purple. The waves are arranged in a vertical stack, with each pair overlapping the one above and below it. The central text is white and positioned between the second and third pairs of waves.

Realizing an
Andreev Spin  Qubit

Max Hays

Foreword

Traditional physics courses tend to separate nature into two worlds. On one hand, there is the world of macroscopic systems such as cars, bicycles and grandfather's clocks. This world obeys the laws of classical physics. On the other hand, there is the world of microscopic systems such as molecules, atoms, nuclei and quarks. This world obeys the laws of quantum mechanics. In favor of such classification, one usually advances that macroscopic systems contain a very large number of atoms and have therefore a huge number of degrees of freedom. These degrees of freedom are in turn hosting so many excitation quanta that quantum effects, which can be witnessed only when there are only a few variable quanta, are completely blurred. In contrast, microscopic systems contain sufficiently small number of particles that their total number of quanta can be well controlled. Therefore, the behavior of these systems can escape from the crude classical laws, and the sophisticated quantum physics laws are free to reign in their world. A dogma had been inscribed in the mind of physicists: many atoms \rightarrow classical physics, few atoms \rightarrow quantum physics. In the 1980's, this dogma had to be profoundly revised. It had become possible, thanks to progress in lithography techniques using electron beams and in sub-kelvin refrigeration techniques, to fabricate a whole new class of miniature system which could be measured at very low temperatures. They were baptized *mesoscopic* systems: while having still a very large number of atoms, they had so few relevant excitations above their ground state that they were behaving quantum-mechanically, even when measured with the seemingly grubby leads of electrical measurements. One of the most recognizable feature of these novel mesoscopic systems were that they were exhibiting interference effects involving the fundamental quantum constants e and \hbar through classical measurement tools, while at the same time having all their parameters controlled as engineered quantities. These parameters involved for instance the area of a chip, the density of charge carriers, the value of a capacitance or an inductance, instead of the invariable, God-given mass of the microscopic free electron or proton. One may object that Millikan had observed in 1909 the quantum of charge e by measuring the fall of droplets of oil with a microscope and a chronometer, but

in this proto-mesoscopic physics experiment, there were no manifestation of the superposition and entanglement that uniquely characterize quantum mechanics. The same can be said of the photoelectric effect that measured $\hbar c/e$.

In his PhD thesis work, which the present dissertation explains particularly clearly, Max Hays has achieved a quintessential goal of mesoscopic physics: manipulate a single electron spin, the most microscopic of all quantum degrees of freedom, by the tools of an advanced version of mesoscopic physics: ultra-low-noise microwave reflection measurements. In his experiment, a single fermion is interfaced with a macroscopically measurable supercurrent. So far, only the much less exotic bosonic degree of freedom of a non-linear oscillator had been similarly controlled. Another appeal of the quantum manipulation demonstrated in the research covered by this monograph is that it has the potential to become one day an important platform for quantum information processing, since it combines a microscopic regularity with the flexibility of an engineered, macroscopic mode of coupling signals in and out.

I wish the reader of this dissertation as much pleasure learning about a key mesoscopic physics experiment as I had supervising this remarkable work.

– Michel Devoret, New Haven, June 2021

Realizing of an Andreev Spin Qubit:
Exploration of Sub-gap Structure in Josephson Nanowires Using Circuit QED

A Dissertation
Presented to the Faculty of the Graduate School
of
Yale University
in Candidacy for the Degree of
Doctor of Philosophy

by
Max Hays

Dissertation Director: Michel H. Devoret
Committee Members: Attila Geresdi, Leonid Glazman, Robert Schoelkopf
External Readers: Cristián Urbina and Hugues Pothier

December 2020

Contents

List of Symbols	v
Acknowledgements	xviii
I Key concepts and contributions	1
1 Introduction	2
1.1 The magic of superconductors and semiconductors	2
1.2 What's so special about a weak link?	4
1.3 Structure of this thesis	5
2 Andreev levels	6
2.1 How do Andreev levels arise?	6
2.2 Many-body configurations and microwave manipulation	11
2.3 From tunnel junctions to Josephson nanowires	13
2.4 The Andreev pair qubit	16
3 Probing Andreev levels with cQED	20
3.1 What is cQED?	20
3.2 Coupling to the Andreev levels	24
3.3 The device	25
3.4 Investigating pair transitions	27
4 Unlocking the spin of a quasiparticle	32
4.1 Breaking spin degeneracy: long weak links and spin-orbit coupling	34
4.2 The Andreev spin qubit	37
4.2.1 Playing with the spin of a single quasiparticle	37
4.2.2 Spin detection	40
4.2.3 Spin manipulation	43

5	Future directions	55
II	The beautiful, messy details	58
6	BCS superconductivity	59
6.1	The BCS Hamiltonian	59
6.2	Diagonalization of the BCS Hamiltonian	61
6.3	Discussion of the single-particle states	64
6.4	Density of states	69
6.5	Superconducting ground state and the Cooper pairs	70
6.6	Quasiparticle excitations	72
6.7	Pictures of superconductivity	73
6.7.1	One-particle picture	73
6.7.2	Excitation picture	73
6.7.3	Semiconductor picture	75
7	Andreev reflection, Andreev levels, and the Josephson effect	81
7.1	Andreev reflection	81
7.2	Andreev levels: the "short junction" limit	86
7.3	The Josephson effect	93
8	Andreev levels in Josephson nanowires	97
8.1	Scattering of holes	97
8.2	Beyond the short-junction approximation	99
8.2.1	Increasing junction length	99
8.2.2	Single scatterer	101
8.2.3	Double barrier	103
8.2.4	Resonant level	105
8.2.5	Comparing models of disorder	108
8.3	Spin-orbit coupling	109
8.3.1	The Rashba effect	110

8.3.2	In an infinite nanowire	111
8.4	Spin-orbit split Andreev levels	113
8.4.1	Single scatterer	115
8.4.2	Double-barrier	116
8.4.3	Resonant level	117
9	What would happen in a topological weak link?	119
9.1	Tight-binding model of a p -wave weak link	120
9.1.1	The Kitaev chain	120
9.1.2	Kitaev chain as a weak link	123
9.2	Continuous model of a p -wave weak link	127
9.2.1	From tight-binding to the continuous case	127
9.2.2	Diagonalizing the p -wave Hamiltonian	129
9.2.3	A p -wave weak link	131
9.3	Majoranas as Andreev levels between a p -wave superconductor and vacuum	133
9.4	Making an effective p -wave superconductor	135
9.5	Probing the Majorana level in a cQED architecture	137
10	The device	140
10.1	Principle	140
10.2	Design	143
10.3	Modeling	145
10.4	Fabrication	147
10.5	Progression	149
10.6	Cryogenic setup	151
11	Spectroscopy and dispersive shifts	154
11.1	Andreev level/resonator coupling	156
11.1.1	The Andreev pair qubit	158
11.1.2	Long-junction regime	160
11.2	Extended spectroscopy	167

11.2.1 Comparing spin-flipping/-conserving single particle transitions . . .	167
11.2.2 Zeeman splitting of single-particle transitions	171
11.2.3 Other observations	172
12 Raman transitions of the quasiparticle spin	176
12.1 Theory of Raman transitions	176
12.2 Tuning up the device	180
12.3 Searching for Raman transitions	183
12.4 Coherent spin dynamics	187
13 Interactions of Andreev levels with the environment	190
13.1 Environment-induced transitions	190
13.1.1 Parity dynamics and hidden Markov models	191
13.1.2 Pair decay	194
13.1.3 Inter-doublet quasiparticle decay	194
13.1.4 Spin flips	198
13.2 Dephasing	207
13.2.1 The Andreev spin qubit	207
13.2.2 Comparing to inter-doublet transitions	208
13.2.3 Comparing to pair transitions	210
14 Unexplained observations	213
14.1 Quasiparticle interaction with unknown sub-gap states	213
14.2 Temperature dependence of quasiparticle parity jumps	219

List of Symbols

Acronyms

AC	alternating current ($\omega > 0$)
BCS	Bardeen-Cooper-Schrieffer (theory of superconductivity)
cQED	circuit quantum electrodynamics
DC	direct current ($\omega = 0$)
HEMT	high-electron-mobility transistor
QND	quantum non-demolition
SPA	SNAIL parametric amplifier
RF	radio-frequency

Physical constants

h	Planck's constant
\hbar	reduced Planck's constant ($= h/2\pi$)
e	charge of an electron
m_e	mass of an electron
c	speed of light
Φ_0	magnetic flux quantum ($= h/2e$)
k_B	Boltzmann constant
μ_B	Bohr magneton
R_q	superconducting resistance quantum ($= h/(2e)^2$)
G_q	superconducting conductance quantum ($= 1/R_q$)

g electron g -factor

Electron variables

k electronic momentum

v_F Fermi velocity

k_F Fermi wavenumber

μ chemical potential

E single-particle energy: excitation picture

Microwave variables

f microwave frequency

ω angular microwave frequency

β wavenumber

λ wavelength

c_{eff} speed of light on transmission line

Z_0 transmission line characteristic impedance

Bias knobs

Φ magnetic flux

V_0 electrostatic voltage

V_c cutter gate voltage

V_p plunger gate voltage

V_{rms} RMS voltage noise

B_{\perp} magnetic field perpendicular to the substrate

Andreev levels: general

Δ superconducting gap
 φ superconducting phase
 r_A Andreev reflection coefficient
 ϕ_A Andreev reflection phase
 H_A weak link Hamiltonian

Weak link properties

L weak link length
 ξ_0 coherence length ($= \hbar v_F / \Delta$)
 r reflection coefficient
 ϕ_r reflection phase ($= \text{Arg}(r)$)
 τ channel transparency ($= 1 - |r|^2$)

Andreev levels: short junction regime

$|g\rangle$ ground state
 $|\downarrow\rangle$ one quasiparticle, spin down
 $|\uparrow\rangle$ one quasiparticle, spin up
 $|e\rangle$ two quasiparticles
 E_A level energy: excitation picture

f_{pair} frequency of pair transition $|g\rangle \leftrightarrow |e\rangle$ ($= 2E_A/h$)

Andreev levels: long Josephson nanowires

$|g\rangle$ ground state

$|\downarrow_q\rangle$ one quasiparticle in lower doublet, spin down

$|\uparrow_q\rangle$ one quasiparticle in lower doublet, spin up

$|\uparrow_a\rangle$ one quasiparticle in upper doublet, spin up

$|\downarrow_a\rangle$ one quasiparticle in upper doublet, spin down

P_\downarrow occupation probability of $|\downarrow_q\rangle$

P_\uparrow occupation probability of $|\uparrow_q\rangle$

$E_{n,\pm}$ ballistic energies of a long junction, $n \in \mathbb{Z}$

E_s energy splitting between $|\downarrow_q\rangle$ and $|\uparrow_q\rangle$

E_Z Zeeman energy

$f_{ss'}$ inter-doublet transition frequencies, $s, s' \in \{\downarrow, \uparrow, \uparrow, \downarrow\}$

$\omega_{ss'}$ inter-doublet angular transition frequencies, $s, s' \in \{\downarrow, \uparrow, \uparrow, \downarrow\}$

Timescales

T_p parity lifetime

T_s spin lifetime

$T_{aq,\uparrow}$ interdoublet-decay rate, spin up

$T_{aq,\downarrow}$ interdoublet-decay rate, spin down

T_1 qubit energy lifetime

T_ϕ	pure dephasing lifetime
T_2	coherence lifetime
T_{2R}	coherence lifetime measured with Ramsey sequence
T_{2E}	coherence lifetime measured with a Hahn-echo sequence

Microwave resonators

f_r	resonator frequency
ω_r	angular resonator frequency
Z_r	resonator impedance
κ_c	angular decay frequency to transmission line
κ_i	angular decay frequency to "internal" of freedom
ℓ	coplanar strip resonator length

Readout

ω_{ro}	readout frequency
Γ	resonator reflection coefficient
I, Q	real and imaginary parts of Γ ($I = \text{Re}(\Gamma)$, $Q = \text{Im}(\Gamma)$)
θ	angle of Γ ($= \text{Arg}(\Gamma)$)
σ	standard deviation of Γ
\mathcal{F}	readout fidelity

General cQED

ω_q	angular qubit frequency
σ_i	pauli matrices, $i \in \{x, y, z, +, -\}$
a, a^\dagger	photonic creation and annihilator operators
n	number of photons
H_c	system/resonator coupling Hamiltonian
g_c	qubit/resonator coupling
g_{ij}	multilevel-system/resonator coupling
χ	dispersive shift
H_{JC}	Jaynes-Cummings Hamiltonian
$\epsilon_{n,\sigma}$	joint qubit/resonator energy $\sigma \in \{+1, -1\}$
$H_{\text{dispersive}}$	dispersive Hamiltonian

Andreev level/microwave coupling

J_A	weak link current operator
I_A	average level current
\mathfrak{C}_A	weak link inverse inductance operator
ϕ	RF flux drive amplitude over shared inductance
p	participation ratio of shared inductance
Φ_{zpf}	resonator zero-point flux fluctuations ($= \sqrt{\hbar Z_r/2}$)
Φ_r	zero-point flux fluctuations over shared inductance ($= p\Phi_{\text{zpf}}$)
Z_L	shared inductance impedance
Γ_L	shared inductance reflection coefficient

χ_{\downarrow} χ of $|\downarrow_q\rangle$

χ_{\uparrow} χ of $|\uparrow_q\rangle$

Microwave drives

f_d drive frequency

ω_d angular drive frequency

A normalized pulse amplitude

τ inter-pulse delay

Raman transitions

f_s frequency of spin s drive

ω_s angular frequency of spin s drive

A_s normalized amplitude of spin s drive

Δ_R detuning of drives from $|s_q\rangle \leftrightarrow |\uparrow_a\rangle$

Δ'_R detuning of drives from $|s_q\rangle \leftrightarrow |\downarrow_a\rangle$

δ detuning of drives from virtual level

Ω_s rabi rate of spin s drive

$M_{ss'}$ inter-doublet drive matrix elements, $s, s' \in \{\downarrow, \uparrow, \uparrow, \downarrow\}$

δ_{eff} effective detuning of Raman qubit

Ω_{eff} effective Rabi rate of Raman qubit

H_r transformation Hamiltonian

$\gamma_{\text{de-trap}}$ drive-induced quasiparticle de-trapping rate

Chapters 6, 7, 8, and 9

These chapters are a bit notation heavy, a lot of which isn't used elsewhere in the thesis. As such, it's grouped separately. For some symbols involving electrons and holes, we will use color as the sole differentiator. For example, k is the wavenumber of an electron-like Bogoliubon, while \bar{k} is the wavenumber of a hole-like Bogoliubon.

Electron variables

k	electronic momentum
s	electronic spin
v_F	Fermi velocity
k_F	Fermi wavenumber
μ	chemical potential
\mathcal{E}_k	kinetic energy ($= \hbar^2 k^2 / 2m_e - \mu$)
$\psi_s(x)$	electron annihilation operator, position x and spin s
$c_{k,s}$	electron annihilation operator, momentum $\hbar k$ and spin s
H	1D free-electron Hamiltonian
ν_N	normal density of states

BCS: general

p	electron pair correlation ($= \langle \psi_s^\dagger(x) \psi_{\bar{s}}^\dagger(x) \rangle$)
V	strength of electron-electron attraction
φ	superconducting phase ($= -\text{Arg}(p)$)
Δ	BCS gap ($= pV$)

H_{BCS}	1D BCS Hamiltonian
ξ_0	coherence length ($= \hbar v_{\text{F}}/\Delta$)
ν_{S}	superconducting density of states
$ g_{\varphi}\rangle$	superconducting ground state, phase φ
$ N\rangle$	superconducting ground state, N Cooper pairs

BCS: one-particle picture

ϵ	single-particle energy
c_k	electron annihilation operator, momentum $\hbar k$ ($= c_{k,s}$)
h_k	hole annihilation operator, momentum $\hbar k$ ($= c_{-k,\bar{s}}^\dagger$)
Ψ_k	electron/hole spinor, momentum $\hbar k$ ($= \begin{pmatrix} c_k \\ h_k \end{pmatrix}$)
σ_i	Pauli matrices acting in electron-hole space, $i \in \{x, y, z\}$
U_k	unitary diagonalization matrix, fixed momentum $\hbar k$
$\gamma_{k,\pm}$	Bogoliubon annihilation operator, energy $\pm\epsilon_k$
$\gamma_{\pm,\rightarrow}$	electron-like Bogoliubon, $k > 0$
$\gamma_{\pm,\leftarrow}$	electron-like Bogoliubon, $k < 0$
$\gamma_{\pm,\rightarrow}$	hole-like Bogoliubon, $k > 0$
$\gamma_{\pm,\leftarrow}$	hole-like Bogoliubon, $k < 0$
u_k, v_k	coherence factors, momentum $\hbar k$
ψ_{\pm}	Bogoliubon wavefunction, energy $\pm\epsilon_k$
u	electron amplitude, electron-like Bogoliubon
v	hole amplitude, electron-like Bogoliubon

k	wavenumber, electron-like Bogoliubon
ψ_{\rightarrow}	wavefunction, $k > 0$ electron-like Bogoliubon
ψ_{\leftarrow}	wavefunction, $k < 0$ electron-like Bogoliubon
u	electron amplitude, hole-like Bogoliubon
v	hole amplitude, hole-like Bogoliubon
k	wavenumber, electron-like Bogoliubon
ψ_{\rightarrow}	wavefunction, $k > 0$ hole-like Bogoliubon
ψ_{\leftarrow}	wavefunction, $k < 0$ hole-like Bogoliubon

BCS: excitation picture

E	single-particle energy
$\gamma_{k,s}$	Bogoliubon annihilation operator, spin s

BCS: semiconductor picture

\tilde{E}	single-particle energy
σ_i	Pauli matrices acting in electron-hole space, $i \in \{x, y, z\}$
s_i	Pauli matrices acting in spin space, $i \in \{x, y, z\}$
$c_{k,s}$	electron annihilation operator, momentum $\hbar k$ and spin s ($= c_{k,s}$)
$h_{k,s}$	hole annihilation operator, momentum $\hbar k$ and spin s ($= c_{-k,\bar{s}}^\dagger$)
Υ_k	electron/hole spinor, momentum $\hbar k$
ψ_i	Bogoliubon wavefunction, $i \in \{1, 2, 3, 4\}$

\mathcal{P}	electron-hole symmetry operator
K	complex-conjugation operator

Andreev reflection

r_A	Andreev reflection coefficient
ϕ_A	Andreev reflection phase (= $\text{Arg}(r_A)$)
$\psi_{\rightarrow,N}$	wavefunction, electron-like Bogoliubon in normal region $k > 0$
$\psi_{\rightarrow,N}$	wavefunction, hole-like Bogoliubon in normal region $k > 0$
$\psi_{\rightarrow,S}$	wavefunction, electron-like Bogoliubon in superconductor $k > 0$
$\psi_A(x)$	wavefunction, Andreev reflection process
ξ	energy-dependent coherence length
ϵ_A	short-junction level energy: one-particle picture
c_{in}	incoming electron annihilation operator
h_{in}	incoming hole annihilation operator
Ψ_{in}	incoming electron-hole spinor
c_{out}	outgoing electron annihilation operator
h_{out}	outgoing hole annihilation operator
Ψ_{out}	outgoing electron-hole spinor
S_A	Andreev scattering matrix

Normal region properties

S_N	scattering matrix
$S_{e,s}$	electron scattering matrix, spin s
$S_{h,s}$	hole scattering matrix, spin s
L	length
ϕ_p	propagation phase
r	reflection amplitude
t	transmission amplitude
τ	channel transparency ($= t ^2 = 1 - r ^2$)
x_0	single-scatterer model, scatterer position
ε_{\pm}	double-barrier model, normalized energies
r_i	double-barrier model, reflection amplitude $i \in \{L, R\}$
t_i	double-barrier model, transmission amplitude $i \in \{L, R\}$
t_{DB}	double-barrier model, full transmission amplitude
t_{RL}	resonant-level model, full transmission amplitude
Γ_i	resonant-level model, lead coupling $i \in \{L, R\}$
Γ	resonant-level model, total lead coupling ($= \Gamma_L + \Gamma_R$)
E_r	resonant-level model, level energy

Spin-orbit coupling

H_{SO}	spin-orbit coupling Hamiltonian
σ_i	Pauli matrices in spin space, $i \in \{x, y, z\}$
\mathbf{p}	3D electron momentum

\mathbf{E}_{nuc}	electric field produced by nucleus
\mathbf{B}_{SO}	spin-orbit-induced effective magnetic field
g	g -factor
H_{R}	Rashba Hamiltonian
E	homogeneous crystal electric field
α	spin-orbit coupling strength
ω	frequency between nanowire sub-bands
ϕ_1	propagation phase, slow
ϕ_2	propagation phase, fast
v_1	Fermi velocity, slow
v_2	Fermi velocity, fast
k_1	Fermi wavenumber, slow
k_2	Fermi wavenumber, fast
ε_1	double-barrier model, slow normalized energy
ε_2	double-barrier model, fast normalized energy

Josephson effect

E_{J}	Josephson energy
L_{J}	Josephson inductance
R_{N}	normal-state resistance
G_{N}	normal-state conductance

Acknowledgements

Put simply, my years at Yale have been some of the happiest of my life. Of course, there have been ups and downs, but on average, it has been wonderful. It all comes down to the people that have made New Haven home. And in no small way, the people of the superconducting quantum information group have done that for me. Michel and Rob have built a lab where people flourish, work hard, and have fun. But most importantly, people on the fourth floor support each other. We want each other to succeed, in physics and in life. Of course not everyone is the best of friends, and there are always times of tension and stress. But when I leave this place, I will do so having enjoyed the presence of every person in Qlab and RSL.

There are some people that I must thank in particular, for without them my time in Qlab would have been drastically different (worse). First, my adviser, Michel Devoret. I have never met someone quite like Michel. Given his reputation, I expected him to be incredibly intelligent and driven, and on those points I was not surprised. What I did not expect was his dedication to his students. Whatever I was excited about, he was excited about. Not once did he tell me that I needed to stop pursuing some small puzzle and focus on something “more important”; he has proven to me that he is interested in knowledge purely for the sake of it. No matter what else he had going on (which was often quite a lot), he always made time to help me in whatever way he could. His endurance is unmatched, the amount of time he can discuss physics (or really any subject) seemingly unlimited. His ability to skirt often difficult mathematics and explain using only intuition and analogy is something I can only hope to aspire to. I am honored to have been his Ph.D. student.

The fourth floor would not exist without Rob Schoelkopf, and for this I am grateful to him. His vision is truly inspiring, and his ability to break any problem down to its fundamentals is unparalleled. His questions and comments during presentations (those of others, as well as my own) have often helped me understand the physics in question on a deeper level. Leonid Glazman. A stereotype of physicists is that they are terrible communicators and teachers. While I don't think this is actually true in general, Leonid proves once and for all that the stereotype is false. Aside from the many enjoyable and fruitful

discussions about various quasiparticle puzzles, I had the pleasure of taking his classes on quantum many-body physics. Definitely my favorite classes of my physics education (and let's be honest, my education in general. I'm a physicist for a reason).

Without Attila Geresdi and his students David van Woerkom and Daniël Bouman, this dissertation would not exist. They made the devices upon which all of this work was based, and for that I am eternally grateful. It was not an accident that it only took six rounds of fabrication to produce all of the results in this thesis; it was due to the skill of these wonderful scientists. The patience and ability of David and Daniël in placing the nanowires and fabricating the devices was incredible to witness. Attila's understanding of microwaves, device design, and condensed matter physics has made him an invaluable resource during my Ph.D. I could not imagine more wonderful collaborators.

And of course, this work would not have been possible without the nanowires themselves. For this I must thank Peter Krogstrup and Jesper Nygård. I count myself lucky to have been able to measure the properties of these beautiful, atomically-precise systems that Peter and Jesper have engineered. This thesis is but a fraction of what can be learned from these nanowires.

It has been a pleasure to get to know the Saclay group, who pioneered the investigation of individual Andreev levels: Cristián Urbina, Hugues Pothier, Leandro Tosi, Marcelo Goffman, and Cyril Metzger. This thesis work would not have been possible without their elegant experiments and well-written publications. They have always given thoughtful, constructive feedback on our manuscripts, including this thesis; for that I am grateful.

Qlab would not run without Luigi Frunzio. Even with all his work to make sure the pursuit of physics on the fourth floor kept moving forward, he always made sure I had enough liquid helium to keep my fridge cold. Similarly, everything would fail without the administrative staff: Giselle M. DeVito, Theresa Evangeliste, Nuch Graves, Maria Rao. Thank you for all you do, and for all the wonderful conversation whenever I visited 401 to chase a caffeine high.

The quasiparticle crew: Kyle Serniak, Valla Fatemi, and Spencer Diamond, made the everyday work in lab wonderful. Nick Frattini also deserves a special mention. Not everyone gets to work with such steadfast friends. Kyle taught me so much about all aspects of

lab, from measurement to fab (even if I was only learning vicariously for the latter). He's one of the most hard-working people I've ever met, his understanding of superconducting qubits on all levels is truly impressive, and his friendship is dear to me. His departure from Yale marked a big change; the fourth floor just wasn't quite the same. I am excited to live and work in Boston with him again. Without Valla, much of this thesis would not have happened. He was with me every step of the way in our investigations of quasiparticle spin. Valla's enthusiasm for physics is incredible. You can come to him with any idea, big or small, and he will immediately turn his considerable faculties towards understanding every piece of it. This is truly special; people are typically reticent to be distracted from whatever personal goal they are working on. I aspire to be more like Valla in this respect, among others. Spencer's arrival to lab marked the beginning of what felt like the "golden age" of my PhD, and I owe that feeling in large part to him. He's just incredibly fun to work with. He is super quick to pick up on concepts and works hard, but doesn't take things more seriously than they should be. I have feeling that his PhD will mark a turning point in the mysterious case of the non-equilibrium quasiparticles. Nick is a wonderful friend. He is one of the smartest people I've met, but somehow he remains humble. He is a genuinely good person. I will always value the years we have spent together at Yale, and look forward to staying friends with him in the years to come. I am excited to see what he will accomplish. It will surely be great.

The investigation of Andreev physics at Yale began with Gijs de Lange. I knew next to nothing about Andreev levels when I joined the project; it was Gijs who got it off the ground. When Gijs used to explain physics to me, I would often get frustrated at the lack of math. He seemed to work based largely off of intuition, and very successfully at that. His code was often difficult to read, and he would make changes seemingly at random without logging anything in the notebook. Of course, these were just the impressions of a young grad student who had trouble keeping everything straight. Gijs's mathematical grasp of physics and experimental diligence were never in question. In the end, he taught me how to focus on the critical aspects of an experiment, and to ignore unimportant minutia. As I leave the fourth floor behind, it is comforting to know that the investigation of Andreev levels will continue on in the more-than-capable hands of Tom Connolly and Pavel Kurilovich. I

look forward to seeing what they discover.

And to all of the others in Qlab that I had a chance to work with: Anirudh Narla, Chris Wang, Evan Zalys-Geller, Ioan Pop, Mike Hatridge, Shyam Shankar, Shantanu Munhada, Katrina Sliwa, Zlatko Minev, Zaki Leghtas, Uri Vool, Ananda Roy, Steven Touzard, Angela Kou, Clarke Smith, Zhixin Wang, Alex Grimm, Mazyar Mirrahimi, Sumita Ghosh, Alec Eickbusch, Wei Dai, Andy Ding, Vidul Joshi, Akshay Koottandavida, Vlad Kurilovich, Vladimir Sivak, Jaya Venkatraman, Zhixin Wang, Xu Xiao, Gangqiang Liu, Ioannis Tsioutsios, Philippe Campagne-Ibarcq, Andrew Lingenfelter and many more. I owe you all so much.

It's hard to imagine life in New Haven, or life in general, without Josh Phillips. He has made this place home for me through all these years. He has always been there, through my dark ages, his dark ages, our dark ages. So many delicious dinners, delicious beers. Life would've been so much worse without you.

I have many other friends to thank, both those made in New Haven and those from earlier periods of life: Josh Phillips, Hanna Ehrlich, Randi Martinez, Jeremiah Jewel, Jacob Neis, Andy Zhang, Martin Fuchs, Sarah Babinski, Matt Tyler, Taylor Southworth, Haley Dennis, Shannon Leslie. Willem Wyndham, Kirsten Hall, Leif Reinert, Eric Brenner. Patrick Gray, Dan Plattenberger. Taylor Vidal, Max Rose, Ari Zitin.

To my family. My sister, Ruth. Always supportive. Always thinking of me, making sure we stay close even across distance. So kind. So fun, even if she always goes to bed too early. I never would have guessed growing up how much of a friend Ruth would become (she used to be quite annoying). My parents, Tommy and Connie. Having lived a decent chunk of life by now, I have listened to so many people talk about all the ways their parents made mistakes in the upbringing, some big, some small. But in such conversations, I can't come up with a single example (I've really tried). I now know how rare this is; I now know how lucky I am. I could not have done this without you. Thank you.

And finally, to my beautiful, wonderful, wife Radha Sarkar. You light up my life in a way I didn't think possible. I am so happy I met you.

Part I

Key concepts and contributions

1

Introduction

1.1 The magic of superconductors and semiconductors

Much of condensed matter physics is concerned with understanding and controlling the behavior of electrons on the quantum-mechanical level. To this end, superconductors and semiconductors are two of the most well-studied classes of materials. Individually, superconductors and semiconductors possess incredible properties with far-reaching applications. In superconductors, pairing between electrons results in the flow of dissipation-less current, even in the presence of disorder. The defining characteristic of semiconductors, on the other hand, is a low density of charge carriers. The chemical potential can thus be controlled directly by applying an electric field (the field effect). In some semiconductors, relativistic effects result in enhanced g -factors and strong spin-orbit coupling.

In the context of quantum information processing, the properties of superconductors and semiconductors lend themselves to quantum mechanical control of electrons on vastly different scales. In superconducting circuits, a condensate composed of trillions of electrons can behave as a single continuous degree of freedom [Devoret and Schoelkopf 2013]. For instance, the complete quantum mechanical state of a superconducting LC oscillator can be described by the amount of charge on the capacitor. In contrast, semiconductors lend themselves to control over individual electrons [Hanson et al. 2007]. The field effect can be used to trap electrons in quantum dots, while enhanced g -factors make it easier to

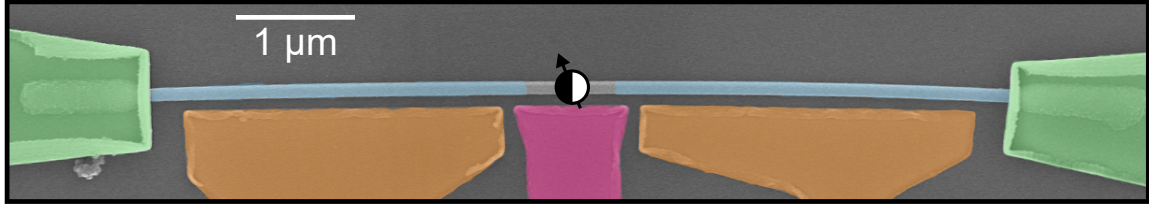


Figure 1.1: A single spinful quasiparticle trapped in a Josephson nanowire | Most of the 10 μm -long indium arsenide nanowire is coated in epitaxial aluminum (light blue), but a gap forms a weak link where a single quasiparticle can become trapped. In this thesis, we explore how the spin state of a such a quasiparticle can be detected and manipulated. Gates for electrostatic control are shown in pink/orange, and the leads to the rest of the circuit are shown in green.

achieve a sizeable energy splitting between the spin states. In addition, spin-orbit coupling can be used to achieve spin manipulation via an AC electric field [Nadj-Perge et al. 2010].

What would happen if we had the properties of both superconductors *and* semiconductors in the same electronic system? What new physics would emerge? What additional control could we achieve? These are the questions posed by experiments on **superconductor-semiconductor heterostructures**. The basic idea with such heterostructures is that if the contact between the two materials can be made good enough, the electrons can move back and forth across the interface unimpeded (their wavefunctions are no longer localized to one material or the other). In this way, the electrons can inherit characteristics of both materials, and simultaneously possess all the properties discussed above.

The work presented in this thesis was all done on a particular mesoscopic heterostructure: a superconductor-proximitized semiconductor nanowire [Chang et al. 2015; Krogstrup et al. 2015]. However, there is a critical detail: in the middle of the nanowire, there is a spatial gap in the proximitizing superconductor [Fig. 1.1]. The nanowire is thus a particular example of a **weak link**: two superconductors separated linked by a non-superconducting (aka “normal”) region. In this thesis, we will refer to this nanowire weak link as a **Josephson nanowire**.

1.2 What's so special about a weak link?

Weak links are the backdrop for what is perhaps the most famous phenomenon in mesoscopic superconductivity: the Josephson effect, in which a dissipation-less current flows across the weak link, even in the absence of a voltage bias [Josephson 1962]. Much less well-known than the Josephson effect, however, are the **Andreev levels**: single-particle, sub-gap, electronic degrees of freedom that are localized to the weak link [Beenakker and Van Houten 1991; Furusaki and Tsukada 1991]. Fundamentally, it is the Andreev levels that transport the Josephson supercurrent, and it is the Andreev levels that are the focus of this thesis.

In the context of superconducting qubits, Andreev levels are often forgotten. Why is this? Typically, superconducting quantum circuits are based on superconductor-insulator-superconductor weak links (also known as tunnel junctions). While these weak links possess millions of Andreev levels, the energies of the Andreev levels are very close to (but always below) the superconducting gap. As such, they are essentially frozen out, remaining in their supercurrent-carrying ground state. Yet fundamentally, they are fermionic degrees of freedom populated by the electronic spin-1/2 quasiparticle excitations of superconductors.

The physics of the Andreev levels (and therefore emergent Josephson effects) is determined by the geometric and material properties of the host weak link. In tunnel junctions, the Andreev level energies remain close to the superconducting gap. But as we will see, the Andreev levels of Josephson nanowires can have energies far below the gap edge. Moreover, thanks to the properties of the semiconductor, this sub-gap structure is strongly influenced by a rich interplay between superconductivity, electromagnetic field effects, device geometry, and spin-orbit coupling. In past experiments on Josephson nanowires, these effects have been harnessed to demonstrate gate-tunable weak links for superconducting qubits [Larsen et al. 2015; De Lange et al. 2015], non-abelian Andreev levels known as Majorana zero modes [Fu and Kane 2008; Lutchyn, Sau, and Das Sarma 2010; Oreg, Refael, and Oppen 2010; Mourik et al. 2012; Deng et al. 2016], and, critically for this work, spin-split Andreev levels even in the absence of a Zeeman field [Tosi et al. 2019].

Can we use the richness of Josephson nanowires to our advantage? Can we achieve control over the Andreev levels in ways which were previously impossible? What new Andreev physics can we observe? In this thesis, we explore these questions using the techniques of **circuit quantum electrodynamics (cQED)** [Blais et al. 2004; Wallraff et al. 2004]. Originally developed for manipulation and measurement of superconducting qubits, cQED gives us spectroscopic resolution and time-domain information that is inaccessible in more conventional DC transport experiments. Moreover, cQED is less invasive than DC transport. While transport necessarily entails pushing electrons through the system under study, in cQED the number of electrons in the circuit is often fixed, and only photons are exchanged with the system.

1.3 Structure of this thesis

This thesis is arranged into two parts: a main body where we present the ideas and results central to this thesis (chapters 2-5), and a series of later chapters that give detailed explanations and information concerning those same ideas and results.

In the main chapters, we will first give an overview of how Andreev levels arise in weak links, with a focus on how the Andreev levels of Josephson nanowires differ from those of conventional tunnel junctions. We will then discuss how Andreev levels can be probed using cQED, and present as a case study our investigation of pair transitions in Josephson nanowires. Finally, we will present the main result of thesis: the realization of the Andreev spin qubit, which is formed from the two spin states of a quasiparticle trapped in the Andreev levels of a Josephson nanowire.

2

Andreev levels

In this Chapter, we discuss on a qualitative level how Andreev levels arise in weak links, and how the Andreev levels of a Josephson nanowire differ from those of a tunnel junction. In addition, we give an overview of how the many-body states of Andreev levels can be expressed in terms of their quasiparticle occupation. For a more detailed explanation of these concepts, we direct the reader to Chapters 6 and 7. Note that throughout the main text (Chapters 2-5), we will restrict ourselves to the excitation picture of superconductivity. For a discussion of the pictures of superconductivity, see Chapter 6.

2.1 How do Andreev levels arise?

The Andreev levels of a weak link can be thought of as the electronic bound states of a finite square well, where the walls of the well are formed by the superconducting pair potential of the two leads [Fig. 2.1]. Just as with the finite square well taught in an introductory quantum course, the Andreev level energies can be found by demanding that the wavefunctions match at the boundaries of the well. To orient ourselves, let's first solve for the energies of electrons trapped in the familiar finite square well, where the potential walls have height V_0 [Fig. 2.1(a)].

We could solve this problem in the normal way by matching first and second derivatives at the well boundaries, but we can also come at things from the perspective of constructive interference. First, let's imagine an electron with energy $E < V_0$ moving to the right. Upon

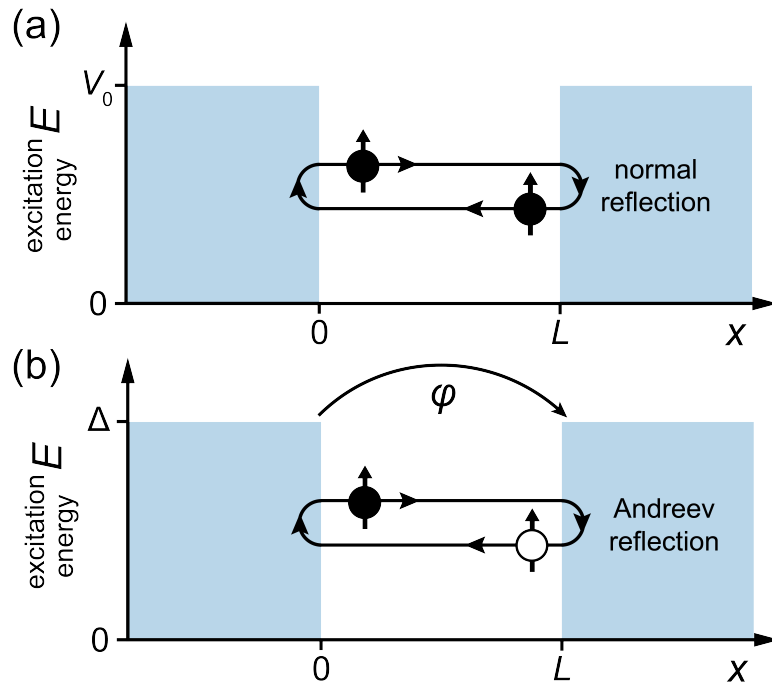


Figure 2.1: Comparing the levels of a finite square well to those of a weak link | (a) The electronic levels of a finite square well form due to constructive interference of the phases acquired in propagation and reflection. (b) While the same is true of the levels of a weak link, boundary conditions at the superconductor/normal interfaces result in Andreev reflection, whereby electrons are reflected into holes of the same spin, and vice versa. The total phase acquired in the depicted loop depends on the phase drop φ across the weak link.

encountering the right wall, it will be reflected with phase $\phi_r = -\cos^{-1}(2E/V_0 - 1)$, as can be seen from the formula for the step potential reflection coefficient (see “step potential” page of Wikipedia). It will then travel back to the left, reflect off the other wall, and pick up another factor of ϕ_r . In addition, the electron will acquire a dynamical phase kL as it travels between the walls. Constructive interference occurs when all the phases acquired in a round trip sum to a multiple of 2π :

$$2\pi n = 2\phi_r + 2kL \quad \phi_r = -\cos^{-1}(2E/V_0 - 1) \quad (2.1)$$

This equation can then be solved (though only numerically) for the energies of the bound states. Note that while in Fig. 2.1 we have only depicted spin up electrons, the constructive interference condition for spin down electrons is identical. Electrons trapped in a finite square well are thus spin-degenerate, as expected for a time-reversal-invariant system.

Now let’s follow the same logic for the Andreev levels of a weak link [Fig. 2.1(b)]. Similar to above, suppose we have an electron moving to the right in the normal region of the weak link with energy $E < \Delta$. Upon encountering the right superconductor, it must be reflected. However, there is a catch. Due to the superconducting pair potential, the single-particle wavefunctions in the superconductor are quite different than those of a normal metal: *they are superpositions of electrons and holes*. Wavefunction matching at the boundary therefore results in **Andreev reflection**: instead of the right-moving electron reflecting into a left-moving electron, it is reflected into a left-moving hole [Andreev 1964]. Perhaps the oddest thing about Andreev reflection is that it does not seem to conserve charge: $-e$ goes in, and $+e$ comes out. Where does this charge go? It turns out that it is injected into the superconductor in the form of a **Cooper pair**. We will come back to this in a second.

Similar to normal reflection, in Andreev reflection the charge carriers acquire a phase $\varphi - \cos^{-1}(E/\Delta)$, where φ is the phase of the superconducting pair potential. For conceptual/notational simplicity, we define the Andreev reflection phase ϕ_A as the φ -independent part. In this discussion, we set the phase of the pair potential to be zero in the left lead and φ in the right lead, so that φ is also the phase difference across the weak link [Fig. 2.1(b)].

We thus have a constructive interference condition similar to above:

$$2\pi n = 2\phi_A - \varphi \quad \phi_A = -\cos^{-1}(E/\Delta) \quad (2.2)$$

However, note that in this case we are neglecting the dynamical phase kL acquired by the charge carriers as they move across the weak link. This is known as the **short junction approximation**. Importantly, this approximation will not apply to all the results in this thesis; we will generalize Eqn. 2.2 in Chapter 4. Proceeding with the case of a short junction for now, we can solve the constructive interference condition to obtain an analytic expression for the energies:

$$E_A = \Delta |\cos \varphi/2| \quad (2.3)$$

Thus we see that the energy of the Andreev levels depends on the phase difference φ between the two superconductors. The Andreev levels therefore carry a current $I_A = \frac{dE_A}{d\varphi}$. Actually, we know this must be true from Andreev reflection. Let's focus on the loop depicted in Fig. 2.1(b), now re-depicted as the **blue loop** in Fig. 2.2(a). For every round trip of the charge carrier, $+/- 2e$ is injected into the left/right superconductor (a Cooper pair is lost/gained), and thus the loop carries positive current (charge moves left). For $\pi < \varphi < 2\pi$, the **blue loop** is the loop for which a solution to the constructive interference condition exists, as is consistent with the current carried $I_A = \frac{2\pi}{\Phi_0} \frac{dE_A}{d\varphi}$ by $E_A = \Delta |\cos \varphi/2|$ over this range of φ [Fig. 2.2(b)]. For $0 < \varphi < \pi$, however, it is the **red loop** of Fig. 2.2(a) whose solution exists. In this loop, the electrons and holes move in opposite directions as compared to the blue loop, again consistent with the energy-phase relation.

We are not quite done with our derivation of short-junction Andreev levels. In reality, every weak link will have some degree of disorder, which is ignored by Eqn. 2.3. Due to such disorder, electrons (holes) moving in the normal region can elastically scatter into electrons (holes) moving in the opposite direction. Mathematically, this is described by the transmission probability τ from one side of the normal region to the other, and is often referred to as the **transparency**. This coherently couples the red and blue loops as depicted by the black arrows in Fig. 2.2(a), and results in an avoided crossing between the two

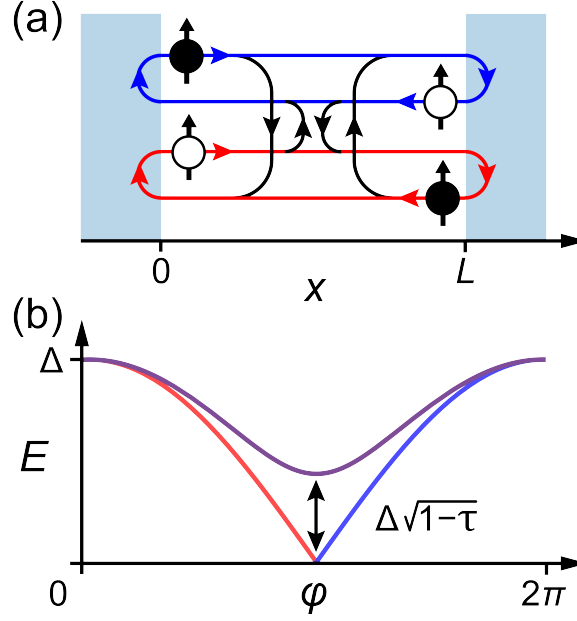


Figure 2.2: The spin-up Andreev level of a short junction | (a) Two loops of electrons and holes are possible, one with electrons moving to the right, and the other with electrons moving to the left. They are coupled by scattering within the normal region (black paths). (b) The Andreev level energy E_A without (red line for $0 < \varphi < \pi$, blue for $\pi < \varphi < 2\pi$) and with (purple line) scattering in the normal region. Scattering induces an avoided crossing of strength $\Delta\sqrt{1-\tau}$.

energies[Beenakker and Van Houten 1991]:

$$E_A = \Delta \sqrt{1 - \tau \sin^2 \frac{\varphi}{2}} \quad (2.4)$$

This equation is plotted in purple in Fig. 2.2(b), and is often called the short junction formula.

The final important feature of the Andreev levels is spin. Just as in the case of electrons trapped in a finite square well, the Andreev levels are spin-degenerate.¹ For the rest of this thesis, we will refer to each pair of spinful levels as an **Andreev doublet**. In the short junction regime, we have found that a weak link hosts a single Andreev doublet.

¹However, this is not a consequence of Kramers theorem, as φ breaks time-reversal symmetry. Thus, as we will see in Chapter 4, this degeneracy can be lifted without applying a Zeeman field.

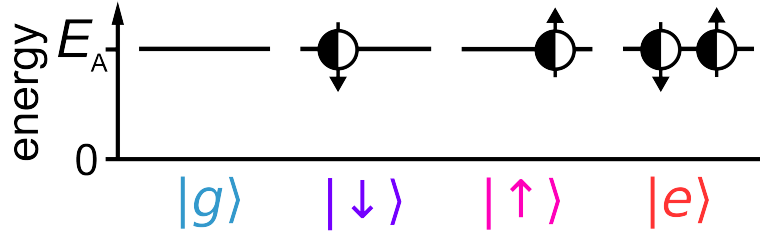


Figure 2.3: The four many-body configurations of an Andreev doublet | The even-parity states $|g\rangle$ and $|e\rangle$ have zero energy and energy $2E_A$ respectively, while the odd-parity states both have energy E_A .

2.2 Many-body configurations and microwave manipulation

This thesis explores manipulation and measurement of the quantum mechanical state of Andreev levels using cQED, and at its heart, cQED is a microwave technology. To understand how the Andreev levels can be manipulated with microwaves, we first need a concrete description of the quantum mechanical state of the weak link.

In the last section, we found that a short weak link hosts a single Andreev doublet. Each level of the doublet is fundamentally a fermionic mode, and as such can be described by whether it is occupied by a fermion or not. But what do we call the fermions that occupy the Andreev levels? Due to the superconducting pairing they are neither electrons nor holes, but rather superpositions of the two. These new fermions are known as **Bogoliubov quasiparticles**. Just like the electrons and holes from which they are built, the quasiparticles are spin-1/2 fermions. Because each level of an Andreev doublet can either be occupied by a quasiparticle or not, there are four possible many-body states [Fig. 2.3]:

1. **The ground state $|g\rangle$.** Both Andreev levels are unoccupied.
- 2/3. **The spin states $|\downarrow\rangle/|\uparrow\rangle$.** A spin down/up quasiparticle occupies the doublet.
4. **The excited state $|e\rangle$.** Both Andreev levels are occupied with quasiparticles.

How can these states be coupled with microwaves? Which states can we drive transitions between? For the case of a single Andreev doublet, the answer is straightforward; the only possible microwave transition is between $|g\rangle$ and $|e\rangle$. This reasons for this will be explained

below, but we will also introduce some concepts that will be useful when we move beyond the case of a single Andreev doublet in Chapter 4.²

To understand the possible microwave transitions between the Andreev levels, it is helpful to split the many-body configurations into two manifolds given by the parity of the number of quasiparticles: the even-parity states $|g\rangle$, $|e\rangle$, and the odd-parity states $|\uparrow\rangle$, $|\downarrow\rangle$. In an isolated system, it is impossible for microwaves to couple these two manifolds. The reason for this is conservation of **fermion parity**. In an isolated fermionic system, we would typically assume that the number of particles is conserved. In particular, we know that microwaves don't have nearly enough energy to produce/destroy electrons. However, in the description of superconductivity that we are using here, the number of particles is not conserved (note that this is just a mathematical artifact; in reality the number of electrons is still fixed). Instead, within this description, it is only the parity of quasiparticles that must be conserved (quasiparticles must be created/destroyed in pairs).

So long as we stay within a particular parity manifold, it is in principle possible to drive transitions between states. For instance, there is a microwave transition of frequency $2E_A/h$ between $|g\rangle$ and $|e\rangle$ [Fig. 2.4]. We will refer to transitions such as this, which create/destroy pairs of quasiparticles, as **pair transitions**. Transitions which maintain the number of quasiparticles, on the other hand, are known as **single-particle transitions**. For the case of an individual spin-degenerate Andreev doublet, there is a zero-frequency single-particle transition between $|\uparrow\rangle$ and $|\downarrow\rangle$. While we can't hope to drive this transition while it remains at zero frequency, we will see in Chapter 4 that it is difficult to drive even if spin degeneracy is broken. However, we will show that there are still ways to manipulate the spin states by using higher-energy Andreev doublets, though this requires going beyond the short-junction regime.

Sticking with the case of a single Andreev doublet for now, we are thus restricted to the pair transition of Fig. 2.4. At the end of this chapter, we will see how the pair transition can be used to coherently manipulate the even manifold, but first it's important to understand under what physical conditions a single pair transition will actually be addressable by a

²This is actually why we refer to $|e\rangle$ as the excited state, as opposed to the spin states which are also technically excited states. This notation/language was built around the Andreev pair qubit, as first demonstrated by the Saclay group [Janvier et al. 2015].

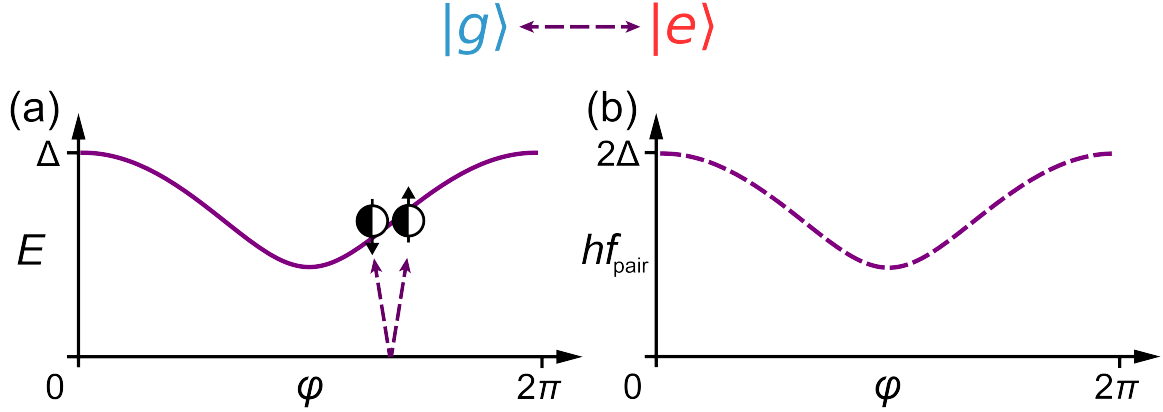


Figure 2.4: The pair transition $|g\rangle \leftrightarrow |e\rangle$ of an Andreev doublet| (a) A Cooper pair is broken by a photon with frequency $f_{\text{pair}} = 2E_A/h$, exciting two quasiparticles into the doublet. (b) Frequency f_{pair} of the pair transition as a function of φ . It is identical to E_A up to a factor $2/h$.

microwave drive.

2.3 From tunnel junctions to Josephson nanowires

In this section, we highlight the characteristics of Josephson nanowires that make coherent manipulation of pair transitions possible. In the next chapter, we will show how additional characteristics of Josephson nanowires enable manipulation of the spin states.

We have so far discussed Andreev physics on a fairly abstract level without considering the physical details of the weak link. While there are many physical instantiations of weak links, perhaps the most common is the tunnel junction. In a tunnel junction, the normal region of the weak link is insulating such that charge carriers must quantum tunnel from one side to the other. Tunnel junctions certainly host Andreev levels, and as was mentioned in the introduction, it is the Andreev levels that give rise to the Josephson effect that makes tunnel junctions useful in the first place. However, the Andreev levels of a Josephson nanowire are quite distinct from that of a tunnel junction due to geometric and material differences between the two kinds of weak links [Fig. 2.5].

One of the biggest differences between tunnel junctions and Andreev levels is the structure of their **conduction channels**. Throughout our discussion of Andreev physics, we have been pretending that a weak link is a one dimensional system. Of course, this is not

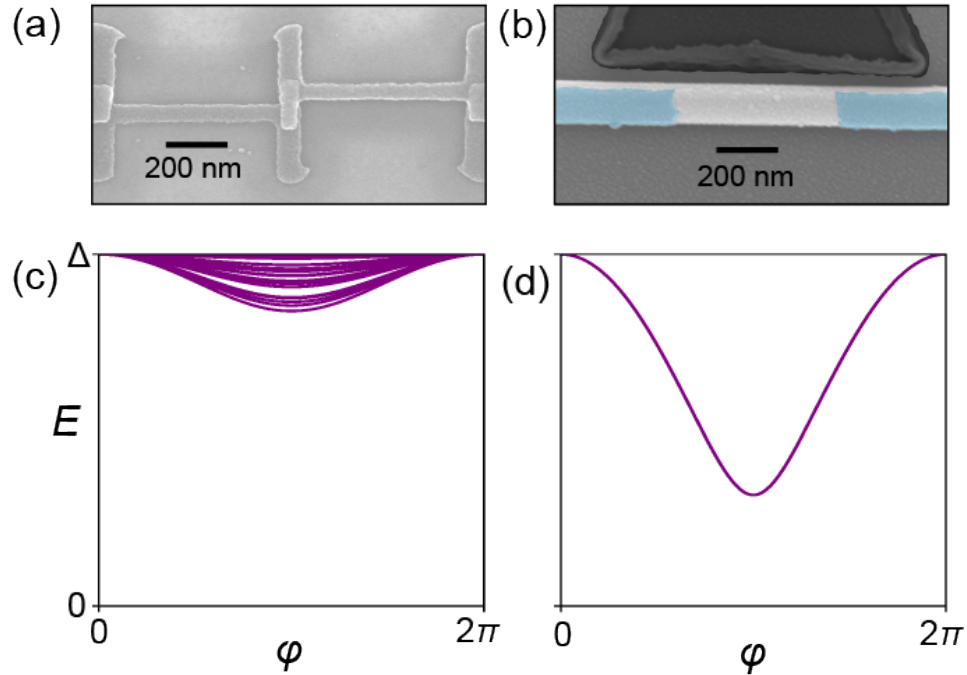


Figure 2.5: Comparing the Andreev spectrum of a tunnel junction to a Josephson nanowire | (a) Scanning electron micrographs of an aluminum/aluminum-oxide tunnel junction fabricated using a bridge-free technique. (b) Micrograph of an indium arsenide Josephson nanowire coated in epitaxial aluminum (blue), with a gap in the middle forming the weak link. The black structure is a gate, which we will ignore for the moment. Note the scale bars; despite what one might expect given the name, a nanowire is actually roughly the same physical size as a typical tunnel junction. Moreover, the charge carriers in the semiconductor nanowire have a much slower Fermi velocity than in the aluminum junction; this makes the nanowire “look” even bigger. (c) In a tunnel junction, there are millions of low- τ conduction channels, each hosting an Andreev doublet. Note that the number of Andreev doublets has been decreased and $\bar{\tau}$ has been increased for visual clarity. (d) A Josephson nanowire can host a single, high- τ Andreev doublet. The spectrum is thus much simpler, and near $\varphi = \pi$ the level energy is in the range accessible with cQED experiments.

true; both the superconducting leads and the normal region must have some 3D structure. Nonetheless, we can hold onto this 1D-ness by introducing the concept of a conduction channel.³ Imagine the leads of the junction as electronic waveguides; the conduction channels are then the modes of those waveguides. Just as with waveguides in other contexts, each conduction channel (mode) is given by a particular quantization of the fields in the transverse direction. Unlike a typical waveguide, the disorder present in all junctions results in coherent mixing between the transverse modes. Nonetheless, just as with a typical waveguide, the resultant eigenstates (the conduction channels) can still be treated as separate 1D systems, each with its own transparency τ_i . Our above discussion of Andreev levels can then be applied to each conduction channel separately, such that each will host a single Andreev doublet.

The Andreev spectrum of a weak link is strongly influenced both by the number of conduction channels as well as their transparency. Suppose we have typical aluminum/aluminum-oxide tunnel junction that might be used in a transmon qubit. Such a junction possesses millions of conduction channels, and thus hosts millions of Andreev doublets [Fig. 2.5(a/c)]. However, because the charge carriers have to quantum tunnel across the oxide, each conduction channel has an extremely low transparency, say $\bar{\tau}_i = 10^{-6}$. The avoided crossing depicted in Fig. 2.2 is thus quite strong, and all of the Andreev level energies are close to the gap edge. If we want to study individual Andreev levels, and in particular, if we want to use the microwave techniques of cQED, there are two problems with the Andreev levels hosted by tunnel junctions. The first is that for aluminum, $\Delta/h \approx 44$ GHz, and thus all of the Andreev levels will have energies close to this value. This is outside the frequency range of cQED experiments, which typically operate between 1 and 10 GHz. The second problem is that, even if the Andreev levels were at lower energies, there would just be too many of them; they essentially form a continuum. We would have no hope of probing individual levels.

Josephson nanowires can solve both of these problems for us [Fig. 2.5(b/d)]. Due to the low carrier density of the semiconductor, the nanowire has only a few conduction chan-

³This description of conduction channels is a bit rough. For a more in depth and precise discussion of conduction channels, I recommend “Quantum Transport” by Nazarov and Blanter.

nels. Moreover, due to the atomic-level order of the nanowire and the epitaxial aluminum, each channel can have a transparency that approaches one. The few Andreev levels of a Josephson nanowire can thus be brought down to a regime that our microwave generators can reach (< 20 GHz). We now outline how such microwave techniques can be used to coherently manipulate Andreev levels in the short junction regime.

2.4 The Andreev pair qubit

The **Andreev pair qubit** was proposed in 2003 by Zazunov *et al.*, and realized experimentally in 2015 by Janvier *et al.* in atomic point contacts made from break junctions. The idea is to use the $|g\rangle$ and $|e\rangle$ states of a short weak link as a qubit, using a microwave drive on the pair transition to achieve coherent manipulation. In this work, we realized an Andreev pair qubit using the Andreev levels of a Josephson nanowire. A schematic of such a device is shown in Fig. 2.6(a). Here we give an overview of how the device works, and leave experimental results for Chapter 3.

As we saw in the last section, the ground state $|g\rangle$ of the Andreev doublet has zero energy by definition, while the doubly-occupied state $|e\rangle$ has energy $2E_A$. Ignoring an overall offset, the Hamiltonian for the Andreev pair qubit is thus

$$H_A = E_A \sigma_z \quad (2.5)$$

Here we will focus on two aspects of how such a qubit works when it is realized using a Josephson nanowire: how the qubit frequency can be tuned, and how we can use microwaves to manipulate the qubit state.

First, let's focus on tuning the qubit frequency. In section 2.2, we saw that the frequency of the pair transition was given by

$$f_{\text{pair}} = 2E_A/h = \frac{2\Delta}{h} \sqrt{1 - \tau \sin^2 \frac{\varphi}{2}} \quad (2.6)$$

In this experiment, we had two *in-situ* control knobs over f_{pair} . The first was a loop flux Φ as shown in Fig. 2.6(a), which set the nanowire phase according to $\varphi = 2\pi\Phi/\Phi_0$. The second

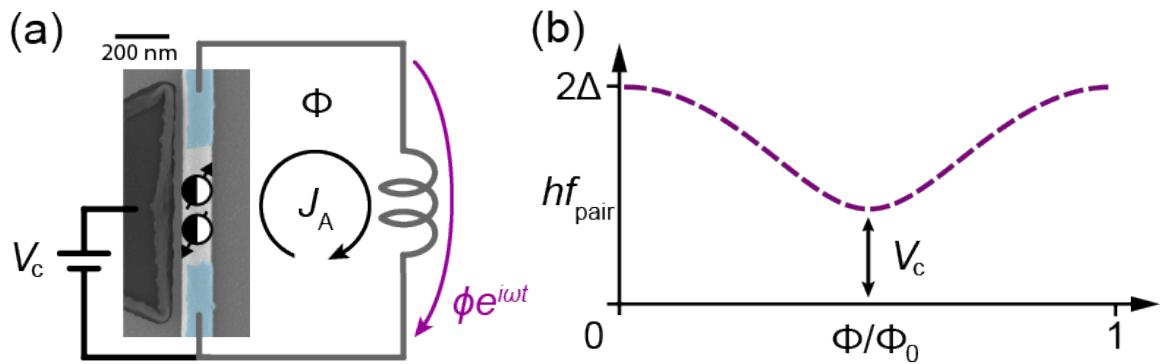


Figure 2.6: An Andreev pair qubit in a Josephson nanowire | (a) Scanning electron micrograph of a Josephson nanowire and schematic of DC bias circuitry. The pair qubit is depicted in its excited state $|e\rangle$, where two quasiparticles are trapped in the weak link. A flux Φ threads the grey superconducting loop, which controls f_{pair} as shown in (b). The transparency τ is affected by the gate voltage V_c , thereby giving us control over the strength of the avoided crossing. The pair transition is driven by an AC flux $\phi e^{i\omega t}$, which couples to the current operator of the weak link J_A . The drive is depicted as dropping across the loop inductance, but can equally be thought of as dropping across the weak link as the two elements are wired in parallel.

was a gate voltage V_c (c for “cutter”), which we used to tune the chemical potential in the nanowire via the field effect. As adjusting the chemical potential affected τ and therefore the strength of the avoided crossing,⁴ V_c provided further control over the Andreev pair qubit frequency [Fig. 2.6(b)]. In general, both control knobs were necessary to bring the pair transition down to a frequency accessible by our microwave generators. We needed the flux bias to be roughly $\Phi \approx \Phi_0/2$, and we needed the gate voltage to achieve a high transparency such that the avoided crossing was not too large.

Even with the pair transition frequency in an accessible range, it is not a given that it can be driven. In general, how does microwave radiation couple to Andreev levels? This question is a topic of ongoing research, but here we present the basic ideas [Zazunov et al. 2003; Bretheau 2013; Janvier et al. 2015]. Suppose we apply a microwave drive to the Josephson nanowire. This will produce an oscillating flux across the nanowire $\phi e^{i\omega t}$ [Fig. 2.6(a)]. If we suppose that ϕ is small, we can take it into account by Taylor expanding the Hamiltonian about the DC flux bias Φ :

$$H = H_A + \phi e^{i\omega t} \frac{\partial H_A}{\partial \Phi} + \dots \quad (2.7)$$

The first term is just our original Hamiltonian H_A , but in the second term we see that our microwave drive couples to a new operator $\frac{\partial H_A}{\partial \Phi}$. It turns out that this is the **current operator** of the weak link:

$$J_A = \frac{\partial H_A}{\partial \Phi} = \frac{2\pi}{\Phi_0} \frac{\partial H_A}{\partial \varphi} \quad (2.8)$$

Similarly to the conventional equation for the current $I = \frac{2\pi}{\Phi_0} \frac{dE}{d\varphi}$, the current operator is the derivative of the Hamiltonian with respect to flux. However, we need to be careful when computing J_A . We know that the qubit energy E_A depends on φ , so that will give us some contribution to the current operator. But it turns out the Andreev level wavefunctions also depend on φ . And because σ_z in Eqn. 2.5 is written in the basis of the Andreev levels, it inherits their φ -dependence. The math associated with computing $\frac{\partial \sigma_z}{\partial \varphi}$ is a bit hairy, so here

⁴For the measured gate-voltage dependence of the Andreev spectrum, see Chapter 11.

we just present the final result and leave the derivation for Chapter 11:

$$J_A = I_A[\sigma_z(\varphi) + \sqrt{1 - \tau} \tan \frac{\varphi}{2} \sigma_x(\varphi)] \quad (2.9)$$

While the diagonal elements are still given by $I_A = \frac{2\pi}{\Phi_0} \frac{dE_A}{d\varphi}$, we find that the derivative of σ_z has created off-diagonal elements. This is extremely important. It is the off-diagonal elements of the current operator that allow us to drive transitions between Andreev levels, as we must have an operator with a non-zero matrix element between $|g\rangle$ and $|e\rangle$.

This concludes our overview of Andreev levels in short Josephson nanowires, and how they can be manipulated using microwave drives. In the next chapter, we will see how the many-body state of the weak link can be detected using cQED.

References

- Andreev, A., “Thermal conductivity of the intermediate state of superconductors”, Zh. Eksperim. i Teor. Fiz. **46** (1964).
- Beenakker, C. and H. Van Houten, “Josephson current through a superconducting quantum point contact shorter than the coherence length”, Phys Rev. Lett. **66**, 3056 (1991).
- Brethau, L., “Localized excitations in superconducting atomic contacts: probing the Andreev doublet.”, PhD thesis (Ecole Polytechnique X, 2013).
- Janvier, C., L. Tosi, L. Brethau, Ç. Ö. Girit, M. Stern, P. Bertet, P. Joyez, D. Vion, D. Esteve, M. F. Goffman, H. Pothier, and C. Urbina, “Coherent manipulation of Andreev states in superconducting atomic contacts”, Science **349**, 1199–1202 (2015).
- Zazunov, A., V. Shumeiko, E. Bratus, J. Lantz, and G. Wendin, “Andreev level qubit”, Phys. Rev. Lett. **90**, 087003 (2003).

3

Probing Andreev levels with cQED

In this chapter, we first present the basic ideas of circuit quantum electrodynamics. We then describe the operating principles of the device used in this work, before demonstrating how we used it to investigate pair transitions in Josephson nanowires.

3.1 What is cQED?

Just based on the name, circuit quantum electrodynamics (cQED) sounds a bit intimidating. But despite what the name implies, you really don't need a strong grasp of quantum electrodynamics in order to understand cQED. The main idea behind cQED is much more straightforward, and can be understood by anyone who has taken an introductory course in quantum mechanics: interesting and useful things can happen when you couple a quantum harmonic oscillator to another quantum system. In cQED, the oscillators in question are superconducting microwave resonators, which form a part of a larger microwave circuit (hence the "circuit" part of the name).¹ The superconducting nature of these resonators makes them extremely low loss, which minimizes decoherence and makes the joint quantum dynamics of the resonator/quantum system much easier to observe. Moreover, be-

¹Historically, the QED part of the name was inherited from cavity QED, which investigates interactions between matter and light on the single quantum level.

cause the resonators are at microwave frequencies, technology developed in the telecommunications industry (generators, passive microwave components, etc.) can be directly applied.

Originally, cQED was developed for readout and control of superconducting qubits [Blais et al. 2004; Wallraff et al. 2004]. The idea is this: suppose you have a quantum system in which you have stored information. How do you detect what state the system is in? Experimentally, this can be quite challenging. However, one thing we certainly know how to do in the real world is measure the frequency of a resonator. How can we use this to our advantage? Suppose we couple our system of interest to a resonator. It turns out that if you arrange things just so, *the frequency of the resonator will depend on the quantum state of the system*. Thus, we can determine the system state by measuring the resonator's frequency.

Let's see how this works for a two-level system (a qubit). Imagine we couple the system of interest to a resonator via an operator that can exchange excitations between the system and the resonator. The full Hamiltonian for the resonator, qubit and the excitation-exchanging coupling is

$$H_{\text{JC}} = \hbar\omega_r a^\dagger a + \frac{\hbar\omega_q}{2} \sigma_z + \hbar g_c (a^\dagger \sigma_- + a \sigma_+) \quad (3.1)$$

In the literature, this is known as the Jaynes-Cummings Hamiltonian. In cQED, experiments are typically designed such that the frequency difference between the resonator and the qubit is much bigger than the coupling between them $g_c \ll |\omega_r - \omega_q|$. This is known as the **dispersive regime**. In this regime, we can use standard time-independent perturbation theory to describe the effect on the energies. In particular, we find that to second-order in $g/|\omega_r - \omega_q|$ the correction to the joint qubit-resonator energies $E_{n,\sigma}$ is (the first-order correction is zero):

$$E_{n,-1} = \frac{|\langle n-1, +1 | \hbar g_c a \sigma_+ | n, -1 \rangle|^2}{\hbar\omega_r(n - (n-1)) - \hbar\omega_q} = -\frac{\hbar g_c^2 n}{(\omega_q - \omega_r)} \quad (3.2)$$

$$E_{n,+1} = \frac{|\langle n+1, -1 | \hbar g_c a^\dagger \sigma_- | n, +1 \rangle|^2}{\hbar\omega_r(n - (n+1)) + \hbar\omega_q} = \frac{\hbar g_c^2 (n+1)}{(\omega_q - \omega_r)}$$

Taking the difference and ignoring the n -independent part in the first step, we have:

$$\begin{aligned} E_{n,+1} - E_{n,-1} &\rightarrow \frac{\hbar g_c^2 n}{(\omega_q - \omega_r)} + \frac{\hbar g_c^2 n}{(\omega_q - \omega_r)} \\ &= \frac{2\hbar g_c^2 n}{(\omega_q - \omega_r)} \end{aligned} \quad (3.3)$$

Replacing n with $a^\dagger a$, the Hamiltonian can be expressed as

$$H_{\text{dispersive}} = \hbar(\omega_r + \chi\sigma_z)a^\dagger a + \frac{\hbar\omega_q}{2}\sigma_z \quad \chi = \frac{g_c^2}{\omega_q - \omega_r} \quad (3.4)$$

where χ is known as the dispersive shift.² *This is probably the most important equation in cQED.* It tells us that, in the dispersive regime, the Jaynes-Cummings coupling leads to a qubit-state-dependent shift of the resonator frequency by $\pm\chi$. Therefore, if we measure the frequency of the resonator, we can detect the quantum state of the qubit. In general, we want χ to be large such that the state-dependent frequency shift is easier to detect. This can be achieved by cranking up g_c , though we have to be careful that we don't leave the perturbative regime. We can usually stay safely perturbative by increasing $|\omega_r - \omega_q|$, which only enters once in χ as compared to the power of 2 on g_c .

But how do we actually engineer the coupling between the resonator and the system of interest? While in theory we can imagine making g_c arbitrarily large, this is much more difficult in practice, and depends a lot on the nature of the system that we want to couple to the resonator. If the system is a transmon qubit [Koch et al. 2007], for instance, we typically use an electric dipole-dipole coupling between the qubit and the resonator. This is straightforward because the transmon (and therefore its dipole moment) is reasonably large ($\sim 100 \mu\text{m}$). However, if our system of interest is a single electron spin, achieving a large coupling is much more difficult since the direct interaction between the spin and the resonator magnetic field is fairly small. Moreover, sometimes the system of interest doesn't couple directly to electromagnetic fields at all, such as phonons in a substrate. In

²In this thesis, we will stick to the convention that χ is shift of the resonator frequency given a particular system state. Some authors use $\chi \rightarrow \chi/2$.

such situations, we must invent new mechanisms of coupling.³

Things become even more complicated if our system of interest is not a qubit. Luckily, we can generalize the arguments presented above for the Jaynes-Cummings Hamiltonian. In general, any finite-sized quantum system can be treated in the above way (though it does need to be highly coherent). At the end of the day, if we want to distinguish between two quantum states, we need their dispersive shifts to be significantly different. The generalized equation for the dispersive shift χ_i of state $|i\rangle$ can be written as⁴

$$\chi_i = \sum_j \frac{2\omega_{ij}g_{ij}^2}{\omega_{ij}^2 - \omega_r^2} \quad (3.5)$$

We see that there are two options if the dispersive shifts are to be different: either we need the coupling strengths g_{ij} to be substantially different, or we need the spectrum to be sufficiently non-degenerate. This will be important when we consider spin in Chapter 4.

Supposing we can engineer significant dispersive shifts of the resonator frequency, we can then detect the system state by measuring the resonator frequency. In this work, the resonator frequency was probed using microwave reflectometry: by capacitively coupling the resonator to a transmission line, the reflection coefficient Γ of a probe tone incident on the resonator was measured. Critically, Γ depends on the frequency of the resonator, and therefore on the quantum state of the system of interest. This is discussed quantitatively in Chapter 10. In the following we will, often break the reflection coefficient into its real and imaginary parts $\Gamma = I + iQ$.

Before moving on, a final comment on cQED. In this section, we have motivated why coupling a coherent quantum system with a discrete number of levels is a useful thing to do from the point of view of measuring the system. However, cQED has come to mean much more than this. At Yale, for instance, instead of storing quantum information in qubits and measuring them with resonators, the situation has been reversed. Quantum information is instead stored in resonators and manipulated/detected using coupled qubits.

³For phonons, piezoelectric couplings have been used successfully [Chu et al. 2017].

⁴Note that when we apply this equation to the two-level case, we must assume $\omega_r \simeq \omega_q$ to get back to Eqn. 3.4. This is known as the rotating wave approximation, and amounts to ignoring terms like $\sigma_+ a^\dagger$ in the coupling Hamiltonian [Manucharyan 2012].

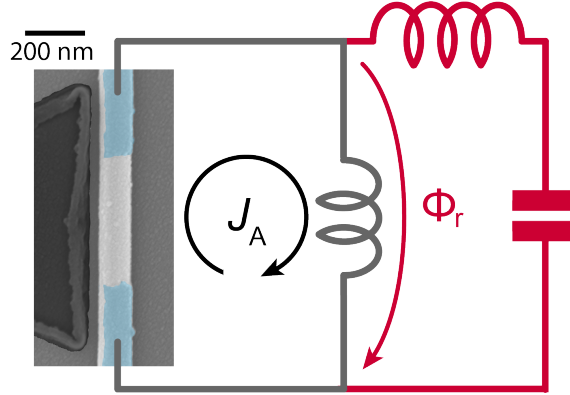


Figure 3.1: Coupling a Josephson nanowire to a superconducting microwave resonator | The Josephson nanowire (scanning electron micrograph) is wired up in parallel with a portion of the resonator’s inductance (gray), over which a portion of the resonator’s flux drops Φ_r . The quantum-mechanical current J_A created by the Andreev levels flows through the nanowire and around the gray loop, passing through the shared inductance. This results in a coupling term in the Hamiltonian between the resonator (red) and Andreev levels of the form $H_c = \Phi_r J_A$.

3.2 Coupling to the Andreev levels

Here we outline the basic ideas behind an inductive coupling between Andreev levels and a microwave resonator. While this can give us a flavor for how the coupling works, a full theoretically rigorous treatment of the coupling is a topic of ongoing research. For a more in-depth discussion, see Chapter 11.

As we touched on in the last section, the coupling between a resonator and a quantum system of interest must be engineered depending on the nature of the system. This thesis focuses on using cQED to probe Andreev levels. How do we couple the Andreev levels to a microwave resonator? One of the most miraculous things about Andreev levels is that, despite the fact that their wavefunction is completely localized to the weak link, they can carry a current that extends over much larger distance scales. As we saw in Chapter 2, we can drive transitions by coupling a microwave drive to the current operator J_A . We can couple the Andreev levels to a resonator using a similar trick [Fig. 3.1]. By wiring the Josephson nanowire up in parallel with a portion of the resonator’s inductance, a fraction of the resonator’s flux drop will couple to J_A , just as we saw with the flux of the microwave drive. The difference here is that the resonator’s flux is now a quantum-mechanical oper-

ator $\Phi_r(a + a^\dagger)$. The coupling term is thus [Bretheau 2013; Janvier et al. 2015]

$$H_c = \Phi_r(a + a^\dagger)J_A \rightarrow g_c(\varphi)(a^\dagger\sigma_- + a\sigma_+); \quad g_c(\varphi) = \Phi_r\sqrt{1 - \tau}I_A(\varphi)\tan(\varphi/2) \quad (3.6)$$

where we have dropped the diagonal part of the current operator and performed a rotating wave approximation. We thus find the the inductive coupling can be expressed as the Jaynes-Cummings Hamiltonian with a φ -dependent g_c . We discuss this point in more detail in Chapter 11, but we do note here that g_c is maximum at $\varphi = \pi$ for the Andreev pair qubit. This is very convenient: at half flux, $\chi = \frac{g_c^2}{2\pi f_{\text{pair}} - \omega_r}$ is maximized both because the numerator becomes big and because the denominator becomes small.

3.3 The device

At this point, I'd like to give a special thanks to my wonderful overseas collaborators, without whom none of this work would have been possible. The devices had quite a journey before they found their way to our lab at Yale. The nanowires themselves were grown in Copenhagen by Jesper Nygård and Peter Krogstrup before being shipped to the group of Attila Geresdi at TU Delft. Two of Attila's students, David van Woerkom and Daniël Bouman, then fabricated the devices. David fabricated the early iterations, and Daniël the later. Again, many thanks to all of these scientists.

Thus far in this thesis, we have covered the basics of the two sub-fields that these experiments merge: the physics of Andreev levels hosted by weak links, and circuit quantum electrodynamics. We now discuss how probing Andreev levels with cQED works on the experimental level. Here we highlight the salient features of the device and its design [Fig. 3.2], leaving a full discussion of the experimental setup for Chapter 10. Throughout these experiments, the device design evolved somewhat (again, see Chapter 10), but the basic layout remained essentially unchanged. The micrographs in Fig. 3.2 are of the device design at the time of this writing.

On the practical level, perhaps the ingredient that most distinguishes these experiments from more typical cQED is the need for DC voltages. This made things a bit tricky: we

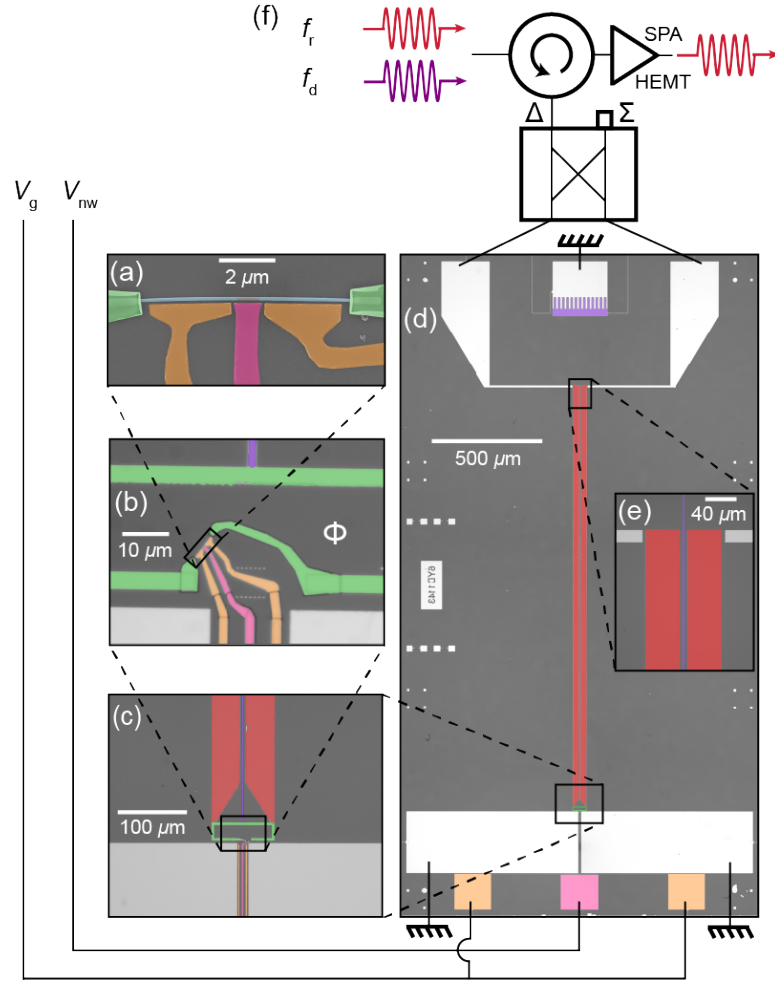


Figure 3.2: The device | (a) An indium arsenide nanowire coated in epitaxial aluminum (blue), with a gap in the aluminum forming the weak link. The cutter gate (pink) was biased to V_c , while the plunger gates (orange) were biased to V_p . The Josephson nanowire was connected to the rest of the circuit using niobium titanium nitride contacts (green). (b/c) Zooming out, we see that the nanowire is embedded in a superconducting loop (green). This loop was used to bias the Josephson nanowire with a flux Φ . In addition, one arm of the loop served as the shared inductance between the nanowire and the resonator (maroon). (d) Full device. The differential $\lambda/4$ mode of the coplanar strip resonator (maroon) is inductively coupled to the nanowire at its current anti-node (lower end). At its voltage anti-node (upper end), it is capacitively coupled to microstrip lines that lead to the depicted external microwave circuitry. The purple trace that runs between the microwave lines connects to a finger capacitor, serving as a reference for the gates voltages. (f) Both the readout tone (maroon, frequency f_r) and the drive tone (purple, frequency f_d) were routed to the resonator via a 180° hybrid. The reflected readout tone was amplified by an SPA [Fratini et al. 2018] followed by a HEMT, before being processed at room temperature.

had to engineer the device such that we could couple in DC voltages, while at the same time ensuring that microwave photons from the resonator would not get lost down the DC lines. In principle there are filters one could design for this purpose, but we took a different approach. Looking at the full device in Fig. 3.2(d), one can see that it is almost perfectly mirror symmetric. This is very intentional. Because the resonator is a differential mode with a voltage node at the location of the Josephson nanowire, this symmetry ensures that the microwave voltage is zero everywhere along the line bisecting the device. Placing the gates along this zero-voltage line thus mitigated microwave loss.

Aside from mitigating resonator loss, there was another important design consideration for the purposes of DC gating. In order for the field effect to work, we need a strong electric field between the gate and the nanowire. In other words, we need the nanowire to be at DC ground such that the gate voltage drops between the gate and the nanowire. However, the nanowire is galvanically connected to the resonator. We thus needed to ground the nanowire/resonator island without perturbing the resonator mode. Again, we took advantage of the symmetry of the device. In Fig. 3.2(d), a purple trace can be seen running between the two strips of the resonator. This connects to a large capacitor, effectively grounding the island (this capacitance is much larger than the gate/nanowire capacitance). Like the gates, because this strip runs along the zero-voltage line, it does not perturb the resonator mode.

Finally, the differential resonator mode was read out in reflection using a 180° hybrid [Fig. 3.2(f)]. The signal was amplified by the wonderful SNAIL parametric amplifier designed by Nick Frattini and Vlad Sivak [Frattini et al. 2018], as well as a HEMT. In the most recent version of the device, we also supplied the drive tone via the 180° hybrid.⁵

3.4 Investigating pair transitions

The results presented in this section summarize our paper entitled "Direct Microwave Measurement of Andreev-Bound-State Dynamics in a Semiconductor-Nanowire Josephson Junction" by Hays et al., published in PRL in 2018. For more detailed information, see Chapters 13 and 10.

⁵In earlier experiments we used a separate drive port. See Chapter 10 for details.

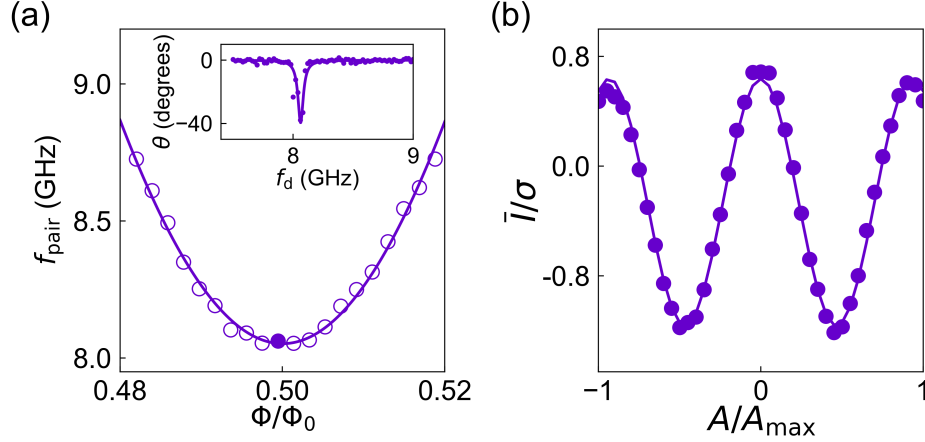


Figure 3.3: Control of the Andreev pair qubit frequency | (a) Inset: Continuous-wave two-tone spectroscopy reveals the qubit transition (θ is the average phase of the reflected readout tone). The transition frequency f_{pair} is extracted from a best fit to a Lorentzian line shape. Main figure: dependence of f_{pair} on Φ . Solid line is a fit to the short-junction formula for f_{pair} [Eqn. 2.6]. (b) Rabi oscillations of the Andreev pair qubit. The qubit oscillates between $|g\rangle$ and $|e\rangle$ as the amplitude A of a pulse resonant with f_{pair} is varied. The y -axis is normalized by the standard deviation σ of the $|g\rangle$ distribution, see Fig. 3.4.

The first step in our investigation of the Andreev pair qubit was locating the pair transition. After some tuning of the Josephson nanowire using the gate voltage V_c (see Chapter 11 for details on this), we located the pair transition near half flux $\Phi = \Phi_0/2$ using two-tone spectroscopy [Fig. 3.3(a), inset]. As expected, we found that the pair transition frequency increased symmetrically away from half flux [Fig. 3.3(a)]. This spectroscopy data was some of the first we obtained, and had to be taken very quickly due to electrostatic instabilities in the system (an issue that was later solved, see Chapter 10). This is the reason the data was taken over such a small flux range. Later in this thesis, we will see more detailed examples of two-tone spectroscopy measurements of Andreev levels in Josephson nanowires.⁶

Having found the pair transition, we proceeded to coherent manipulation of the Andreev pair qubit. Fig. 3.3(b) shows Rabi oscillations of the qubit as a function of the drive amplitude A . Measurements of the energy lifetime T_1 and coherence lifetime T_2 of the qubit can be found in Chapter 13. This data represents the first coherent manipulation of Andreev levels in Josephson nanowires.

For the entirety of this chapter thus far, we have only discussed the even manifold of

⁶In particular, we direct the reader to Chapter 11 for many examples of rich Andreev spectra.

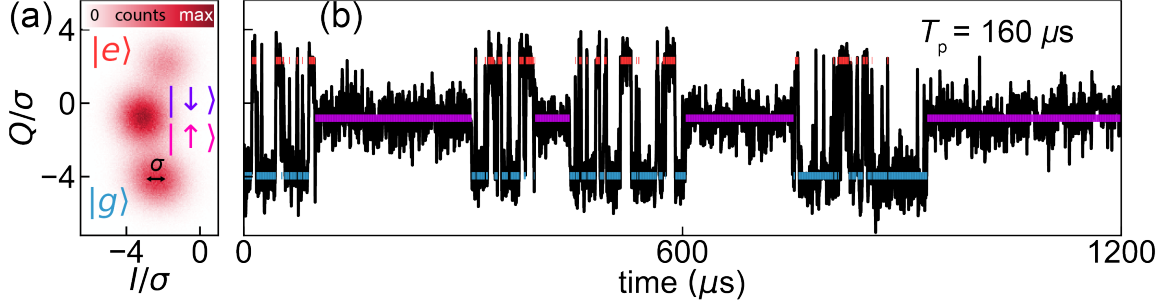


Figure 3.4: Quantum jumps between the many-body configurations of a single Andreev doublet | (a) Histogram of the I and Q quadratures of the resonator readout tone ($f_{\text{pair}} = 8.5$ GHz). Each count corresponds to an integration period of 480 ns and the total number of counts is 9.6×10^5 . The (I, Q) -pairs cluster into three Gaussian distributions corresponding to the many-body configurations of the Andreev levels [see Fig. 2.3]. Data are rescaled by the standard deviation σ of the $|g\rangle$ distribution. (b) Time evolution of Q/σ for a sample of the data in (a). The state assignments shown by the blue, purple, and red bars result from a maximum-likelihood estimation to a hidden Markov model (see Chapter 13). This also yields the parity lifetime of the doublet $T_p = 160 \mu\text{s}$. We note that the data was taken with only a ~ 500 MHz detuning between f_{pair} and f_r , such that f_{pair} was being off-resonantly driven by the readout tone. It has also been observed that the readout tone can affect the parity dynamics [Janvier 2016].

an Andreev doublet ($|g\rangle$ and $|e\rangle$). What about the spin states $|\uparrow\rangle$ and $|\downarrow\rangle$? When we left the spin states in section 2.2, we had pointed out that in the short junction regime, there was no available microwave transition for either spin state, and thus there was no hope of manipulating them. However, it turns out that we can still detect them even in the short junction regime. While the Andreev doublet is in the even manifold, we know the resonator frequency is shifted by $+/- \chi$ depending on whether the Andreev doublet is in $|e\rangle/|g\rangle$. However, if a quasiparticle falls into the Josephson nanowire, the only transition for it to undergo is back out of the nanowire up onto the gap edge (~ 40 GHz). This is so far detuned from the resonator transition that χ is essentially zero. We thus expect three different values for the resonator frequency: in the even manifold, the resonator frequency is $\omega_r \mp \chi$, but in the odd manifold, it is ω_r . This means that we can directly probe the real-time dynamics of an Andreev doublet between $|g\rangle$, $|e\rangle$ and the odd manifold, as shown in the quantum jumps experiment displayed in Fig. 3.4.

We see that while the system moves quickly⁷ between $|g\rangle$ and $|e\rangle$, it can remain in the

⁷Note that due to the relatively weak coupling $g_c/2\pi = 23$ MHz in this original experiment, we had to operate the system with f_{pair} quite close to the resonator at a detuning of only ~ 500 MHz. The readout tone was thus

odd manifold on much longer timescales [Janvier et al. 2015; Zgirski et al. 2011]. We refer to this timescale as the **parity lifetime**. Sometimes known as the poisoning time, here we define the parity lifetime as:

$$T_p = (\gamma_{\text{even,odd}} + \gamma_{\text{odd,even}})^{-1} \quad (3.7)$$

The parity lifetime is thus a T_1 -like quantity; it is one of the timescales that limit Andreev qubits. Moreover, the parity lifetime will limit the operation of future topological qubits. The idea with these potential qubits is to encode quantum information in the parity of Majorana modes. While protected from local noise, these qubits will be just as susceptible to parity switches as our Andreev qubit is.

In this initial experiment, we were able to study the even manifold of a single Andreev doublet in detail, and we were able to obtain some information on the odd manifold. However, there were many questions left unanswered. What are the internal dynamics of the odd manifold? How long does an individual spin state live? To answer these questions, we took advantage of additional properties of Josephson nanowires that split the energy and associated resonator response of the spin states. This is what we explore in the next chapter.

References

- Blais, A., R.-S. Huang, A. Wallraff, S. M. Girvin, and R. J. Schoelkopf, “Cavity quantum electrodynamics for superconducting electrical circuits: an architecture for quantum computation”, *Phys. Rev. A* **69**, 062320 (2004).
- Bretheau, L., “Localized excitations in superconducting atomic contacts: probing the Andreev doublet.”, PhD thesis (Ecole Polytechnique X, 2013).
- Chu, Y., P. Kharel, W. H. Renninger, L. D. Burkhardt, L. Frunzio, P. T. Rakich, and R. J. Schoelkopf, “Quantum acoustics with superconducting qubits”, *Science* **358**, 199–202 (2017).

off-resonantly driving f_{pair} , and inducing the observed large excited state population. In later experiments, we were able to increase the coupling and so enter the QND regime typical of cQED.

- Frattini, N. E., V. V. Sivak, A. Lingenfelter, S. Shankar, and M. H. Devoret, “Optimizing the nonlinearity and dissipation of a snail parametric amplifier for dynamic range”, *Phys. Rev. Applied* **10**, 054020 (2018).
- Janvier, C., L. Tosi, L. Bretheau, Ç. Ö. Girit, M. Stern, P. Bertet, P. Joyez, D. Vion, D. Esteve, M. F. Goffman, H. Pothier, and C. Urbina, “Coherent manipulation of Andreev states in superconducting atomic contacts”, *Science* **349**, 1199–1202 (2015).
- Janvier, C., “Coherent manipulation of Andreev bound states in an atomic contact”, PhD thesis (2016).
- Koch, J., M. Y. Terri, J. Gambetta, A. A. Houck, D. Schuster, J. Majer, A. Blais, M. H. Devoret, S. M. Girvin, and R. J. Schoelkopf, “Charge-insensitive qubit design derived from the cooper pair box”, *Physical Review A* **76**, 042319 (2007).
- Manucharyan, V., “Superinductance ph. d”, PhD thesis (thesis Yale University, 2012).
- Wallraff, A., D. I. Schuster, A. Blais, L. Frunzio, R.-S. Huang, J. Majer, S. Kumar, S. M. Girvin, and R. J. Schoelkopf, “Strong coupling of a single photon to a superconducting qubit using circuit quantum electrodynamics”, *Nature* **431**, 162–167 (2004).
- Zgirski, M., L. Bretheau, Q. Le Masne, H. Pothier, D. Esteve, and C. Urbina, “Evidence for long-lived quasiparticles trapped in superconducting point contacts”, *Phys. Rev. Lett.* **106**, 257003 (2011).

4

Unlocking the spin of a quasiparticle

In this chapter, we first discuss how the geometric and material properties of Josephson nanowires can result in spin-split Andreev levels even in the absence of a Zeeman field. We then present the central experimental results of this thesis: the realization of an Andreev spin qubit, which is formed from the spin of a single quasiparticle trapped in the Andreev levels of a Josephson nanowire. We first summarize how we detect the spin of the quasiparticle [Hays et al., Nat. Phys. (2020)], and then how we manipulate the spin [Hays et al., Science (2021)]. All of these results were obtained on one device, which we fondly call 6YD1111.

In the last chapter, we explored how cQED can be used to detect the quantum state of a single Andreev doublet. But there was a big limitation: when the doublet was in the odd manifold, we were unable to detect whether the state was $|\uparrow\rangle$ or $|\downarrow\rangle$. What if we could detect this spin? What if we could manipulate it? This is the idea behind the Andreev spin qubit as proposed by Chtchelkatchev et al. in 2003: *when a quasiparticle becomes trapped in the weak link, its two spin states $|\uparrow\rangle, |\downarrow\rangle$ can be used for quantum information processing.*

Why would one want to manipulate an electronic spin in this context? After all, electronic spin manipulation is well-established in semiconductor quantum dots [Hanson et al. 2007]. First off, as we will see, there is a lot of interesting physics associated with superconductor-semiconductors heterostructures that can be probed in this context. But

the Andreev spin qubit also has one big technological advantage over conventional spin qubits: the coupling of the qubit to a superconducting resonator can be made much larger.

In quantum information processing with semiconductor quantum dots, there is an active effort to integrate cQED techniques with spin qubits [Petersson et al. 2012; Samkharadze et al. 2018; Mi et al. 2018; Harvey et al. 2018; Landig et al. 2018; Cubaynes et al. 2019; Borjans et al. 2020; Zheng et al. 2019; West et al. 2019; Urdampilleta et al. 2019]. This is partially for qubit readout, but mainly for qubit-qubit coupling. Because the dipole moments of spin qubits are so small, it has been extremely difficult to achieve long-range qubit-qubit coupling. The idea is thus to couple multiple qubits to the same resonator, thereby engineering qubit-qubit interactions [Majer et al. 2007].

The challenge is then pushed to achieving strong interaction between a spin qubit and a superconducting resonator. However, this is also complicated by the inherently weak interaction between the electron magnetic dipole moment and magnetic fields. In semiconductor quantum dots, this problem has been solved by hybridizing the spin with a charge degree of freedom, either via spin-orbit coupling [Petersson et al. 2012] or with a strong magnetic field gradient [Harvey et al. 2018; Landig et al. 2018]. This hybridized state can then couple to the resonator electric field. However, such capacitive coupling schemes will always be limited by the size of the dot.

In the case of a quasiparticle trapped in the Andreev levels of a Josephson nanowire, we have another option. The key difference between Andreev levels and the levels of an electrostatically-defined quantum dot is that the Andreev levels carry supercurrent. Thus, as we saw in the last chapter, we can harness the current operator J_A of the weak link to achieve coupling between the resonator mode and the Andreev pair qubit. In this chapter, we will see how the special properties of Josephson nanowires allow us to extend this coupling to the Andreev spin qubit. Critically, the size of this coupling is not dictated by the length of the junction, but by the value of the shared inductance with the resonator. This should be contrasted with the dot-size-limited capacitive coupling discussed above.¹

But how can we achieve spin detection and manipulation? The first step is to break the

¹In principle, the Andreev level/resonator coupling could also be capacitive. Instead of coupling to the current operator $J_A = \frac{\partial H_A}{\partial \Phi}$, one would couple to the charge operator $Q_A = \frac{\partial H_A}{\partial V}$. But then one would be back to being limited by the size of the weak link.

spin degeneracy of a quasiparticle trapped in the weak link. As we now outline, this can be done by taking advantage of spin-orbit effects in the indium arsenide nanowire. For a detailed explanation, see Chapter 8.

4.1 Breaking spin degeneracy:

long weak links and spin-orbit coupling

While the Andreev spectrum of a single-channel, short, Josephson nanowire [Fig. 2.5(d)] is maximally simple and within the frequency range accessible to cQED, it is limited. Because the spin states $|\uparrow\rangle, |\downarrow\rangle$ are degenerate, we have no hope of manipulating them with microwaves. Yet once again, the magic of Josephson nanowires saves the day. In particular, we will see that spin-orbit coupling in the semiconductor can be used to break the spin degeneracy. However, in order for spin-orbit coupling to have an effect, we must go beyond short junction physics: the charge carriers must spend enough time traversing the normal region that spin-orbit coupling can act.

First, let's ignore spin-orbit coupling and understand how increasing the length L of the normal region will affect the Andreev spectrum [Nazarov and Blanter 2009, pg. 150]. We start with the constructive interference condition Eqn. 2.2, but now include the propagation phase as we did with the original finite square well Eqn. 2.1:

$$2\pi n = 2\phi_A \pm \varphi + 2kL \quad \phi_A = -\cos^{-1}(E/\Delta) \quad (4.1)$$

Note that we also now include both signs of the phase $\pm\varphi$, where $+$ applies to loops carrying **positive current** and $-$ to loops carrying negative current. To gain some intuition, we will perform two approximations: we will linearize the kinetic energy $E = \hbar v_F k$, and then we will assume $E \ll \Delta$ so that we can expand $\phi_A \approx E/\Delta - \pi/2$. We can then solve the constructive interference condition for the energy:

$$E_{n,\pm} = \pm \frac{\Delta \hbar v_F / L}{2(\Delta + \hbar v_F / L)} (\varphi + \pi(2n + 1)) \quad (4.2)$$

What we find is that the states of a long weak link disperse linearly with phase, and that

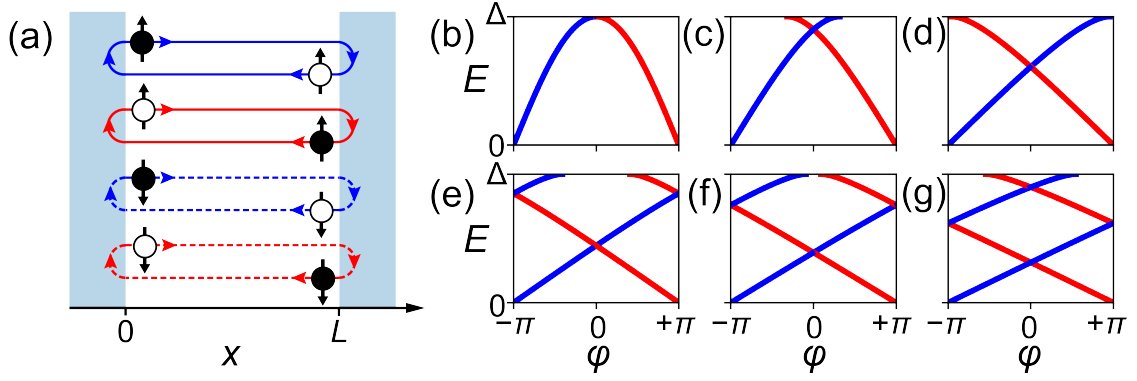


Figure 4.1: Dependence of the Andreev levels on the length of the weak link L | (a) The four possible current-carrying loops of ballistic Andreev levels. For the moment, the spin-up loops (solid lines) are degenerate with the spin-down loops (dashed lines). (b-g) Because the experiments presented in this chapter were all performed with $\varphi \sim 0$, we now plot $\varphi \in \{-\pi, \pi\}$ as opposed to $\varphi \in \{0, 2\pi\}$. The spectra shown in panels (b) through (g) correspond to effective junction lengths L/ξ_0 of 0.0, 0.5, 1.5, 2.5, 3.0, and 4.0. As with any confined quantum system, the level spacing decreases as the size of the system grows.

their slope is a competition between two energy scales: the superconducting gap Δ and the dwell energy $\hbar v_F/L$. Alternatively, we can express this as a competition between L and the coherence length $\xi_0 = \hbar v_F/\Delta$, such that the slope is $\Delta \frac{\xi_0/L}{1+\xi_0/L}$. Fig. 4.1 shows this Andreev spectrum as the length of the weak link is increased. As with any confined quantum system, the level spacing goes down as the system gets bigger. We see that while in the short junction regime we are restricted to one Andreev doublet per conduction channel, as we increase L the number of doublets steadily grows.

Although we now have more than one doublet per channel, the Andreev spectrum is still spin-degenerate. The other necessary ingredient to break the spin degeneracy is spin-orbit coupling, which is naturally found in indium arsenide nanowires.² While we leave a detailed discussion of the nanowire spin-orbit coupling for Chapter 8, here we will highlight the central result. As the name suggests, spin-orbit coupling is an interaction between a spin and motional degrees of freedom. *In a Josephson nanowire, the critical effect of spin-orbit coupling is that the Fermi velocity depends both on the spin of the Andreev level and on the sign of the momentum* [Governale and Zülicke 2002]. Specifically, two of the loops depicted in 4.2 have a slower velocity ($\uparrow, +k$ and $\downarrow, -k$) and two will have a faster velocity ($\downarrow, +k$ and

²Of course, spin-degeneracy could be broken in other ways, such as by applying a magnetic field.

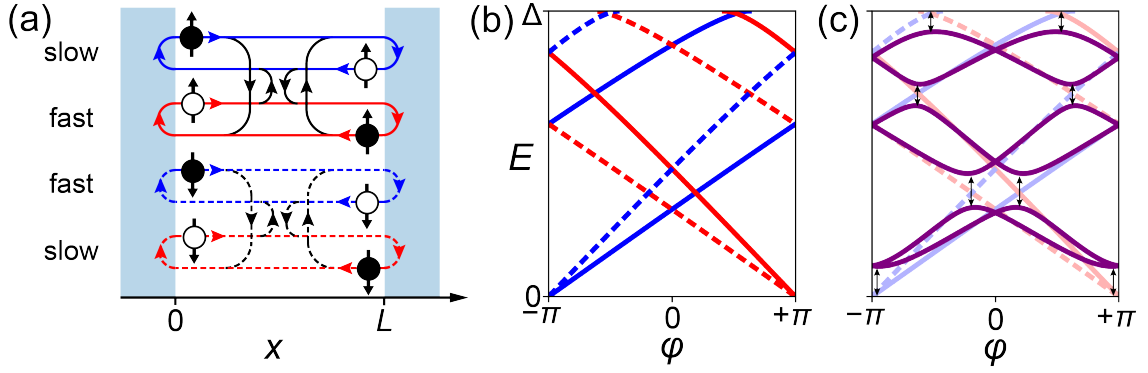


Figure 4.2: Adding spin-orbit coupling | (a) Due to spin-orbit coupling, the Andreev levels possess slower/faster Fermi velocities. (b) This makes the effective weak link length correspondingly longer/shorter, and the slope of the Andreev energies with phase smaller/larger. (c) Disorder results in avoided crossings (black arrows) between Andreev levels of the same spin, but crossings at $\varphi = 0, \pi$ are protected by time-reversal symmetry.

$\uparrow, -k$). What this means for the Andreev spectrum is that, for the faster loops, the effective weak link length is shorter, and thus they disperse faster with φ [Fig. 4.2(b)]. For the slower loops, the effective weak link length is longer, and thus they disperse slower with φ . In this way, spin degeneracy is broken in a long Josephson nanowire. There have been many theoretical works investigating such a spin-orbit-split Andreev spectrum [Chtchelkatchev and Nazarov 2003; Béri, Bardarson, and Beenakker 2008; Padurariu and Nazarov 2010; Reynoso et al. 2012; Yokoyama, Eto, and Nazarov 2014; Cayao et al. 2015; Murani et al. 2017; Heck, Väyrynen, and Glazman 2017], but experimentally has been observed only recently [Tosi et al. 2019].

It is interesting to note that the spin degeneracy that was present without the spin-orbit interaction [Fig. 4.1] was not a Kramers degeneracy. Spin-orbit coupling does not break time-reversal symmetry; here the two faster velocity loops ($\downarrow, +k$ and $\uparrow, -k$) are a Kramers pair, as are the slower velocity loops ($\downarrow, +k$ and $\uparrow, -k$). Instead, time-reversal symmetry is broken by the superconducting phase φ , which was present even in the case of a spin-degenerate Andreev doublet in a short weak link. Indeed, we see that each Andreev level maps to its Kramers partner with $\varphi \rightarrow -\varphi$; in Fig 4.2(b) $\downarrow, +k$ and $\uparrow, -k$ are mirror-symmetric about $\varphi = 0$, as are $\downarrow, +k$ and $\uparrow, -k$.

As in the short junction regime, we must include disorder if we want a realistic model

of the Andreev spectrum. Unless the disorder is due in part to something that breaks time-reversal symmetry (such as magnetic impurities), it can only induce scattering between states of like spin. As such, only Andreev levels of the same spin undergo avoided crossings [Fig. 4.2(c)]; the other crossings at $\varphi = 0, \pi$ are protected by time-reversal symmetry.³ We will now explore how we can use this spin-split spectrum to detect and manipulate the spin of a single quasiparticle trapped in the weak link.

4.2 The Andreev spin qubit

4.2.1 Playing with the spin of a single quasiparticle

First off, why can we restrict ourselves to a single quasiparticle? In the short-junction regime where we had only a single Andreev doublet, there were only four possible many-body states. However, because a long Josephson nanowire can host more than one doublet per conduction channel, at first glance it looks like we will have to account for a much larger number of many-body states. As with any fermionic system, the Hilbert space of the Andreev levels will grow like 2^n , where n is the number of levels; already with two doublets we have $2^4 = 16$ many-body states. Thankfully, we are saved by the tendency of the system to relax to the lowest-energy state. Experimentally, we find that when the system is in any excited state of the even manifold, it decays to the ground state $|g\rangle$ on μs timescales. Similarly, when the system is in the odd manifold, it quickly decays to the two spin states of the lowest-energy doublet $|\uparrow\rangle$ and $|\downarrow\rangle$ on μs timescales (measurements of all these decay processes can be found in Chapter 13). So if we're not applying any drives to disturb the system, it will predominantly be in either $|g\rangle$, $|\uparrow\rangle$, or $|\downarrow\rangle$. Thus, when a quasiparticle is trapped in the junction, we can imagine manipulating its spin state.

Do we even need to consider the higher energy states? After all, the Andreev spin qubit is built from the two spin states of the lowest-energy doublet. However, it turns out that the lowest-energy doublet is not enough; we need the higher-energy levels both for spin state detection and spin manipulation. The problem is that even though spin degeneracy is bro-

³Unlike in the short-junction regime, the effect of such disorder can no longer be captured purely by the channel transparency τ . For a discussion of modeling disorder in long weak links, see Chapter 8.

ken and thus the transition $|\uparrow\rangle \leftrightarrow |\downarrow\rangle$ is no longer at zero frequency, it is difficult to couple to this direct spin-flip transition via the current operator J_A . For a transverse-symmetric wire, we have $\langle \downarrow | J_A | \uparrow \rangle = 0$ for all φ [Park and Yeyati 2017]. Even if transverse symmetry is broken, $\langle \downarrow | J_A | \uparrow \rangle$ is still suppressed, perhaps due to an approximate time-reversal symmetry [Hays et al. 2021]. Because both the resonator and the drive couple to the Andreev levels via J_A , this restriction applies both to spin manipulation and spin detection. We note that in Metzger et al. 2021, $|\uparrow\rangle \leftrightarrow |\downarrow\rangle$ was driven by breaking transverse symmetry with a microwave drive applied to the gate, though the above considerations still apply to the Andreev level/resonator coupling.

We are saved by transitions from the spin states $|\uparrow\rangle/|\downarrow\rangle$ to higher-energy Andreev levels. As we will see, these transitions induce spin-dependent dispersive shifts that allow us to detect the spin states. Moreover, by using $|\uparrow\rangle$ and $|\downarrow\rangle$ in conjunction with a higher-energy Andreev level as a Λ -system, we can achieve coherent manipulation of the quasiparticle spin. It is enough to consider just one higher energy doublet [Fig. 4.3(a)], thus restricting a trapped quasiparticle to the 4-D Hilbert space spanned by the four levels of the two doublets. To deal with the fact that the quasiparticle is no longer limited to just the lowest-energy doublet, we need to modify our notation slightly. We will add a “ q ” subscript on the spin states of the lower doublet $|\downarrow_q\rangle, |\uparrow_q\rangle$ to indicate that these states form the basis of the Andreev spin qubit. The spin-splitting between these two qubit states will be labeled as E_s . Finally, we will denote the spin states of the upper doublet as $|\uparrow_a\rangle, |\downarrow_a\rangle$, where the “ a ” subscript stands for “ancillary”.

As shown in Fig. 4.3(b/c), there are four microwave transitions between the qubit states and the ancillary states. Because the φ -dependent spin-splitting is different for the two doublets, the transitions are all split from each other except at the spin-degenerate points of $\varphi = 0, \pi$. Note that these single-particle transitions have minima around $\varphi = 0$ and maxima around $\varphi = \pi$ (opposite that of the pair transition we studied in the short junction regime). Moreover, the single-particle transition/resonator coupling is largest at $\varphi = 0$. As such, the majority of the experiments presented in this chapter were performed close to $\varphi = 0$. Here, the detuning between the transitions and the resonator were the smallest and the dispersive shifts were the largest, as we discuss in the next section.

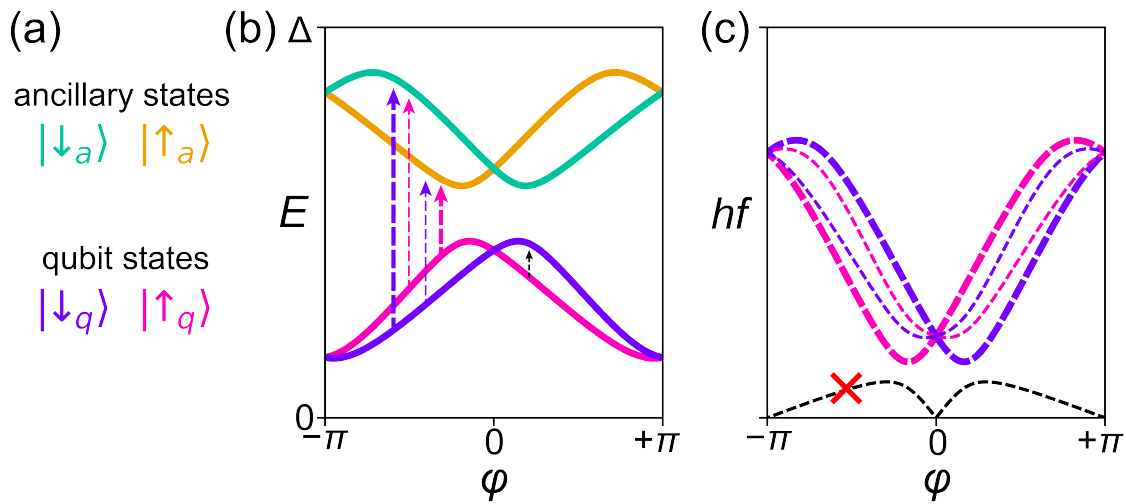


Figure 4.3: Level structure of the Andreev spin qubit | (a) The qubit basis is formed from the two spin states of the lowest-energy doublet $|\downarrow_q\rangle$ and $|\uparrow_q\rangle$. The ancillary states $|\uparrow_a\rangle$ and $|\downarrow_a\rangle$ are necessary for qubit readout and manipulation. (b) The dependence of the level energies on φ . Arrows indicate single-particle transitions from the qubit states to the ancillary states, with thin/thick lines representing whether the spin is flipped/conserved. Color (purple/pink) corresponds to the qubit state. The direct spin-flip transition is indicated by a black arrow. (c) The φ -dependence of the single-particle transitions reveals a characteristic spider-like shape. As discussed in the text, we cannot drive the direct spin-flip transition. This is indicated by the red cross.

4.2.2 Spin detection

As discussed in Chapter 3, state readout of a quantum system using cQED relies on the existence of microwave transitions between the system states $|i\rangle$ to create a state-dependent dispersive shift χ_i of a superconducting resonator's frequency. The extent to which each transition participates in χ_i is determined by the coupling operator between the system and the resonator. Here, we will summarize our attempts to capture these dispersive shifts assuming the resonator and Andreev levels are coupled via the current operator J_A .

We began by probing the spectrum using two-tone spectroscopy [Fig. 4.4(b)], finding the characteristic spider-like pattern of the four inter-doublet transitions [Fig. 4.3(c)] [Tosi et al. 2019]. However, we found that all the transitions were not of equal brightness. At this particular gate-voltage bias ($V_{\text{nw}} = 0.9$ V and $V_c = -1.36$ V), we found that the spin-conserving inter-doublet transitions were much brighter than the spin-flipping inter-doublet transitions. We attributed this stark contrast in brightness to the drive coupling predominantly via a spin-conserving J_A . As such, we fit the spectrum with a simple model in which linearly-dispersing Andreev levels of like spin undergo avoided crossings due to normal scattering (see Chapter 11 for details). Around $\Phi = 0$, we extracted the slope of the $|\downarrow_q\rangle/|\uparrow_q\rangle$ energy splitting $dE_s/d\Phi = 1.8$ nA.

To estimate the Φ -dependent dispersive shifts $\chi_\downarrow, \chi_\uparrow$ and therefore the distribution centers observed in Γ [Fig. 4.4(c,d)], we calculated the current operator J_A based on the same simple model we used to fit the transition spectrum. Because this model assumed that normal scattering does not mix Andreev levels of different spin, the calculated J_A was automatically block-diagonal. As such, only the spin-conserving transitions contributed to the dispersive shifts:

$$\chi_\downarrow \cong -\frac{\Phi_r^2}{2\pi\hbar^2} \frac{2f_{\downarrow\downarrow}}{f_{\downarrow\downarrow}^2 - f_r^2} |\langle \downarrow_a | J_A | \downarrow_q \rangle|^2 \quad \chi_\uparrow \cong -\frac{\Phi_r^2}{2\pi\hbar^2} \frac{2f_{\uparrow\uparrow}}{f_{\uparrow\uparrow}^2 - f_r^2} |\langle \uparrow_a | J_A | \uparrow_q \rangle|^2 \quad (4.3)$$

where $f_r = 9.188$ GHz is the bare resonator frequency and Φ_r is the zero-point fluctuation of the resonator flux drop across the shared inductance, as discussed in Chapter 3. We

attribute the observed correspondence in Φ between 4.4(b,d) to this spin-conserving current operator; when $f_{\downarrow\downarrow}$ is tuned closer to f_r , the denominator in the expression for χ_{\downarrow} gets small. However, we note that this isn't the full story: $g_c \propto |\langle \uparrow_a | J_A | \uparrow_q \rangle|$ was also Φ -dependent. We leave a more in depth discussion of this for Chapter 11, and here just quote the maximum value $g_c \approx 2\pi \times 35$ MHz, which occurred at $\Phi = \pm 0.08\Phi_0$.

The third distribution observed in Fig. 4.4(c,d) corresponds to $|g\rangle$; all three states are simultaneously visible due to the finite trapping lifetime of a quasiparticle in the Josephson nanowire, just as we saw with the quantum jumps experiment on the Andreev pair qubit in Chapter 3. But in this regime of spin-orbit-split Andreev levels, we had access to a spin-dependent dispersive shift. Thus, we could also probe the spin dynamics and quantify our spin detection fidelity.

We observed quantum jumps between the two spin states and the ground state by applying a continuous readout tone and partitioning the reflected signal into consecutive $1.9 \mu\text{s}$ shots [Fig. 4.5(b)], with the state assigned based on the black dashed lines in Fig. 4.5(a). We summarize the spin-flip dynamics by the spin lifetime:

$$T_s = (\gamma_{\uparrow,\downarrow} + \gamma_{\downarrow,\uparrow})^{-1} \quad (4.4)$$

We found the spin lifetime, given by to be $T_s = 51 \pm 4 \mu\text{s}$ at this particular phase bias. In addition, we found a parity lifetime that was a bit shorter than in our investigation of the Andreev pair qubit at $31 \pm 1 \mu\text{s}$. Both spin flips and parity switches limited the fidelity of our spin readout. For perfectly QND measurement, consecutive shots should always yield the same result, which means that transitions should never be observed. To compare to this ideal, we histogrammed Q conditioned on the state assignment of the previous shot [Fig. 4.5(c)]. We observed that consecutive shots found the same state $|m\rangle$ with high probability $P_{m,m}$, with occasional transitions and miss-assignments resulting in the observed peaks at the other distribution centers. We quantified these effects with the quantum non-demolition metric [Touzard et al. 2019] $\mathcal{F} = (P_{\downarrow q, \downarrow q} + P_{\uparrow q, \uparrow q})/2 = 92.2 \pm 0.1\%$. To our knowledge, this was only the second example of QND readout of a spin-1/2 particle (as opposed to a two-electron system), the first having been achieved by the Tarucha group in

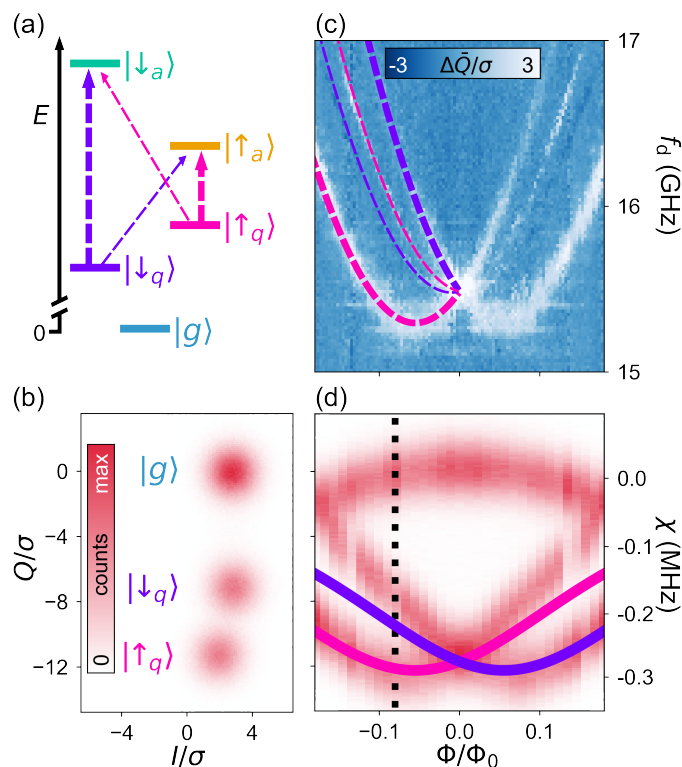


Figure 4.4: Dispersive readout and spectroscopy of a trapped quasiparticle | (a) Level structure and transitions out of the lower doublet for $\Phi < 0$. (b) Measured histogram of Γ/σ , where σ is the standard deviation of one distribution. The data cluster into three distributions, corresponding to $|g\rangle$, $|\downarrow_q\rangle$, and $|\uparrow_q\rangle$. (c) Drive-probe spectroscopy of the nanowire reveals the four transitions depicted in (a), with fits to a simple model (see Chapter 11 for details) plotted for $\Phi < 0$. (d) The distributions shown in (b) shift with Φ as the detuning between the quasiparticle transitions and the resonator varies, from which the absolute dispersive shift (right axis) can be determined. Dashed line indicates Φ for data in (b), and colored curves are predictions based on the extracted model parameters in (c) with only one additional free parameter (see Chapter 11), which captures the scale and shape of the behavior.

2019 [Nakajima et al. 2019].

Although a Zeeman effect was not necessary for our detection scheme, interaction with magnetic fields is a fundamental property of spins. We determined the spin lifetime T_s as a function of both $\varphi \cong 2\pi \frac{\Phi}{\Phi_0} \text{mod}(2\pi)$ and a magnetic field B_\perp applied perpendicular to the chip substrate [Fig. 4.5(d)] using a hidden Markov model algorithm. At $B_\perp = 0 \mu\text{T}$, we observed that T_s increased with $|\varphi|$ symmetrically about $\varphi = 0$. This dependence of T_s on φ is correlated with the spin splitting E_s , which goes to 0 at $\varphi = 0$. Applying a positive (negative) B_\perp resulted in a positive (negative) shift of the φ -dependence. This can be explained by a Zeeman-like shift of the Andreev levels, consistent with the observed spectrum at $B_\perp = 380 \mu\text{T}$ (see Chapter 11 for this spectroscopy data) and expected for a magnetic field applied parallel to the spin-orbit field [Reynoso et al. 2012; Tosi et al. 2019]. For the dependence of all six transition rates between $|g\rangle$, $|\downarrow_q\rangle$, and $|\uparrow_q\rangle$, see Chapter 13.

Does this spin lifetime seem reasonable? This is a difficult question to answer, because at the time of this writing, the source of quasiparticle spin flips is unknown. Electron spin flips in semiconductor quantum dots are typically caused by some combination of hyperfine interactions, spin-orbit coupling, and phonon emission [Hanson et al. 2007]. Away from $E_s = 0$, direct electron/nuclei “flip-flops” quickly become suppressed because of the small nuclear spin energy scale. As E_s is increased further, T_s typically decreases due to, among other factors, an increasing phonon density of states. This trend is opposite to our observations, though we note that for this experiment the phonons may be quasi-1D for the investigated spin energies $E_s/h < 600 \text{ MHz}$ due to transverse confinement. An additional clue is that increasing the temperature did not affect T_s until approximately 150 mK (see Chapter 13). Moreover, when the the rates did start to increase at higher temperatures, they did so independent of flux. For a more detailed discussion of possible spin-flip mechanisms, see Chapter 13.

4.2.3 Spin manipulation

Throughout this section, we present data in terms of spin state occupation probabilities P_\downarrow , P_\uparrow . These were computed based on the thresholds displayed in Fig. 4.6(c).

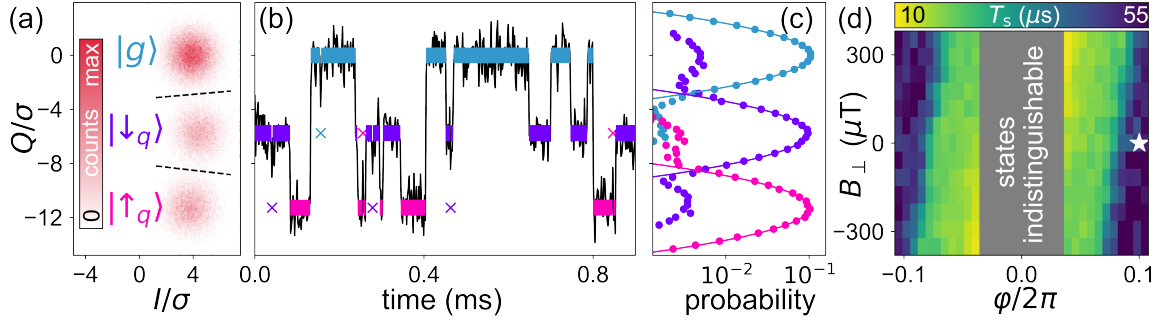


Figure 4.5: Quantum non-demolition readout of the quasiparticle spin ($\Phi = 0.100\Phi_0$) | (a) The system state was assigned to be $|g\rangle$, $|\downarrow_q\rangle$, or $|\uparrow_q\rangle$ based on thresholds indicated by the black dashed lines. (b) $Q(t)$ reveals quantum jumps between the three states. Colored bars indicate state assignments, with isolated points indicated by crosses and colored by the most likely state. (c) Histogram of Q conditioned on the state assignment of the previous measurement (indicated by color). Solid lines are Gaussian fits. (d) By analyzing $\Gamma(t)$ using a hidden Markov model, the spin lifetime T_s was determined as a function of both φ and a magnetic field B_\perp applied perpendicular to the chip substrate. The star indicates the bias for data in (a), (b), and (c).

We have seen how to detect the spin state of a quasiparticle trapped in a Josephson nanowire, but this is only half of what we need to realize the Andreev spin qubit. We must also be able to coherently manipulate quasiparticle spin. However, as we have discussed, the direct spin-flip transition $|\downarrow_q\rangle \leftrightarrow |\uparrow_q\rangle$ is forbidden when we couple via the current operator. To get around this, we again turn to the inter-doublet transitions between the qubit and ancillary states [Fig. 4.3]. Specifically, we exploit the natural Λ system consisting of $|\downarrow_q\rangle$, $|\uparrow_q\rangle$ and $|\uparrow_a\rangle$ as depicted in Fig 4.6. By applying two drives with carrier frequencies f_\downarrow, f_\uparrow equally detuned from the two inter-doublet transitions $|\downarrow_q\rangle \leftrightarrow |\uparrow_a\rangle$, $|\uparrow_q\rangle \leftrightarrow |\uparrow_a\rangle$, we induced a coherent **Raman process** between the two spin states. For a rigorous description of such a Raman process, see Chapter 12.

But based on the results of the last section, we have a bit of a problem. There, we saw that the spin-flipping inter-doublet transitions were much dimmer than the spin-conserving ones. In such a situation, it would be difficult to drive the Raman process depicted in Fig. 4.6(b); we need the matrix elements associated with both transitions in the Λ system to be approximately equal. However, we found that this difference in brightness between the spin-flipping and spin-conserving transitions was not universally observed. At other gate-bias points, the spin-flipping transitions were as bright as the spin-conserving

ones, and we even found one bias point where the spin-flipping ones were brighter.⁴ For the results presented below, we parked the gates at one of these bias points with approximately equal brightness of spin-flipping and spin-conserving transitions ($V_c = -71.9$ mV, and $V_p = 4.0$ mV). In addition, we tuned the flux to $\Phi = -0.14\Phi_0$ (see Chapter 11 for spectrum gate and flux dependence). With the bias conditions set, we then proceeded to manipulation of the quasiparticle spin.

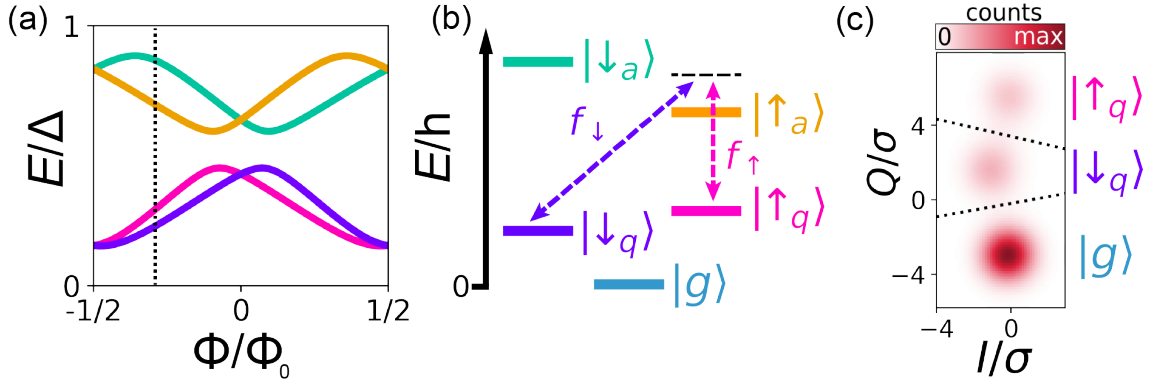


Figure 4.6: Principle of the Andreev spin qubit | (a) Calculated Andreev spectrum versus weak link phase bias Φ/Φ_0 . Here $L/\xi_0 = 2$, resulting in two Andreev doublets. Away from the time-reversal invariant points $\Phi = 0, \Phi_0/2$, the doublet spin degeneracy is lifted due to an inter-subband spin-orbit coupling. A quasiparticle trapped in such a weak link resides with near-unity probability in the two spin states of the lower-energy doublet $|\downarrow_q\rangle$ and $|\uparrow_q\rangle$. (b) With Φ set to the value indicated by the dotted line in (a), two microwave drives (frequencies f_\downarrow and f_\uparrow) are equally detuned from the transitions $|\downarrow_q\rangle \leftrightarrow |\uparrow_a\rangle$ and $|\uparrow_q\rangle \leftrightarrow |\uparrow_a\rangle$. This induces a Raman process between $|\downarrow_q\rangle$ and $|\uparrow_q\rangle$. (c) Our single-shot spin readout was crucial for demonstrating coherent spin manipulation. Throughout this section, we present data in terms of spin state probabilities P_\downarrow, P_\uparrow , which are computed based on the thresholds indicated by the black dotted lines.

The Andreev spin qubit existed exclusively when a quasiparticle was stochastically trapped in the Josephson nanowire, which occurred on a timescale $T_p = 22 \pm 1 \mu\text{s}$ at this bias point. We found that a trapped quasiparticle occupied the two spin states of the lowest doublet with roughly equal probability, as shown in Fig. 4.6(c) (this was extremely bias dependent, see Chapter 14). Thus, even when the transition $|\downarrow_q\rangle \leftrightarrow |\uparrow_q\rangle$ was driven via a Raman process, the observed spin state populations would not change. We overcame this problem by using the single-shot spin detection discussed in the last section. In each

⁴Further discussion and accompanying data can be found in Chapter 11.

Raman measurement presented below, we began by preparing the quasiparticle in $|\uparrow_q\rangle$ via an initial readout pulse and post-selection. Our single-shot spin readout was thus critical to the coherent manipulation of the quasiparticle spin.

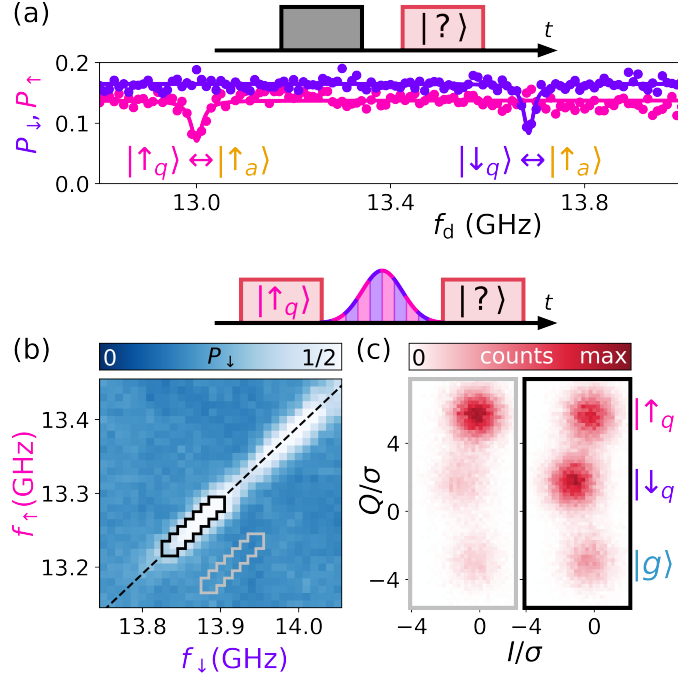


Figure 4.7: Raman transitions of a trapped quasiparticle | (a) In a two-tone measurement, the Josephson nanowire was first driven by a saturation pulse (gray) of variable carrier frequency f_d before the quasiparticle state was determined with a readout pulse (maroon). A dip is observed in P_{\uparrow} corresponding to the $|\uparrow_q\rangle \leftrightarrow |\uparrow_a\rangle$ transition and in P_{\downarrow} corresponding to the $|\downarrow_q\rangle \leftrightarrow |\uparrow_a\rangle$ transition. (b) The quasiparticle was first prepared in $|\uparrow_q\rangle$ via an initial readout pulse and post-selection. Simultaneous Gaussian pulses (100 ns standard deviation, 30 dB more power than used in (a)) of variable frequencies $f_{\downarrow}, f_{\uparrow}$ were then applied, followed by a final readout pulse. The observed peak in the final $|\downarrow_q\rangle$ population lies along $f_{\downarrow} = f_{\uparrow} + 609$ MHz (black dashed line). (c) Full Γ histograms of the final readout pulse for the two subsets of measurements enclosed by the gray and black solid lines in (b). Data in the region enclosed by the gray line shows little population transfer from the post-selected $|\uparrow_q\rangle$ (left panel), while data in the region enclosed by the black shows significant population transfer to $|\downarrow_q\rangle$ (right panel).

The first step in driving the Raman process [Fig. 4.6(b)] was locating the two transitions that defined the Λ system: $|\downarrow_q\rangle \leftrightarrow |\uparrow_a\rangle$ and $|\uparrow_q\rangle \leftrightarrow |\uparrow_a\rangle$. After tuning the transitions to a local maximum in V_c, V_p to mitigate charge noise (see Chapter 12), we measured the spectrum shown in Fig. 4.7(a) using two-tone spectroscopy (without spin initialization). The dip in P_{\uparrow} at 13.000 GHz corresponds to the drive coming into resonance with the $|\uparrow_q\rangle \leftrightarrow |\uparrow_a\rangle$ transition, resulting in population transfer out of $|\uparrow_q\rangle$ and into $|\uparrow_a\rangle$. Similarly, the dip in

P_{\downarrow} at 13.684 GHz corresponds to the $|\downarrow_q\rangle \leftrightarrow |\uparrow_a\rangle$ transition.⁵ In addition to establishing the existence of the Λ system, this measurement also revealed the $|\downarrow_q\rangle/|\uparrow_q\rangle$ energy splitting at the presented bias point $E_s/h = 13.684 \text{ GHz} - 13.000 \text{ GHz} = 684 \text{ MHz}$. As E_s is comparable to the thermal energy at the base stage of our dilution refrigerator ($T \simeq 30 \text{ mK}$), this is consistent with our observation of approximately equal spin state probabilities.

Having characterized the Λ system, we then investigated two-photon Raman transitions of the trapped quasiparticle. After initializing the quasiparticle in $|\uparrow_q\rangle$, we applied two simultaneous Gaussian pulses with variable respective carrier frequencies f_{\uparrow} and f_{\downarrow} and then measured the final qubit spin state [Fig. 4.7(b)]. Throughout this section, we present data with f_{\uparrow} and f_{\downarrow} blue-detuned from $|\uparrow_q\rangle \leftrightarrow |\uparrow_a\rangle$ and $|\downarrow_q\rangle \leftrightarrow |\uparrow_a\rangle$ respectively.⁶ Along a line given by $f_{\downarrow} = f_{\uparrow} + 609 \text{ MHz}$, we observe increased $|\downarrow_q\rangle$ population that we attribute to the onset of a Raman process. As expected for Raman transitions, the slope of this line is equal to one, since a shift of one drive frequency must be compensated by an equal shift of the other. The discrepancy between the spin splitting $E_s = 684 \text{ MHz}$ and the 609 MHz offset was due to an uncontrolled shift of the Andreev spectrum that occurred in between the measurements shown in Fig. 4.7(a) and Fig. 4.7(b) (see Chapter 14).

To further illustrate the dynamics of the quasiparticle under the Raman transitions, we histogram Γ for data points off/on resonance with the Raman process [Fig. 4.7(c)]. Off resonance, the quasiparticle was found predominantly in $|\uparrow_q\rangle$, as expected from post-selection on the initial readout pulse. On resonance, there was significant population transfer to $|\downarrow_q\rangle$ as desired, as well as a small population transfer to $|g\rangle$. This is due to drive-induced quasiparticle de-trapping, which we comment on further below.

Finally, having induced spin population transfer using Raman transitions, we demonstrate the first coherent manipulation of the spin of an individual quasiparticle. We first chose our Raman drive frequencies using a procedure similar to that shown in Fig. 4.7: we detuned f_{\downarrow} by 290 MHz from $|\downarrow_q\rangle \leftrightarrow |\uparrow_a\rangle$ and varied f_{\uparrow} until we observed maximum spin population transfer. We then varied the amplitudes $A_{\downarrow}, A_{\uparrow}$ of the two Gaussian pulses before determining the final quasiparticle state [Fig. 4.8(a)]. The observed oscillations in

⁵The gate voltage and Φ dependence of these transitions can be found in Chapter 12.

⁶Data over a wider frequency range can be found in Chapter 14.

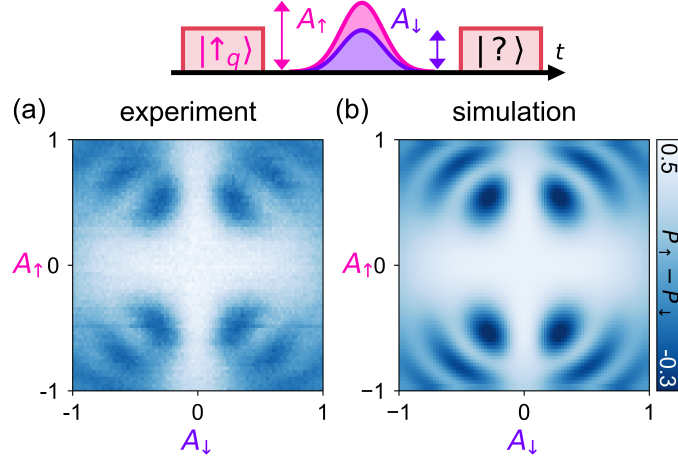


Figure 4.8: Coherent Λ -Rabi oscillations of the quasiparticle spin | (a) Independently varying the amplitudes A_{\uparrow} and A_{\downarrow} of the simultaneous Gaussian drive pulses (40 ns standard deviation, similar power to Fig. 4.7(b)) resulted in coherent oscillations between $|\uparrow_q\rangle$ and $|\downarrow_q\rangle$ characteristic of a Raman process. The oscillations are only present away from $A_{\downarrow}, A_{\uparrow} = 0$, and are symmetric under sign flips of $A_{\downarrow}, A_{\uparrow}$. (b) Simulated dynamics of the quasiparticle under the action of the drive pulse.

the population difference between the two spin states are characteristic of a coherent Raman process. Qualitatively, when either $A_{\downarrow} = 0$ or $A_{\uparrow} = 0$ there is no population transfer because both drives are required to induce the Raman process. As the amplitudes of both drives are increased (roughly along the diagonals $|A_{\downarrow}| \simeq |A_{\uparrow}|$), the spin population difference undergoes coherent oscillations. As expected, the data are symmetric under $A_{\downarrow} \rightarrow -A_{\downarrow}$ and $A_{\uparrow} \rightarrow -A_{\uparrow}$.

Quantitatively, the data are well-represented by a simulation of the coherent quasiparticle dynamics under the action of the drive pulses [Fig. 4.8(b)]. Here we outline this simulation, with further details included in Chapter 12. The dynamics of the quasiparticle between the two Andreev doublets were numerically calculated using the Lindblad master equation [Johansson, Nation, and Nori 2013], with the inter-doublet transition frequencies and dephasing rates, spin dephasing rate, state-dependent readout fidelities, and pulse frequencies and envelopes fixed to values determined by independent measurements and instrument settings. We then fit the simulation to the measured data by varying the four inter-doublet transition matrix elements, as well as the detuning from the Raman resonance condition 5.5 ± 0.1 MHz. We also included a phenomenological quasiparticle de-trapping

rate $\gamma_{\text{de-trap}}$ to capture the measured increase of $|\downarrow_q\rangle, |\uparrow_q\rangle \rightarrow |g\rangle$ for larger drive powers. We were thus able to capture the measured Raman spin dynamics of a quasiparticle trapped in the Andreev levels of a Josephson nanowire.

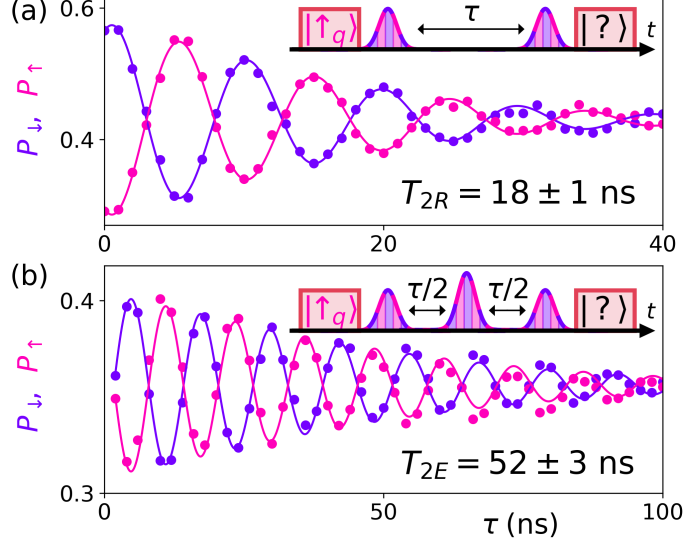


Figure 4.9: Coherence decay of the quasiparticle spin | Bias settings were $V_c = -59.1$ mV, $V_p = -33.3$ mV, $\Phi = -0.115\Phi_0$. (a) A Ramsey experiment reveals $T_{2R} = 18 \pm 1$ ns. (b) A Hahn-echo experiment reveals $T_{2E} = 52 \pm 3$ ns. Oscillations were introduced in both cases by adding a phase proportional to τ to the final Raman pulse.

With the ability to perform coherent spin manipulation in hand, we then characterized the coherence lifetime of an Andreev spin. A Ramsey measurement [Fig. 4.9(a)] revealed spin coherence decay with a timescale $T_{2R} = 18 \pm 1$ ns, while a Hahn-echo pulse sequence [Fig. 4.9(b)] resulted in a slightly longer timescale $T_{2E} = 52 \pm 3$ ns. Both measurements were well-described by a decay envelope $\exp[-(\tau/T_2)^{1+\alpha}]$ with $\alpha = 0.3 \pm 0.1$, indicative of broadband noise $1/f^\alpha$ [Martinis et al. 2003]. We note, however, that the observed ratio of $T_{2E}/T_{2R} = 2.9$ would predict a different exponent $\alpha = 0.8 \pm 0.1$, though still broadband compared to $1/f$ where $T_{2E}/T_{2R} \rightarrow \infty$. The observed oscillations in P_s are centered about a lower value in Fig. 4.9(b) as compared to 4.9(a), which we attribute to additional quasiparticle de-trapping caused by the echo pulse. Both the observed Ramsey and Hahn-echo coherence times are comparable to that of spin-orbit qubits, perhaps the closest cousins of the Andreev spin qubit [Nadj-Perge et al. 2010; Petersson et al. 2012; Van den Berg et al. 2013]. However, because here the quasiparticle was trapped in Andreev levels, we possessed a

different experimental lens with which to investigate the effects of the environment on the spin coherence.⁷

As the Andreev levels of a Josephson nanowire are tunable via both electrostatic voltages and Φ , we first suspected charge or flux noise as the source limiting the Andreev spin qubit coherence. However, we found that neither T_{2R} nor T_{2E} varied with V_c in the vicinity of the sweet-spot bias point. This indicated that the spin coherence was not limited by charge noise, consistent with the observed weak dependence of E_s on V_c . By comparing to the charge-noise-limited inter-doublet transitions, we extracted a lower-bound of $4.2 \mu\text{s}$ on the charge-noise-induced dephasing time of the quasiparticle spin (see Chapter 12). Moreover, the spin coherence time was not limited by flux noise, as we found no measurable dependence on Φ .

To better understand what was limiting the coherence of the Andreev levels, we additionally measured the coherence lifetimes of both inter-doublet transitions and so-called “pair transitions” at several gate bias points [Tab. 4.1]. The latter correspond to the excitation of two quasiparticles out of the condensate into both levels of a doublet [Bretheau et al. 2013; Janvier et al. 2015; Hays et al. 2018; Tosi et al. 2019]. We found that the pair transition coherence times were systematically an order of magnitude longer than inter-doublet transition coherence times. To first order, perturbations that couple to spin (such as a Zeeman field) result in equal and opposite energy shifts of the two doublet levels [Tosi et al. 2019]. As such, these perturbations do not change the frequency of the doublet pair transition, and therefore do not cause dephasing. However, such spin-specific perturbations do induce dephasing of both inter-doublet transitions and the Andreev spin qubit. We thus concluded that the coherence lifetime of the Andreev spin qubit was limited by a spin-specific noise source such as hyperfine interactions with the spinful nuclei of indium and arsenic (though nuclear baths are typically lower frequency than the measured ratio $T_{2E}/T_{2R} = 2.9$ would indicate [Malinowski et al. 2017]), phonon-induced fluctuations of the nanowire spin-orbit coupling, or noisy paramagnetic impurities on the surface of the nanowire [Hanson et al. 2007].

⁷This analysis can also be found in Chapter 13, along with a full discussion of the interactions between the Andreev levels and the environment.

Transition	V_c (mV)	V_p (mV)	T_{2E} (ns)
$ \uparrow_q\rangle \leftrightarrow \uparrow_a\rangle$	-166.3	-127.6	39 ± 8
pair	-164.9	-127.6	257 ± 9
$ \downarrow_q\rangle \leftrightarrow \uparrow_a\rangle$	144.5	24.9	9 ± 1
pair	116.2	23.8	420 ± 20
$ \uparrow_q\rangle \leftrightarrow \uparrow_a\rangle$	32.7	-4.7	11 ± 3
pair	30.0	-4.7	490 ± 10

Table 4.1: Coherence lifetimes of various Andreev transitions.

References

- Béri, B., J. H. Bardarson, and C. W. J. Beenakker, “Splitting of Andreev levels in a Josephson junction by spin-orbit coupling”, *Phys. Rev. B* **77**, 045311 (2008).
- Borjans, F., X. Croot, X. Mi, M. Gullans, and J. Petta, “Resonant microwave-mediated interactions between distant electron spins”, *577*, 195–198 (2020).
- Bretheau, L., Ç. Girit, H. Pothier, D. Esteve, and C. Urbina, “Exciting Andreev pairs in a superconducting atomic contact”, *Nature* **499**, 312–315 (2013).
- Cayao, J., E. Prada, P. San-Jose, and R. Aguado, “Sns junctions in nanowires with spin-orbit coupling: role of confinement and helicity on the subgap spectrum”, *Phys. Rev. B* **91**, 024514 (2015).
- Chtchelkatchev, N. M. and Y. V. Nazarov, “Andreev quantum dots for spin manipulation”, *Phys. Rev. Lett.* **90**, 226806 (2003).
- Cubaynes, T., M. R. Delbecq, M. C. Dartiailh, R. Assouly, M. M. Desjardins, L. C. Contamin, L. E. Bruhat, Z. Leghtas, F. Mallet, A. Cottet, and T. Kontos, “Highly coherent spin states in carbon nanotubes coupled to cavity photons”, *npj Quantum Inf.* **5**, 1–5 (2019).
- Governale, M. and U. Zülicke, “Spin accumulation in quantum wires with strong rashba spin-orbit coupling”, *Phys. Rev. B* **66**, 073311 (2002).
- Hanson, R., L. P. Kouwenhoven, J. R. Petta, S. Tarucha, and L. M. K. Vandersypen, “Spins in few-electron quantum dots”, *Rev. Mod. Phys.* **79**, 1217–1265 (2007).

- Harvey, S. P., C. G. L. Böttcher, L. A. Orona, S. D. Bartlett, A. C. Doherty, and A. Yacoby, “Coupling two spin qubits with a high-impedance resonator”, *Phys. Rev. B* **97**, 235409 (2018).
- Hays, M., G. de Lange, K. Serniak, D. van Woerkom, D. Bouman, P. Krogstrup, J. Nygård, A. Geresdi, and M. Devoret, “Direct microwave measurement of Andreev-bound-state dynamics in a semiconductor-nanowire Josephson junction”, *Phys. Rev. Lett.* **121**, 047001 (2018).
- Hays, M., V. Fatemi, D. Bouman, J. Cerrillo, S. Diamond, K. Serniak, T. Connolly, P. Krogstrup, J. Nygård, A. L. Yeyati, A. Geresdi, and M. H. Devoret, “Coherent manipulation of an andreev spin qubit”, *Science* **373**, 430–433 (2021).
- Heck, B. van, J. I. Väyrynen, and L. I. Glazman, “Zeeman and spin-orbit effects in the Andreev spectra of nanowire junctions”, *Phys. Rev. B* **96**, 075404 (2017).
- Janvier, C., L. Tosi, L. Bretheau, Ç. Ö. Girit, M. Stern, P. Bertet, P. Joyez, D. Vion, D. Esteve, M. F. Goffman, H. Pothier, and C. Urbina, “Coherent manipulation of Andreev states in superconducting atomic contacts”, *Science* **349**, 1199–1202 (2015).
- Johansson, J. R., P. D. Nation, and F. Nori, “Qutip 2: a Pndreev framework for the dynamics of open quantum systems”, *Computer Physics Communications* **184**, 1234–1240 (2013).
- Landig, A. J., J. V. Koski, P. Scarlino, U. Mendes, A. Blais, C. Reichl, W. Wegscheider, A. Wallraff, K. Ensslin, and T. Ihn, “Coherent spin–photon coupling using a resonant exchange qubit”, *Nature* **560**, 179–184 (2018).
- Majer, J., J. Chow, J. Gambetta, J. Koch, B. Johnson, J. Schreier, L. Frunzio, D. Schuster, A. Houck, A. Wallraff, et al., “Coupling superconducting qubits via a cavity bus”, *Nature* **449**, 443–447 (2007).
- Malinowski, F. K., F. Martins, P. D. Nissen, E. Barnes, Ł. Cywiński, M. S. Rudner, S. Fallahi, G. C. Gardner, M. J. Manfra, C. M. Marcus, et al., “Notch filtering the nuclear environment of a spin qubit”, *Nature nanotechnology* **12**, 16 (2017).
- Martinis, J. M., S. Nam, J. Aumentado, K. Lang, and C. Urbina, “Decoherence of a superconducting qubit due to bias noise”, *Physical Review B* **67**, 094510 (2003).

- Mi, X., M. Benito, S. Putz, D. M. Zajac, J. M. Taylor, G. Burkard, and J. R. Petta, "A coherent spin-photon interface in silicon", *Nature* **555**, 599–603 (2018).
- Murani, A., A. Chepelianskii, S. Guéron, and H. Bouchiat, "Andreev spectrum with high spin-orbit interactions: revealing spin splitting and topologically protected crossings", *Phys. Rev. B* **96**, 165415 (2017).
- Nadj-Perge, S., S. Frolov, E. Bakkers, and L. P. Kouwenhoven, "Spin-orbit qubit in a semiconductor nanowire", *Nature* **468**, 1084–1087 (2010).
- Nakajima, T., A. Noiri, J. Yoneda, M. R. Delbecq, P. Stano, T. Otsuka, K. Takeda, S. Amaha, G. Allison, K. Kawasaki, et al., "Quantum non-demolition measurement of an electron spin qubit", *Nat. Nanotechnol.* **14**, 555–560 (2019).
- Padurariu, C. and Y. V. Nazarov, "Theoretical proposal for superconducting spin qubits", *Phys. Rev. B* **81**, 144519 (2010).
- Park, S. and A. L. Yeyati, "Andreev spin qubits in multichannel rashba nanowires", *Phys. Rev. B* **96**, 125416 (2017).
- Petersson, K. D., L. W. McFaul, M. D. Schroer, M. Jung, J. M. Taylor, A. A. Houck, and J. R. Petta, "Circuit quantum electrodynamics with a spin qubit", *Nature* **490**, 380–383 (2012).
- Reynoso, A. A., G. Usaj, C. A. Balseiro, D. Feinberg, and M. Avignon, "Spin-orbit-induced chirality of Andreev states in Josephson junctions", *Phys. Rev. B* **86**, 214519 (2012).
- Samkharadze, N., G. Zheng, N. Kalhor, D. Brousse, A. Sammak, U. Mendes, A. Blais, G. Scappucci, and L. Vandersypen, "Strong spin-photon coupling in silicon", *Science* **359**, 1123–1127 (2018).
- Tosi, L., C. Metzger, M. Goffman, C. Urbina, H. Pothier, S. Park, A. L. Yeyati, J. Nygård, and P. Krogstrup, "Spin-orbit splitting of Andreev states revealed by microwave spectroscopy", *Phys. Rev. X* **9**, 011010 (2019).
- Touzard, S., A. Kou, N. Frattini, V. Sivak, S. Puri, A. Grimm, L. Frunzio, S. Shankar, and M. Devoret, "Gated conditional displacement readout of superconducting qubits", *Phys. Rev. Lett.* **122**, 080502 (2019).

- Urdampilleta, M., D. J. Niegemann, E. Chanrion, B. Jadot, C. Spence, P.-A. Mortemousque, C. Bäuerle, L. Hutin, B. Bertrand, S. Barraud, R. Maurand, M. Sanquer, X. Jehl, S. D. Franceschi, M. Vinet, and T. Meunier, “Gate-based high fidelity spin readout in a CMOS device”, *Nat. Nanotechnol.* **14**, 737–741 (2019).
- Van den Berg, J., S. Nadj-Perge, V. Pribiag, S. Plissard, E. Bakkers, S. Frolov, and L. Kouwenhoven, “Fast spin-orbit qubit in an indium antimonide nanowire”, *Physical review letters* **110**, 066806 (2013).
- West, A., B. Hensen, A. Jouan, T. Tanttu, C.-H. Yang, A. Rossi, M. F. Gonzalez-Zalba, F. Hudson, A. Morello, D. J. Reilly, et al., “Gate-based single-shot readout of spins in silicon”, *Nat. Nanotechnol.* **14**, 437–441 (2019).
- Yokoyama, T., M. Eto, and Y. V. Nazarov, “Anomalous Josephson effect induced by spin-orbit interaction and zeeman effect in semiconductor nanowires”, *Phys. Rev. B* **89**, 195407 (2014).
- Zheng, G., N. Samkharadze, M. L. Noordam, N. Kalhor, D. Brousse, A. Sammak, G. Scappucci, and L. M. Vandersypen, “Rapid gate-based spin read-out in silicon using an on-chip resonator”, *Nat. Nanotechnol.* **14**, 742–746 (2019).

5

Future directions

The experiments presented in this thesis have barely scratched the surface of Andreev levels in Josephson nanowires. At the time of this writing, the quasiparticle crew is busy working on new experiments involving detailed modeling of the resonator/Andreev level coupling, readout of degenerate spin states, and multiplexed device designs. But there is so much more one can imagine.

One exciting direction could be the exploration of **Andreev molecules** [Su et al. 2017; Pillet et al. 2019; Scherübl, Pályi, and Csonka 2019; Kornich, Barakov, and Nazarov 2019]. Suppose we had two weak links in a single Josephson nanowire. If the weak links are within a coherence length of each other, their Andreev levels will become coupled. In such an Andreev molecule, the current across one weak link can thus depend on the phase of the other. This effect can be used to realize a φ_0 -junction, where the minimum energy of the ground state is not at $\varphi = 0$, but at some phase $\varphi = \varphi_0$. Or, more closely related to the work in this thesis, this cross-weak-link interaction could be used to couple two separate Andreev spin qubits.

Perhaps the grandest realm of physics that could be explored in Josephson nanowires is that of topological superconductors and **Majorana zero modes**. In principle, the devices presented in this thesis could host such physics upon the addition of one ingredient: a large magnetic field (~ 1 T) applied along the nanowire [Fig. 9.3]. Under these conditions, the two proximitized sections could be driven into a topological phase with Majoranas bound to the ends of each section. The two Majoranas near the junction would hybridize into an

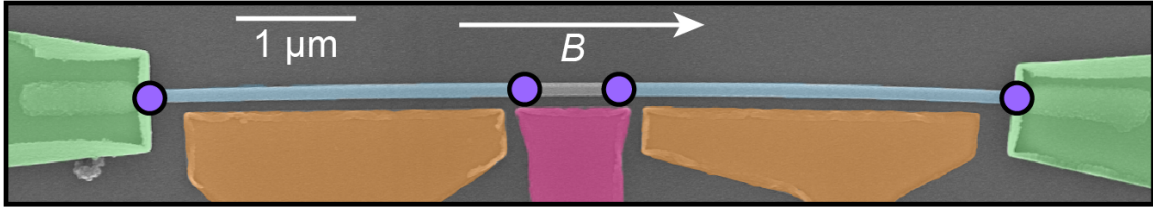


Figure 5.1: A topological Josephson nanowire | A ~ 1 T magnetic field B is applied along the Josephson nanowire, driving the proximitized sections into a topological phase. Majorana zero modes are bound to the end of each topological section. The two Majoranas flanking the weak link hybridize to form an Andreev level.

Andreev level, which, independent of disorder, would have zero energy for some value of φ . The Andreev spectrum of such a topological junction could be probed using microwave spectroscopy, as laid out in Ref. [Väyrynen et al. 2015] and explained in Chapter ?? . By driving transitions involving the Majorana level, one could observe a signature of the zero-energy crossing.

And of course, there are many experiments that we haven't even begun to imagine. I hope that Chapter 14, where I've laid out some unexplained puzzles in this thesis, may be helpful in dreaming some of these up. I look forward to seeing where the exploration of Josephson nanowires leads us.

References

- Kornich, V., H. S. Barakov, and Y. V. Nazarov, "Fine energy splitting of overlapping Andreev bound states in multiterminal superconducting nanostructures", *Physical Review Research* **1**, 033004 (2019).
- Pillet, J.-D., V. Benzoni, J. Griesmar, J.-L. Smirr, and Ç. Ö. Girit, "Nonlocal Josephson effect in Andreev molecules", *Nano letters* **19**, 7138–7143 (2019).
- Scherübl, Z., A. Pályi, and S. Csonka, "Transport signatures of an Andreev molecule in a quantum dot–superconductor–quantum dot setup", *Beilstein journal of nanotechnology* **10**, 363–378 (2019).

Su, Z., A. B. Tacla, M. Hocevar, D. Car, S. R. Plissard, E. P. Bakkers, A. J. Daley, D. Pekker, and S. M. Frolov, "Andreev molecules in semiconductor nanowire double quantum dots", *Nature communications* **8**, 1–6 (2017).

Väyrynen, J. I., G. Rastelli, W. Belzig, and L. I. Glazman, "Microwave signatures of majorana states in a topological Josephson junction", *Physical Review B* **92**, 134508 (2015).

Part II

The beautiful, messy details

6

BCS superconductivity

The central insight of Bardeen, Cooper, and Schrieffer (BCS) was that superconductivity can arise due to an attractive interaction between electrons in a metal, which they showed can occur via a virtual, phonon-mediated process. In this chapter, we will assume an attractive interaction between electrons, and show how under simple assumptions this leads to the original BCS pairing term (for a full derivation including the origin of the attractive interaction, self-consistency, etc. we direct the reader to “Introduction to Superconductivity” by Michael Tinkham). We then explore how this pairing term affects the physics of the many-body electron system. For additional reading, I also recommend the thesis of Landry Bretheau [Bretheau 2013]; I find his description of the various pictures of superconductivity very helpful.

6.1 The BCS Hamiltonian

The simplest attractive interaction between electrons we can imagine is one that is point-like in space. However, we know from Pauli exclusion that two electrons of the same spin can't be in the same spot. The simplest possible attractive term is thus given by a point-like interaction between opposite spin species:

$$-V \int dx \psi_s^\dagger(x) \psi_s(x) \psi_{\bar{s}}^\dagger(x) \psi_{\bar{s}}(x) \quad (6.1)$$

Here $-V$ is the strength of the attractive interaction, and $\psi_s^\dagger(x)$ creates an electron of spin s at point x . Throughout this chapter, we will refrain from implying a spin quantization

axis and simply label the two spin-1/2 species s and \bar{s} . We do this to emphasize that BCS superconductivity only requires an interaction between opposite spin species, and that no one spin direction is preferred over another.

In general, it is difficult to diagonalize many-body Hamiltonians that possess interactions between particles. However, any Hamiltonian that is bilinear in creation and annihilation operators can be brought to a diagonal form (only two operators per term, not four like we have now). Therefore, our goal is to approximate Eqn. 6.1 and bring it to a bilinear form. We start with the following observation: *the attractive term is such that if there is an electron with spin s at x , there will also be an electron with spin \bar{s} with some probability.* Mathematically, there will be a nonzero correlation for a pair of electrons $p = \langle \psi_s^\dagger(x) \psi_{\bar{s}}^\dagger(x) \rangle$. We are then well within our rights to consider the dynamics of this system around this average $\delta p = \psi_s^\dagger(x) \psi_{\bar{s}}^\dagger(x) - p$. We insert $\psi_s^\dagger(x) \psi_{\bar{s}}^\dagger(x) = p + \delta p$ into Eqn. 6.1:

$$\begin{aligned}
& -V \int dx \psi_s^\dagger(x) \psi_s(x) \psi_{\bar{s}}^\dagger(x) \psi_{\bar{s}}(x) \\
&= -V \int dx \psi_s^\dagger(x) \psi_{\bar{s}}^\dagger(x) \psi_{\bar{s}}(x) \psi_s(x) \\
&= -V \int dx (p + \delta p)(p^* + \delta p^\dagger) \\
&= -V \int dx |p|^2 + p \delta p^\dagger + \delta p p^* + \delta p \delta p^\dagger
\end{aligned} \tag{6.2}$$

The approximation then amounts to assuming δp is small such that $\delta p \delta p^\dagger$ is negligible. This is known as a mean-field approximation. Dropping this term (as well as constant terms that won't affect the dynamics), we have

$$= -V \int dx p \psi_{\bar{s}}(x) \psi_s(x) + p^* \psi_s^\dagger(x) \psi_{\bar{s}}^\dagger(x) \tag{6.3}$$

Finally, we define the BCS **pair potential** $\Delta e^{-i\varphi} = -Vp$. Here we keep Δ real, and define the **superconducting phase** φ to account for the fact that, in general, $p = \langle \psi_s^\dagger(x) \psi_{\bar{s}}^\dagger(x) \rangle$ is a

complex number. Injecting these definitions brings the BCS pairing term to its final form:

$$\int dx \Delta e^{i\varphi} \psi_s^\dagger(x) \psi_{\bar{s}}^\dagger(x) + \Delta e^{-i\varphi} \psi_{\bar{s}}(x) \psi_s(x) \quad (6.4)$$

While this interaction is simple in form, its effect on the physics of the electrons is profound. We will spend the rest of this chapter understanding these effects. Note that due to the mean-field approximation, the number of electrons is no longer conserved. Instead, electrons can be created/destroyed in pairs: *the parity of the number of electrons is conserved*.

This is often referred to as conservation of **fermion parity**.

Before we move on, one final manipulation will be helpful. As we will largely be working with plane waves, it is convenient to move to the momentum basis:

$$\begin{aligned} & \int dx \Delta e^{i\varphi} \psi_s^\dagger(x) \psi_{\bar{s}}^\dagger(x) + \text{H.c.} \\ &= \sum_{k,k'} \int dx \Delta e^{i\varphi} c_{k,s}^\dagger e^{ikx} c_{k',\bar{s}}^\dagger e^{ik'x} + \text{H.c.} \\ &= \sum_{k,k'} \Delta e^{i\varphi} c_{k,s}^\dagger c_{k',\bar{s}}^\dagger \int dx e^{i(k+k')x} + \text{H.c.} \\ &= \sum_k \Delta e^{i\varphi} c_{k,s}^\dagger c_{-k,\bar{s}}^\dagger + \text{H.c.} \end{aligned}$$

Note that in momentum space, the pairing is between species with opposite k .

6.2 Diagonalization of the BCS Hamiltonian

First, let's forget about superconductivity for a second and imagine a 1D system of freely propagating electrons. In second quantization, this system is described by the Hamiltonian

$$H = \sum_{k,s} \mathcal{E}_k c_{k,s}^\dagger c_{k,s}; \quad \mathcal{E}_k = \frac{\hbar^2 k^2}{2m_e} - \mu \quad (6.5)$$

where $c_{k,s}$ annihilates an electron with momentum $\hbar k$ and spin s . Note how we have sub-

tracted the chemical potential μ from the kinetic energy. The lowest energy state is achieved when all negative energy states $\mathcal{E}_k < 0$ are occupied. This is the usual Fermi sea: in the ground state, a state is occupied iff $\frac{\hbar^2 k^2}{2m_e} < \mu$.

As we saw in the last section, BCS theory describes superconductivity by introducing a pairing between electrons of the form $\Delta c_{k,s}^\dagger c_{-k,\bar{s}}^\dagger + \text{H.c.}$ (for now, we assume $\varphi = 0$). However, if we add this term to the Hamiltonian Eqn. 6.5, then it will no longer be diagonal (all terms are not of the form $c^\dagger c$). In order to bring the Hamiltonian back to a diagonal form, we make the following crucial observation: *the pairing term can be viewed as the simultaneous creation of two electrons, but it can also be viewed as the transmutation of a hole into an electron.*

Let's see what this statement means mathematically. First, we define the **hole** annihilation operator $h_k = c_{-k,\bar{s}}^\dagger$ (creating an electron is the same as destroying a hole). Note that the hole carries the opposite momentum of the electron. For symmetry of notation, we also redefine the **electron** annihilation operator $c_k = c_{k,s}$. Importantly here, we have dropped the spin labels. This is because in this picture of superconductivity, we are trading the spin degree of freedom for the electron/hole degree of freedom (see section 6.7 for more on this). With these new operators, the pairing term becomes $\Delta c_{k,s}^\dagger c_{-k,\bar{s}}^\dagger + \text{H.c.} = \Delta c_k^\dagger h_k + \text{H.c.}$, which is the mathematical equivalent of the observation we made above.

Before we actually include the pairing term in the Hamiltonian, let's re-express Eqn. 6.5 in terms of these new operators:

$$H = \sum_{k,s} \mathcal{E}_k c_{k,s}^\dagger c_{k,s} = \sum_k \mathcal{E}_k (c_k^\dagger c_k + h_k h_k^\dagger) \rightarrow \sum_k \mathcal{E}_k (c_k^\dagger c_k - h_k^\dagger h_k) \quad (6.6)$$

where we have dropped a constant offset resulting from the fermionic anti-commutation relations. While the new Hamiltonian is equivalent to Eqn. 6.5, the introduction of the holes has transformed the energy spectrum: one band has undergone a flip of momentum $k \rightarrow -k$ (the holes carry opposite the momentum of the electrons), as well as a flip in energy $\mathcal{E}_k \rightarrow -\mathcal{E}_k$ due to the fermionic anti-commutation relation as shown in Eqn. 6.6. This is shown pictorially in Fig. 6.1(a) and (b).

We now write the full BCS Hamiltonian for a bulk 1D superconductor by adding the

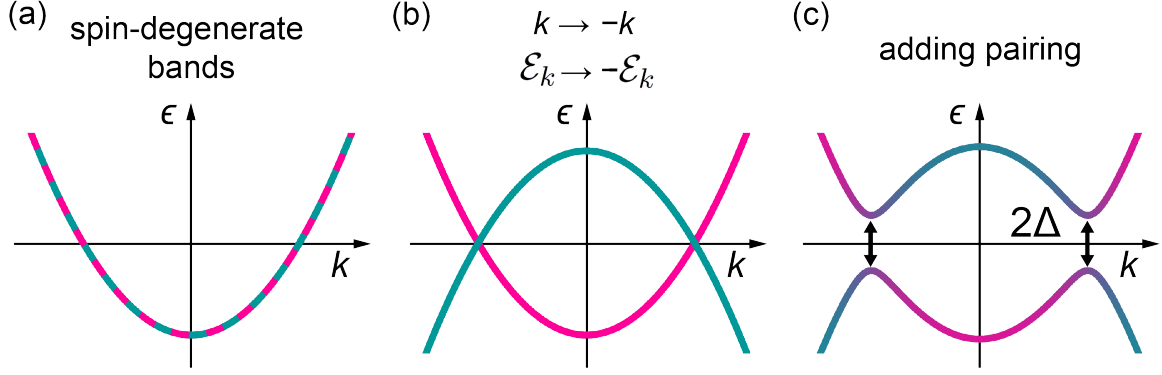


Figure 6.1: Building the band structure of a BCS superconductor | (a) We start with the spin-degenerate parabolic energy bands of a 1D system of free electrons. (b) Describing one of the bands as **holes** results in a flip of momentum as well as energy. (c) Adding pairing creates an avoided crossing of strength 2Δ between the two bands, with the new eigenstates having mixed **electron-hole** character.

pairing term to Eqn. 6.6:

$$H_{\text{BCS}} = \sum_k \mathcal{E}_k (c_k^\dagger c_k - h_k^\dagger h_k) + \Delta c_k^\dagger h_k + \Delta h_k^\dagger c_k \quad (6.7)$$

In this representation, we see that the pairing term coherently mixes the electron and hole branches of the original Hamiltonian. Specifically, the pairing term results in avoided crossings of strength 2Δ between the two branches [Fig. 6.1(c)]. Thus, we find that in BCS theory, there are no states within Δ of the Fermi energy. This is known as the **superconducting gap**.¹

We show this rigorously by first defining the **electron-hole spinor** $\Psi_k = \begin{pmatrix} c_k \\ h_k \end{pmatrix}$ such that the Hamiltonian can be expressed in the compact form

$$H_{\text{BCS}} = \sum_k \Psi_k^\dagger H_k \Psi_k; \quad H_k = [\mathcal{E}_k \sigma_z + \Delta \sigma_x] \quad (6.8)$$

Here the Pauli matrices σ_i operate in electron-hole space. This expression is useful because it shows explicitly that H_{BCS} does not mix k . We can then consider a single k , and diagonalize the two-by-two matrix H_k (if you like, we can think of k as parameterizing H_k). Because the Pauli matrices form a basis in this truncated Hilbert space, the energies can be

¹In BCS theory, the superconducting gap has the same value as the pair potential. However, this is not in general true; it depends on the momentum-dependence of the electron-electron attraction.

read off immediately:

$$\pm\epsilon_k = \pm\sqrt{\mathcal{E}_k^2 + \Delta^2} \quad (6.9)$$

As for any two-by-two system, full diagonalization is then achieved by applying a unitary U_k such that $U_k H_k U_k^\dagger = \epsilon_k \sigma_z$. This transformation is often expressed in terms of two parameters known as **coherence factors**:

$$u_k = \frac{1}{\sqrt{2}} \sqrt{1 + \mathcal{E}_k/\epsilon_k}; \quad v_k = \frac{1}{\sqrt{2}} \sqrt{1 - \mathcal{E}_k/\epsilon_k} \quad (6.10)$$

The unitary is then written $U_k = \begin{pmatrix} u_k & v_k \\ -v_k & u_k \end{pmatrix}$, and our diagonalization of H_k is complete (note that while in 6.6 the coherence factors are purely real, this will not be the case below). However, to diagonalize the full Hamiltonian H_{BCS} we must define new fermionic operators $\begin{pmatrix} \gamma_{k,+} \\ \gamma_{k,-} \end{pmatrix} = U_k \Psi_k$. With these new definitions, we can inject $I = U_k^\dagger U_k$ and simplify:

$$H_{\text{BCS}} = \sum_k \Psi_k^\dagger U_k^\dagger U_k H_k U_k^\dagger U_k \Psi_k = \sum_k \epsilon_k (\gamma_{k,+}^\dagger \gamma_{k,+} - \gamma_{k,-}^\dagger \gamma_{k,-}) \quad (6.11)$$

and thus reach a fully diagonal Hamiltonian. The new operators $\gamma_{k,\pm}$ are known as **Bogoliubons** (named after Nikolay Bogoliubov, who was one of the first physicists to point out the above transformation), and are the effective particles of BCS superconductors. Note that here, $\gamma_{k,+}$ destroys a Bogoliubon at positive energy $+\epsilon_k$, while $\gamma_{k,-}$ destroys a Bogoliubon at negative energy $-\epsilon_k$.

6.3 Discussion of the single-particle states

In this section, we will develop a notation for the Bogoliubons and their wavefunctions that is particularly helpful for understanding Andreev reflection. For all following sections in this chapter, however, we will use the notation already introduced above.

While we did not note it explicitly above, we can see from the definition of the Bogoli-

ubons that they are superpositions of electrons and holes:

$$\begin{pmatrix} \gamma_{k,+} \\ \gamma_{k,-} \end{pmatrix} = U_k \Psi_k = \begin{pmatrix} +u_k^* c_k + v_k^* h_k \\ -v_k c_k + u_k h_k \end{pmatrix} \quad (6.12)$$

This relation can also be expressed as $\gamma_{k,\pm}^\dagger = \Psi_k^\dagger \psi_\pm$, where ψ_\pm are the electron-hole wavefunctions of the Bogoliubons:

$$\psi_+ = \begin{pmatrix} u_k \\ v_k \end{pmatrix} \quad \psi_- = \begin{pmatrix} -v_k^* \\ u_k^* \end{pmatrix} \quad (6.13)$$

The upper component of the spinor is the electron amplitude, while the lower component is the hole amplitude. At the gap edge where $\mathcal{E}_k = 0$ ($|k| = k_F$), Eqn. 6.10 gives $|u_k| = |v_k| = \frac{1}{\sqrt{2}}$. *The minimum energy Bogoliubons $|\epsilon_k| = \Delta$ are thus equal superpositions of electrons and holes.* This mixed nature of the single-particle eigenstates is an important property of superconductors, and, as we will see, leads to interesting phenomena such as Andreev reflection. To discuss such phenomena, however, it is first important to understand the nature of the Bogoliubons in detail.

Away from the gap edge, each Bogoliubon is either **electron-like** (larger electron amplitude) or **hole-like** (larger hole amplitude). A common pitfall is to assume that because $\gamma_{k,+}^\dagger$ has a positive energy, it is electron-like, and vice versa for $\gamma_{k,-}^\dagger$. However, as can be seen graphically in Fig. 6.2, the electron/hole character of the Bogoliubons depends not only on their energy, but also on their momentum (for now, ignore the γ labels in Fig. 6.2). If $|k| > k_F$, it is indeed the case that the positive energy Bogoliubons are electron-like, while the negative energy Bogoliubons are hole-like. But if $|k| < k_F$, the situation is flipped: the positive energy Bogoliubons are hole-like, while the negative energy Bogoliubons are electron-like. All of this is consistent with what we know about a normal metal: if we are above the Fermi energy, holes are energetically favorable, while below the Fermi energy electrons are favored.

When considering the electron/hole character of the Bogoliubons, a large amount of confusion can stem from the fact that the notation $\gamma_{k,\pm}$ hides their four-fold degeneracy. For illustrative purposes, let's focus on the positive energy band ϵ_k as plotted in Fig. 6.2. As

can be seen in the figure, there is the typical two-fold degeneracy associated with $k \rightarrow -k$ (the kinetic energy does not care about the sign of the momentum). But about each of the two Fermi points, there exists a second two-fold degeneracy because for every state slightly above k_F , there is an equal energy state slightly below k_F (mathematically, ϵ_k is invariant under $\mathcal{E}_k \rightarrow -\mathcal{E}_k$). From Fig. 6.2, we see that each pair of such states has opposite electron/hole character. So in total, we find that for every energy (strictly, $\Delta < |\pm \epsilon_k| < \mu$), there is one electron-like and one hole-like Bogoliubon for positive momentum, and the same for negative momentum. A final comment on the degeneracies: in this picture of superconductivity we have lost spin degeneracy because we swapped it for the mirror symmetry of the energies $\pm \epsilon_k$. This is discussed further in section 6.7.

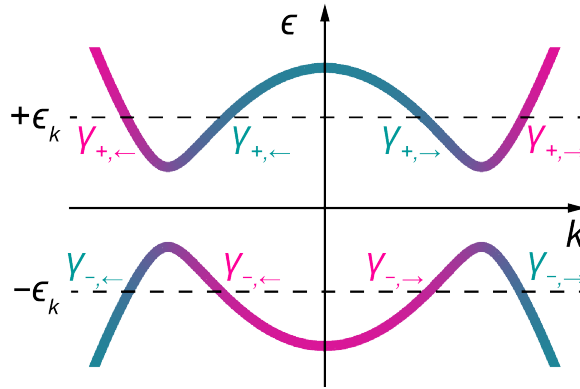


Figure 6.2: Breaking up the Bogoliubons γ for each value of ϵ_k | Color indicates the electron/hole character (pink is larger electron amplitude, and teal is larger hole amplitude). The subscript $+$ ($-$) indicates whether acting with γ^\dagger adds (removes) energy, and \rightarrow (\leftarrow) indicates positive (negative) momentum.

In order to codify the electron/hole character of the Bogoliubons into notation and mitigate confusion around the degeneracy, we break the Bogoliubons $\gamma_{k,\pm}$ up into four species of equal energy. Pink/teal indicates whether a Bogoliubon is **electron-like** or **hole-like**, \rightarrow / \leftarrow indicates whether it has positive/negative momentum, and $+/-$ continues to indi-

cate positive/negative energy (see γ labels in Fig. 6.2 for a graphical representation):

$$\gamma_{k,+} = \begin{cases} \gamma_{+,\leftarrow} \\ \gamma_{+,\leftarrow} \\ \gamma_{+,\rightarrow} \\ \gamma_{+,\rightarrow} \end{cases} \quad \gamma_{k,-} = \begin{cases} \gamma_{-,\leftarrow} & k < -k_F \\ \gamma_{-,\leftarrow} & -k_F < k < 0 \\ \gamma_{-,\rightarrow} & 0 < k < k_F \\ \gamma_{-,\rightarrow} & k > k_F \end{cases} \quad (6.14)$$

To understand Andreev reflection, we will also need the electron-hole wavefunctions $\psi(x)$ for these Bogoliubons, where we now explicitly include the position dependence:

$$\psi_{\rightarrow} = \begin{pmatrix} u \\ v \end{pmatrix} e^{+ikx} \quad \psi_{\leftarrow} = \begin{pmatrix} u \\ v \end{pmatrix} e^{+ikx} \quad \psi_{\leftarrow} = \begin{pmatrix} u \\ v \end{pmatrix} e^{-ikx} \quad \psi_{\rightarrow} = \begin{pmatrix} u \\ v \end{pmatrix} e^{-ikx} \quad (6.15)$$

Note that while in Eqn. 6.13, the electron amplitude of ψ_+ was u_k while the electron amplitude of ψ_- was $-v_k^*$, now the electron amplitude is always given by u . Eqn. 6.15 applies to both positive and negative energy Bogoliubons, with appropriate definitions of the electron/hole amplitudes:

$$\begin{aligned} u &= \frac{1}{\sqrt{2}} \sqrt{1 + \sqrt{1 - (\Delta/\epsilon)^2}} & v &= \frac{e^{-i\varphi}}{\sqrt{2}} \text{sgn}(\epsilon) \sqrt{1 - \sqrt{1 - (\Delta/\epsilon)^2}} \\ u &= \frac{1}{\sqrt{2}} \sqrt{1 - \sqrt{1 - (\Delta/\epsilon)^2}} & v &= \frac{e^{-i\varphi}}{\sqrt{2}} \text{sgn}(\epsilon) \sqrt{1 + \sqrt{1 - (\Delta/\epsilon)^2}} \end{aligned} \quad (6.16)$$

Importantly, we have reintroduced the superconducting phase φ . This is easy to do at this stage because we know that the phase associated with a pair of electrons is φ , or equivalently that the phase of a hole relative to an electron is $-\varphi$. Finally, we present simplified forms for the momenta by first linearizing the kinetic energy $\mathcal{E} \approx \pm \hbar v_F (k \mp k_F)$, and then using $|\mathcal{E}| = \sqrt{\epsilon^2 - \Delta^2}$ to write

$$\begin{aligned}
k &= k_F + \frac{1}{\hbar v_F} \text{sgn}(\epsilon) \sqrt{\epsilon^2 - \Delta^2} \\
k &= k_F - \frac{1}{\hbar v_F} \text{sgn}(\epsilon) \sqrt{\epsilon^2 - \Delta^2}
\end{aligned} \tag{6.17}$$

Several notes about the wavefunctions 6.15:

- We reiterate that while in 6.13 we had different solutions for positive and negative energies, 6.15 works for all energies. This is taken care of by $\text{sgn}(\epsilon)$ in 6.16 and 6.17.
- We have defined things such that as $\Delta/\epsilon \rightarrow 0$, we have $u, v \rightarrow 1$ and $v, u \rightarrow 0$ [see Fig. 6.3]. Thus while all Bogoliubons have electron character u and hole character v , whether $|u|$ or $|v|$ is larger determines if a Bogoliubon is electron-like or hole-like.
- At the gap edge $\epsilon = \pm\Delta$, $u = |u| = |v| = v = \frac{1}{\sqrt{2}}$. These Bogoliubons are equal superpositions of electrons and holes.
- For $\Delta \ll \mu$ (where linearization is valid), we have $k \approx k \approx k_F$. The correspondence between the \leftarrow / \rightarrow subscripts and the sign in the exponent is thus consistent.

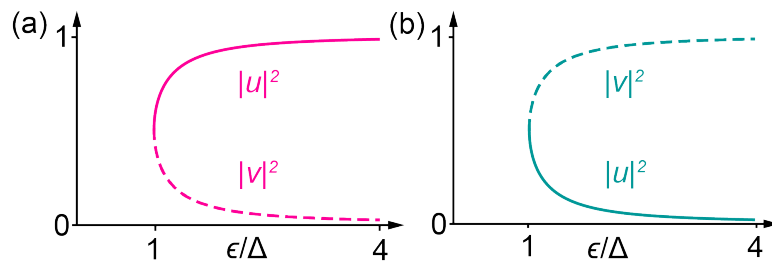


Figure 6.3: Electron amplitudes (u , solid lines) and hole amplitudes (v , dashed lines) of the Bogoliubons | For electron-like Bogoliubons (a), the electron amplitude u approaches 1 as $\epsilon/\Delta \rightarrow \infty$, while for hole-like Bogoliubons (b), the hole amplitude v approaches 1 as $\epsilon/\Delta \rightarrow \infty$. Both kinds of Bogoliubons have equal electron-hole character $|u|^2 = |v|^2$ at $\epsilon = \Delta$.

6.4 Density of states

The most common pictorial representation of a superconductor's state is via the density of states. The density of states is defined as $\nu_S = \frac{dN}{d\epsilon_k}$, where N is the total number of states with energy less than ϵ_k . We make the approximation that the density of states of the normal metal $\nu_N = \frac{dN}{d\mathcal{E}_k}$ is constant on the scale of Δ , then use the chain rule:

$$\begin{aligned} \nu_S &= \frac{dN}{d\epsilon_k} = \frac{dN}{d\mathcal{E}_k} \frac{d\mathcal{E}_k}{d\epsilon_k} \\ &= \nu_N \frac{d}{d\epsilon_k} \sqrt{\epsilon_k^2 - \Delta^2} \\ &= \nu_N \frac{\epsilon_k}{\sqrt{\epsilon_k^2 - \Delta^2}} \end{aligned} \quad (6.18)$$

This is plotted in Fig. 6.4. At $\pm\epsilon_k = \Delta$, there are divergences in the density of states known as **coherence peaks**. Mathematically, they occur because $1/\frac{d\epsilon}{dk} \rightarrow \infty$ at the gap edge. Physically, they occur because the pairing has resulted in an avoided crossing between the electron and hole bands, "pushing" states away from the Fermi energy and to the gap edge.

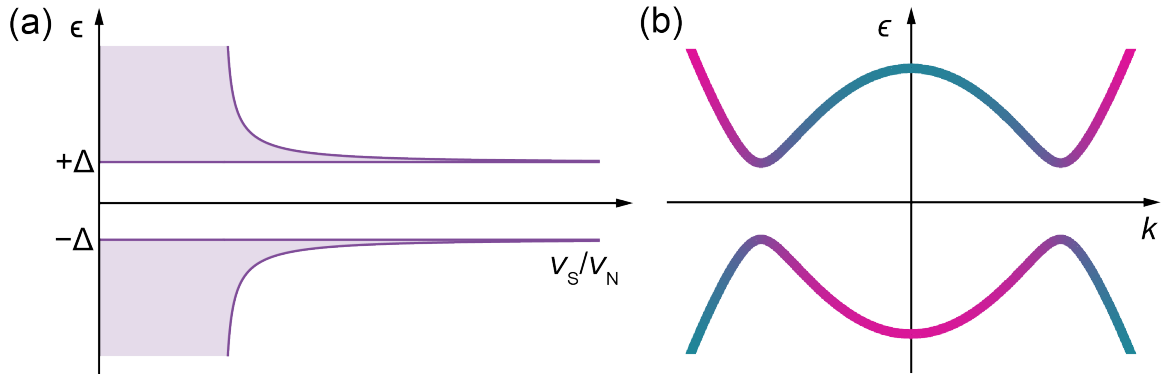


Figure 6.4: Superconducting density of states in the one-particle picture | (a) Light purple shading indicates unoccupied states. As the spectrum is symmetric about zero energy, ν_S must be symmetric as well. A divergence occurs at $|\epsilon| = \Delta$ because $1/\frac{d\epsilon}{dk} \rightarrow \infty$ at the gap edge, as can be seen in (b).

6.5 Superconducting ground state and the Cooper pairs

So far, we have discussed individual Bogoliubons. However, it is clear that we are working with a many-body system. To find the ground state, let's first re-state the diagonalized BCS Hamiltonian:

$$H_{\text{BCS}} = \sum_k \epsilon_k (\gamma_{k,+}^\dagger \gamma_{k,+} - \gamma_{k,-}^\dagger \gamma_{k,-}) \quad (6.19)$$

The ground state of the system is, by definition, the lowest energy state. Every $\gamma_{k,-}^\dagger$ has a negative energy $-\epsilon_k$. Therefore, the ground state is the state with all of these negative energy states populated (see Fig. 6.5(a) for a pictorial representation). To find this state mathematically, we must first find the vacuum state of the Bogoliubons $|V\rangle$. This is defined by

$$\gamma_{k,\pm}|V\rangle = 0 \quad (6.20)$$

for all k . Using the definition of the Bogoliubons (Eqn. 6.12, 6.13):

$$\begin{aligned} \gamma_{k,\pm}|V\rangle &= \psi_\pm^\dagger \Psi_k |V\rangle \\ &= \psi_\pm^\dagger \begin{pmatrix} c_k \\ h_k \end{pmatrix} |V\rangle \\ &= \psi_\pm^\dagger \begin{pmatrix} c_{k,s} \\ c_{-k,\bar{s}}^\dagger \end{pmatrix} |V\rangle \end{aligned} \quad (6.21)$$

So if $|V\rangle = c_{-k,\bar{s}}^\dagger |0\rangle$, then $\gamma_{k,\pm}|V\rangle = 0$ where $|0\rangle$ is the vacuum of electrons. Then we can act on the vacuum state with all the negative energy Bogoliubons to get the ground state:

$$\begin{aligned}
|g_\varphi\rangle &= \prod_k \gamma_{k,-}^\dagger |V\rangle \\
&= \prod_k \Psi_k^\dagger \psi_- |V\rangle \\
&= \prod_k (-v_k^* c_{k,s}^\dagger + u_k^* c_{-k,\bar{s}}) c_{-k,\bar{s}}^\dagger |0\rangle \\
&= \prod_k (u_k^* - v_k^* c_{k,s}^\dagger c_{-k,\bar{s}}^\dagger) |0\rangle \\
&\rightarrow \prod_k (u_k - v_k e^{i\varphi} c_{k,s}^\dagger c_{-k,\bar{s}}^\dagger) |0\rangle
\end{aligned} \tag{6.22}$$

where in the last step we take the expressions for u_k, v_k from Eqn. 6.10 and placed the superconducting phase on the creation operators. Note that for each value of φ there is a different ground state, as indicated by the subscript in $|g_\varphi\rangle$. We see that the ground state is a product state of superpositions of unoccupied and occupied pairs of electrons. This is the first definition of a **Cooper pair**: $u_k - v_k e^{i\varphi} c_{k,s}^\dagger c_{-k,\bar{s}}^\dagger$.

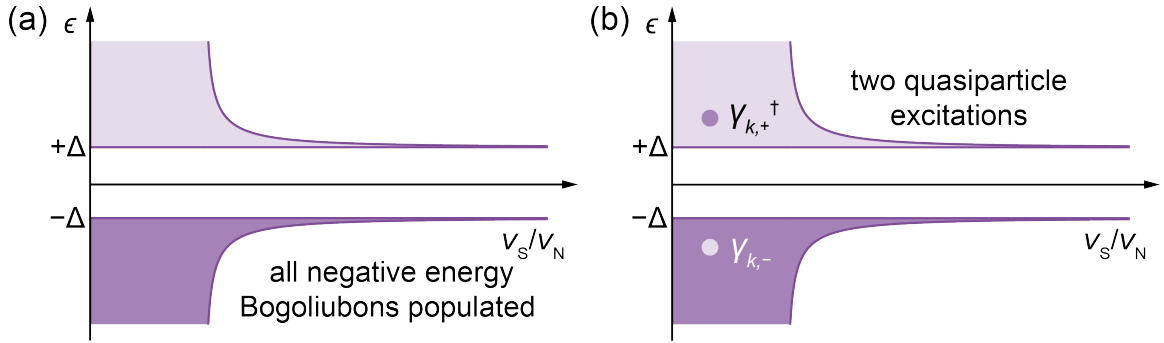


Figure 6.5: BCS ground state and quasiparticle excitations | (a) In the ground state of the superconductor, all the negative energy Bogoliubons are populated, as indicated by dark purple shading. (b) Quasiparticle excitations can be created either by de-populating a negative energy Bogoliubon, or by populating a positive energy one.

We can also construct a ground state with a definite number of electron pairs N . This

is given by the Fourier transform:

$$|N\rangle = \int d\varphi e^{-iN\varphi} |g_\varphi\rangle \quad (6.23)$$

This is known as Anderson projection. How do we see that $|N\rangle$ is indeed the state with a definite number of electron pairs N ? First imagine fully factorizing the product state in the last line of Eqn. 6.22. As each pair of creation operators carries around $e^{i\varphi}$, the number of factors of $e^{i\varphi}$ in a particular term will be the same as the number of pairs. The $e^{-iN\varphi}$ in the integrand will then pick out only terms with N pairs, and all other terms will integrate to zero. The second definition of the Cooper pairs is the electron pairs described by $|N\rangle$. For example, it is often heard that " N Cooper pairs have tunneled across a junction." What is actually meant is that the superconductor on one side of the junction is described by $|N\rangle$.

6.6 Quasiparticle excitations

An excited state of the superconductor can be reached by starting with the ground state $|g_\varphi\rangle$, and then either de-populating one of the negative energy Bogoliubons or populating one of the positive energy Bogoliubons [Fig. 6.5(b)]. Each such excitation is known as a **quasiparticle**. Mathematically,

$$\begin{aligned} \gamma_{k',-} |g_\varphi\rangle &= \gamma_{k',-} \prod_k \gamma_{k,-}^\dagger |V\rangle = c_{-k',\bar{s}}^\dagger \prod_{k \neq k'} (u_k - v_k e^{i\varphi} c_{k,s}^\dagger c_{-k,\bar{s}}^\dagger) |0\rangle \\ \gamma_{k',+}^\dagger |g_\varphi\rangle &= \gamma_{k',+}^\dagger \prod_k \gamma_{k,-}^\dagger |V\rangle = c_{k',s}^\dagger \prod_{k \neq k'} (u_k - v_k e^{i\varphi} c_{k,s}^\dagger c_{-k,\bar{s}}^\dagger) |0\rangle \end{aligned} \quad (6.24)$$

We see that in a bulk superconductor, an individual quasiparticle actually corresponds to an unpaired electron. All other electrons still form Cooper pairs, but the unpaired electron no longer participates in the condensate.

It's important to note that for an isolated hunk of superconductor, quasiparticles must always be created in pairs. While we have lost conservation of electron number in the BCS

Hamiltonian, parity is still conserved. However, the action of an individual Bogoliubon $\gamma_{k,\pm}^\dagger = (c_k^\dagger h_k^\dagger)\psi_\pm$ breaks parity: it is a superposition of creating/destroying a single electron. As such, any excitation of an isolated superconductor must be in the form of pairs of quasiparticles.

6.7 Pictures of superconductivity

6.7.1 One-particle picture

Everything that has been presented so far in this chapter has been in what is known as the “one-particle picture” of superconductivity. This is a convenient picture because it lets us see the ground state directly from the negative energy Bogoliubons. We can get to the other two pictures from the one-particle picture via some simple transformations.

For illustrative purposes, let’s imagine starting from the ground state of the superconductor and then creating an excitation. We can then see how this excitation looks in the different pictures. Specifically, let’s suppose that we have a photon incident on our superconductor with energy $\hbar\omega > 2\Delta$. Because the photon doesn’t carry much momentum, the momentum of the Bogoliubons must be conserved in the absorption. The absorption thus consists of destroying a negative energy Bogoliubon and creating a positive energy one with the same momentum:

$$\gamma_{k,+}^\dagger \gamma_{k,-} |g_\varphi\rangle \quad 2\epsilon_k = \hbar\omega \quad (6.25)$$

This situation is exactly what is depicted in Fig. 6.5(b). Now let’s see how this many-body configuration looks in the other pictures of superconductivity.

6.7.2 Excitation picture

Perhaps the most common representation of superconductivity is the excitation picture. In this picture, we construct the Bogoliubons such that they all describe excitations out of the ground state. While in this picture the properties of the ground state are hidden, it has the advantage of highlighting the spinful nature of the Bogoliubons, and it is for this reason

that we use it in Chapters 2 through 4.

The transformation is straightforward from the one-particle picture. We keep the positive energy Bogoliubons $\gamma_{k,+}$ as they are, but describe the negative energy Bogoliubons by their Hermitian conjugate:

$$\begin{pmatrix} \gamma_{k,s}^\dagger \\ \gamma_{-k,\bar{s}}^\dagger \end{pmatrix} = \begin{pmatrix} \gamma_{k,+}^\dagger \\ \gamma_{k,-}^\dagger \end{pmatrix} = \begin{pmatrix} +u_k c_k^\dagger + v_k h_k^\dagger \\ -v_k c_k + u_k h_k \end{pmatrix} = \begin{pmatrix} +u_k c_{k,s}^\dagger + v_k c_{-k,\bar{s}} \\ -v_k c_{k,s} + u_k c_{-k,\bar{s}}^\dagger \end{pmatrix} \quad (6.26)$$

Note the flip of momentum and spin on $\gamma_{-k,\bar{s}}^\dagger$ and how this tracks back correctly to the underlying electrons as seen on the far right-hand side. With these new definitions, the Hamiltonian becomes

$$H_{\text{BCS}} = \sum_k \epsilon_k (\gamma_{k,+}^\dagger \gamma_{k,+} - \gamma_{k,-}^\dagger \gamma_{k,-}) \rightarrow \sum_k E_k (\gamma_{k,s}^\dagger \gamma_{k,s} + \gamma_{k,\bar{s}}^\dagger \gamma_{k,\bar{s}}), \quad E_k = \epsilon_k \quad (6.27)$$

Where we have dropped a constant resulting from the fermionic anti-commutation relations and rearranged the sum over momentum for $\gamma_{k,\bar{s}}$. Note that we have also redefined the energy $E_k = \epsilon_k$; we do this to highlight that if we switched to a new picture of superconductivity. The effect on the spectrum is shown graphically in Fig. 6.6: we have taken the negative energy band of the one particle picture and flipped it in momentum $-k \rightarrow +k$ as well as energy $-\epsilon_k \rightarrow +\epsilon_k$.

We see that in the excitation picture, we once again have spin degeneracy: both $\gamma_{k,s}^\dagger$ and $\gamma_{k,\bar{s}}^\dagger$ create a particle with positive energy E_k . In fact, our example excitation 6.25 is exactly this:

$$\gamma_{k,+}^\dagger \gamma_{k,-} |g_\varphi\rangle = \gamma_{k,s}^\dagger \gamma_{-k,\bar{s}}^\dagger |g_\varphi\rangle \quad 2E_k = \hbar\omega \quad (6.28)$$

Instead of moving a Bogoliubon from negative to positive energy as in the one-particle picture, here we see that we create two Bogoliubons (quasiparticles) with opposite spin and momentum. In general, when moving from the one particle picture to the excitation picture, we can imagine flipping each negative energy state both in energy and momentum,

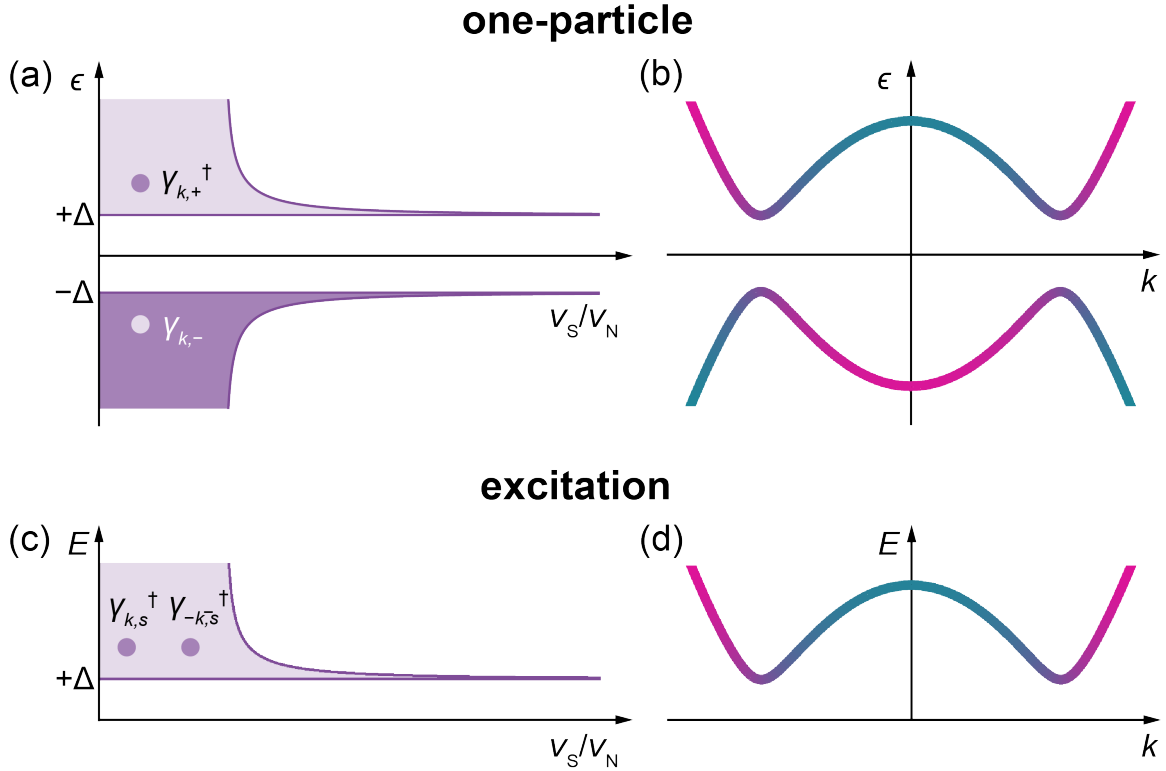


Figure 6.6: Comparing density of states, energy spectra, and quasiparticle excitations in the one-particle (a/b) and excitation pictures (c/d) | Note how in moving to the excitation picture, the depopulated state at negative energy has become a populated state at positive energy.

as well as inverting the population.

6.7.3 Semiconductor picture

The final picture of superconductivity we present here is the semiconductor picture. It has become prominent in recent years as investigations of the interplay between superconductivity, spin-orbit coupling, and Zeeman fields have picked up speed, such as in topological quantum computation [Fu and Kane 2008; Lutchyn, Sau, and Das Sarma 2010; Oreg, Refael, and Oppen 2010].

The semiconductor picture is useful when we have conflicting pairings of creation and annihilation operators in our Hamiltonian. For instance, suppose we have both supercon-

ducting pairing and a Zeeman field perpendicular to the spin quantization axis:

$$\Delta c_{k,s}^\dagger c_{-k,\bar{s}}^\dagger + B_\perp c_{k,s}^\dagger c_{k,\bar{s}} + \text{H.c.} \quad (6.29)$$

In the one-particle picture, we brought the pairing term to a diagonal form by replacing one of the electron creation operators with a hole annihilation operator $c_{-k,\bar{s}}^\dagger = h_{k,s}$ (note that we are now keeping the spin label for reasons that will become apparent). However, if we apply this transformation to Eqn. 6.29, then we just move the problem over to the Zeeman term:

$$\Delta c_{k,s}^\dagger h_{k,s} + B_\perp c_{k,s}^\dagger h_{-k,s}^\dagger + \text{H.c.} \quad (6.30)$$

So should we perform the electron/hole transformation or not? The answer is that yes, we should, but that we should also keep the original electrons. Moreover, we apply the transformation to both spin species: $c_{-k,\bar{s}}^\dagger = h_{k,s}$ and $c_{k,s}^\dagger = h_{-k,\bar{s}}$. Let's see how this works with the free particle Hamiltonian:

$$\begin{aligned} H &= \sum_k \mathcal{E}_k (c_{k,s}^\dagger c_{k,s} + c_{k,\bar{s}}^\dagger c_{k,\bar{s}}) \\ &= \frac{1}{2} \sum_k \mathcal{E}_k (c_{k,s}^\dagger c_{k,s} + c_{k,\bar{s}}^\dagger c_{k,\bar{s}} + c_{k,s}^\dagger c_{k,s} + c_{k,\bar{s}}^\dagger c_{k,\bar{s}}) \\ &= \frac{1}{2} \sum_k \mathcal{E}_k (c_{k,s}^\dagger c_{k,s} + c_{k,\bar{s}}^\dagger c_{k,\bar{s}} - h_{-k,\bar{s}}^\dagger h_{-k,\bar{s}} - h_{-k,s}^\dagger h_{-k,s}) \\ &= \frac{1}{2} \sum_k \mathcal{E}_k (c_{k,s}^\dagger c_{k,s} + c_{k,\bar{s}}^\dagger c_{k,\bar{s}} - h_{k,\bar{s}}^\dagger h_{k,\bar{s}} - h_{k,s}^\dagger h_{k,s}) \end{aligned} \quad (6.31)$$

where we have rearranged the sum of momentum for the holes term in the last step. Note the factor of $\frac{1}{2}$ that has appeared out front; this is often forgotten. Now we define the four-component ‘‘Nambu’’ spinor $\Upsilon_k^\dagger = \begin{pmatrix} c_{k,s}^\dagger & c_{k,\bar{s}}^\dagger & h_{k,s}^\dagger & -h_{k,\bar{s}}^\dagger \end{pmatrix}$. Note the minus sign on the last hole operator; this is important so that terms don't cancel due to fermionic anti-

commutation. The Hamiltonian can thus be written as

$$H = \sum_k \frac{\mathcal{E}_k}{2} \Upsilon_k^\dagger \sigma_z s_I \Upsilon_k \quad (6.32)$$

where the Pauli matrices σ_i act in electron-hole space and the Pauli matrices s_i act in spin space. Now the Zeeman term can be written as

$$B_\perp c_{k,s}^\dagger c_{k,\bar{s}} + \text{H.c.} = \frac{B_\perp}{2} \Upsilon_k^\dagger \sigma_I s_X \Upsilon_k \quad (6.33)$$

and the pairing term can be written as

$$\Delta c_{k,s}^\dagger h_{k,s} + \text{H.c.} = \frac{\Delta}{2} \Upsilon_k^\dagger \sigma_X s_I \Upsilon_k \quad (6.34)$$

and then we can proceed as we did in the one-particle picture to find the eigenstates, only this time with a four-component wavefunction.

However, one must be quite careful when using the semiconductor picture. By describing things with the four-component spinor Υ_k , we have artificially doubled the degrees of freedom. Let's explore what effects this leads to. First, we re-express the spinor in terms of only electron operators:

$$\Upsilon_k^\dagger = \begin{pmatrix} c_{k,s}^\dagger & c_{k,\bar{s}}^\dagger & c_{-k,\bar{s}} & -c_{-k,s} \end{pmatrix} \quad (6.35)$$

Notice that the first term in the spinor is equal to minus the Hermitian conjugate of the fourth, and the second is equal to the Hermitian conjugate of the third. Mathematically, this is expressed via the symmetry operation

$$\mathcal{P} = \sigma_Y s_Y K = \begin{pmatrix} 0 & 0 & 0 & -1 \\ 0 & 0 & 1 & 0 \\ 0 & 1 & 0 & 0 \\ -1 & 0 & 0 & 0 \end{pmatrix} K \quad \mathcal{P} \Upsilon_k^\dagger = \Upsilon_k \quad (6.36)$$

where K is the complex conjugation operator. This artificial symmetry is sometimes known as **electron-hole symmetry**, and is purely an artifact of the semiconductor picture (this is not to be confused with a different usage of "electron-hole symmetry", which is an approximate symmetry that can occur in systems when particles above the Fermi energy behave

the same as those below). Applying this to each of the terms in the Hamiltonian:

$$H_k = \mathcal{E}_k \sigma_Z s_I + \Delta \sigma_X s_I + B_\perp \sigma_I s_X \quad (6.37)$$

$$\begin{aligned} \text{kinetic: } & \mathcal{P} \left[\mathcal{E}_k \sigma_Z s_I \right] \mathcal{P}^\dagger = \mathcal{E}_k \sigma_Y s_Y \sigma_Z s_I \sigma_Y s_Y = -\mathcal{E}_k \sigma_Z s_I \\ \text{pairing: } & \mathcal{P} \left[\Delta \sigma_X s_I \right] \mathcal{P}^\dagger = \Delta \sigma_Y s_Y \sigma_X s_I \sigma_Y s_Y = -\Delta \sigma_X s_I \\ \text{Zeeman: } & \mathcal{P} \left[B_\perp \sigma_I s_X \right] \mathcal{P}^\dagger = B_\perp \sigma_Y s_Y \sigma_I s_X \sigma_Y s_Y = -B_\perp \sigma_I s_X \end{aligned}$$

So in total, H_k picks up a minus sign under the transformation $\mathcal{P} H_k \mathcal{P}^\dagger = -H_k$. Let's see what this means for the eigenstates ψ_i (in the one-particle picture we had only two solutions \pm , but since H_k is now 4-D there are four solutions indexed by i):

$$\begin{aligned} H_k \psi_i &= \epsilon_{k,i} \psi_i & (6.38) \\ \mathcal{P} H_k \mathcal{P}^\dagger \mathcal{P} \psi_i &= \mathcal{P} \epsilon_i \psi_i \\ H_k \mathcal{P} \psi_i &= -\epsilon_i \mathcal{P} \psi_i \end{aligned}$$

The last line tells us that $\psi_j = \mathcal{P} \psi_i$ is also an eigenstate of H_k with energy $\epsilon_j = -\epsilon_i$. However, it is not just that there is a mirror symmetry, but that the associated Bogoliubons are very much the same:

$$\gamma_{k,i}^\dagger = \Upsilon_k^\dagger \psi_i = \Upsilon_k^\dagger \mathcal{P}^\dagger \mathcal{P} \psi_i = \Upsilon_k \psi_j = \gamma_{k,j} \quad (6.39)$$

We do not have independent Bogoliubons: creating the Bogoliubon $\gamma_{k,i}^\dagger$ with energy ϵ_i is equivalent to destroying the Bogoliubon with energy $-\epsilon_i$. Thus not only do we have a

forced mirror symmetry in the spectrum (even in the presence of the time-reversal symmetry breaking B_{\perp}), but when filling levels with Bogoliubons, we must take care to respect property 6.39. For our example excitation, this means that we now have two populated Bogoliubons at positive energy, and two de-populated Bogoliubons at negative energy (see Fig. a.7). Note that in Fig. 6.7, we are playing it a bit loose with the spin labels. We originally applied the Zeeman term perpendicular to the spin quantization axis defining s and \bar{s} , but in Fig. 6.7 we are still labeling the spin-split states as s and \bar{s} .

References

- Brethau, L., "Localized excitations in superconducting atomic contacts: probing the Andreev doublet.", PhD thesis (Ecole Polytechnique X, 2013).
- Fu, L. and C. L. Kane, "Superconducting proximity effect and majorana fermions at the surface of a topological insulator", *Phys. Rev. Lett.* **100**, 096407 (2008).
- Lutchyn, R. M., J. D. Sau, and S. Das Sarma, "Majorana fermions and a topological phase transition in semiconductor-superconductor heterostructures", *Phys. Rev. Lett.* **105**, 077001 (2010).
- Oreg, Y., G. Refael, and F. von Oppen, "Helical liquids and majorana bound states in quantum wires", *Phys. Rev. Lett.* **105**, 177002 (2010).

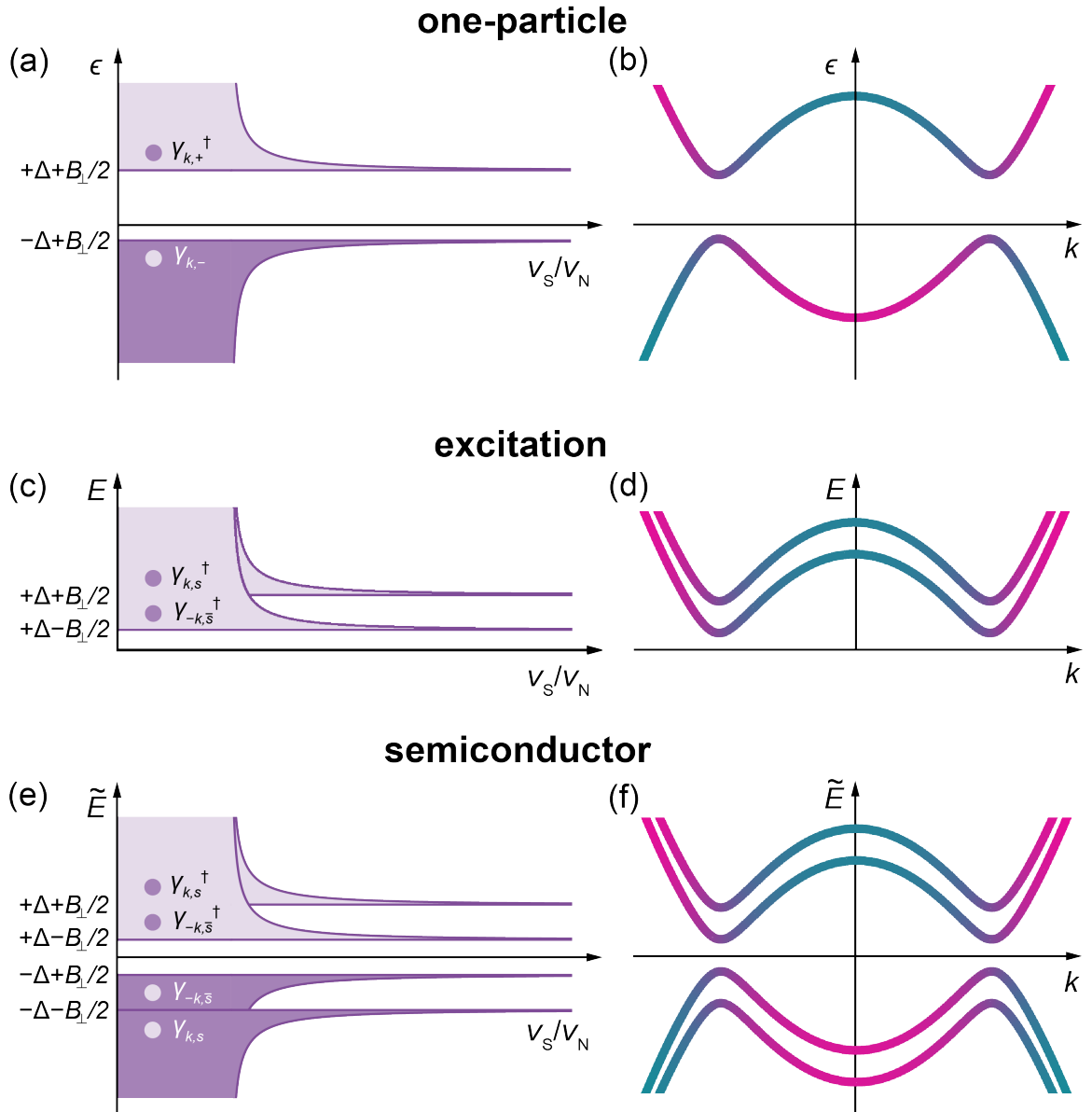


Figure 6.7: Comparing density of states and quasiparticle excitations for each of the three pictures | For illustrative purposes, a Zeeman field is included to break spin degeneracy. (a/b) For the one-particle picture, the Zeeman field shifts all energies upward. (c/d) In the excitation picture, one spin species is shifted up while the other is shifted down. Here we see an example of how the excitation picture is more intuitive when dealing with spin-dependent interactions. (e/f) In the semiconductor picture, we can imagine duplicating the excitation picture, but then flipping the duplicate to negative energy. The two quasiparticles are then represented by two filled states at positive energy, and two empty ones at negative energy.

7

Andreev reflection, Andreev levels, and the Josephson effect

7.1 Andreev reflection

Andreev reflection is the fundamental process underpinning mesoscopic superconductivity. It is at the heart of the proximity effect, kinetic inductance of disordered superconductors, and, as will be shown at the end of this chapter, the Josephson effect. But what is Andreev reflection? Put simply, it is a quantum-mechanical process by which electrons are converted into holes at the boundary between a normal region and a superconductor. As we will show, it arises due to the requirement of wavefunction continuity across the interface between the two materials. In this Chapter, we use the notation developed in Chapter 6 and work in the one-particle picture.

Imagine an electron moving in the normal region N incident on an interface with a superconductor S . Furthermore, suppose its energy ϵ is positive but less than the superconducting gap Δ [Fig. 7.1]. Upon encountering the interface, it can't continue into the superconductor because there are no states below Δ for it to occupy, and therefore it must be reflected. However, instead of being reflected as an electron, it is reflected as a hole. This is known as Andreev reflection [Andreev 1964].

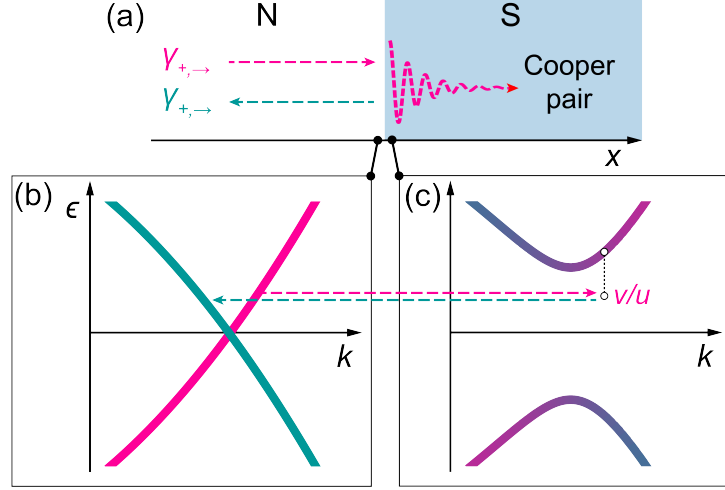


Figure 7.1: Schematic of Andreev reflection | (a) A right-moving electron $\gamma_{+, \rightarrow}$ is Andreev reflected into a left-moving hole $\gamma_{+, \rightarrow}$, injecting a Cooper pair into the superconductor. (b) Decay of the wavefunction in the superconductor demands that the electron momentum is slightly above k_F ($k = k_F + i/\xi$). This allows us to read of the reflection coefficient v/u from the color of the band in (c), as indicated by the vertical dotted line. Note that while the momentum carried by the hole is still positive, its velocity is negative.

Mathematically, we can see why Andreev reflection occurs by matching the electron-hole wavefunctions at the boundary. In the normal region where $\Delta \rightarrow 0$, the incoming electron is described by $\psi_{N, \rightarrow} = A_N \begin{pmatrix} 1 \\ 0 \end{pmatrix} e^{ikx}$ where A_N is a normalization constant. While there is no state at $|\epsilon| < \Delta$ in the superconductor, we can get evanescent waves. This can be seen by rearranging Eqn. 6.17, but assuming $\epsilon < \Delta$:

$$\begin{aligned}
 k &= k_F + i \frac{1}{\hbar v_F} \text{sgn}(\epsilon) \sqrt{\Delta^2 - \epsilon^2} = k_F + i \frac{1}{\xi} \text{sgn}(\epsilon) \\
 k &= k_F - i \frac{1}{\hbar v_F} \text{sgn}(\epsilon) \sqrt{\Delta^2 - \epsilon^2} = k_F - i \frac{1}{\xi} \text{sgn}(\epsilon)
 \end{aligned} \tag{7.1}$$

where we have defined the energy-dependent **coherence length** $\xi = \hbar v_F / \sqrt{\Delta^2 - \epsilon^2}$. For the state currently considered ($k > 0$, $\epsilon > 0$, $x > 0$), e^{ikx} decays but e^{ikx} blows up. Thus, the evanescent wavefunction inside the superconductor must be described by the electron-like

solution $\psi_{S,\rightarrow} = A_S \begin{pmatrix} u \\ v \end{pmatrix} e^{+ik_F x} e^{-x/\xi}$. Now the crucial observation: *because the wavefunction in the superconductor has a nonzero hole-amplitude v , the outgoing particle in the normal region must be a hole* $\psi_{N,\rightarrow} = A_N \begin{pmatrix} 0 \\ 1 \end{pmatrix} e^{ikx}$. The hole is “outgoing” in the sense that its Fermi velocity is negative. The continuity equation at the boundary reads

$$\psi_{N,\rightarrow}|_{x=0} + \psi_{N,\leftarrow}|_{x=0} = \psi_{S,\rightarrow}|_{x=0} \quad (7.2)$$

$$A_N \begin{pmatrix} 1 \\ 0 \end{pmatrix} + A_N \begin{pmatrix} 0 \\ 1 \end{pmatrix} = A_S \begin{pmatrix} u \\ v \end{pmatrix}$$

Using the lower vector equation, we can eliminate A_S to solve for the ratio of the reflected hole amplitude to the incoming electron amplitude:

$$A_N/A_N = v/u \quad (7.3)$$

For $|\epsilon| < \Delta$, a bit of algebra shows that this reflection coefficient $A_N/A_N = v/u$ has modulus one:

$$\begin{aligned} v/u &= e^{-i\varphi} \sqrt{\frac{1 - i\sqrt{(\Delta/\epsilon)^2 - 1}}{1 + i\sqrt{(\Delta/\epsilon)^2 - 1}}} \\ &= e^{-i\varphi} \sqrt{\left(\frac{\epsilon}{\Delta}\right)^2 (1 - i\sqrt{(\Delta/\epsilon)^2 - 1})^2} \\ &= e^{-i\varphi} \left| \frac{\epsilon}{\Delta} \right| (1 - i\sqrt{(\Delta/\epsilon)^2 - 1}) \end{aligned} \quad (7.4)$$

$$\begin{aligned}
|v/u|^2 &= \left(\frac{\epsilon}{\Delta}\right)^2 (1 - i\sqrt{(\Delta/\epsilon)^2 - 1})(1 + i\sqrt{(\Delta/\epsilon)^2 - 1}) \\
&= \left(\frac{\epsilon}{\Delta}\right)^2 (1 + ((\Delta/\epsilon)^2 - 1)) \\
&= 1
\end{aligned} \tag{7.5}$$

The reflection coefficient can thus be fully described by a phase ϕ_A in the complex plane: $v/u = e^{-i\varphi} e^{i\phi_A}$. We know the real part ϵ/Δ will be equal to $\cos \phi_A$. Further, we see that the imaginary part is negative, which tells us that ϕ_A must also be negative. In summary, we find

$$v/u = e^{-i\varphi} e^{i\phi_A} \quad \phi_A = -\cos^{-1}(|\epsilon/\Delta|)$$

The electron→hole transmutation discussed above is only one of several possible Andreev reflection processes. For instance, if the orientation of the superconductor and normal region are flipped (S on right, N on left), a left-moving electron may be reflected into a hole. Moreover, it is also possible for holes to be Andreev reflected into electrons. In total, there are thus four possible Andreev reflection processes for a particular energy of particle.

Is the phase acquired in each of these Andreev reflection processes the same? In each case, one must follow the logic we went through above (incident electron with positive momentum and energy). These steps are summarized by the below algorithm:

1. Which momentum (k or \bar{k}) gives a decaying wavefunction into the superconductor (consider ϵ , k , and x)?
 - If k , reflection coefficient is v/u .
 - If \bar{k} , reflection coefficient is v/u .
2. Is the incoming particle an electron or a hole?
 - If electron, the reflection coefficient found in step one is correct.

- If hole, take the complex conjugate.

In the end however, the result is quite simple: if $\epsilon > 0$, the Andreev reflection phase is $+\phi_A$, while if $\epsilon < 0$, the Andreev reflection phase is $-\phi_A$. We can thus take all energies into account and define the **Andreev reflection coefficient**:

$$r_A \equiv e^{i\phi_A}; \quad \phi_A = -\text{sgn}(\epsilon) \cos^{-1}(|\epsilon/\Delta|) \quad (7.6)$$

Note that for simplicity of notation r_A does not include φ dependence.

Notes on the physics of Andreev reflection So far in this section, we have reached a concrete, mathematical understanding of Andreev reflection. However, there are several points that are important from a physics perspective. We can consider them from the point of view of conservation laws:

1. **Conservation of charge.** In Andreev reflection, an incoming electron is transmuted into an outgoing hole (or vice versa). But an electron has charge $-e$, and a hole $+e$. Where did the $-2e$ of charge go? It turns out that it is injected into the superconductor in the form of a Cooper pair (see section 6.5). As we will see in our discussion of the Josephson effect, Andreev reflection can thus lead to the flow of current between normal and superconducting regions.
2. **Conservation of energy.** This one is not so interesting, but I include it for completeness. Throughout our discussion of Andreev reflection, we have assumed energy conservation. This is exactly the same as in introductory 1D quantum scattering problems (e.g. step potential).
3. **Conservation of momentum.** Andreev reflection differs from a typical scattering problem in that it involves states with roughly the same momentum (in typical 1D scattering, we might have $e^{ikx} \rightarrow e^{-ikx}$). Starting with the continuity equation 7.2, let's take a look at the full wavefunction $\psi_A(x)$ for the first Andreev reflection process we considered:

$$\psi_{N,\rightarrow}|_{x=0} + \psi_{N,\leftarrow}|_{x=0} = \psi_{S,\rightarrow}|_{x=0} \quad (7.7)$$

$$A_N \begin{pmatrix} 1 \\ 0 \end{pmatrix} + A_N \begin{pmatrix} 0 \\ 1 \end{pmatrix} = A_S \begin{pmatrix} u \\ v \end{pmatrix}$$

↓

$$\psi_A(x) = \Theta(-x) \left[\begin{pmatrix} 1 \\ 0 \end{pmatrix} e^{ikx} + r_A \begin{pmatrix} 0 \\ 1 \end{pmatrix} e^{ikx} \right] + \Theta(x) \begin{pmatrix} u \\ v \end{pmatrix} e^{ikx} \quad (7.8)$$

while Andreev reflection involves states with roughly the same momentum, it isn't *quite* conserved. In $\psi_A(x)$, the momentum of the hole is slightly less than that of the electron: $k - k = \frac{2\epsilon}{\hbar v_F}$. While we ignored this momentum mismatch in our discussion above (we did not demand continuity of the derivative at the boundary), in principle it can lead to normal reflection. For most superconductors, the gap is small compared to the Fermi energy (the momentum mismatch is small compared to the Fermi momentum), and so this effect is small. However, for the proximitized semiconductors considered in this thesis (smaller Fermi energies), this approximation may not be a great one [Sriram et al. 2019].

7.2 Andreev levels: the "short junction" limit

Andreev levels are spatially localized, fermionic modes which form due to constructive interference of Andreev reflection processes. They are the microscopic modes responsible for the Josephson supercurrent, and are central to the results presented in this thesis. In this section, we derive the Andreev spectrum in the so-called "short junction" limit [Beenakker and Van Houten 1991; Furusaki and Tsukada 1991].

The prototypical Andreev level occurs in a superconductor-normal-superconductor

junction [Fig. 7.2]. An electron moving to the right in the normal region is Andreev reflected into a left-moving hole upon encountering the right superconductor. Upon reaching the left superconductor, the hole is then Andreev reflected back into a right-moving electron. We can already see that this loop will carry current: every round trip, the right superconductor loses $2e$ of charge, and the left superconductor gains it. To gain a deeper understanding of the Andreev levels, we next derive their energy spectrum as function of the superconducting phase drop φ across the junction.

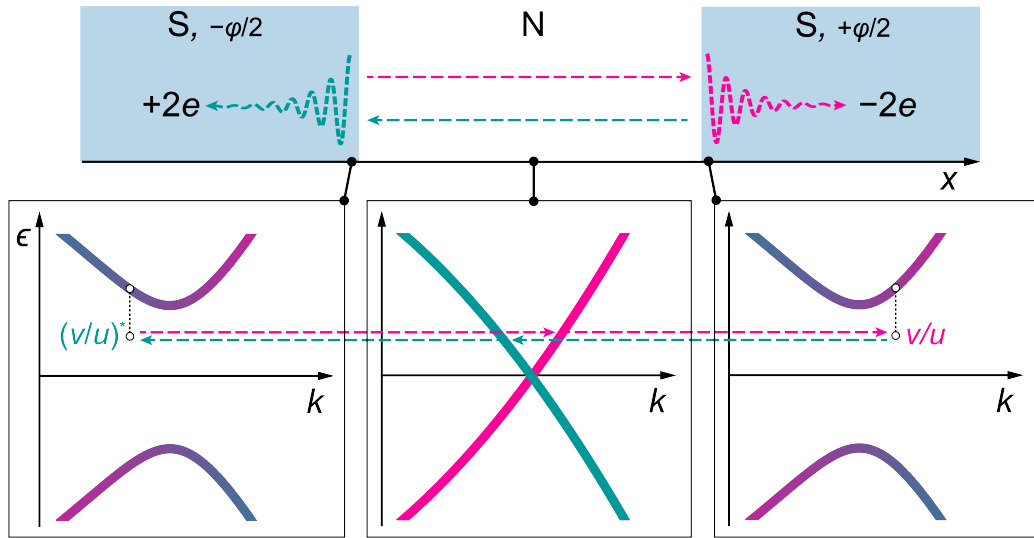


Figure 7.2: Formation of an Andreev level | A right-moving electron in the normal region is reflected into a hole with amplitude $v/u = r_A e^{-i\varphi/2}$ upon encountering the right superconductor. The hole travels back to the left, whereupon it is reflected back into an electron with $(v/u)^* = r_A e^{-i\varphi/2}$. The constructive interference of these two processes forms an Andreev level.

Andreev levels form when the loop shown in Fig. 7.2 satisfies a constructive interference condition. First, we choose a gauge and divide the phase drop equally between the left and right superconductors. When the electron is Andreev reflected off of the right superconductor (superconducting phase $+\varphi/2$), the hole picks up a phase $+\phi_A - \varphi/2$. Note that the phase between the electron and hole includes *minus* the superconductor's phase, since the transmutation of an electron into a hole is equivalent to the *destruction* of two electrons. The hole then travels back to the right (although it also has momentum $\approx k_F$, its velocity is

negative) and encounters the left superconductor (superconducting phase $-\varphi/2$). It is then Andreev reflected back into the electron, acquiring a phase $+\phi_A - \varphi/2$. An Andreev level will form if these processes constructively interfere, i.e. if the total phase is a multiple of $2\pi n$. For now, we will restrict ourselves to $n = 0$, which will correspond to $\varphi \in \{-\pi, +\pi\}$. This gives us a condition on the level energy:

$$\begin{aligned}
\varphi &= 2\phi_A & (7.9) \\
\varphi &= -2 \operatorname{sgn}(\epsilon) \cos^{-1}(|\epsilon/\Delta|) \\
-\operatorname{sgn}(\epsilon)\varphi &= 2 \cos^{-1}(|\epsilon/\Delta|) \\
\rightarrow \epsilon &= \pm\Delta \cos(\varphi/2)
\end{aligned}$$

However, note that $2 \cos^{-1}(|\epsilon/\Delta|)$ can only take values from 0 to π . So in Eqn. 7.9, the step with the right arrow is only valid for $\epsilon > 0$ if $\varphi \in \{-\pi, 0\}$, and for $\epsilon < 0$ if $\varphi \in \{0, \pi\}$. A similar constructive interference condition exists for left-moving electrons and right-moving holes, but because the electron \rightarrow hole and hole \rightarrow electron processes are occurring on the opposite superconductors, the superconducting phase acquires a sign flip:

$$\begin{aligned}
-\varphi &= 2\phi_A & (7.10) \\
\varphi &= 2 \operatorname{sgn}(\epsilon) \cos^{-1}(|\epsilon/\Delta|) \\
\operatorname{sgn}(\epsilon)\varphi &= 2 \cos^{-1}(|\epsilon/\Delta|) \\
\rightarrow \epsilon &= \pm\Delta \cos(\varphi/2)
\end{aligned}$$

Here the step with the right arrow is only valid for $\epsilon > 0$ if $\varphi \in \{0, \pi\}$, and for $\epsilon < 0$ if $\varphi \in \{-\pi, 0\}$.

In the end, we see that the Andreev level energies are $\epsilon_A = \pm\Delta \cos(\varphi/2)$ no matter the

value of φ , and all these considerations about the range of \cos^{-1} seem a bit trivial. However, because we expect the current carried by the Andreev levels to be given by $\frac{d\epsilon}{d\varphi}$, it is nice to see that they are built out of states with appropriate momentum/velocity for each range of φ . This is summarized by Fig. 7.3 and by the equation below:

$$\epsilon_A = \begin{cases} \pm\Delta \cos(\varphi/2) \text{ with momentum } \pm k_F \text{ for } \varphi \in \{-\pi, 0\} \\ \pm\Delta \cos(\varphi/2) \text{ with momentum } \mp k_F \text{ for } \varphi \in \{0, +\pi\} \end{cases} \quad (7.11)$$

In our derivation of the Andreev energies Eqn 7.11, we have neglected any dynamical phase acquired by the charge carriers as they propagate across the normal region. The dynamical phase is given by $\epsilon t/\hbar$, where $t = L/v_F$ is the propagation time for a normal region of length L . The Andreev reflection phase is set by ϵ/Δ , so the dynamical phase is negligible if

$$\epsilon/\Delta \gg \epsilon L/\hbar v_F \quad (7.12)$$

$$\hbar v_F/\Delta \gg L$$

$$\xi_0 \gg L$$

where ξ_0 is the zero-energy coherence length (see text after Eqn. 7.1). This condition is known as the **short junction limit**.

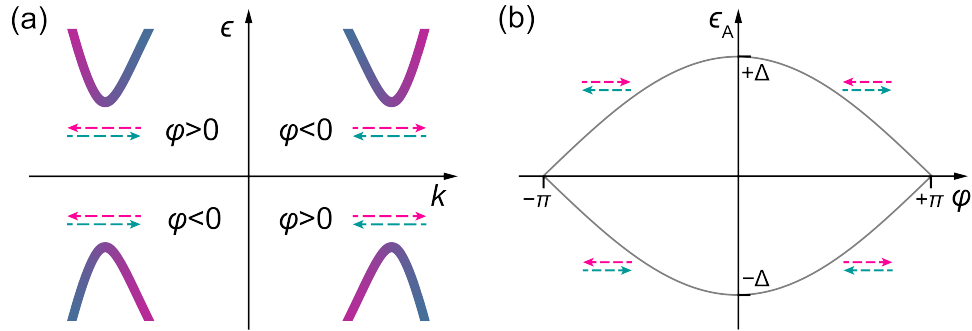


Figure 7.3: Momentum of the Andreev levels | For $\varphi \in \{-\pi, 0\}$, the upper energy state is built of positive momentum particles and the lower energy state is negative momentum particles. For $\varphi \in \{0, +\pi\}$, the situation is reversed.

Including disorder: scattering formalism

Eqn. 7.11 is not the end of the story when it comes to the Andreev levels. In reality, any junction will possess some amount of disorder, and thus we must take scattering in the normal region into account. To do this, it is convenient to change notation slightly and consider outgoing/incoming particles relative to the normal region. This is depicted schematically in Fig. 7.4 for both positive and negative momentum loops.

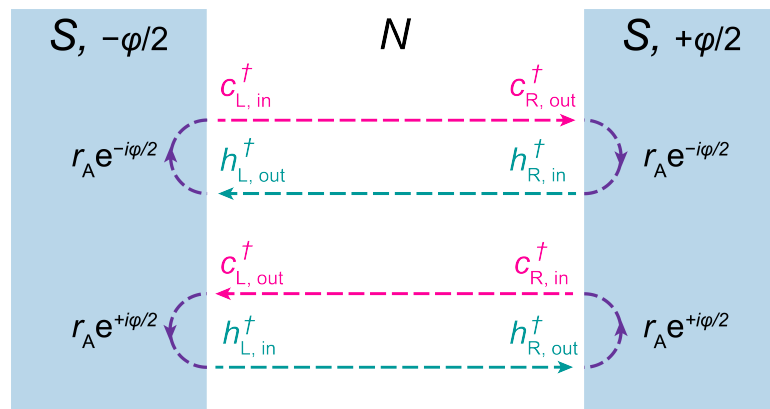


Figure 7.4: Formation of both positive and negative momentum Andreev levels depicted in a scattering picture | Particles headed out of the normal region encounter the superconductors and are reflected back towards the normal region via an Andreev process. The incoming particles then pass through the normal region and head back out toward the other superconductor.

As we have seen, and as is re-depicted in Fig. 7.4, outgoing particles from the normal

region will get Andreev reflected back into incoming particles. In this incoming/outgoing scattering picture, we have

$$\Psi_{\text{in}}^\dagger = S_A \Psi_{\text{out}}^\dagger \quad (7.13)$$

$$\Psi_{\text{in}}^\dagger = \begin{pmatrix} c_{\text{R,in}}^\dagger \\ c_{\text{L,in}}^\dagger \\ h_{\text{R,in}}^\dagger \\ h_{\text{L,in}}^\dagger \end{pmatrix} \quad \Psi_{\text{out}}^\dagger = \begin{pmatrix} c_{\text{R,out}}^\dagger \\ c_{\text{L,out}}^\dagger \\ h_{\text{R,out}}^\dagger \\ h_{\text{L,out}}^\dagger \end{pmatrix}$$

$$S_A = \begin{pmatrix} 0 & 0 & r_A e^{-i\varphi/2} & 0 \\ 0 & 0 & 0 & r_A e^{+i\varphi/2} \\ r_A e^{+i\varphi/2} & 0 & 0 & 0 \\ 0 & r_A e^{-i\varphi/2} & 0 & 0 \end{pmatrix}$$

Assuming no scattering in the normal region for a second, the incoming particles will then become outgoing particles as follows:

$$\Psi_{\text{out}}^\dagger = S_N \Psi_{\text{in}}^\dagger \quad (7.14)$$

$$S_N = \begin{pmatrix} 0 & 1 & 0 & 0 \\ 1 & 0 & 0 & 0 \\ 0 & 0 & 0 & 1 \\ 0 & 0 & 1 & 0 \end{pmatrix}$$

We can plug Eqn. 7.14 into 7.13 to obtain an eigenvalue equation:

$$S_A S_N \Psi_{\text{in}}^\dagger = \Psi_{\text{in}}^\dagger \quad (7.15)$$

This equation holds if $\det(S_A S_N - I) = 0$. This is the equivalent of the constructive interference condition we had before, and indeed solving it gives $\epsilon_A \pm \Delta \cos(\varphi/2)$.

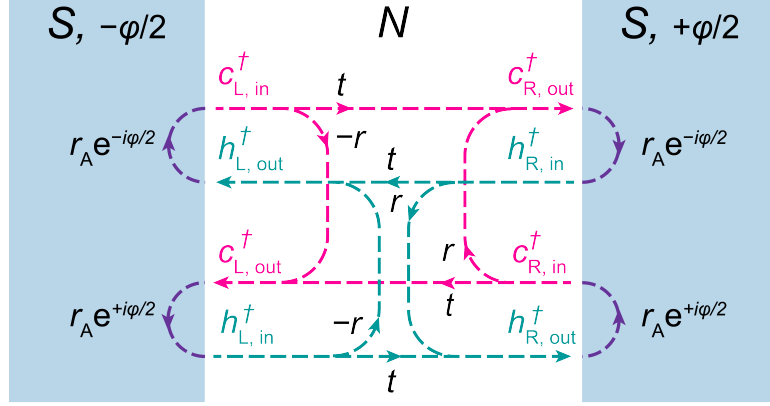


Figure 7.5: Including disorder | Due to disorder in the normal region, incoming particles are transmitted only with probability $|t|^2$ and reflected back with probability $|r|^2$. This coherently couples the positive and negative momentum loops, forming hybridized Andreev levels.

Now we include scattering in the normal region [Fig. 7.5]. The scattering matrix for the electrons is given by $\begin{pmatrix} c_{R,out}^\dagger \\ c_{L,out}^\dagger \end{pmatrix} = \begin{pmatrix} r & t \\ t & -r \end{pmatrix} \begin{pmatrix} c_{R,in}^\dagger \\ c_{L,in}^\dagger \end{pmatrix}$, where we assume $r, t \in \mathbb{R}$ and $r^2 + t^2 = 1$. Note that r and t can be complex, but this would not change the final solution. The hole scattering matrix is, in general, the complex conjugate of the electron scattering matrix (see Chapter 8), but here this has no effect since we have assumed real reflection and transmission coefficients. In total, the scattering matrix in the normal region is thus

$$S_N = \begin{pmatrix} r & t & 0 & 0 \\ t & -r & 0 & 0 \\ 0 & 0 & r & t \\ 0 & 0 & t & -r \end{pmatrix} \quad (7.16)$$

Now, solving the equation $\det(S_A S_N - I) = 0$ gives us the final form for the Andreev level energies in the short-junction limit:

$$\epsilon_A = \pm \Delta \sqrt{1 - t^2 \sin^2(\varphi/2)} \quad (7.17)$$

The two solutions are plotted in Fig. 7.6. We see that the effect of adding scattering in the normal region is to create an avoided crossing between the positive and negative current-carrying states of strength $2\Delta r$.

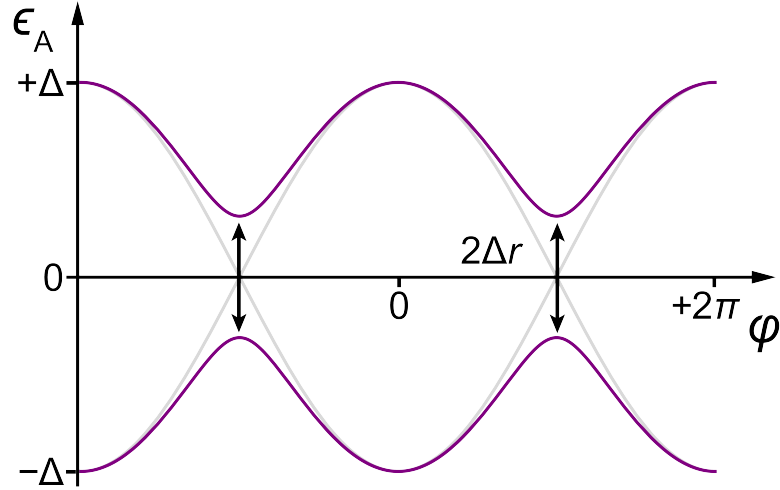


Figure 7.6: Short-junction energies | Disorder in the normal region results in a coherent coupling between the positive/negative momentum Andreev loops ($\epsilon = \pm \cos(\varphi/2)$, gray lines), resulting in an avoided crossing of strength $2\Delta r$. This gives the final form of the short-junction Andreev level energies $\epsilon_A = \pm \sqrt{1 - t^2 \sin^2(\varphi/2)}$ (black lines).

In most other parts of this thesis, the most important feature of the Andreev levels will not be their electron/hole character, but instead the direction of current flow. In addition, as can be guessed from the title of this thesis, the spinful nature of the Andreev levels will be important. As such, we will often depict the scattering in a slightly simplified form that highlights the current and spin of the Andreev levels [Fig. 7.7].

7.3 The Josephson effect

The Josephson effect, in which a supercurrent flows across an SNS junction even in the absence of an applied voltage, is probably the most famous phenomenon in mesoscopic superconductivity. Moreover, it is the foundation of quantum information processing with superconducting circuits. Here we demonstrate that it is the Andreev levels that are responsible for the flow of this supercurrent. However, note that these results do not apply to Josephson nanowires!

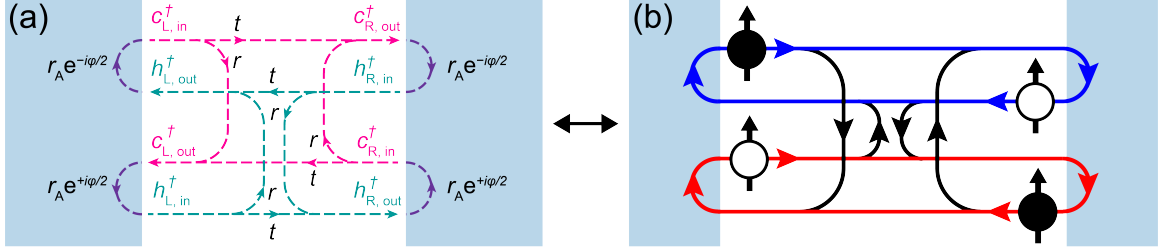


Figure 7.7: Two depictions of scattering processes | Two equivalent pictorial representations of scattering processes that give rise to the Andreev levels. The one on the left has everything nice and labeled, and it highlights the electron/hole character of the Andreev levels. The one on the right is less busy, and instead highlights the spinful nature and current-carrying properties of the Andreev levels. Blue corresponds to current flowing to the left, and red corresponds to current flowing to the right. Black arrows represent normal scattering.

In a superconductor-insulator-superconductor junction (also known as a tunnel junction), the probability for an electron to traverse the insulating region unimpeded is quite small; it must quantum tunnel from one side to the other. As such, when considering the Andreev level energies for a tunnel junction, we can expand Eqn. 7.17 for small t :

$$\begin{aligned}
 \epsilon_A &= \pm\Delta\sqrt{1 - t^2 \sin^2(\varphi/2)} & (7.18) \\
 &\approx \pm\Delta(1 - t^2 \sin^2(\varphi/2)/2) \\
 &= \pm[\Delta - \frac{\Delta t^2}{4}(1 - \cos \varphi)]
 \end{aligned}$$

But the story is not quite this simple. Throughout our discussion of Andreev physics, we have been pretending that we are dealing with a one dimensional system. Of course, this is not true. However, we can model the leads of the junction as electronic waveguides, with the modes of the waveguides determined by quantization in the transverse direction. Each of these modes is known as a **conduction channel**. We can then treat each conduction channel as a separate 1D system, each with its own tunneling amplitude t_i (for a more in depth discussion of conduction channels, I recommend "Quantum Transport" by Nazarov and Blanter). Each "1D" conduction channel will then host a pair of Andreev levels (positive/negative energy), and their energies will add in parallel. The total energy of the junction is thus:

$$\begin{aligned}
&= - \sum_i \left[\Delta - \frac{\Delta t_i^2}{4} (1 - \cos \varphi) \right] \\
&\rightarrow \sum_i \frac{\Delta t_i^2}{4} (1 - \cos \varphi) \\
&= E_J (1 - \cos \varphi); \quad E_J = \frac{\Delta}{4} \sum_i t_i^2
\end{aligned} \tag{7.19}$$

and thus we have found the familiar form for the Josephson energy. Because the current and the inductance of the junction are given by the first and second derivatives of the flux $\Phi/\Phi_0 = \varphi$, the Josephson current and inductance pick up factors of $\Phi_0 = \hbar/(2e)$:

$$I_J = E_J/\Phi_0 \quad L_J^{-1} = E_J/\Phi_0^2 \tag{7.20}$$

The Landauer formula states that the normal state conductance of the junction is given by $G_N = G_0 \sum_i t_i^2$ where the conductance quantum is $G_0 = e^2/\pi\hbar$. We can thus relate the Josephson energy, current and inductance to the normal state conductance, though typically this relation is expressed between the normal state resistance $R_N = 1/G_N$ and the Josephson inductance:

$$\begin{aligned}
L_J^{-1} &= \frac{\Delta(2e)^2}{4\hbar^2} \sum_i t_i^2 \\
L_J^{-1} &= \frac{\Delta e^2}{\hbar^2} G_N/G_0 \\
L_J &= \frac{\hbar}{\pi\Delta} R_N
\end{aligned} \tag{7.21}$$

When relating the supercurrent to the normal-state resistance, this is known as the **Ambegaokar-Baratoff relation**. This relationship between the transmission of the conduction channels and the supercurrent has been verified directly in atomic point con-

tacts[Goffman et al. 2000; Della Rocca et al. 2007].

References

- Andreev, A., “Thermal conductivity of the intermediate state of superconductors”, *Zh. Eksperim. i Teor. Fiz.* **46** (1964).
- Beenakker, C. and H. Van Houten, “Josephson current through a superconducting quantum point contact shorter than the coherence length”, *Phys Rev. Lett.* **66**, 3056 (1991).
- Della Rocca, M. L., M. Chauvin, B. Huard, H. Pothier, D. Esteve, and C. Urbina, “Measurement of the current-phase relation of superconducting atomic contacts”, *Phys. Rev. Lett.* **99**, 127005 (2007).
- Furusaki, A. and M. Tsukada, “Current-carrying states in Josephson junctions”, *Phys. Rev. B* **43**, 10164–10169 (1991).
- Goffman, M. F., R. Cron, A. Levy Yeyati, P. Joyez, M. H. Devoret, D. Esteve, and C. Urbina, “Supercurrent in atomic point contacts and andreev states”, *Phys. Rev. Lett.* **85**, 170–173 (2000).
- Sriram, P., S. S. Kalantre, K. Gharavi, J. Baugh, and B. Muralidharan, “Supercurrent interference in semiconductor nanowire Josephson junctions”, *Phys. Rev. B* **100**, 155431 (2019).

8

Andreev levels in Josephson nanowires

In this chapter, we calculate the energy spectrum of Andreev levels in Josephson nanowires. First, we show how increasing the junction length results in more Andreev doublets per conduction channel. Then, after discussing spin-orbit physics in unproximitized semiconductor nanowires, we demonstrate how spin-orbit effects break the Andreev level spin degeneracy. As we will primarily be concerned with single quasiparticle excitations, we will restrict ourselves to the excitation picture of superconductivity.

There has been quite a bit of theory on spin-orbit-split Andreev levels [Chtchelkatchev and Nazarov 2003; Béri, Bardarson, and Beenakker 2008; Padurariu and Nazarov 2010; Reynoso et al. 2012; Yokoyama, Eto, and Nazarov 2014; Cayao et al. 2015; Murani et al. 2017; Heck, Väyrynen, and Glazman 2017], and the spectrum of such a weak link was recently probed using cQED techniques [Tosi et al. 2019]. Here we apply the scattering formalism developed in Chapter 7 [Beenakker and Van Houten 1991] and derive the transcendental equations published in [Nazarov and Blanter 2009; Beenakker and Van Houten 1992] and [Tosi et al. 2019].

8.1 Scattering of holes

This chapter focuses on how changing the properties of the normal region affects the Andreev levels of a weak link. As we approach this question using the scattering picture

formulated in Chapter 7, the problem boils down to writing down the correct scattering matrix for the normal region S_N . As we saw in Chapter 7, S_N has both an electron part S_e and a hole part S_h . In the short-junction regime, we had the simple relation $S_e = S_h$. However, this is not generically true. Additionally, we will encounter spin-dependent scattering matrices in this chapter, so we need to differentiate between $S_{e,\downarrow}$ and $S_{e,\uparrow}$.

Let's consider spin down electrons incident on the normal region:

$$\begin{pmatrix} c_{R,\text{out},\downarrow}^\dagger \\ c_{L,\text{out},\downarrow}^\dagger \end{pmatrix} = S_{e,\downarrow} \begin{pmatrix} c_{R,\text{in},\downarrow}^\dagger \\ c_{L,\text{in},\downarrow}^\dagger \end{pmatrix} \quad (8.1)$$

We can get the hole scattering matrix by taking the Hermitian conjugate of this expression. We're working in the excitation picture, so we'll hold on to (and flip) the spin label when converting to holes:

$$\begin{aligned} \begin{pmatrix} c_{R,\text{out},\downarrow} & c_{L,\text{out},\downarrow} \end{pmatrix} &= \begin{pmatrix} c_{R,\text{in},\downarrow} & c_{L,\text{in},\downarrow} \end{pmatrix} S_{e,\downarrow}^\dagger \\ \begin{pmatrix} h_{R,\text{out},\uparrow}^\dagger & h_{L,\text{out},\uparrow}^\dagger \end{pmatrix} &= \begin{pmatrix} h_{R,\text{in},\uparrow}^\dagger & h_{L,\text{in},\uparrow}^\dagger \end{pmatrix} S_{e,\downarrow}^\dagger \\ \begin{pmatrix} h_{R,\text{out},\uparrow}^\dagger \\ h_{L,\text{out},\uparrow}^\dagger \end{pmatrix} &= S_{e,\downarrow}^{*} \begin{pmatrix} h_{R,\text{in},\uparrow}^\dagger \\ h_{L,\text{in},\uparrow}^\dagger \end{pmatrix} \end{aligned} \quad (8.2)$$

So we find that $S_{h,\uparrow} = S_{e,\downarrow}^*$. Note we don't have to toggle the in/out labels since the holes have the same Fermi velocity as their electron counterparts. But there's still another detail to consider if the scattering matrix has energy dependence. We'll be working in the excitation picture in this chapter, so all particles (both electrons and holes) will always have positive energy. However, a positive energy hole is the absence of a negative energy electron. The hole scattering matrix must therefore be evaluated at negative energy. The final relation between the electron and hole scattering matrices is thus:

$$S_{h,\uparrow}(E) = S_{e,\downarrow}^*(-E) \quad (8.3)$$

Note that this relation holds for any of the pictures of superconductivity.

8.2 Beyond the short-junction approximation

In this section, we detail how the Andreev level spectrum is modified when the dynamical phase acquired by the weak-link-traversing charge carriers can no longer be neglected. In this situation, disorder can no longer be represented by the channel transparency alone. We therefore investigate several crude models of disorder, and comment on their validity.

8.2.1 Increasing junction length

In Chapter 7, we found the spectrum of Andreev levels in the short-junction regime by considering constructive interference of Andreev reflection and normal reflection. However, as discussed in the text around Eqn. 7.12, we neglected the dynamical phase acquired by the charge carriers as they traverse the normal region of the weak link. Let's see what happens when we take the dynamical phase into account, first assuming that the weak link is free of disorder.

The first step is to linearize the kinetic energy (the only energy for a particle in the normal region). For the two Fermi points (\pm), we have $E = \pm\hbar v_F(k \mp k_F)$. As an electron traverses the normal region of length L , it picks up a propagation phase

$$\phi_p = kL = (+k_F + E/\hbar v_F)L \quad (8.4)$$

Note that this is independent of the direction it's traveling; the sign in the momentum cancels with the sign of $\pm L$. The disorder-free scattering matrix Eqn. 7.14 is then modified as

$$S_N = \begin{pmatrix} 0 & e^{i(+k_F + E/\hbar v_F)L} & 0 & 0 \\ e^{i(+k_F + E/\hbar v_F)L} & 0 & 0 & 0 \\ 0 & 0 & 0 & e^{i(-k_F + E/\hbar v_F)L} \\ 0 & 0 & e^{i(-k_F + E/\hbar v_F)L} & 0 \end{pmatrix} \quad (8.5)$$

As discussed in section 8.1, the hole part of the scattering matrix been conjugated and the sign of the energy has been flipped $E \rightarrow -E$. Note that the net result is thus a sign flip

on k_F in the propagation phase. As before, we can then compute $\det(S_A S_N - 1)$ to find the Andreev level energies. However, without disorder, this is overkill; we can simply tack the dynamical phase onto the sum of phases we had in the disorder-free short junction case.¹ Eqns. 7.9/10 then become:

$$\pm\varphi = 2\phi_A + 2EL/\hbar v_F + 2\pi n \quad (8.6)$$

Note the factor of two on the dynamical phase; in a full round trip, the charge carriers traverse the normal region twice. We also find that the dependence on k_F has dropped out. For a disorder-free weak link, the electron portion $+k_F L$ cancels with the hole portion $-k_F L$. Unlike the short-junction case, the constructive interference condition Eqn. 8.6 has no analytic solution. Instead, we solve for $E(\varphi)$ numerically [Fig. 8.1], and find that as we increase L , the number of Andreev doublets also increases. This is the same as in any other confined quantum system: when the system size grows, the level density increases.

What is different about the Andreev levels of a long junction as compared to say, a particle in a box, is that the Andreev levels still disperse with φ , and therefore carry a supercurrent. In the long-junction case, we find that the Andreev levels form a characteristic “shoe-lace” pattern [Fig. 8.1]. We can gain some intuition for why this pattern is occurring by Taylor expanding ϕ_A for $E \ll \Delta$:

$$\begin{aligned} \pm\varphi &= 2\phi_A + 2EL/\hbar v_F + 2\pi n & (8.7) \\ &\simeq (-\pi + 2E/\Delta) + 2EL/\hbar v_F + 2\pi n \\ &= 2E(L/\hbar v_F + 1/\Delta) + \pi(2n - 1) \\ E &= \pm \frac{(\hbar v_F/L)\Delta}{(\hbar v_F/L) + \Delta} (\varphi - (2n - 1)\pi) \end{aligned}$$

We see that in the long-junction case with $E \ll \Delta$, the Andreev spectrum is linear in φ with a slope determined by a competition between two energy scales: the superconducting gap Δ and the dwell energy $\hbar v_F/L$ (known as the Thouless energy in a diffusive mesoscopic

¹I write Eqn. 8.5 to compare to the disorder-full case below.

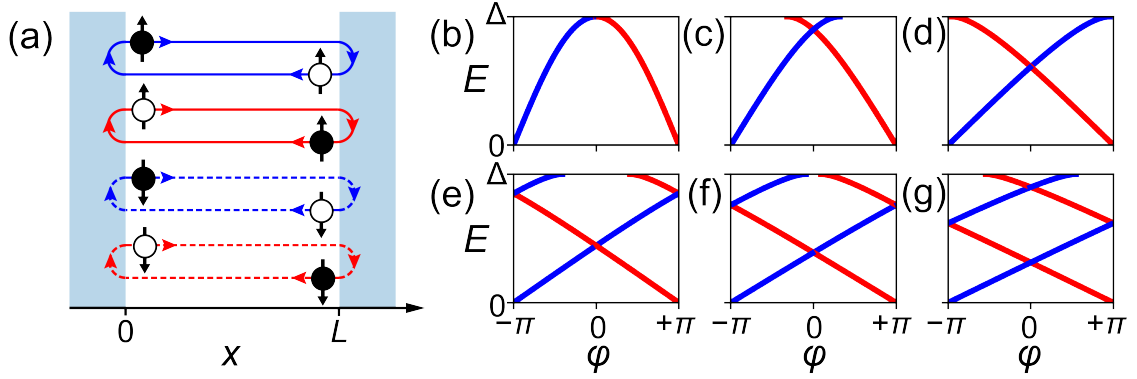


Figure 8.1: Dependence of the Andreev levels on the length of the weak link L | (a) The four possible Andreev loops, with blue/red corresponding to current flowing left/right, and solid/dashed corresponding to spin up/down. (b) The spin-degenerate energies of the Andreev levels as L is increased. As many of the experiments on long weak links in this thesis were performed near $\varphi = 0$, we plot the energies from $\varphi = -\pi$ to $+\pi$. The spectra shown in panels (b) through (g) correspond to effective junction lengths L/ξ_0 of 0.0, 0.5, 1.5, 2.5, 3.0, and 4.0. As with any confined quantum system, the level spacing decreases as the size of the system grows.

system). Taking the further limit of $\Delta \gg L/\hbar v_F$, we find that the current is given by

$$\frac{2\pi}{\Phi_0} \frac{dE}{d\varphi} = \hbar \frac{2\pi}{\Phi_0} v_F / L = 2e v_F / L \quad (8.8)$$

In this limit, the current carried by the Andreev levels is exactly what we would expect for an electron traversing the weak link in time v_F/L before Andreev reflecting off the superconducting lead and injecting a Cooper pair.

As shown in Eqn. 7.12, the extent to which short junction physics breaks can also be expressed in terms of the ratio of the junction length to the coherence length ξ_0/L . The low-energy dispersion relation then becomes

$$E_n = \pm \frac{\Delta}{1 + L/\xi_0} (\varphi - (2n - 1)\pi) \quad (8.9)$$

8.2.2 Single scatterer

As in the short-junction regime, we must include disorder. However, in the case of a long junction, disorder is not so straightforward to model. In Chapter 7, we implicitly assumed

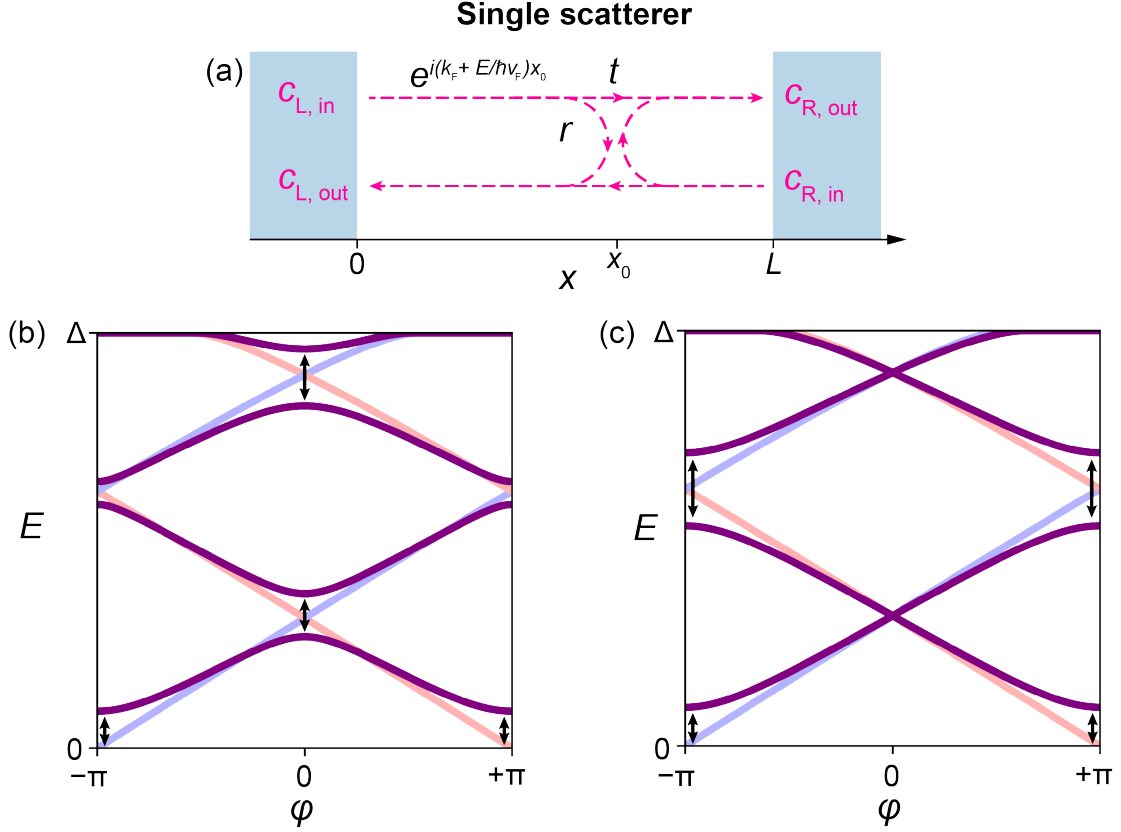


Figure 8.2: Single-scatterer model (a) In the single-scatterer model, we include disorder by assuming a single point-like scatterer at position x_0 in the normal region of the weak link. (b) Calculated spectrum (purple) for $L/\xi_0 = 4.0$, $x_0 = L/4$, and $t = 0.9$. Avoided crossings (black arrows) are induced between the ballistic Andreev levels (red/blue). (c) Spectrum for pathological choice of $x_0 = 0$. Crossings at $\varphi = 0$ are *not* avoided, unlike anything we have ever seen in experiment.

that we had a single scatterer with transmission amplitude t in the zero-dimensional normal region of the weak link. But if we assume a single scatterer in the long junction regime, there is another degree of freedom: the position $x_0 \in \{0, L\}$ of the scatter within the normal region [Fig. 8.2(a)]. While transmitted particles will still acquire the dynamical phase $EL/\hbar v_F$, particles incoming from the left that are reflected will acquire a dynamical phase $2Ex_0/\hbar v_F$; the factor of 2 is present because the particle has to make its way to the scatterer, and then all the way back to the lead. Similarly, incoming particles from the right that are reflected will acquire a dynamical phase $2E(L - x_0)/\hbar v_F$. The full scattering matrix of the

normal region is then

$$S_N = \begin{pmatrix} r e^{2i(+k_F+E/\hbar v_F)(L-x_0)} & t e^{i(+k_F+E/\hbar v_F)L} & 0 & 0 \\ t e^{i(+k_F+E/\hbar v_F)L} & -r e^{2i(+k_F+E/\hbar v_F)x_0} & 0 & 0 \\ 0 & 0 & r e^{2i(-k_F+E/\hbar v_F)(L-x_0)} & t e^{i(-k_F+E/\hbar v_F)L} \\ 0 & 0 & t e^{i(-k_F+E/\hbar v_F)L} & -r e^{2i(-k_F+E/\hbar v_F)x_0} \end{pmatrix} \quad (8.10)$$

Remember that the hole part of the scattering matrix has both been conjugated and $E \rightarrow -E$, such that the net effect is $k_F \rightarrow -k_F$. Taking the determinant of the full scattering matrix $\det(S_A S_N - 1)$ then gives a transcendental equation for the Andreev level energies (I recommend using Mathematica):

$$0 = r^2 \cos(4E(x_0 - L/2)/\hbar v_F) + t^2 \cos(\varphi) - \cos(2EL/\hbar v_F + 2\phi_A) \quad (8.11)$$

The first term takes into account normal reflection and therefore depends on x_0 , while the second and third terms reduce to 8.6 for $t \rightarrow 1$.

While this model of a single scatterer with variable position does indeed give us a spectrum that appears physical (it introduces avoided crossings between Andreev levels of opposite current), it has several problems. The main issue is that it just doesn't seem very realistic; it is highly unlikely that in a real device, there is a single point-like impurity somewhere in the junction that is scattering charge carriers. This non-physicality is reinforced by the fact that there are pathological choices of x_0 . For instance, suppose $x_0 = L/2$. Then we have this funny situation where the crossings around $\varphi = 0$ are no longer avoided due to destructive interference of the reflected particles. We have certainly never seen anything like this in experiment.

8.2.3 Double barrier

We now discuss what seems like a more realistic model of the disorder, though as we will discuss below, current experiments are unable to probe the structure of the disorder directly. This model is based on the following observation: the most likely location for normal

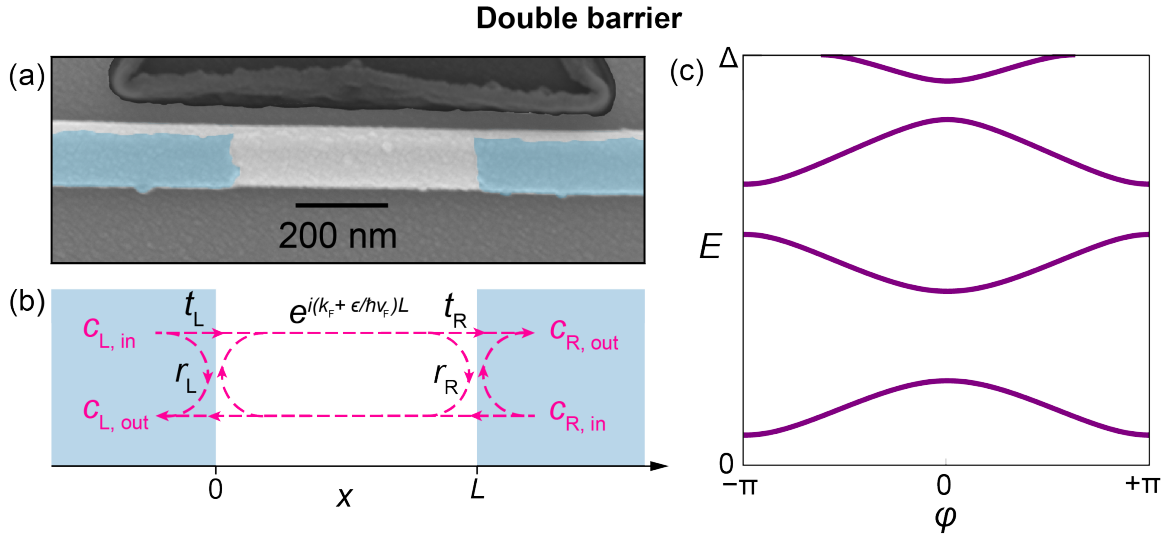


Figure 8.3: Double-barrier model (a) Scanning electron micrograph of a Josephson nanowire. Epitaxial aluminum coats two of the six nanowire facets, with a gap in the middle forming the weak link. While the contact between the indium arsenide and the aluminum is very good, it is not perfect. (b) In the double-barrier model, we account for disorder by placing two fixed scatterers at $x = 0$ and $x = L$, perhaps more accurately capturing the source of scattering in our nanowires. (c) Calculated spectrum (purple) for $L/\xi_0 = 4.0$, $r_L = 0.1$, $r_R = 0.5$, $k_F L = \pi$

reflection to take place is at the boundaries between the semiconductor and the superconductor. Much work has gone into making this interface as transparent as possible; it's why we have so-called "hard gaps" in the nanowire (the density of sub-gap states in a proximitized section of nanowire is very small). Nonetheless, the interface is not perfect; there is a small lattice mismatch between the aluminum shell and indium arsenide nanowire. A more appropriate model is therefore a double-barrier model, where one scatterer is fixed to $x = 0$ and the other to $x = L$.

The overall transparency of this structure can be calculated by summing all possible paths of an electron from the right to the left. The most straightforward path is of course to tunnel straight through both barriers; this occurs with amplitude $t_L t_R$. But if the particle only makes it through the first barrier on its initial try, it still has a chance to make it through the whole structure so long as it completes m loops between the two scatterers. The amplitudes of all these processes add, such that the total transmission amplitude is given by

$$\begin{aligned}
t_{\text{DB}} &= \sum_{m=0}^{\infty} t_{\text{L}} e^{i\phi_{\text{P}}} (-r_{\text{R}} r_{\text{L}} e^{2i\phi_{\text{P}}})^m t_{\text{R}} \\
&= \frac{t_{\text{L}} t_{\text{R}} e^{i\phi_{\text{P}}}}{1 + r_{\text{R}} r_{\text{L}} e^{2i\phi_{\text{P}}}}
\end{aligned} \tag{8.12}$$

where we have taken advantage of the properties of the geometric series. Similar logic can be applied to get the other three elements of S_{e} (or you can just use transfer matrices + Mathematica). In the end, we have

$$S_{\text{e}} = \begin{pmatrix} r_{\text{R}} + \frac{r_{\text{L}} t_{\text{R}}^2 e^{2i\phi_{\text{P}}}}{1 + r_{\text{R}} r_{\text{L}} e^{2i\phi_{\text{P}}}} & \frac{t_{\text{L}} t_{\text{R}} e^{i\phi_{\text{P}}}}{1 + r_{\text{R}} r_{\text{L}} e^{2i\phi_{\text{P}}}} \\ \frac{t_{\text{L}} t_{\text{R}} e^{i\phi_{\text{P}}}}{1 + r_{\text{R}} r_{\text{L}} e^{2i\phi_{\text{P}}}} & -r_{\text{L}} - \frac{r_{\text{R}} t_{\text{L}}^2 e^{2i\phi_{\text{P}}}}{1 + r_{\text{R}} r_{\text{L}} e^{2i\phi_{\text{P}}}} \end{pmatrix} \tag{8.13}$$

Again, we have $S_{\text{h}}(E) = S_{\text{e}}^*(-E)$ which results in $k_{\text{F}} \rightarrow -k_{\text{F}}$ inside ϕ_{P} . Solving for the constructive interference condition (definitely use Mathematica), we get:

$$\begin{aligned}
0 &= -\sin^2(EL/\hbar v_{\text{F}} \mp \varphi/2 + \phi_{\text{A}}) \\
&+ (r_{\text{L}}^2 + r_{\text{R}}^2) \sin^2(EL/\hbar v_{\text{F}} \mp \varphi/2) \\
&- r_{\text{L}}^2 r_{\text{R}}^2 \sin^2(EL/\hbar v_{\text{F}} \mp \varphi/2 - \phi_{\text{A}}) \\
&- 2r_{\text{L}} r_{\text{R}} \cos(2k_{\text{F}} L) (1 - E^2/\Delta^2)
\end{aligned} \tag{8.14}$$

In the last term, we can see that, in the double barrier case, the Fermi momentum *does* matter. We can gain some intuition for this by performing what is known as the resonant level approximation.

8.2.4 Resonant level

Let's go back to the formula for the overall transmission amplitude through the double barrier Eqn. 8.12. When will the transmission be largest? Considering the propagation phase,

the denominator will be smallest when $2\phi_p = (2n + 1)\pi$. This is precisely the constructive interference condition for a level of energy E_r (wavevector k_r) to form between the two barriers in the normal state:

$$\begin{aligned} 2\phi_p &= (2n + 1)\pi \\ k_r &= \frac{(2n + 1)\pi}{2L} \\ E_r &= \hbar v_F(k_r - k_F) = \hbar v_F\left(\frac{(2n + 1)\pi}{2L} - k_F\right) \end{aligned}$$

Note the additional factor of $\pi/2$ as compared to the typical infinite square well; this is because we have chosen the reflection amplitudes of both barriers to be negative only when viewed from the left. In short, this is why k_F matters in the double-barrier case: the effective transparency of the system is largest when on resonance with the level E_r . Let's explore this further by expanding t_{DB} around this resonance condition:

$$\begin{aligned} t_{DB} &= \frac{t_L t_R e^{i\phi_p}}{1 + r_L r_R e^{2i\phi_p}} & (8.15) \\ &\simeq \frac{t_L t_R e^{i\phi_p}}{1 + r_L r_R (-1 + i(2\phi_p - (2n + 1)\pi))} \\ &\simeq \frac{t_L t_R e^{i\phi_p}}{1 + r_L r_R (-1 + 2iL(E - E_r)/\hbar v_F)} \end{aligned}$$

The level E_r is only well-defined if the coupling to the superconductor is weak $t_L, t_R \approx 0$. We thus further expand t_{DB} :

$$\begin{aligned}
t_{\text{DB}} &\simeq \frac{t_{\text{L}}t_{\text{R}}e^{i\phi_{\text{P}}}}{1 + r_{\text{L}}r_{\text{R}}(-1 + 2iL(E - E_{\text{r}})/\hbar v_{\text{F}})} \\
&= \frac{t_{\text{L}}t_{\text{R}}e^{i\phi_{\text{P}}}}{1 + \sqrt{1 - t_{\text{L}}^2}\sqrt{1 - t_{\text{R}}^2}(-1 + 2iL(E - E_{\text{r}})/\hbar v_{\text{F}})} \\
&\simeq \frac{t_{\text{L}}t_{\text{R}}e^{i\phi_{\text{P}}}}{1 + (1 - t_{\text{L}}^2/2)(1 - t_{\text{R}}^2/2)(-1 + 2iL(E - E_{\text{r}})/\hbar v_{\text{F}})} \\
&\simeq \frac{t_{\text{L}}t_{\text{R}}e^{i\phi_{\text{P}}}}{t_{\text{L}}^2/2 + t_{\text{R}}^2/2 + 2iL(E - E_{\text{r}})/\hbar v_{\text{F}}}
\end{aligned} \tag{8.16}$$

In the second-to-last step, we have kept only the leading-order terms in both the real and imaginary parts of the denominator. Finally, it is customary to re-express the transmission amplitudes as the coupling rates of the level into the leads $\Gamma_i = t_i^2/(2L/v_{\text{F}})$; the electron attempts to tunnel out (with success probability t_i^2) every time interval $2L/v_{\text{F}}$. The final form for the resonant level transmission amplitude is thus

$$t_{\text{RL}} = \frac{\sqrt{\Gamma_{\text{L}}\Gamma_{\text{R}}}e^{i\phi_{\text{P}}}}{\Gamma_{\text{L}}/2 + \Gamma_{\text{R}}/2 + i(E - E_{\text{r}})} \tag{8.17}$$

One can perform similar expansions to construct the scattering matrix for the resonant level case, and then use $\det(S_{\text{A}}S_{\text{N}} - 1)$ to obtain a transcendental equation for the energies. Or, it is somewhat easier to simply start with the transcendental equation we found in the double barrier case Eq. 8.14, and expand it instead.

First, we plug in $2k_{\text{F}}L \simeq (2n + 1)\pi - 2E_{\text{r}}L/\hbar v_{\text{F}}$ and $r_i^2 = 1 - (2L/v_{\text{F}})\Gamma_i$:

$$\begin{aligned}
0 &= -\sin^2(EL/\hbar v_{\text{F}} \mp \varphi/2 + \phi_{\text{A}}) \\
&+ (1 - (2L/v_{\text{F}})\Gamma_{\text{L}} + 1 - (2L/v_{\text{F}})\Gamma_{\text{R}}) \sin^2(EL/\hbar v_{\text{F}} \mp \varphi/2) \\
&- (1 - (2L/v_{\text{F}})\Gamma_{\text{L}})(1 - (2L/v_{\text{F}})\Gamma_{\text{R}}) \sin^2(EL/\hbar v_{\text{F}} \mp \varphi/2 - \phi_{\text{A}}) \\
&- 2\sqrt{1 - (2L/v_{\text{F}})\Gamma_{\text{L}}}\sqrt{1 - (2L/v_{\text{F}})\Gamma_{\text{R}}} \cos((2n + 1)\pi - 2E_{\text{r}}L/\hbar v_{\text{F}})
\end{aligned} \tag{8.18}$$

Next, we expand to second order in Γ_i . Finally, we make another approximation that we glossed over in our derivation of t_{DB} above: we assume that the junction is quite short. We therefore expand to lowest-order in L , which ends up being L^2 . After performing all of these approximations (and dividing by L^2 in the last step), we find the transcendental equation [Beenakker and Van Houten 1992]:

$$0 = (\Delta^2 - E^2) \left(E^2 - E_r^2 - \frac{1}{4}\Gamma^2 \right) + E^2\Gamma\sqrt{\Delta^2 - E^2} + \Delta^2\Gamma_L\Gamma_R \sin^2 \frac{\varphi}{2} \quad (8.19)$$

Suppose that we are perfectly on resonance $E_r = 0$, and E is small. Taking terms only at second order in E , we can solve the above transcendental equation to obtain

$$E = \tilde{\Delta} \sqrt{1 - \tilde{\tau} \sin^2 \frac{\varphi}{2}} \quad \tilde{\Delta} = \frac{\Delta}{1 + 2\Delta/\Gamma} \quad \tilde{\tau} = \frac{4\Gamma_L\Gamma_R}{\Gamma^2} \quad (8.20)$$

which looks exactly like the short junction formula Eqn. 7.17 with effective transparency $\tilde{\tau}$ and effective gap $\tilde{\Delta}$. Note that the effective transparency is also given by t_{RL} with $E_r \rightarrow E$. Also, the effective gap shrinks as Γ gets smaller. This makes sense; the level “feels” the superconductors less as the coupling to the leads goes down.

8.2.5 Comparing models of disorder

When we left the single-scatterer model, we had pointed out that for the pathological choice of $x_0 = L/2$, there are no longer avoided crossings at $\varphi = 0$ due to destructive interference of reflected particles [Fig. 8.2(c)]. However, we can also construct “pathological” situations in the double-barrier/resonant-level model. For instance, if we set $\Gamma_L = \Gamma_R$ in Eqn. 8.20, then we find $\tilde{\tau} = 1$ and thus there will be no avoided crossing at $\varphi = \pi$. This is actually just the weak link version of resonant tunneling; when we send in particles exactly on resonance with a level, they are transmitted with unity probability. This can also be viewed as destructive interference of the reflected particles.

So which model of disorder should we use? The simple answer is that, for now, we can’t tell the difference between them; either model can give us very similar looking spectra

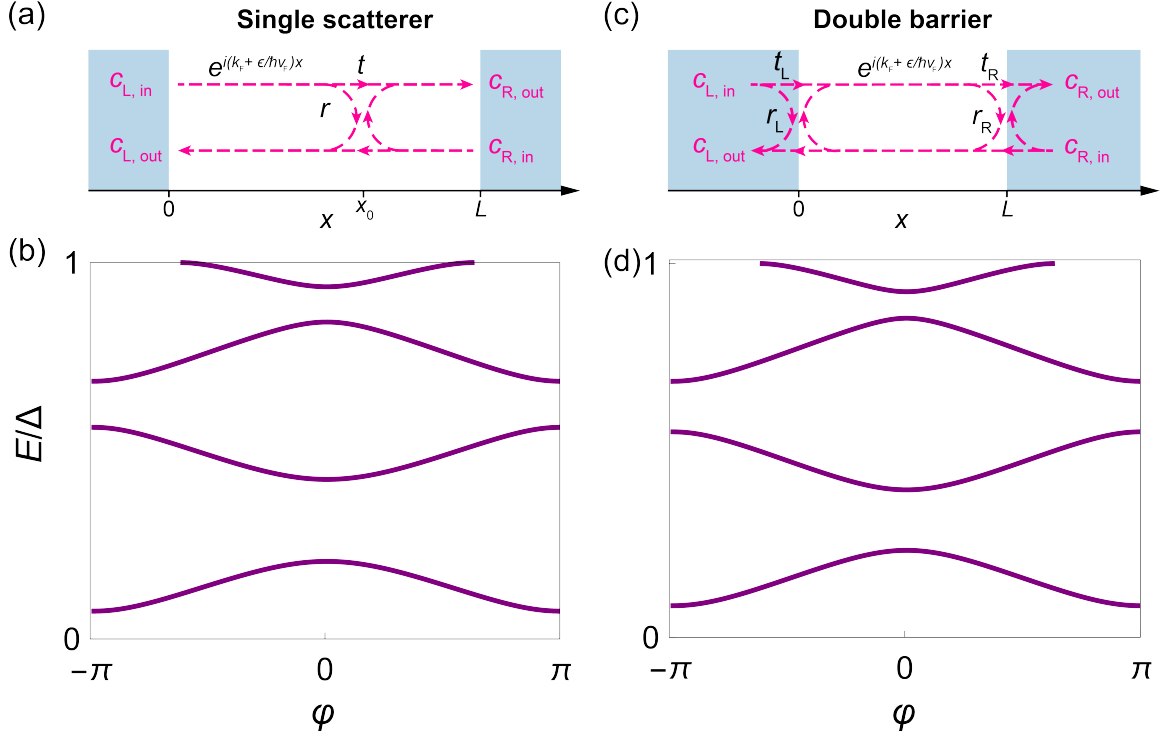


Figure 8.4: Comparing the two models of disorder (a) Calculated spectrum using the single-scatterer model with $L/\xi_0 = 4.0$, $x_0 = L/4$, and $t = 0.9$. (b) Calculated spectrum using the double-barrier model with $L/\xi_0 = 4.0$, $r_L = 0.1$, $r_R = 0.5$, and $k_F L = \pi$.

[Fig. 8.4]. This is a bit frustrating. We would like to be able to extract material properties from the measured spectrum, but the exact values we obtain will depend on the model of disorder we choose [Tosi et al. 2019]. In the experiments presented in this thesis, we also have access to the dispersive shifts. In principle, these contain information about other system operators (e.g. J_A). Perhaps detailed modeling of the dispersive shifts could narrow down the structure of disorder in Josephson nanowires.

8.3 Spin-orbit coupling

We begin this section with a naive derivation of the Rashba interaction. We then proceed to a description of the bands of an infinite nanowire in the normal state under the action of the Rashba spin-orbit coupling, before discussing how this leads to changes in the Andreev spectrum of a Josephson nanowire.

At its core, spin-orbit coupling is a relativistic effect. The first place most physicists learn

about spin-orbit coupling is in the context of the hydrogen atom. The energy levels of the electron are slightly shifted because, upon shifting into the electron's rest frame, the electric field emanating from the proton is partially transformed into a magnetic field:

$$\mathbf{B}_{\text{SO}} = \frac{\mathbf{p} \times \mathbf{E}_{\text{nuc}}}{mc^2} \quad (8.21)$$

where \mathbf{p} is the electron momentum. Note that we have assumed small velocity such that the Lorentz factor is approximately unity. The electron spin can then interact with this magnetic field in a typical Zeeman fashion

$$\mathbf{H}_{\text{SO}} = \frac{g\mu_{\text{B}}}{2} \mathbf{B}_{\text{SO}} \cdot \boldsymbol{\sigma} = \frac{g\mu_{\text{B}}}{2mc^2} (\mathbf{p} \times \mathbf{E}_{\text{nuc}}) \cdot \boldsymbol{\sigma} \quad (8.22)$$

and thus we find that the electron spin is coupled to the electron momentum (its "orbit").

What happens when we are dealing not with an electron bound to a nucleus, but one that is free to propagate through a crystal? There are two main types of spin-orbit coupling in this context, known as the Rashba and Dresselhaus interactions. In this thesis, we will focus on the Rashba interaction, though Dresselhaus is also present in semiconductor nanowires.

8.3.1 The Rashba effect

Suppose that instead of an electron bound to a proton, we have an electron which is free to move through a crystal. Moreover, suppose that there is a constant electric field pointed in the z direction. Similar to the case of the hydrogen atom, the electric field will lead to a spin-orbit coupling:

$$\begin{aligned} H_{\text{R}} &= \frac{g\mu_{\text{B}}}{2mc^2} (\mathbf{p} \times E\hat{z}) \cdot \boldsymbol{\sigma} = \frac{\alpha}{\hbar} \hat{z} \cdot (\boldsymbol{\sigma} \times \mathbf{p}) \\ &= \frac{\alpha}{\hbar} (\sigma_x p_y - \sigma_y p_x) \end{aligned} \quad (8.23)$$

where $\alpha = \frac{\hbar g\mu_{\text{B}} E}{2mc^2}$. The last line of Eqn. 8.23 is known as the Rashba Hamiltonian.

But there's a catch. For $E = 1 \text{ V/nm}$ (a very strong electric field), we would have $\alpha \sim$

10^{-4} meV·nm. However, some semiconductors exhibit much stronger Rashba interactions. For instance, in indium arsenide α can be $\simeq 30$ meV·nm. While the arguments supplied above thus give some flavor of how the Rashba interaction arises, it is too simplistic to properly capture the scale of α . Note that it is not enough to just plug in the effective electron mass to the formula for α ; this does not bridge the five orders of magnitude.

It's not important for the results that follow that we understand exactly why the Rashba interaction can be so strong. However, the naive model above does possess a qualitative feature critical to the Rashba interaction: the external electric field. In bulk materials, such an electric field is not naturally present. However, in mesoscopic heterostructures such as semiconductor nanowires, boundary effects and contact with other materials can cause such electric fields to arise in the system. Electric fields applied with gates can also serve the purpose, though in this thesis, we did observe many effects of spin-orbit near zero gate voltage.

8.3.2 In an infinite nanowire

Now let's specialize the Rashba effect to the case of a semiconductor nanowire. We will assume that this nanowire is aligned along the x direction and is very long, such that the momentum along the nanowire is a good quantum number [Fig. 8.5(a)]. We will again assume that the electric field is in the z direction.² This will give us the Rashba interaction, but it also provides some confinement. We thus assume that the z degree of freedom is frozen out, and model the transverse confinement in the y direction as a harmonic oscillator [Fig. 8.5(b)]. The Hamiltonian without spin-orbit is thus

$$H = \left(\frac{\hbar^2 k_x^2}{2m} - \mu \right) + \left(\frac{p_y^2}{2m} + \frac{1}{2} m \omega^2 y^2 \right) \quad (8.24)$$

While the Hamiltonian in the x -direction is that of a free particle, the y -dependent part of the Hamiltonian is a harmonic oscillator, and thus the wavefunctions and energies in the y -direction are that of a harmonic oscillator. We can thus index the quantum state of the

²In these wires, we're not actually sure which direction the electric field points. One hypothesis (put forward by Valla) is that it is due to band bending effects at the interface with the substrate, but it could also be caused by radial confinement due to changing material properties at the surface of the nanowire.

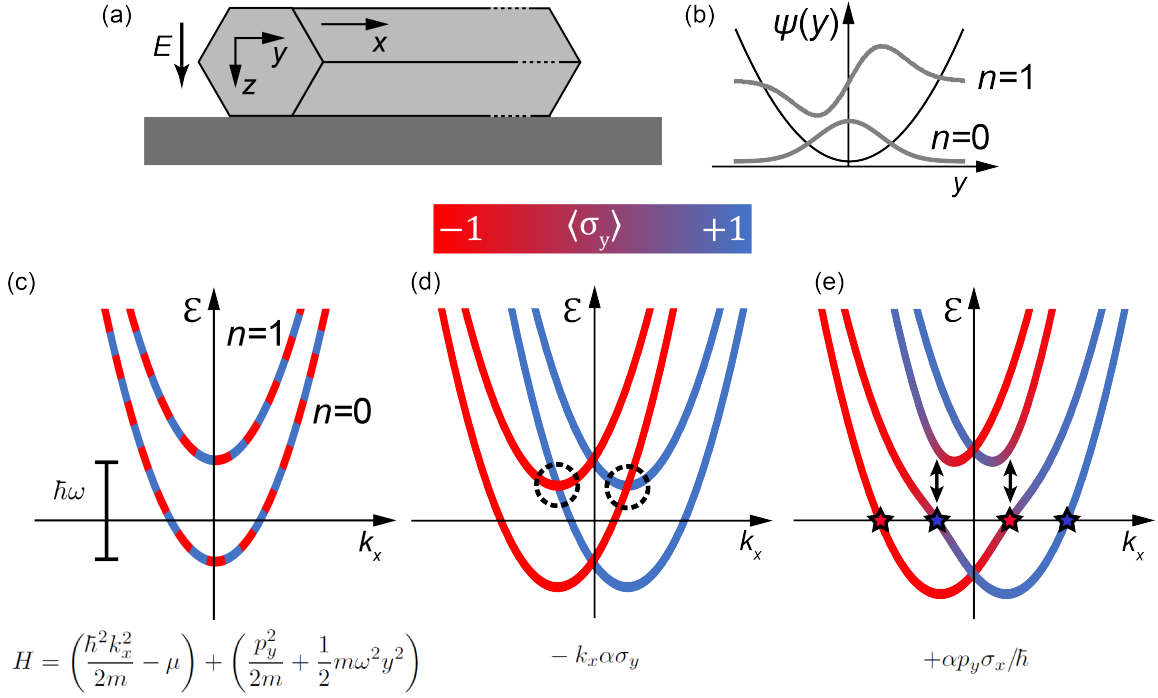


Figure 8.5: Spin-orbit coupling in a semiconductor nanowire | (a) A very long unproximitized nanowire aligned in the x -direction. An electric field E results in a Rashba interaction and confinement in the z direction. (b) The transverse wavefunctions of the first two subbands $n = 0$ and $n = 1$. (c) Energies of the first two sub-bands without spin-orbit coupling. (d) Including the longitudinal term of the Rashba interaction results in a spin-dependent displacement in k_x . The first and second sub-bands now cross at the locations indicated by the black dashed circles. (e) The transverse Rashba term leads to avoided crossings between the bands. The Fermi points (stars) of the new effective lowest-energy band have different velocities: the smaller momentum points have slower velocity, while the velocity of the larger momentum points is roughly the same as in (d). The transverse Rashba term has also entangled spin and translational degrees of freedom; spin is no longer a good quantum number.

electron by three quantum numbers: its momentum in the x direction k_x , the Fock state index in the y direction n , and the spin s ; we will label the state $|k_x, n, s\rangle$. Moreover, we will restrict ourselves to the first two Fock states $n = 0, 1$ such that we are left with the two spin-degenerate bands shown in Fig. 8.5(c).

Now we add a Rashba spin-orbit interaction. As seen in Eqn. 8.23, there are two terms to consider: $-\alpha p_x \sigma_y / \hbar$ and $+\alpha p_y \sigma_x / \hbar$. Let's start by adding the first one, ignoring the y -dependent part of the Hamiltonian for a second:

$$\begin{aligned}
H &= \frac{\hbar^2 k_x^2}{2m} - k_x \alpha \sigma_y - \mu \\
&= \frac{1}{2m} (\hbar^2 k_x^2 - 2m\alpha k_x \sigma_y) - \mu \\
&= \frac{1}{2m} (\hbar k_x - m\alpha \sigma_y / \hbar)^2 - m\alpha^2 / 2\hbar^2 - \mu
\end{aligned} \tag{8.25}$$

We see that the effect of this term is to displace the parabolic kinetic energy bands by $\pm m\alpha/\hbar$ depending on the sign of the spin in the y direction [Fig. 8.5(d)].

Now we add the second Rashba term $+\alpha p_y \sigma_x / \hbar$. This term mixes the already spin-orbit-split bands: avoided crossings form where the $n = 0$ and $n = 1$ states cross each other [see black dashed circles in Fig. 8.5(c), Fig. 8.5(d)], since p_y has a matrix element between these states. Moreover, because this mixing term depends on σ_x , the spin in the y direction is no longer a good quantum number. Instead, we are left with an energy-dependent **spin texture**; the spin is entangled with the translational degrees of freedom. This effect is strongest near the avoided crossing, as can be seen from the coloring of the bands in Fig. 8.5(d).

What's the point of all of this? While there will be some details of our discussion of spin-orbit that we will need to come back to, there is one crucial effect of the Rashba interaction that underpins our investigations of spinful Andreev levels. Restricting ourselves to the lower band in Fig. 8.5(d), *we see that there are two different Fermi velocities*: the two Fermi points closer to $k_x = 0$ have smaller slope, while the two outer Fermi points have larger slope. As we will see in the next section, it is this effect that breaks the spin degeneracy of the Andreev levels in Josephson nanowires.

8.4 Spin-orbit split Andreev levels

As we saw in the last section, an intra-sub-band Rashba interaction can result in a spin- and momentum-dependent Fermi velocity. How does this affect the Andreev levels? Neglecting disorder again for now, let's look go back to our discussion on the effect of the weak link

length L [Fig. 8.1]. We found that by including the propagation phase $\phi_p = (k_F + E/\hbar v_F)L$, the energy spacing between Andreev levels went down and more levels could fit inside the gap. Including the Fermi velocity mismatch induced by spin-orbit, the only difference is that two of the loops shown in Fig. 8.1 have a slower Fermi velocity v_1 , and two have a faster Fermi velocity v_2 . This change is illustrated in Fig. 8.6. For the loops with smaller velocity, the junction looks “longer” (the charge carriers pick up more propagation phase), while for the loops with larger velocity, the junction looks “shorter” (the charge carriers pick up less propagation phase). Critically, for each pair of levels that was before degenerate, *one has a smaller velocity, and one has a larger velocity*. This is how spin-degeneracy can be broken in Josephson nanowires.³

Now let’s add disorder again. Previously, we only including normal scattering between electrons with the same spin. We can do this again, as indicated by the black arrows in Fig. 8.6(a). This results in the avoided crossings shown in panel (c). The crossings at $\varphi = 0, \pi$ are protected by time-reversal symmetry. This is the characteristic spectrum for spin-orbit-split Andreev levels in Josephson nanowires, as was observed in [Tosi et al. 2019] and the experiments presented in this thesis.

However, a word of caution is in order here. While we have drawn the particles in panel (a) as spin up or spin down, this is no longer really true. In 8.5(e), we can see that the slow charge carriers (the Fermi points closer to zero momentum) are no longer eigenstates of σ_y . In fact, they are no longer eigenstates of spin at all, but some superposition of $|s_y = -1, n = 0\rangle$ and $|s_y = +1, n = 1\rangle$ (this is for the positive momentum Fermi point). So is it then correct to only include scattering as indicated in Fig. 8.6(a)? Almost certainly not. However, it may not be such a bad approximation, because as we saw in Fig. 8.6(c), the simple scattering picture [panel (a)] does result in avoided crossings everywhere there should be (again, crossings at $\varphi = 0, \pi$ are protected by time-reversal symmetry). Including other scattering terms would certainly cause additional repulsion between levels, but just between levels that didn’t cross in the first place.

We now derive the Andreev level structure [Fig. 8.6(c)] in both the single-scatterer,

³Note that we don’t have direct access to the band structure, so we can’t actually tell that something like Fig. 8.5 is happening. We see its effects only indirectly in the Fermi velocity mismatch, and even that we only see indirectly as the splitting of the Andreev levels.

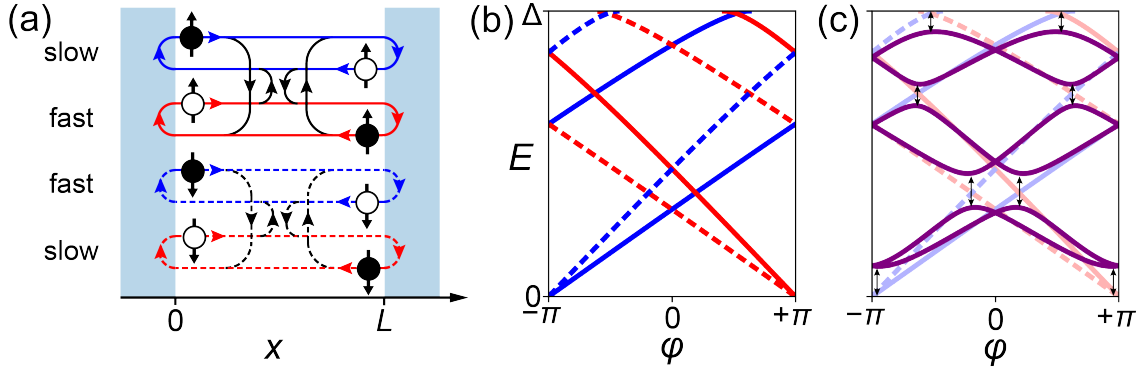


Figure 8.6: Adding spin-orbit coupling | (a) Due to spin-orbit coupling, the Andreev levels possess slower/faster Fermi velocities. (b) This makes the effective weak link length correspondingly longer/shorter, and the slope of the Andreev energies with phase smaller/larger. (c) Disorder results in avoided crossings (black arrows) between Andreev levels of the same spin, but crossings at $\varphi = 0, \pi$ are protected by time-reversal symmetry.

double-barrier, and resonant-level models of disorder. These calculations are the same as those performed earlier in the case without spin-orbit, only this time we include the Fermi velocity mismatch.

8.4.1 Single scatterer

The scattering matrix becomes

$$S_{e,\uparrow} = \begin{pmatrix} e^{i(+k_1+E/\hbar v_1)(L-x_0)} r e^{i(+k_2+E/\hbar v_2)(L-x_0)} & t e^{i(+k_1+E/\hbar v_1)L} \\ t e^{i(+k_2+E/\hbar v_2)L} & -e^{i(+k_2+E/\hbar v_2)x_0} r e^{i(+k_1+E/\hbar v_1)x_0} \end{pmatrix} \quad (8.26)$$

and $S_{e,\downarrow}$ is the same but with $k_2, v_2 \rightarrow k_1, v_1$ and vice versa. The transmitted particles have the same velocity/momentum all the way across the junction, but the reflected particles must switch velocity/momentum upon encountering the scatterer. This leads to a modification of the transcendental equation [Tosi et al. 2019]:

$$\begin{aligned}
0 &= r^2 \cos[2E(x_0 - L/2)(v_1^{-1} + v_2^{-1})/\hbar] \\
&+ t^2 \cos[EL(v_2^{-1} - v_1^{-1})/\hbar - s\varphi] \\
&- \cos[EL(v_2^{-1} + v_1^{-1})/\hbar + 2\phi_A]
\end{aligned} \tag{8.27}$$

where $s \in \{+1, -1\}$ for the two spin species. The numerical solution to this equation is plotted in 8.6(c)

8.4.2 Double-barrier

First, let's add a slow/fast dependence to the propagation phase Eqn. 8.4:

$$\begin{aligned}
\phi_1 &= (+k_1 + E/\hbar v_1)L \\
\phi_2 &= (+k_2 + E/\hbar v_2)L
\end{aligned} \tag{8.28}$$

The scattering matrix for spin-up electrons then becomes

$$S_{e,\uparrow} = \begin{pmatrix} r_R + \frac{r_L t_R^2 e^{i(\phi_1 + \phi_2)}}{1 + r_R r_L e^{i(\phi_1 + \phi_2)}} & \frac{t_L t_R e^{i\phi_1}}{1 + r_R r_L e^{i(\phi_1 + \phi_2)}} \\ \frac{t_L t_R e^{i\phi_2}}{1 + r_R r_L e^{i(\phi_1 + \phi_2)}} & -r_L - \frac{r_R t_L^2 e^{i(\phi_1 + \phi_2)}}{1 + r_R r_L e^{i(\phi_1 + \phi_2)}} \end{pmatrix} \tag{8.29}$$

and $S_{e,\downarrow}$ is the same with $\phi_1 \rightarrow \phi_2$ and vice versa. As always, we use $\det(S_A S_N - 1)$ to obtain a transcendental equation for the energies. It is very similar to what we obtained in the double-barrier model without spin-orbit [Tosi et al. 2019]:

$$\begin{aligned}
0 = & -\sin(\varepsilon_1 + \phi_A) \sin(\varepsilon_2 + \phi_A) \\
& + (r_L^2 + r_R^2) \sin(\varepsilon_1) \sin(\varepsilon_2) \\
& - r_L^2 r_R^2 \sin(\varepsilon_1 - \phi_A) \sin(\varepsilon_2 - \phi_A) \\
& - 2r_L r_R \cos((k_1 + k_2)L)(1 - E^2/\Delta^2)
\end{aligned} \tag{8.30}$$

but now $\varepsilon_1 = EL/\hbar v_1 - s\varphi/2$ and $\varepsilon_2 = EL/\hbar v_2 + s\varphi/2$.

8.4.3 Resonant level

Again, we include spin-orbit in the resonant level case by expanding the transcendental equation obtained in the double-barrier case.

$$\begin{aligned}
0 = & + (\Delta^2 - E^2) \left(E^2 - E_r^2 - \frac{1}{4}\Gamma^2 \right) + E^2 \Gamma \sqrt{\Delta^2 - E^2} + \Delta^2 \Gamma_L \Gamma_R \sin^2 \frac{\varphi}{2} \\
& + s \Gamma_L \Gamma_R \frac{EL}{\hbar} (v_1^{-1} - v_2^{-1}) \sin \varphi
\end{aligned} \tag{8.31}$$

The only additional term as compared to Eqn. 8.19 is the last one. It is asymmetric in φ as expected, with a sign that depends on s . However, it also has an additional factor of L . As we have assumed small L in the resonant level case, it is a very small correction. This is expected for small L : in order for spin-orbit interaction in the normal region to have a significant effect, the charge carriers must spend an appreciable amount of time in crossing the weak link.

References

Beenakker, C. and H. Van Houten, "Josephson current through a superconducting quantum point contact shorter than the coherence length", *Phys. Rev. Lett.* **66**, 3056 (1991).

- Beenakker, C. and H. Van Houten, “Resonant Josephson current through a quantum dot”, in *Single-electron tunneling and mesoscopic devices* (Springer, 1992), pp. 175–179.
- Béri, B., J. H. Bardarson, and C. W. J. Beenakker, “Splitting of Andreev levels in a Josephson junction by spin-orbit coupling”, *Phys. Rev. B* **77**, 045311 (2008).
- Cayao, J., E. Prada, P. San-Jose, and R. Aguado, “Sns junctions in nanowires with spin-orbit coupling: role of confinement and helicity on the subgap spectrum”, *Phys. Rev. B* **91**, 024514 (2015).
- Chtchelkatchev, N. M. and Y. V. Nazarov, “Andreev quantum dots for spin manipulation”, *Phys. Rev. Lett.* **90**, 226806 (2003).
- Heck, B. van, J. I. Väyrynen, and L. I. Glazman, “Zeeman and spin-orbit effects in the Andreev spectra of nanowire junctions”, *Phys. Rev. B* **96**, 075404 (2017).
- Murani, A., A. Chepelianskii, S. Guéron, and H. Bouchiat, “Andreev spectrum with high spin-orbit interactions: revealing spin splitting and topologically protected crossings”, *Phys. Rev. B* **96**, 165415 (2017).
- Nazarov, Y. V. and Y. M. Blanter, *Quantum transport: introduction to nanoscience* (Cambridge University Press, 2009).
- Padurariu, C. and Y. V. Nazarov, “Theoretical proposal for superconducting spin qubits”, *Phys. Rev. B* **81**, 144519 (2010).
- Reynoso, A. A., G. Usaj, C. A. Balseiro, D. Feinberg, and M. Avignon, “Spin-orbit-induced chirality of Andreev states in Josephson junctions”, *Phys. Rev. B* **86**, 214519 (2012).
- Tosi, L., C. Metzger, M. Goffman, C. Urbina, H. Pothier, S. Park, A. L. Yeyati, J. Nygård, and P. Krogstrup, “Spin-orbit splitting of Andreev states revealed by microwave spectroscopy”, *Phys. Rev. X* **9**, 011010 (2019).
- Yokoyama, T., M. Eto, and Y. V. Nazarov, “Anomalous Josephson effect induced by spin-orbit interaction and zeeman effect in semiconductor nanowires”, *Phys. Rev. B* **89**, 195407 (2014).

9

What would happen in a topological weak link?

In this chapter, we sketch how the Andreev spectrum of a topological weak link would be modified by the presence of Majorana zero modes. By probing the spectrum using two-tone spectroscopy, the presence of topological superconductivity could thus be verified. For more detail on why Majoranas are cool, I recommend “Introduction to topological superconductivity and Majorana fermions” by Martin Leijnse and Karsten Flensberg. For a general introduction to topology in condensed matter systems, I recommend the online course “Topology in condensed matter systems” organized by Anton Akhmerov (<https://topocondmat.org>).

The biggest reason physicists are so excited about superconductor-proximitized semiconductor nanowires is that, by applying a large magnetic field (~ 1 T) and carefully tuning of the chemical potential, the system could be driven through a topological phase transition to a p -wave superconducting state. This situation is depicted in Fig. 9.1 for one of our Josephson nanowires. If both proximitized sections were driven to the topological phase, then the system would host a total of four Majorana zero modes located at the ends of both topological sections. The two Majoranas closest to the weak link would hybridize into a single Andreev level. The energy of this special Majorana level could be brought to zero by tuning φ , independent of disorder. This parity-protected zero-energy crossing could be probed using the spectroscopy techniques presented in this thesis [Väyrynen et al. 2015],

verifying the presence of topological superconductivity.

This chapter is structured as follows: we begin with a tight-binding toy model of a topological weak link, and derive the energy of the Majorana level as a function of φ . We then show how, due to a simple modification of the Andreev reflection coefficient by p -wave pairing, that the Majorana level energy can also be derived using the same scattering formalism employed in Chapters 7 and 8. Next, we present a qualitative description of how the topological phase can be reached using the Josephson nanowires discussed in this thesis, and conclude with an outline of how two-tone spectroscopy could be used to probe the Majorana level.

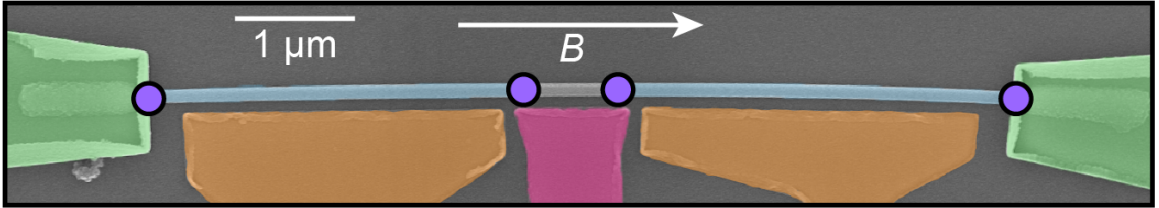


Figure 9.1: A topological Josephson nanowire | A ~ 1 T magnetic field B is applied along the Josephson nanowire, driving the proximitized sections into a topological phase. Majorana zero modes (purple circles) are bound to the end of each topological section. The two Majoranas flanking the weak link hybridize to form an Andreev level.

9.1 Tight-binding model of a p -wave weak link

9.1.1 The Kitaev chain

The unpaired Majoranas of this tight-binding model were first pointed out by by Alexei Kitaev [Kitaev 2001], hence the name.

Suppose we had a 1D, spinless, fermionic system. Its tight-binding Hamiltonian is given by

$$H = \sum_{n=1}^{N-1} \mu c_n^\dagger c_n + t c_n c_{n+1}^\dagger + \text{H.c.} \quad (9.1)$$

where μ is the chemical potential and t is the nearest-neighbor hopping strength. What kind of superconductivity can we imagine in this situation? For a BCS superconductor,

the pairing term would look like $\Delta c_{n,\uparrow}c_{n,\downarrow} + \text{H.c.}$ However, we are considering the case of spinless fermions. We can't have $\Delta c_n c_n + \text{H.c.}$ because of Pauli exclusion, so the next thing we can imagine is nearest-neighbor pairing: $\Delta c_n c_{n+1} + \text{H.c.}$ This is actually the pairing term for a p -wave superconductor. To understand the name, it's helpful to imagine p -orbitals overlapping, as depicted in Fig. 9.2(a). Our full Hamiltonian then becomes

$$H = \sum_{n=1}^{N-1} \mu c_n^\dagger c_n + t c_n c_{n+1}^\dagger + \Delta c_n c_{n+1} + \text{H.c.} \quad (9.2)$$

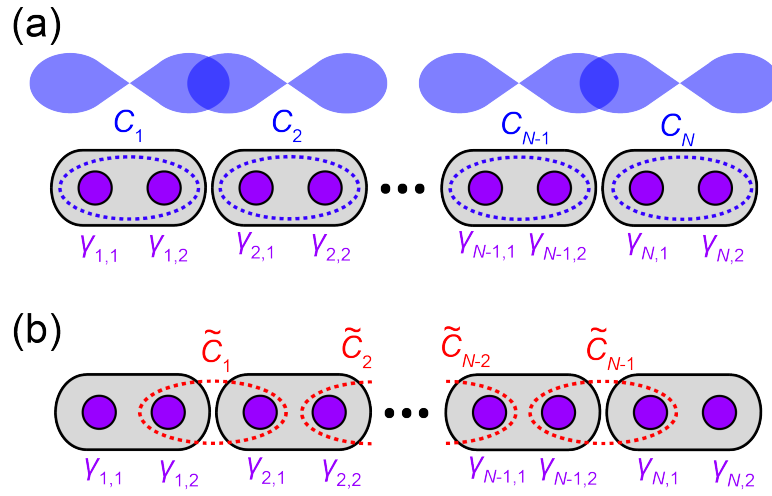


Figure 9.2: Tight-binding model of a spinless p -wave superconductor | (a) A tight-binding model with N sites (gray rectangles). Each site hosts a fermion c_n (dotted blue ovals), each of which can be broken into two Majoranas $\gamma_{n,1}, \gamma_{n,2}$ (purple circles). The model has a pairing between fermions on adjacent sites, as depicted by the blue p orbitals. (b) The Majoranas can also be grouped into the fermions \tilde{c}_n (dotted red ovals). These are the eigenstates of the Hamiltonian for $t = \Delta$ and $\mu = 0$. In this case, $\gamma_{1,1}$ and $\gamma_{N,2}$ are left unpaired.

As we shall see, we gain a lot of insight into this Hamiltonian by breaking the fermions into their Majorana operators [Fig. 9.2(a)]:

$$c_n = \frac{1}{2}(\gamma_{n,1} + i\gamma_{n,2}) \quad \gamma_n = \gamma_n^\dagger \quad \{\gamma_n, \gamma_m\} = 2\delta_{nm} \quad (9.3)$$

Despite the fact that I'm using γ to represent the Majoranas, note that they are not the same as the Bogoliubons. For one thing, they are Hermitian; this is why Majoranas are sometimes referred to as their own anti-particle. They have an anti-commutation relation similar to

normal fermions, but there is an additional factor of 2.

Before we continue, it will make the algebra a lot easier if we restrict ourselves to the special situation of $\Delta = t$ and $\mu = 0$. The results below generalize to other parameter regimes, but let's go with this for the moment. Plugging the Majorana operators in, we find

$$\begin{aligned}
H/\Delta &= \sum_{n=1}^{N-1} c_n c_{n+1}^\dagger + c_n c_{n+1} + \text{H.c.} \\
&= \sum_{n=1}^{N-1} c_n (c_{n+1}^\dagger + c_{n+1}) + \text{H.c.} \\
&= \sum_{n=1}^{N-1} \frac{1}{2} (\gamma_{n,1} + i\gamma_{n,2}) \gamma_{n+1,1} + \text{H.c.} \\
&= \sum_{n=1}^{N-1} \frac{1}{2} (\gamma_{n,1} + i\gamma_{n,2}) \gamma_{n+1,1} - \frac{1}{2} (\gamma_{n,1} - i\gamma_{n,2}) \gamma_{n+1,1} \\
&= \sum_{n=1}^{N-1} \frac{i}{2} \gamma_{n,2} \gamma_{n+1,1}
\end{aligned} \tag{9.4}$$

We then define new fermions $\tilde{c}_n = \frac{1}{2}(\gamma_{n,2} + i\gamma_{n+1,1})$ such that the Hamiltonian can be written as [Fig. 9.2(b)]

$$\begin{aligned}
H/\Delta &= \sum_{n=1}^{N-1} \frac{i}{2} \gamma_{n,2} \gamma_{n+1,1} \\
&= \sum_{n=1}^{N-1} \frac{1}{2} (\tilde{c}_n + \tilde{c}_n^\dagger) (\tilde{c}_n - \tilde{c}_n^\dagger) \\
&= \sum_{n=1}^{N-1} \tilde{c}_n^\dagger \tilde{c}_n
\end{aligned} \tag{9.5}$$

We thus find that the new fermions \tilde{c}_n are the eigenstates, and all possesses energy Δ . However, there are only $N - 1$ of the new fermions, and we started with N sites! Where'd

the last one go? In Fig. 9.2(b), we see that in writing the new fermions \tilde{c}_n , we have left out the Majoranas at the ends of the wires $\gamma_{1,1}$ and $\gamma_{N,2}$. Moreover, these Majoranas don't appear in the Hamiltonian! We thus find that we have two isolated, unpaired Majoranas; this is what is so exciting about a 1D spinless p -wave superconductor. We can still imagine grouping these two Majoranas together into a new fermion:

$$\tilde{c}_M = \frac{1}{2}(\gamma_{N,2} + i\gamma_{1,1}) \quad (9.6)$$

But again, because this fermion does not appear in the Hamiltonian Eqn. 9.5, the energy is the same whether $\tilde{c}_M^\dagger \tilde{c}_M = 0$ or $\tilde{c}_M^\dagger \tilde{c}_M = 1$. The system thus has a degenerate ground state, indexed by the parity of this special fermionic mode.

In this section, we have assumed $t = \Delta$ and $\mu = 0$. However, it turns out that the Majoranas at the end of the wire will be unpaired so long as $|\mu| < t$, though they will not be perfectly localized at the ends and instead their wavefunctions will decay into the chain. For $|\mu| > t$, the gap closes, the system undergoes a topological phase transition, and the unpaired Majoranas are no more.

9.1.2 Kitaev chain as a weak link

Now let's turn our tight-binding model into a topological weak link. We do this simply by connecting the two ends of the chain by a tunnel coupling $t'e^{i\varphi/2}c_Nc_1^\dagger + \text{H.c.}$, as depicted in Fig. 9.3(a). Here, as usual, φ is the superconducting phase difference across the weak link. However, instead of leaving it on the pairing term $\Delta e^{-i\varphi}c_nc_{n+1}$, we use a gauge transformation to move it onto the tunneling term $c_n \rightarrow c_n e^{-i\varphi/2}$. *This is where the factor of two in the exponent comes from; the phase gets split between the two fermions in the pairing term.* This will be very important for the φ dependence of the Andreev levels, as we will see below.

Let's break the tunneling term down into the Majorana operators:

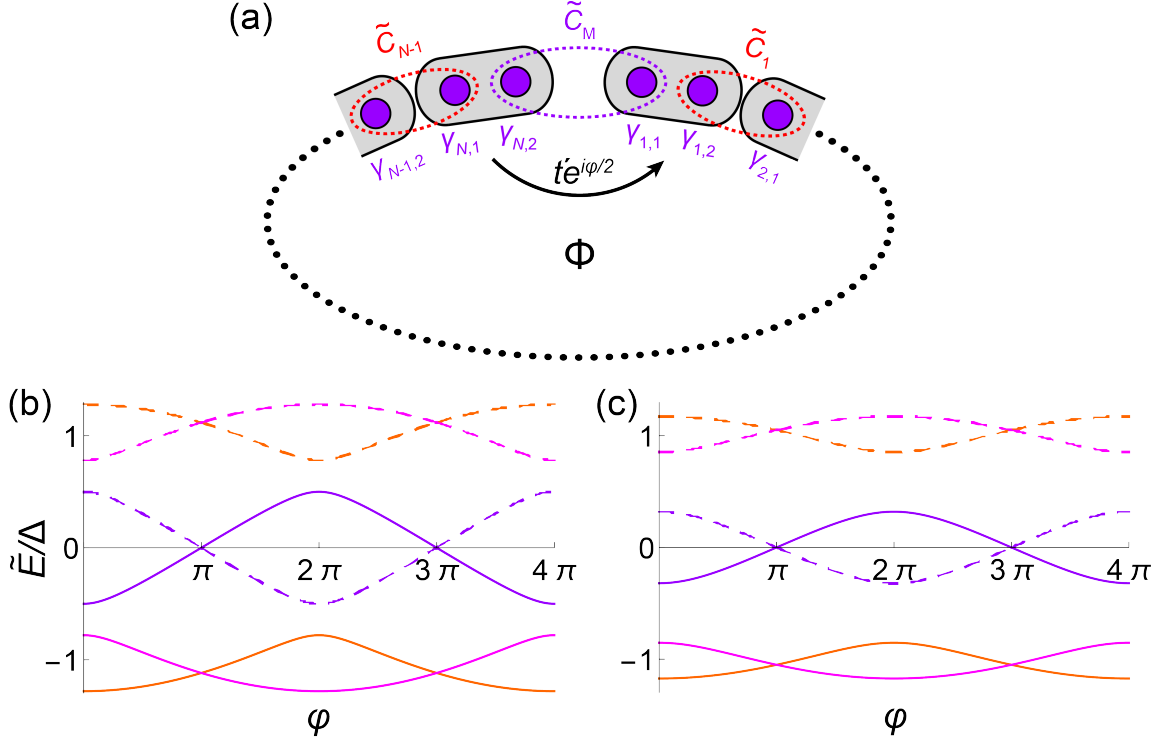


Figure 9.3: Tight-binding model of a spinless p -wave weak link | (a) We can imagine a weak link by connecting the two ends of the chain depicted in Fig.9.2 with a tunnel coupling $t'e^{i\varphi/2}c_Nc_1^\dagger + \text{H.c.}$ As usual, the phase is controlled by an external flux $\varphi = 2\pi\Phi/\Phi_0$. To rediagonalize the Hamiltonian, we have to consider the six labeled Majoranas for a total of three fermionic modes \tilde{c}_{N-1} , \tilde{c}_M and \tilde{c}_1 . In the presence of the tunnel coupling, the eigenmodes are given by \tilde{c}_M and $\tilde{c}_\pm = \frac{1}{\sqrt{2}}(\tilde{c}_{N-1} \pm \tilde{c}_1)$. (b) Energies of the three modes as a function of φ for $t' = 0.5$. In this semiconductor-like picture of superconductivity, the degrees of freedom are doubled such that the solid/dashed curves actually correspond to the same state, hence the mirror symmetry about $\tilde{E} = 0$. Orange corresponds to \tilde{c}_+ , pink to \tilde{c}_- , and purple to the Majorana level \tilde{c}_M . (c) Energies for $t' = 0.3$. As we enter the low-transparency regime, the Majorana level energy is well-approximated by $\tilde{E}_M \approx \Delta t' \cos \frac{\varphi}{2}$.

$$\begin{aligned}
t'e^{i\varphi/2}c_Nc_1^\dagger - t'e^{-i\varphi/2}c_N^\dagger c_1 &= +t'e^{+i\varphi/2}\frac{1}{2}(\gamma_{N,1} + i\gamma_{N,2})\frac{1}{2}(\gamma_{1,1} - i\gamma_{1,2}) \\
&\quad - t'e^{-i\varphi/2}\frac{1}{2}(\gamma_{N,1} - i\gamma_{N,2})\frac{1}{2}(\gamma_{1,1} + i\gamma_{1,2}) \\
&= +\frac{it'}{2}\sin\frac{\varphi}{2}(\gamma_{N,1}\gamma_{1,1} + \gamma_{N,2}\gamma_{1,2}) \\
&\quad +\frac{it'}{2}\cos\frac{\varphi}{2}(\gamma_{N,2}\gamma_{1,1} - \gamma_{N,1}\gamma_{1,2})
\end{aligned} \tag{9.7}$$

So once we add this term to the Hamiltonian, it will no longer be the case that $\gamma_{1,1}$ and $\gamma_{N,2}$ are absent. They are coupled to each other, and also to $\gamma_{1,2}$ and $\gamma_{N,1}$. And since $\gamma_{1,2}$ and $\gamma_{N,1}$ were coupled to $\gamma_{2,1}$ and $\gamma_{N-1,2}$ respectively in Eqn. 9.5, we have to keep track of all six of these Majoranas to re-diagonalize the Hamiltonian. To do this, we define the spinor of Majoranas

$$\Gamma = \begin{pmatrix} \gamma_{N-1,2} \\ \gamma_{N,1} \\ \gamma_{N,2} \\ \gamma_{1,1} \\ \gamma_{1,2} \\ \gamma_{2,1} \end{pmatrix} \quad (9.8)$$

such that the Hamiltonian of the weak link can be written as $\frac{1}{4}\Gamma^\dagger H_\varphi \Gamma$ where

$$H_\varphi = i \begin{pmatrix} 0 & +\Delta & 0 & 0 & 0 & 0 \\ -\Delta & 0 & 0 & +t' \sin \frac{\varphi}{2} & -t' \cos \frac{\varphi}{2} & 0 \\ 0 & 0 & 0 & +t' \cos \frac{\varphi}{2} & +t' \sin \frac{\varphi}{2} & 0 \\ 0 & -t' \sin \frac{\varphi}{2} & -t' \cos \frac{\varphi}{2} & 0 & 0 & 0 \\ 0 & +t' \cos \frac{\varphi}{2} & -t' \sin \frac{\varphi}{2} & 0 & 0 & -\Delta \\ 0 & 0 & 0 & 0 & +\Delta & 0 \end{pmatrix} \quad (9.9)$$

This is kind of like the semiconductor picture; one of the factors of $\frac{1}{2}$ in $\frac{1}{4}\Gamma^\dagger H_\varphi \Gamma$ is coming from the fact that we have included, for example, both $\gamma_{1,1}\gamma_{N,2}$ and $\gamma_{N,2}\gamma_{1,1}$. The other factor of $\frac{1}{2}$ would go away if we converted from Majoranas back to fermions, as in Eqn. 9.5.

To gain some intuition about what's going on here, let's start with the simpler case of

$\varphi = 0$. Then we have for the Hamiltonian:

$$H_{\varphi=0} = i \begin{pmatrix} 0 & +\Delta & 0 & 0 & 0 & 0 \\ -\Delta & 0 & 0 & 0 & -t' & 0 \\ 0 & 0 & 0 & +t' & 0 & 0 \\ 0 & 0 & -t' & 0 & 0 & 0 \\ 0 & +t' & 0 & 0 & 0 & -\Delta \\ 0 & 0 & 0 & 0 & +\Delta & 0 \end{pmatrix} \quad (9.10)$$

Here we see that if $t' = 0$, we have three two-by-two blocks along the diagonal corresponding to the three fermions of the unpaired case: two fermions \tilde{c}_{N-1} , \tilde{c}_1 with energy Δ (the first and third blocks) and one with zero energy \tilde{c}_M (the second block). Due to t' , the first and third blocks are mixed and the second block no longer has zero energy, as can be seen by computing the energy eigenvalues:

$$\tilde{E}_M = t' \quad \tilde{E}_{\pm} = \sqrt{\Delta^2 + \frac{t'^2}{2} \pm \frac{t'}{\sqrt{2}} \sqrt{t'^2 + 4\Delta^2}} \quad (9.11)$$

The Majorana level has energy $\tilde{E}_M = t$, while \tilde{c}_1 and \tilde{c}_{N-1} have been hybridized into $\tilde{c}_{\pm} = \frac{1}{\sqrt{2}}(\tilde{c}_{N-1} \pm \tilde{c}_1)$: their energies \tilde{E}_{\pm}^2 have been pushed up by $t'^2/\sqrt{2}$ and then split by $\frac{t'}{\sqrt{2}}\sqrt{t'^2 + 4\Delta^2}$.

Now let's look at the φ -dependence of the energies. I don't include the full expressions here because they are quite messy, but instead plot the result in Fig. 9.3(b). Remarkably, even though the Majoranas are coupled via tunneling, we find that \tilde{E}_M crosses zero energy at $\varphi = \pi$. Moreover, its period in φ is 4π instead of 2π like we are used to; this is known as the 4π Josephson effect. Note that the dashed/solid lines of the same color in Fig. 9.3(b) are not independent solutions of H_{φ} , and instead represent the same state. This is very similar to the semiconductor picture discussed in Chapter 6.

We can make a general argument that tells us that the Majorana level must cross zero energy between $\varphi = 0$ and $\varphi = 2\pi$. For $\varphi = 0$, we saw that all three levels have positive energy [Eqn. 9.11], and are thus unoccupied in the ground state. therefore, the parity of the ground state is even. Now suppose that $\varphi = 2\pi$; this just flips the sign of t' . The energies

of \tilde{c}_\pm are unaffected, but the energy of the Majorana level is inverted $\tilde{E}_E \rightarrow -\tilde{E}_E$. Now, the Majorana level is occupied in the ground state, and thus the parity is odd. The only way the parity of the ground state can change is if $\tilde{E}_M = 0$ for some value of $\varphi \in \{0, 2\pi\}$. The crossing of \tilde{E}_M with zero is thus **parity-protected**.

Finally, we note that within this tight-binding model, for low t' we can approximate the Majorana level energy as [Fig. 9.3(c)]

$$\tilde{E}_M \approx \Delta t' \cos \frac{\varphi}{2} \quad (9.12)$$

This is the commonly-quoted form of the 4π Josephson effect. In the coming sections, we will see that this is actually the form of \tilde{E}_M for a short weak link in the continuous case, independent of t' .

9.2 Continuous model of a p -wave weak link

9.2.1 From tight-binding to the continuous case

To move from the tight-binding model of the last section to the continuous case, I find it easiest to first shift to the momentum basis. We will focus on the pairing term:

$$\begin{aligned}
H &= \sum_n \Delta c_n c_{n+1} + \text{H.c.} \tag{9.13} \\
&= \sum_n \Delta \sum_k c_k e^{-ikna} \sum_{k'} c_{k'} e^{-ik'(n+1)a} + \text{H.c.} \\
&= \Delta \sum_k e^{ika} c_k c_{-k} + \text{H.c.} \\
&\approx \Delta \sum_k (1 + ika) c_k c_{-k} + \text{H.c.} \\
&= \Delta \sum_k c_k c_{-k} + \Delta \sum_k ika c_k c_{-k} + \text{H.c.} \\
&= \Delta \sum_k \sum_n e^{ikna} c_n \sum_{n'} e^{-ikn'a} c_{n'} + \Delta \sum_k ika c_k c_{-k} + \text{H.c.} \\
&= \Delta \sum_k ika c_k c_{-k} + \text{H.c.} \\
&\rightarrow \sum_k (\Delta ka) c_k c_{-k} + \text{H.c.}
\end{aligned}$$

where in the fourth line we have assumed that the lattice spacing a is small (this gets us to the continuous case), and in the last step we have absorbed the factor of i into the fermions with a gauge transformation $c_k \rightarrow c_k e^{-i\pi/4}$. We find something similar to s -wave pairing $\Delta c_{k,\uparrow} c_{-k,\downarrow}$ except that Δ has been replaced with Δka , and of course we've lost the spin degree of freedom. And that's it! The big change in the p -wave case is that the pairing is linear in k , instead of just constant. We will now track this change through our discussions of superconductivity and Andreev reflection in Appendices A/B to see how the Andreev spectrum is modified. To make this clearer, let's define the momentum-dependent pairing

$$\Delta_k = \Delta_0 k \quad \Delta_0 = \Delta a \tag{9.14}$$

so that the pairing term is just $\Delta_k c_k c_{-k} + \text{H.c.}$

Before moving on, let's quickly write the p -wave pairing term in position space (assuming $\varphi = 0$):

$$\begin{aligned}
& \sum_k k \Delta_0 c_k c_{-k} + \text{H.c.} \\
&= - \sum_{k,k'} k' \Delta_0 c_k c_{k'} \int dx e^{i(k+k')x} + \text{H.c.} \\
&= -\frac{1}{\hbar} \sum_{k,k'} \int dx \Delta_0 c_k e^{ikx} p c_{k'} e^{ik'x} + \text{H.c.} \\
&= -\frac{1}{\hbar} \int dx \Delta_0 \psi(x) p \psi(x) + \text{H.c.}
\end{aligned}$$

So we see that the pairing term is the momentum operator sandwiched between the same fermionic annihilation operator $\psi(x)$.

9.2.2 Diagonalizing the p -wave Hamiltonian

This section is almost identical to Chapter 6.2. We simply track the modified p -wave pairing term through the same calculation and find one important difference from the s -wave case.

The free-particle Hamiltonian is

$$H = \sum_k \mathcal{E}_k c_k^\dagger c_k; \quad \mathcal{E}_k = \frac{\hbar^2 k^2}{2m_e} - \mu \quad (9.15)$$

We don't have spin anymore, so we have to work in the semiconductor picture (see Chapter 6) where we double the degrees of freedom. We define $h_k = c_{-k}^\dagger$ and $c_k = c_k$ and thus pick up a factor of $\frac{1}{2}$ in front of the Hamiltonian:

$$H = \sum_k \mathcal{E}_k c_k^\dagger c_k \rightarrow \frac{1}{2} \sum_k \mathcal{E}_k (c_k^\dagger c_k - h_k^\dagger h_k) \quad (9.16)$$

where we have dropped a constant offset resulting from the fermionic anti-commutation relations. This transformation is shown pictorially in Fig. 9.4(a) and (b).

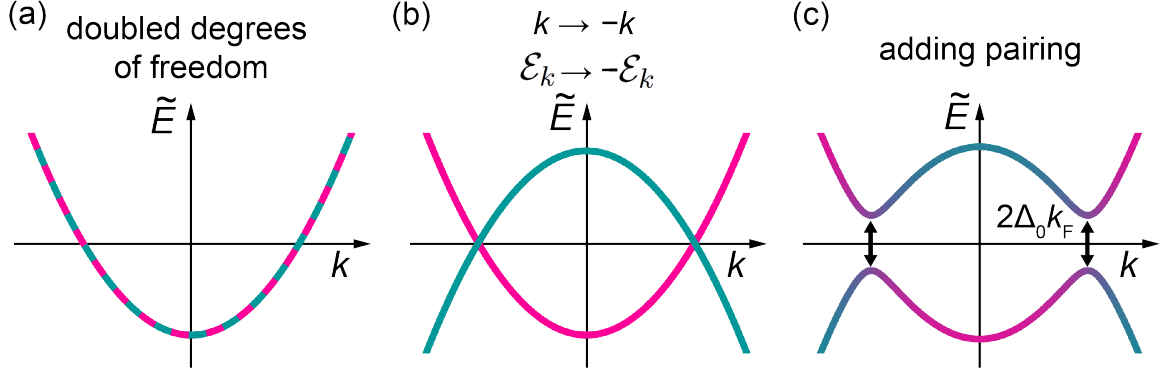


Figure 9.4: Building the band structure of a p-wave superconductor | (a) We start with the parabolic energy band of a 1D system of free electrons, and double the degrees of freedom. (b) Then, we describe one of the bands as **holes**. This results in a flip of momentum as well as energy. (c) Adding pairing creates an avoided crossing of strength $2\Delta_0 k_F$ between the two bands, with the new eigenstates having mixed **electron-hole** character.

Next, we add the pairing term

$$H_{\text{p-wave}} = \frac{1}{2} \sum_k \mathcal{E}_k (c_k^\dagger c_k - h_k^\dagger h_k) + k\Delta_0 c_k^\dagger h_k + k\Delta_0 h_k^\dagger c_k \quad (9.17)$$

And just like in the BCS case, we define the **electron-hole** spinor $\Psi_k = \begin{pmatrix} c_k \\ h_k \end{pmatrix}$ such that the Hamiltonian can be expressed in the compact form

$$H_{\text{p-wave}} = \frac{1}{2} \sum_k \Psi_k^\dagger H_k \Psi_k; \quad H_k = [\mathcal{E}_k \sigma_z + k\Delta_0 \sigma_x] \quad (9.18)$$

Here the Pauli matrices σ_i operate in electron-hole space. Because the Pauli matrices form a basis for a particular k , the energies can be read off immediately:

$$\pm \epsilon_k = \pm \sqrt{\mathcal{E}_k^2 + k^2 \Delta_0^2} \quad (9.19)$$

Again, we define the coherence factors. This is where the critical difference from the BCS case arises:

$$u_k = \frac{1}{\sqrt{2}} \sqrt{1 + \mathcal{E}_k/\epsilon_k}; \quad v_k = \frac{\text{sgn}(k)}{\sqrt{2}} \sqrt{1 - \mathcal{E}_k/\epsilon_k} \quad (9.20)$$

The critical difference as compared to the BCS coherence factors is the factor of $\text{sgn}(\epsilon)$ on v_k . This will modify the Andreev reflection coefficient, as we will discuss in the next section. First,

let's continue with our diagonalization of the Hamiltonian. The diagonalizing unitary matrix is written $U_k = \begin{pmatrix} u_k^* & v_k^* \\ -v_k & u_k \end{pmatrix}$, and our diagonalization of H_k is complete. To diagonalize the full Hamiltonian $H_{p\text{-wave}}$, we define the Bogoliubons $\begin{pmatrix} \gamma_{k,+} \\ \gamma_{k,-} \end{pmatrix} = U_k \Psi_k$. With these new definitions, we can inject $I = U_k^\dagger U_k$ and simplify:

$$H_{p\text{-wave}} = \sum_k \Psi_k^\dagger U_k^\dagger U_k H_k U_k^\dagger U_k \Psi_k = \sum_k \epsilon_k (\gamma_{k,+}^\dagger \gamma_{k,+} - \gamma_{k,-}^\dagger \gamma_{k,-}) \quad (9.21)$$

and thus reach a fully diagonal Hamiltonian.

9.2.3 A p -wave weak link

Using the same scattering arguments as we used in Chapter 7 for an s -wave weak link, we can construct the Andreev levels of a p -wave weak link. There are two important differences. First, we must remember that we only have one spin state, and that we have doubled the degrees of freedom. The spectrum will thus contain a purely mathematical symmetry.

Second, and this is the critical feature that will give us zero-energy states, the Andreev reflection coefficient r_A has been modified. We can ignore the momentum-dependence of the pairing (we assume $|k| \approx k_F$), but we can't ignore the factor of $\text{sgn}(k)$ on v_k . This results in a simple modification of the Andreev reflection coefficient in moving from the s -wave case to the p -wave case:

$$r_A \rightarrow \text{sgn}(k)r_A \quad (9.22)$$

Now we apply the scattering formalism developed in Chapter 7. All we have to do is include the sign of the momentum on r_A . Note that right-moving holes have negative momentum, so it's $c_{L,\text{out}}^\dagger$ and $h_{R,\text{out}}^\dagger$ that pick up the minus sign:

$$\Psi_{\text{in}}^\dagger = S_A \Psi_{\text{out}}^\dagger \quad (9.23)$$

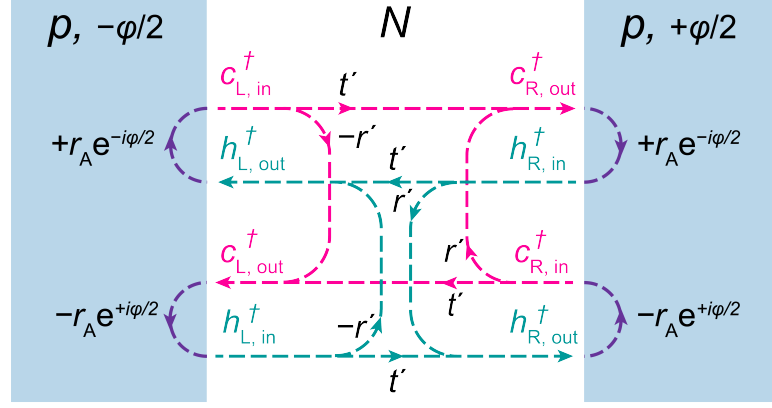


Figure 9.5: Scattering formalism for a p-wave superconductor | As compared to the s -wave case, the only difference is that the Andreev reflection coefficient picks up the sign of the momentum.

$$\Psi_{\text{in}}^\dagger = \begin{pmatrix} c_{R,\text{in}}^\dagger \\ c_{L,\text{in}}^\dagger \\ h_{R,\text{in}}^\dagger \\ h_{L,\text{in}}^\dagger \end{pmatrix} \quad \Psi_{\text{out}}^\dagger = \begin{pmatrix} c_{R,\text{out}}^\dagger \\ c_{L,\text{out}}^\dagger \\ h_{R,\text{out}}^\dagger \\ h_{L,\text{out}}^\dagger \end{pmatrix}$$

$$S_A = \begin{pmatrix} 0 & 0 & -r_A e^{-i\varphi/2} & 0 \\ 0 & 0 & 0 & +r_A e^{+i\varphi/2} \\ +r_A e^{+i\varphi/2} & 0 & 0 & 0 \\ 0 & -r_A e^{-i\varphi/2} & 0 & 0 \end{pmatrix}$$

We'll use the same scattering matrix for the normal region as we did in Chapter 7:

$$S_N = \begin{pmatrix} r & t' & 0 & 0 \\ t' & -r & 0 & 0 \\ 0 & 0 & r & t' \\ 0 & 0 & t' & -r \end{pmatrix} \quad (9.24)$$

Now, solving the equation $\det(S_A S_N - I) = 0$ gives us the formula for the single Andreev

level of a short, p -wave weak link:

$$E_M = (\Delta_0 k_F)^2 t' \cos \frac{\varphi}{2} \quad (9.25)$$

This is the same expression for the Majorana level energy that we found in the low- t' , tight-binding model Eqn. 9.11. Note that here, in this more accurate continuous model, we have found that this expression is correct independent of t . To generalize to the case of a long weak link, one would simply use the modified Andreev scattering matrix S_A in conjunction with the various models of S_N discussed in Chapter 8.

9.3 Majoranas as Andreev levels between a p -wave superconductor and vacuum

This section follows naturally from the results of the last section, but as this is my favorite way to think about the emergence of Majoranas, I'm grouping it separately.

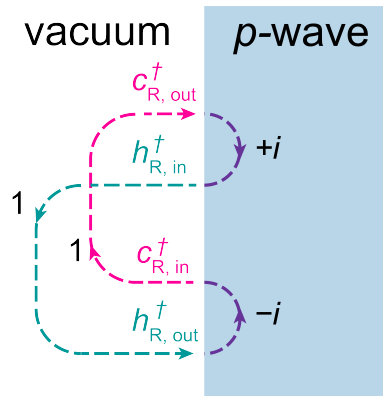


Figure 9.6: Majoranas as Andreev levels | Constructive interference of normal and Andreev reflection for $r' = 1$. The particles are all moving at zero energy, so $r_A = i$.

We can understand the Majoranas bound to the end of a p -wave superconductor as the Andreev level of a p -wave weak link where $t' \rightarrow 0$. Then, the two sides of the weak link don't talk to each other, and we can throw one of them away; let's keep only the right superconductor [Fig. 9.6]. From Eqn. 9.25, we see that $E_M = 0$ for $t' = 0$. So far so good; this is consistent with what we learned from the Kitaev chain. What about the operator properties? Let's convert all the electron/hole scattering operators to the position basis,

focusing on the part of the wavefunction in the superconductor (which decays with ξ_0):

$$\begin{aligned}
c_{\text{R,out}}^\dagger &= \int dx e^{+ikx} e^{-x/\xi_0} \psi^\dagger(x) \\
h_{\text{R,in}}^\dagger &= \int dx e^{+ikx} e^{-x/\xi_0} \psi(x) \\
h_{\text{R,out}}^\dagger &= \int dx e^{-ikx} e^{-x/\xi_0} \psi(x) \\
c_{\text{R,in}}^\dagger &= \int dx e^{-ikx} e^{-x/\xi_0} \psi^\dagger(x)
\end{aligned} \tag{9.26}$$

Now we can see from Fig. 9.6 that the Majorana level will be a superposition of these operators. We will reference the phase to $c_{\text{R,out}}^\dagger$ and ignore normalization:

$$\begin{aligned}
\gamma &= c_{\text{R,out}}^\dagger + ih_{\text{R,in}}^\dagger + ih_{\text{R,out}}^\dagger + c_{\text{R,in}}^\dagger \\
&= 2 \int \cos(kx) e^{-x/\xi_0} [\psi^\dagger(x) + i\psi(x)] \\
&\rightarrow 2e^{i\pi/4} \int \cos(kx) e^{-x/\xi_0} [\psi^\dagger(x) + \psi(x)]
\end{aligned} \tag{9.27}$$

where in the last step we have performed a gauge transformation $\psi(x) \rightarrow \psi(x)e^{-i\pi/4}$. Now if we look at the position space creation operators, we see that we are left with exactly the properties of a Majorana [Eqn. 9.3]:

$$\psi^\dagger + \psi = (\psi^\dagger + \psi)^\dagger \quad \{\psi^\dagger + \psi, \psi^\dagger + \psi\} = 2 \tag{9.28}$$

Majoranas arise when the eigenmodes of the system are described by superpositions of a creation operator and its complex conjugate, as shown above. One way to see why this occurs at the edge of a p -wave superconductor is to recognize that Andreev reflection results in superpositions between electrons and holes. But in a spinful s -wave superconductor, the superposition is between two different spin species $\psi_\downarrow^\dagger + \psi_\uparrow$, and thus it doesn't have the properties Eqn. 9.28. Only when we have spinless p -wave pairing can Majoranas arise.

9.4 Making an effective p -wave superconductor

The topological phase transition in proximitized semiconductor nanowires was pointed out independently by Oreg et al. and Lutchyn et al. in 2010. For a rigorous description, see those works; “Introduction to topological superconductivity and Majorana fermions” also has a good discussion. Here, we present on a qualitative level how a combination of ingredients in nanowire systems can result in a topological spinless 1D superconductor.

1D system First, let’s start with a plain nanowire with no spin-orbit coupling, oriented along the x direction [Fig. 9.7(a)] (pretend the superconductor isn’t there for a second). Restricting ourselves to one sub-band, we are left with spin-degenerate parabolas [Fig. 9.7(b)].

Magnetic field So we have a 1D system, but we need to make it spinless. This we do with a strong magnetic field ($\sim 1\text{T}$), pushing one of the bands up and the other down [Fig. 9.7(b)].

On the Hamiltonian level, we have added a term

$$\frac{g\mu_B B}{2}\sigma_x \quad (9.29)$$

Then, if we restrict ourselves to the lower band, we have essentially frozen out the spin degree of freedom. Note that we have applied the magnetic field along the nanowire; the reason for this will be explained below.

Trying to add superconductivity, but failing As far as well-behaved low-temperature superconductors go, the only materials we know of all have s -wave pairing:

$$\Delta c_{k,\uparrow}^\dagger c_{-k,\downarrow}^\dagger + \text{H.c.} \quad (9.30)$$

The idea is to coat the nanowire with an s -wave superconductor [Fig. 9.7(d)], thereby allowing the correlation between pairs in the superconductor to leak into the semiconductor (the proximity effect). But as we see above, s -wave pairing is an interaction between electrons of opposite momentum, *but also opposite spin*. And we’ve frozen out the spin degree of freedom with magnetic field; all the spins in the lower band of Fig. 9.7(c) are pointing along the x direction. As such, the s -wave correlations cannot make their way into the nanowire.

Spin-orbit coupling can fix this problem for us.

Spin-orbit coupling Let's assume the electric field generating the Rashba term is pointing in the $+y$ direction [Fig. 9.7(a)]. The Rashba term is then

$$\begin{aligned} H_R &= \frac{\alpha}{E} (\hbar k \hat{x} \times E \hat{y}) \cdot \sigma \\ &= \alpha k \sigma_z \end{aligned} \quad (9.31)$$

Adding this term to our nanowire thus adds some momentum-dependent spin texture [Fig. 9.7(d)]. Specifically, for the lower-energy subband that we are interested in, it rotates the spin towards \uparrow for $+k$ and towards \downarrow for $-k$. Note that the spin degree of freedom is still frozen out, it's just that the spin rotates as we vary momentum. In experiment, we're not actually sure which way the Rashba-generating electric field is pointing. But since the Rashba term is a cross product between the electric field and momentum along the nanowire, we know that the Rashba field will be perpendicular to the nanowire. And because the magnetic field must be perpendicular to the Rashba field to get the spin texture [Fig. 9.7(a)], the magnetic field is applied parallel to the nanowire. Additionally, the critical field of thin-film superconductors is much larger when the field is applied parallel to the film. This is a happy coincidence.

Adding superconductivity Now when we add a proximitizing s -wave superconductor, it will actually have an effect [Fig. 9.7(e)]. Here we are working in the semiconductor picture, so we've doubled the degrees of freedom and then flipped them in momentum and energy. Due to s -wave pairing, an avoided crossing forms between the bands. We are thus left with a spinless p -wave superconductor. However, it turns out this is only true if $g\mu_B|B| > \sqrt{\Delta^2 + \mu^2}$; tuning the system to satisfy this inequality drives it into the topological phase.

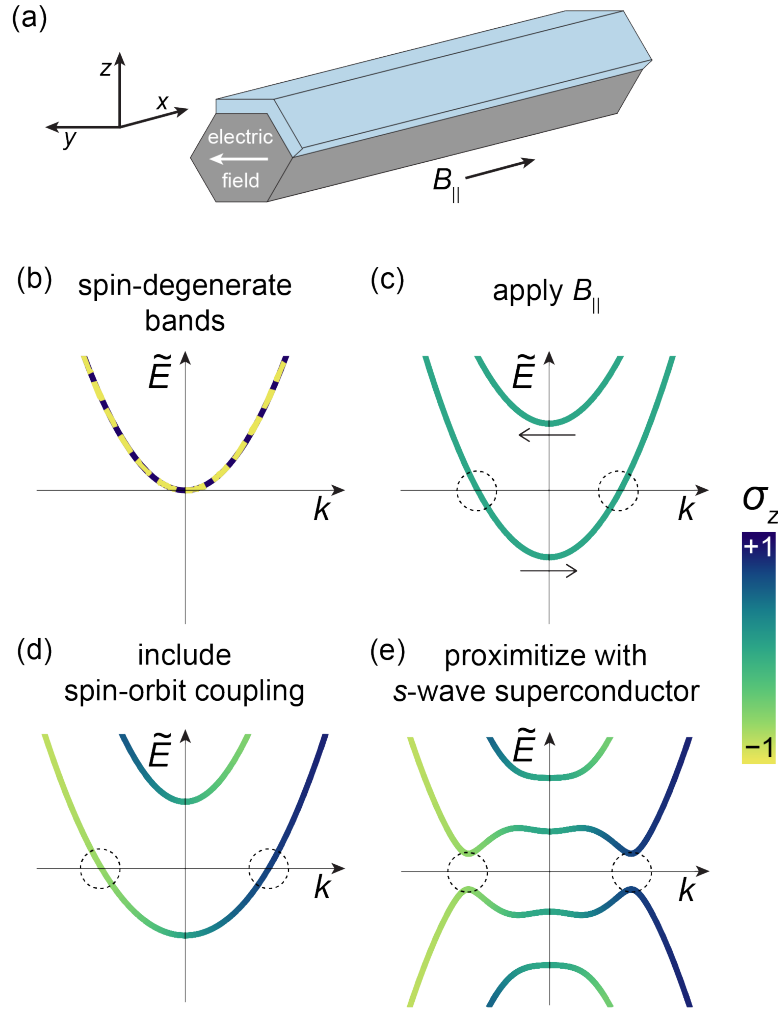


Figure 9.7: A nanowire as an effective spinless p-wave superconductor | (a) A semiconductor nanowire oriented along the x direction (gray), with a proximitizing superconductor on two facets (blue). A magnetic field B_{\parallel} is applied along the nanowire, while an electric field oriented in the y direction results in Rashba spin-orbit coupling. (b) The spin-degenerate bands of one subband of the nanowire with no magnetic field, spin-orbit coupling, or superconductivity. (c) The magnetic field splits the bands, pushing one up and one down. As indicated by the arrows, the spins of the higher-energy band point along negative x , while the spins of the lower-energy band point along positive x . We want to introduce superconductivity by coupling the states circled with the black dots with an s -wave pairing term. (d) Including spin-orbit coupling ensures that while the spin degree of freedom is still frozen out, the spin at $+k$ is slightly different than at $-k$. (e) Thus by including s -wave pairing, we end up with a spinless superconductor.

9.5 Probing the Majorana level in a cQED architecture

In this section, we briefly outline the main idea presented in Väyrynen et al. 2015.

Suppose that, using the device presented in this thesis, we managed to drive the Josephson nanowire into the topological phase. How could we detect the presence of the Majorana level? Throughout this thesis, we have emphasized that microwaves must conserve parity, and the situation is no different here. Whereas in transport experiments evidence of Majoranas has been found by direct tunneling of electrons into a zero energy mode [Mourik et al. 2012], here we must maintain parity.

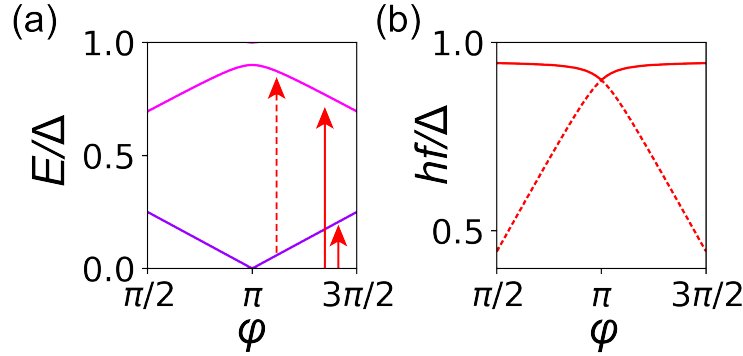


Figure 9.8: Probing a p -wave weak link with microwaves | (a) Schematic of the Majorana level and the next lowest energy Andreev level around $\varphi = \pi$. Note that this is just a cartoon spectrum. Two microwave transitions are possible: a pair transition that populates the Majorana level and the Andreev level at the same time (solid arrows), or if the Majorana level is already populated, the quasiparticle can be driven to the Andreev level (dotted arrow). (b) The frequencies of this two transitions versus φ meet at $\varphi = \pi$. Critically, they both exhibit a kink due to the Majorana level crossing zero energy.

To get around this problem, one could use an additional auxiliary Andreev level to probe the Majorana level. A cartoon spectrum is plotted in Fig. 9.8(a) in the excitation picture. Restricting ourselves to only these two levels, there are two microwave transitions one could imagine. If both levels are depopulated, then a pair transition could be driven to create a quasiparticle in both. On the other hand, if one of the levels is occupied by a quasiparticle, a single-particle transition could be driven to shuffle the quasiparticle between the two levels.

The frequencies of these two transitions are plotted in Fig. 9.8(b). The critical feature of this spectrum is that, where the transitions meet at $\varphi = \pi$, they are kinked. This is due to the Majorana level crossing zero energy, and it is thus this kink that one would look for in two-tone spectroscopy in order to verify the presence of the topological phase.

References

- Kitaev, A. Y., “Unpaired majorana fermions in quantum wires”, *Physics-Uspekhi* **44**, 131 (2001).
- Mourik, V., K. Zuo, S. M. Frolov, S. R. Plissard, E. P. A. M. Bakkers, and L. P. Kouwenhoven, “Signatures of majorana fermions in hybrid superconductor-semiconductor nanowire devices”, *Science* **336**, 1003–1007 (2012).
- Väyrynen, J. I., G. Rastelli, W. Belzig, and L. I. Glazman, “Microwave signatures of majorana states in a topological Josephson junction”, *Physical Review B* **92**, 134508 (2015).

10

The device

In this Chapter, we first discuss the basic working principle of the device and how it was realized in practice. We then outline the details of the design and fabrication of the device. Finally, we show the small but important changes to the design that took place over the course of these experiments.

10.1 Principle

The original idea behind these experiments was to investigate the Andreev levels of Josephson nanowires using CQED. In superconducting atomic point contacts, cQED techniques had been successfully implemented to investigate the weak link Andreev levels [Janvier et al. 2015]. We adopted the general structure of those devices, but replaced the atomic point contacts with Josephson nanowires.

As was discussed in Chapter 3, we used an inductive coupling between the resonator (frequency f_r) and the Josephson nanowire [Fig. 10.1]. While the specifics of this coupling are discussed in Chapter 11, the basic idea is this: the Josephson nanowire was wired up in parallel with a portion of the resonator's inductance such that the coupling between the two systems was approximately $H_c = J_A \Phi_r$, with J_A the weak link current operator and Φ_r the fraction of the resonator zero-point flux fluctuations that dropped over the shared inductance. The resonator was capacitively coupled to a transmission line with strength κ_c . By monitoring the resonator response to a probe tone sent down the transmission line, we were able to detect dispersive shifts due to the Andreev levels and thereby determine

their quantum state.

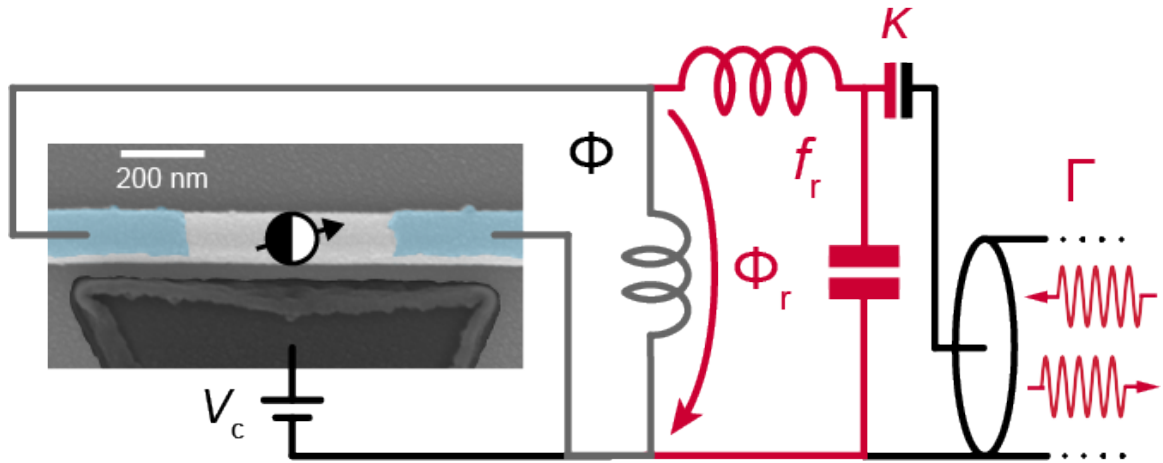


Figure 10.1: Coupling a Josephson nanowire to a superconducting microwave resonator | Color-enhanced scanning electron micrograph of a Josephson nanowire. The InAs nanowire was partially coated by epitaxial Al (blue), with an uncovered region forming the weak link. A flux Φ applied through a small-inductance loop set the weak-link phase bias $\varphi \cong 2\pi \frac{\Phi}{\Phi_0} \text{mod}(2\pi)$, and a gate voltage V_c was used to tune the chemical potential. The Josephson nanowire was inductively coupled to a superconducting resonator (red, frequency $f_r = 9.188$ GHz), which was capacitively coupled with strength κ to a transmission line to probe the reflection amplitude Γ .

Looking back through the last paragraph, we see that there are three important resonator properties: f_r , κ_c , and Φ_r . When designing the last iteration of the device, we tailored these to what little we knew about the Andreev levels of Josephson nanowires, as we now discuss.

The frequency

We chose $f_r \simeq 9$ GHz, which is on the high end of the typical cQED frequency range. We thought the transparency of the nanowire might be low, which would mean high-frequency Andreev transitions. As the conventional Jaynes-Cummings-style dispersive shift falls off with the detuning, we wanted our resonator mode to be as close as possible to the Andreev transitions.

The transmission line coupling

The main design constraint on the coupling to the transmission line κ_c was that we wanted it to be bigger than the internal loss κ_i of the resonator.¹ In previous devices, we had found $\kappa_i/2\pi$ as large as 1 MHz, so we wanted κ_c to be at least this large. But we also don't want κ_c to be too big, because it would reduce our sensitivity to dispersive shifts. We thus chose $\kappa_c/2\pi \simeq 4$ MHz, which was a happy medium.

The flux drop

The flux drop Φ_r sets the scale of the coupling to the Andreev levels. As is derived in Chapter 11, the resonator-pair qubit coupling for a short junction was given by

$$g_c(\varphi) = \Phi_r \sqrt{1 - \tau} I_A(\varphi) \tan(\varphi/2) \quad I_A(\varphi) = \frac{2\pi d\epsilon_A}{\Phi_0 d\varphi} = \frac{2\pi\Delta}{\Phi_0} \frac{\tau \sin \varphi}{4\sqrt{1 - \tau \sin^2(\varphi/2)}} \quad (10.1)$$

In Ref. [Hays et al. 2018], we fit the pair transition to the short junction formula and extracted $\tau = 0.98$ and $\Delta = h \times 30$ GHz. We didn't really trust this fit; we suspected we weren't quite in the short-junction regime as $\Delta = h \times 44$ GHz for bulk aluminum. Nonetheless, short junction theory was all we had to work with. In designing the next iteration of devices, we thus plugged these numbers into the above equations. Setting $\varphi = \pi$, which is where the above formula is maximum, we get $g_c/\Phi_r = 30$ nA. Thus, we just had to choose a value of Φ_r that would give us a good coupling.

But what is a good coupling? It comes down to the optimal value for the dispersive shift $\chi = g_c^2/(2\pi f_{\text{pair}} - \imath)$. It turns out that, to get maximum SNR for two-state discrimination, we want $\chi = \kappa_c/2$. We can see this from the formula for a resonator measured in reflection, which is frequency-shifted by χ [Axline 2018]:

$$\Gamma = \frac{\omega_{\text{ro}} - (\omega_r \pm \chi) + i(\kappa_c - \kappa_i)/2}{\omega_{\text{ro}} - (\omega_r \pm \chi) - i(\kappa_c + \kappa_i)/2} \quad (10.2)$$

If the readout frequency is on resonance with the bare resonator frequency $\omega_{\text{ro}} = \omega_r$ and

¹The farther we go into this regime, the more information about the Andreev levels comes back down the transmission lines, as opposed to getting lost to other degrees of freedom.

we assume $\kappa_i = 0$, we find

$$\Gamma = \frac{\pm\chi - i\kappa_c/2}{\pm\chi + i\kappa_c/2} = \frac{\chi^2 - (\kappa_c/2)^2 \mp i\chi\kappa_c}{\chi^2 + (\kappa_c/2)^2} \quad (10.3)$$

If $\chi = \kappa_c/2$, then the real part vanishes, and $\Gamma = \mp i$. The responses for the two states are on opposite side of the unit circle, as far away from each other as they can be.

So we want $\chi \approx \kappa_c/2$. What does this mean for Φ_r ? In terms of underlying resonator parameters, Φ_r can be expressed as $\Phi_r = p\Phi_{\text{zpf}}$. Here $\Phi_{\text{zpf}} = \sqrt{\hbar Z_r/2}$ is the zero-point fluctuations of the resonator flux where Z_r is the resonator impedance, and p is the voltage participation ratio.² As we discuss below, our resonator impedance was approximately $Z_r \simeq 90\Omega$. Choosing $p \simeq 0.05$ thus gives us

$$g_c/2\pi = p\sqrt{\hbar Z_r/2} \times 30 \text{ nA}/h \simeq 160 \text{ MHz} \rightarrow \chi/2\pi = \frac{(g_c/2\pi)^2}{2\epsilon_A/h - f_r} \simeq 3.5 \text{ MHz}. \quad (10.4)$$

While this is slightly above the ideal value $\chi = \kappa_c/2$, we figured we could always decrease the detuning by tuning the transition away from the resonator.³ In the experiment, this larger coupling worked out well; we ended up focusing on the single-particle transitions in long junctions. The Andreev levels of long junctions necessarily carry smaller super-currents, so the coupling drops. In the future, we will likely increase this coupling even further.

10.2 Design

So we know what we want the effective circuit to look like [Fig. 10.1], and we have an idea of what we want the parameters of the effective circuit to be. What did it look like in practice?

²For the lumped model depicted in Fig. 10.1, this is just the the ratio of the shared inductance to the total inductance.

³In principle, one could also work at a different readout frequency. While this would work fine for two quantum states, in this experiment we are dealing with a richer system. It would be ideal to be able to detect all states simultaneously, which requires that $\chi \sim \kappa_c$. Adjusting the readout frequency is not enough.

Microwave considerations

At Yale, 2D resonators have fallen out of style, as 3D cavity resonators generally possess much higher coherence. However, as of the time of this writing, no one has integrated DC gates with 3D cavities. In 2D systems, on the other hand, gates have been successfully implemented. We therefore went with the 2D design shown in Fig. 10.2. The resonator is a $\sim \lambda/4$ differential co-planar-strip resonator. To maximize the coupling, the Josephson nanowire was placed at the current anti-node of the device [Fig. 10.2(a, b, c)]. At the other end (the voltage anti-node), the resonator was capacitively coupled to transmission lines as shown in Fig. 10.2(e). Both the readout and drive tones were routed through a circulator and a 180° hybrid, resulting in the necessary differential RF voltage on the transmission lines. The reflected readout signal was then routed through a SNAIL parametric amplifier [Frattoni et al. 2018] and a HEMT before being processed at room temperature.

Gate considerations

This design is a bit unconventional; coplanar waveguide and microstrip are more typical than the coplanar-strip design we used here. The reason we chose coplanar strip was to maximize the symmetry of the readout mode. Up to the slightly off-center nanowire placement [Fig. 10.2(b)], the device is perfectly mirror symmetric about the line running down the center of the chip. As such, the voltage profile of the resonator mode is anti-symmetric about the center of the chip, and the center line is at zero RF voltage. This allowed us to bring in the gate traces along the center line without having to worry about inducing extra resonator loss. Moreover, it gave us a convenient way to ground the device. This is the purpose of the purple trace that runs between the two strips of the resonator [Fig. 10.2(c)]. Grounding the nanowire/resonator island was critical for successful gating. An electric field between the gate and the nanowire is necessary to achieve a field effect, and an electric field is only present if the gate voltage drops between the gate and the nanowire.

Majorana considerations

As there was always the chance that we would want to apply a large magnetic field to drive the nanowire into a topological regime, we used NbTiN for the metallization. The film had a kinetic inductance per square of 0.6 pH/□. This was important to remember when modeling the device, as discussed below.

10.3 Modeling

To model the device, we used a combination of a transmission line model [Fig. 10.3(a)] and the Sonnet Suites microwave simulation package.

The transmission line model was useful for ball-parking the resonator frequency and estimating $\Phi_r = p\Phi_{zpf}$. To get the frequency, we considered the impedance as seen from the right side of the resonator in [Fig. 10.3(a)]:

$$Z = Z_0 \frac{Z_L + iZ_0 \tan(\beta\ell)}{Z_0 + iZ_L \tan(\beta\ell)} \quad (10.5)$$

where $Z_L = i\omega L$, $\beta = \omega/c_{\text{eff}}$, and ℓ is the length of the resonator. Note that this was assuming $\kappa_c = 0$, which is a decent approximation since it was on the order of MHz. The unknown parameters in the above expression were the characteristic impedance of the transmission line Z_0 , the speed of light on the line c_{eff} , and the shared inductance. We estimated Z_0 and c_{eff} by performing transmission simulations of co-planar-strip transmission lines in Sonnet,⁴ and we estimated the shared inductance to be 68 pH using the dimensions of the trace, a geometric inductance of 1.3 pH/ μm , and the kinetic inductance.⁵ Plugging these estimates in and choosing $\ell = 3 \text{ mm}$, we found the value of ω where Z diverged⁶ gave us 9.7 GHz for the resonator frequency.

⁴Not only did we need to extract the effective dielectric constant of the transmission line, we also needed to extract the effective permeability due to the kinetic inductance of the NbTiN. We estimated these by performing transmission line simulations with/without the dielectric and kinetic inductance included.

⁵We made a mistake here and calculated the shared inductance as only half of its actual value. We thought that Sonnet was giving us the “odd-mode” impedance in our transmission simulations, when in actuality it was giving us the differential impedance. We thus should have plugged in $2 \times 68 \text{ pH}$ for the shared inductance. However, as we also neglected the inductance of the tapers up to the shared inductance [Fig. 10.2], the participation ratio ended up being about right.

⁶Actually, we solved for where its inverse was zero.

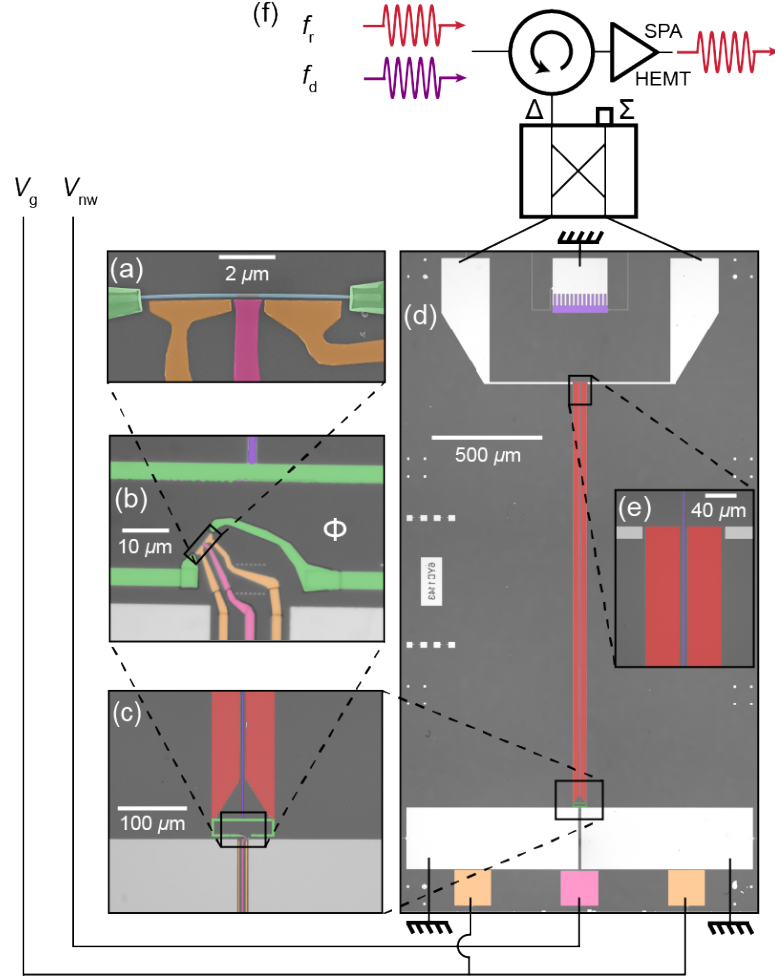


Figure 10.2: The device | (a) An indium arsenide nanowire coated in epitaxial aluminum (blue), with a gap in the aluminum forming the weak link. The cutter gate (pink) was biased to V_C , while the plunger gates (orange) were biased to V_P . The Josephson nanowire was connected to the rest of the circuit using niobium titanium nitride contacts (green). (b/c) Zooming out, we see that the nanowire is embedded in a superconducting loop (green). This loop was used to bias the Josephson nanowire with a flux Φ . In addition, one arm of the loop served as the shared inductance between the nanowire and the resonator (maroon). (d) Full device. The differential $\lambda/4$ mode of the coplanar strip resonator (maroon, frequency $f_r = 9.18843$ GHz, coupling $\kappa_c = 2\pi \times 1.23$ MHz, internal loss $\kappa_i = 2\pi \times 1.00$ MHz) is inductively coupled to the nanowire at its current anti-node (lower end). At its voltage anti-node (upper end), it is capacitively coupled to microstrip lines that lead to the depicted external microwave circuitry. The purple trace that runs between the microwave lines connects to a finger capacitor, serving as a reference for the gates voltages. (f) Both the readout tone (maroon, frequency f_r) and the drive tone (purple, frequency f_d) were routed to the resonator via a 180° hybrid. The reflected readout tone was amplified by an SPA [Frattini et al. 2018] followed by a HEMT, before being processed at room temperature.

To obtain Φ_r , we needed both p and Φ_{zpf} . As stated above, $\Phi_{zpf} = \sqrt{\hbar Z_r/2}$ where Z_r , and we know that for a $\lambda/4$ transmission line resonator we have $Z_r = 4Z_0/\pi = 90 \Omega$,

which is the value quoted above. To estimate p , we calculated the voltage profile along the transmission line [Fig. 10.3(b)]. This is given by

$$V(x) = \operatorname{Re} \left(\frac{e^{i\beta x} + \Gamma_L e^{-i\beta x}}{e^{i\beta \ell} + \Gamma_L e^{-i\beta \ell}} \right) \quad \Gamma_L = \frac{Z_L - Z_0}{Z_L + Z_0} \quad (10.6)$$

The participation ratio is given by $p = V(0) \simeq 0.05$, as quoted above.

We simulated the entire device in Sonnet to check the frequency and tune κ_c . We found that the frequency was 9.1 GHz, close to the value predicted by the transmission line model. Sonnet actually did an incredible job of predicting the measured resonator frequency of 9.2 GHz, properly accounting for the kinetic inductance of the NbTiN. Sonnet also gave us the current profile for the mode, which, while not necessary, is a nice way to visualize the structure of the mode [Fig. 10.3(c)]. Note that we did not include the nanowire in the Sonnet simulations. This is a good approximation so long as the nanowire inductance is large compared to the shared inductance, which is also a necessary condition to avoid flux bias hysteresis.

10.4 Fabrication

The devices had quite a journey before they found their way to our lab at Yale. The nanowires themselves were grown in Copenhagen by Jesper Nygård and Peter Krogstrup [Krogstrup et al. 2015]. The wires were MBE-grown [001] wurtzite indium arsenide nanowires with epitaxial Al coating two of six facets. The nanowires were then shipped, forest style, to the group of Attila Geresdi at TU Delft. Two of Attila's students, David van Woerkom and Daniël Bouman, then fabricated the devices. David fabricated the early iterations, and Daniël the later.

First, the readout resonator and control structures were patterned by electron-beam lithography and reactive ion etching of NbTiN which had been sputtered on the sapphire substrate.⁷ The NbTiN film had a thickness of 150 nm and a sheet kinetic inductance of 0.6 pH/□, which we took into account when calculating the shared inductance between

⁷Earlier iterations were fabricated on silicon substrates which had a thin capping layers of silicon dioxide. However, these devices presented with electrostatic instabilities, so we switched to sapphire.

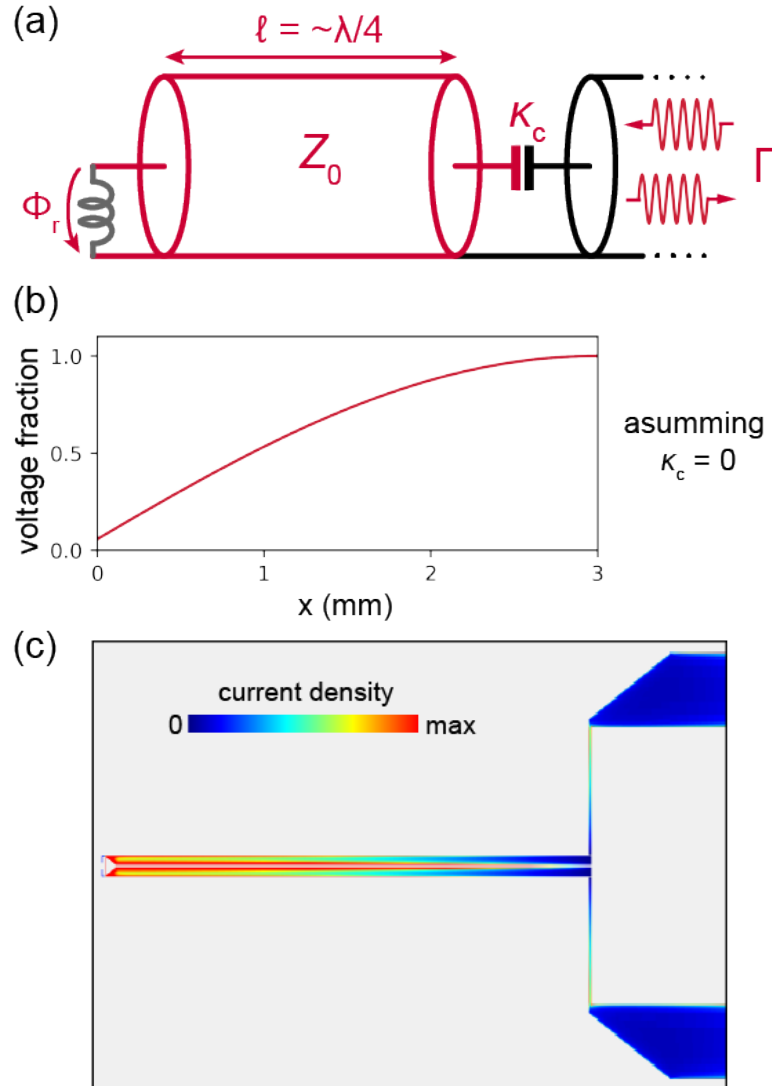


Figure 10.3: Device modeling | (a) Transmission line model of the co-planar strip resonator, shared inductance, and readout transmission line. (b) Calculated voltage profile of the 3 mm resonator, normalized to the voltage anti-node. Here we assume $\kappa_c = 0$ such that we can treat the voltage anti-node as an open. The value at zero position is p , the participation of the shared inductance. (c) Simulated current density using Sonnet Suites. The $\lambda/4$ mode structure has a current anti-node at the right end of the resonator, where the nanowire is coupled.

the nanowire and the resonator as described above. The wires were then deposited using a micromanipulator. Finally, the weak link was defined by selectively wet-etching a 500 nm long section of the Al shell, and contacted to the rest of the circuit using NbTiN.

10.5 Progression

All of the results presented in this thesis were from two batches of devices [Fig. 10.4]. The first batch was used in the Andreev pair qubit experiment [Hays et al. 2018], and the second batch in the Andreev spin qubit experiments [Hays et al. 2020; Hays et al. 2021]. The design didn't change much between these two batches, but we did make an improvement to the resonator/nanowire coupling in the second batch. In the first batch, we used a mutual inductance. However, as a mutual inductance is inherently weaker than a shared inductance, we switched to a shared inductance in the second batch to achieve larger couplings [compare between Fig. 10.4(c/e)]. In the shared case, we can in principle keep cranking up the inductance to achieve stronger couplings. The main constraint is that the shared inductance must be a good bit smaller than the inductance of the nanowire itself. Otherwise, we would enter an RF-SQUID regime that would exhibit hysteretic behavior.

In the first batch, we achieved grounding of the nanowire island via a finger capacitor to the gate ground plane [Fig. 10.4(b)]. In the larger coupling regime of batch 2, however, we found in simulation that this capacitor significantly broke the symmetry of the resonator mode. As such, we switched to the center ground trace as discussed above. We also added two gates on the proximitized section of the nanowire, though we always biased these to the same voltage.

Finally, in batch 1, we supplied the drive via a separate microstrip line [Fig. 10.4(b/c)]. In the atomic point contact experiments [Janvier et al. 2015], the drive had been supplied through the resonator mode. We originally believed this would not work as well for us, as we thought the Andreev transitions could be at higher frequencies, farther away from the resonator mode. This reasoning was incorrect; we forgot about the higher-order modes of the resonator. They make it such that the drive is never attenuated more than ~ 30 dB by the resonator. We thus switched to driving through the resonator in the second batch of devices.

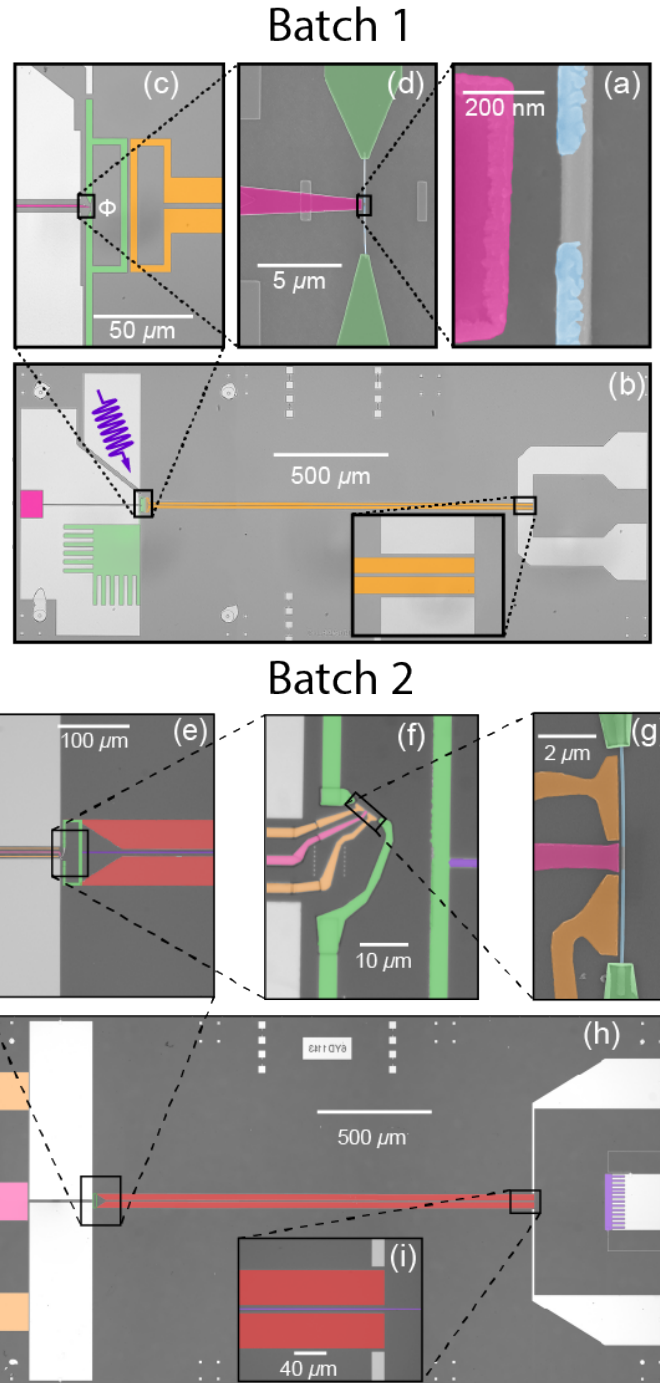


Figure 10.4: Progression of the device design | Comparing the two device designs used in this thesis. Note that colors do not match between the two batches. The central difference between batch 1 and 2 was that we swapped the mutual inductance (c) for a shared inductance (e). This resulted in the need to change our grounding technique, swapping the finger capacitor to the ground plane (green, (b)) for the center ground trace (purple, e). We also switched to driving through the resonator, and removed the separate drive line (b,c).

10.6 Cryogenic setup

Finally, we present the full cryogenic setup for the device [Fig. 10.5]. On the microwave side of things, we used fairly typical attenuation and filtering. We used a directional coupler to couple the drive in after the circulator, as the circulator was only rated from 7 – 10 GHz. The two gate voltage lines were filtered at base using copper powder and RC filters. V_c biased the central “cutter” gate (pink), while both flanking “plunger” gates were biased to V_p (orange).

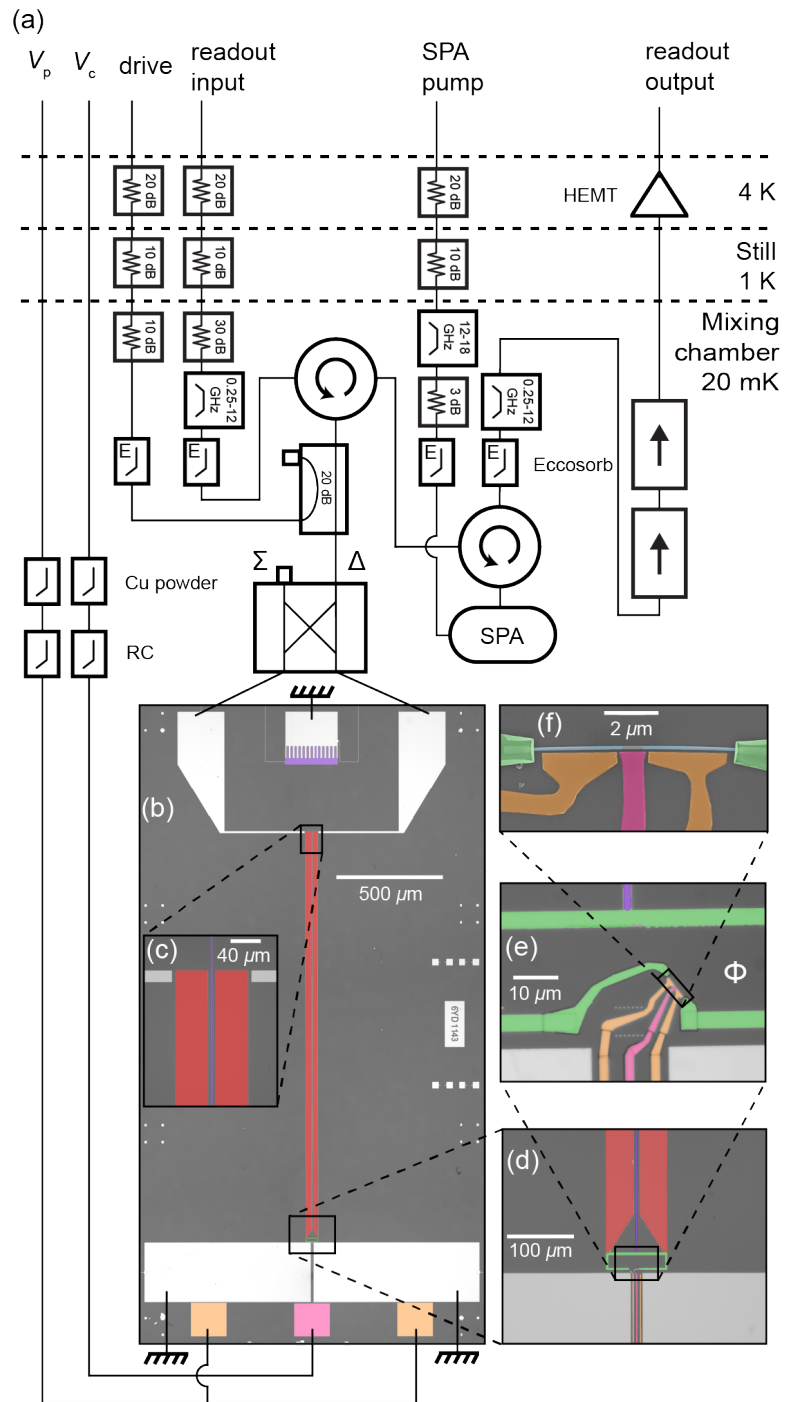


Figure 10.5: Cryogenic wiring diagram and device micrographs for the Andreev spin qubit experiments

References

- Axline, C. J., “Building blocks for modular circuit qed quantum computing”, PhD thesis (Yale University, 2018).
- Frattini, N. E., V. V. Sivak, A. Lingenfelter, S. Shankar, and M. H. Devoret, “Optimizing the nonlinearity and dissipation of a snail parametric amplifier for dynamic range”, *Phys. Rev. Applied* **10**, 054020 (2018).
- Hays, M., V. Fatemi, K. Serniak, D. Bouman, S. Diamond, G. de Lange, P. Krogstrup, J. Nygård, A. Geresdi, and M. Devoret, “Continuous monitoring of a trapped superconducting spin”, *Nature Physics*, 1–5 (2020).
- Hays, M., G. de Lange, K. Serniak, D. van Woerkom, D. Bouman, P. Krogstrup, J. Nygård, A. Geresdi, and M. Devoret, “Direct microwave measurement of Andreev-bound-state dynamics in a semiconductor-nanowire Josephson junction”, *Phys. Rev. Lett.* **121**, 047001 (2018).
- Hays, M., V. Fatemi, D. Bouman, J. Cerrillo, S. Diamond, K. Serniak, T. Connolly, P. Krogstrup, J. Nygård, A. L. Yeyati, A. Geresdi, and M. H. Devoret, “Coherent manipulation of an andreev spin qubit”, *Science* **373**, 430–433 (2021).
- Janvier, C., L. Tosi, L. Bretheau, Ç. Ö. Girit, M. Stern, P. Bertet, P. Joyez, D. Vion, D. Esteve, M. F. Goffman, H. Pothier, and C. Urbina, “Coherent manipulation of Andreev states in superconducting atomic contacts”, *Science* **349**, 1199–1202 (2015).
- Krogstrup, P., N. L. B. Ziino, W. Chang, S. M. Albrecht, M. H. Madsen, E. Johnson, J. Nygård, C. M. Marcus, and T. S. Jespersen, “Epitaxy of semiconductor–superconductor nanowires”, *Nat. Mater.* **14**, 400–406 (2015).

11

Spectroscopy and dispersive shifts

Originally, cQED was developed for state detection of superconducting qubits [Blais et al. 2004; Wallraff et al. 2004]. In this situation, the system of interest (the qubit) was well-understood; it could be accurately modeled as a circuit composed of inductors, capacitors, and Josephson junctions. Nowadays, electromagnetic simulations and room temperature measurements can tell us system parameters (frequencies and couplings) to within 10% even before we cool down. However, cQED can also be used as an exploratory tool; we can use it to probe systems where we *don't* have a complete understanding. Loosely speaking, there are two operators that we can probe when investigating a system with cQED: the Hamiltonian and the coupling operator. We can probe the system Hamiltonian by performing microwave spectroscopy, thereby determining the system energies. Properties of the coupling operator, on the other hand, can be extracted from the dispersive shifts.

In this thesis, we used cQED to investigate the Andreev levels of Josephson nanowires. We now have a decent understanding of how spin-orbit coupling and long junction physics affect the Andreev level spectrum [Tosi et al. 2019]. Furthermore, we have used this level structure to achieve spin-dependent dispersive shifts and Raman processes, enabling the detection and manipulation of the spin of a single quasiparticle. But there is still so much we don't understand. For instance, take a look at how the Andreev levels disperse with the

gate voltage [Fig. 11.1]; there's a lot going on here. Universal conductance fluctuations are causing most of the dispersion, but changing Fermi velocities and other spin-orbit effects are also certainly at play. While we certainly made use of these fluctuations, we made no attempt to rigorously understand them. We simply chose gate voltages where the transition spectrum was not too busy, and where the dispersive shifts were large enough that we had single-shot readout. Often, we also tuned to gate voltage sweet spots to mitigate the effects of electrostatic noise.

Even if we don't understand everything going on in Fig. 11.1, it certainly exemplifies the power of cQED-based two-tone spectroscopy. But two-tone only works because those very same transitions that we see lighting up in Fig. 11.1 are causing dispersive shifts of our readout mode. In this chapter, we will discuss our current understanding of these dispersive shifts, before moving on to extended spectroscopy data.

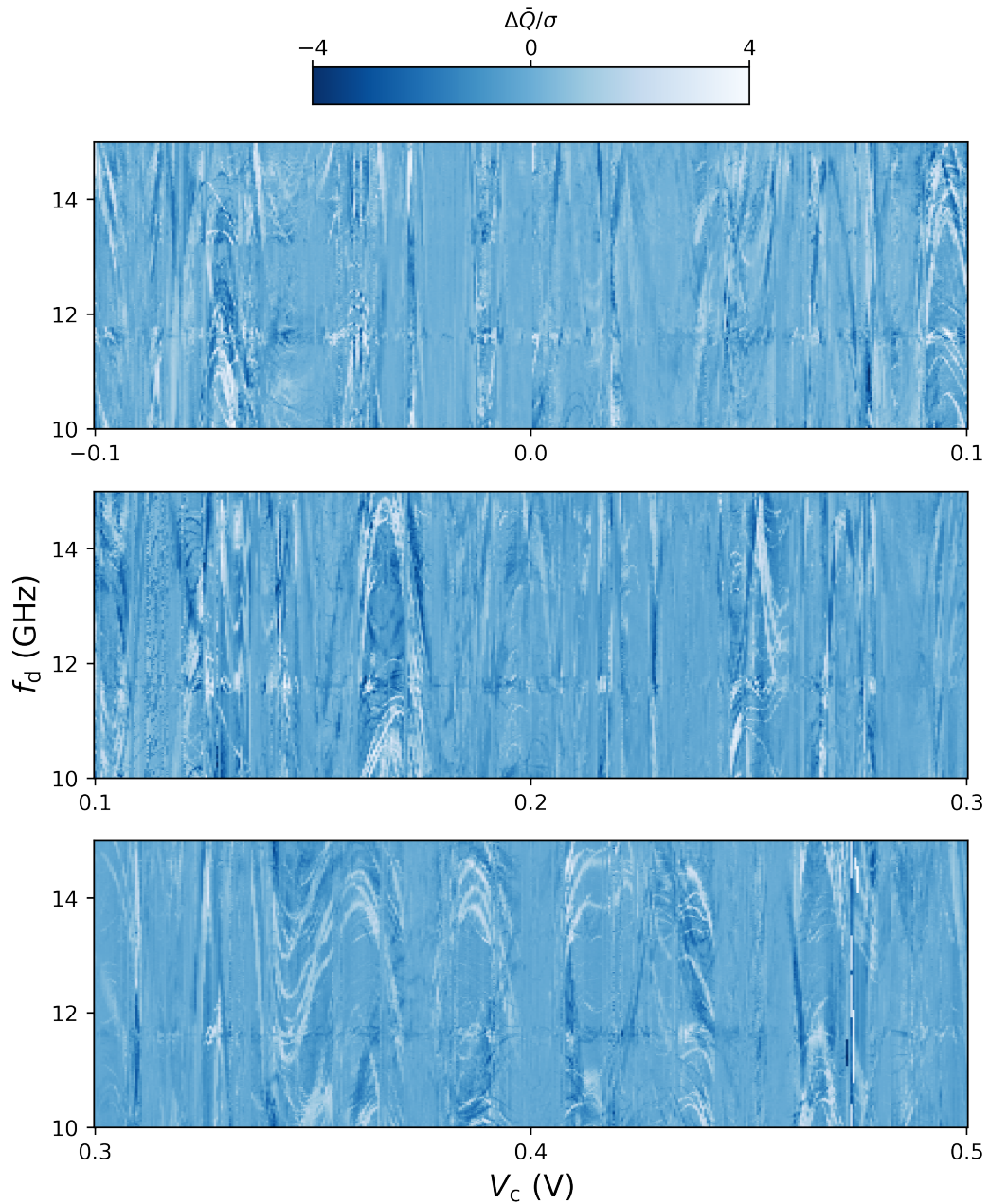


Figure 11.1: Transition spectrum with V_c | We see many transitions moving in and out of the frequency range. What a beautiful mess!

11.1 Andreev level/resonator coupling

In the early years of my PhD, we always assumed that the resonator was coupled to the current operator J_A of the weak link. More recently, we have come to understand that this is not the full story. Nonetheless, the current operator is a good starting point. We designed

these experiments with the current operator in mind, and it got us pretty far.

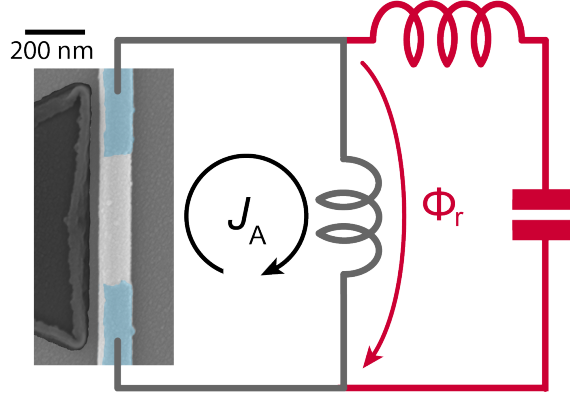


Figure 11.2: Coupling a Josephson nanowire to a superconducting microwave resonator | The Josephson nanowire (scanning electron micrograph) is wired up in parallel with a portion of the resonator's inductance (gray), over which a portion of the resonator's flux drops Φ_r . The quantum-mechanical current J_A created by the Andreev levels flows through the nanowire and around the gray loop, passing through the shared inductance. This results in a coupling term in the Hamiltonian between the resonator and Andreev levels of the form $H_c = \Phi_r J_A$.

As discussed in Chapter 4 and Chapter 10, we coupled the Josephson nanowire to the resonator using an inductive coupling [Fig. 11.2]. This coupling can be seen as arising from the fluctuations of flux $\Phi_r = p\Phi_{zpf}$ induced by the resonator. Assuming Φ_r is small, we can perform an expansion

$$\begin{aligned}
 H &= \hbar\omega_r a^\dagger a + H_A(\Phi + p\Phi_{zpf}(a + a^\dagger)) \\
 &\approx \hbar\omega_r a^\dagger a + H_A(\Phi) + \frac{dH_A}{d\Phi} p\Phi_{zpf}(a + a^\dagger) \\
 &\approx \hbar\omega_r a^\dagger a + H_A(\Phi) + J_A p\Phi_{zpf}(a + a^\dagger)
 \end{aligned} \tag{11.1}$$

where the current operator $J_A = \frac{dH_A}{d\Phi}$.

Our job is then to write down the current operator J_A . This is easier said than done. The problem is that while we can calculate the energy levels and their phase dependence, we don't know the wavefunctions or their phase dependence. The theory exists for the short-junction regime [Zazunov et al. 2003], and for an individual doublet in the long-junction regime [Park and Yeyati 2017], and was finally applied to the multi-doublet long junction regime around the time of this writing [Metzger et al. 2021]. In this section, we will first

discuss the results from the short-junction theory and try to glean some intuition from them. We then present our attempts to model the observed dispersive shifts for a multi-doublet spin-orbit-split weak link, and comment on its short-comings.

11.1.1 The Andreev pair qubit

For the even-parity sector of a short weak link, there are only two possible many-body configurations of the Andreev levels: $|g\rangle$ and $|e\rangle$. Restricting ourselves to the manifold spanned by these states, we can derive the current operator using a phase-independent basis for the Andreev levels [Zazunov et al. 2003]. In this basis, the Hamiltonian for the even manifold is given by

$$H_A = - \begin{pmatrix} 0 & ze^{-ir\varphi/2} \\ z^*e^{ir\varphi/2} & 0 \end{pmatrix} \quad z = \Delta(\cos(\varphi/2) + ir \sin(\varphi/2)) \quad (11.2)$$

As the basis is φ -independent, the current operator is simply the derivative of the matrix elements:

$$J_A = \frac{2\pi}{\Phi_0} \frac{\partial H_A}{\partial d\varphi} = \frac{\pi}{\Phi_0} \begin{pmatrix} 0 & z^* + irze^{-ir\varphi/2} \\ z - irz^*e^{ir\varphi/2} & 0 \end{pmatrix} \quad (11.3)$$

Rotating back to the Andreev basis we have for the Hamiltonian

$$H_A = \epsilon_A \sigma_z(\varphi) \quad \epsilon_A = |z| \quad (11.4)$$

and for the current operator

$$J_A = I_A [\sigma_z(\varphi) + \sqrt{1-\tau} \tan \frac{\varphi}{2} \sigma_y(\varphi)] \quad I_A = \frac{2\pi}{\Phi_0} \frac{d\epsilon_A}{d\varphi} \quad (11.5)$$

where the Pauli matrices are now written in the basis of the Andreev levels, which depends on φ . The coupling term 11.1 is thus

$$H_c = \Phi_r (a + a^\dagger) J_A \rightarrow g_c(\varphi) (a^\dagger \sigma_- + a \sigma_+); \quad g_c(\varphi) = \Phi_r \sqrt{1-\tau} I_A(\varphi) \tan(\varphi/2) \quad (11.6)$$

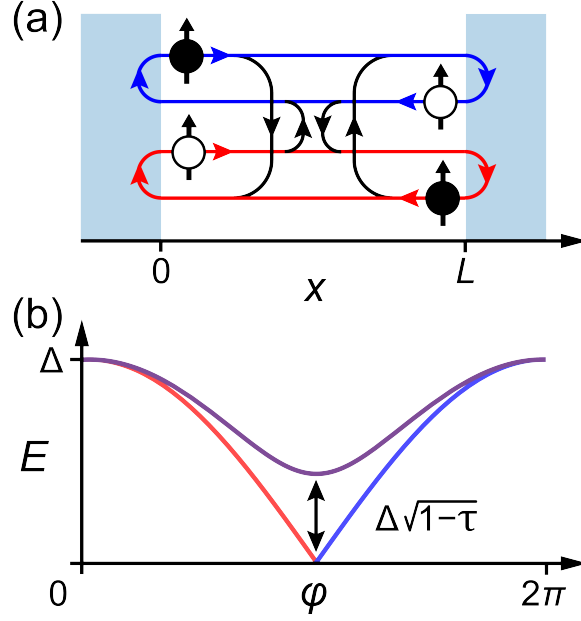


Figure 11.3: The spin-up Andreev level of a short junction | (a) Two loops of electrons and holes are possible, one with electrons moving to the right, and the other with electrons moving to the left. They are coupled by scattering within the normal region (black paths). (b) The Andreev level energy ϵ_A without (red line for $0 < \varphi < \pi$, blue for $\pi < \varphi < 2\pi$) and with (purple line) scattering in the normal region. Scattering induces an avoided crossing of strength $\Delta\sqrt{1-\tau}$.

where we have dropped the diagonal part of the current operator and performed a rotating wave approximations. We thus find the the inductive coupling can be expressed as the Jaynes-Cummings Hamiltonian with a φ -dependent g_c .

It is interesting to note that the eigenvalues of the current operator are not I_A , but rather $\pm(1 - r^2) \sin(\varphi/2)$. While the inclusion of normal reflection has resulted in an avoided crossing between the energy eigenvalues [11.3], the current eigenvalues have only been weakly affected; their eigenvalues have simply been reduced by a factor $(1 - r^2)$. We can gain more intuition by writing down an effective (but slightly hand-wavey) Hamiltonian for the pair qubit around the avoided crossing:

$$H_{\text{eff}} = \Delta \frac{(\varphi - \pi)}{2} \sigma_z + \Delta r \sigma_x \quad (11.7)$$

where the Pauli matrices are now written in the basis of the un-scattered ballistic states. The diagonal components come from expanding the un-scattered energy $\Delta \cos(\varphi/2)$ about

$\varphi = \pi$, and the off-diagonal terms account for scattering to first order in r . If we again compute the current operator as $J_A = \frac{2\pi}{\Phi_0} \frac{\partial H_A}{\partial \varphi}$ and rotate to the energy eigenbasis, we get

$$J_A = I_A \left[\sigma_z(\varphi) - \frac{2\sqrt{1-\tau}}{\varphi - \pi} \sigma_x(\varphi) \right] \quad I_A = \frac{2\pi}{\Phi_0} \frac{d\epsilon_A}{d\varphi} \quad \epsilon_A = \Delta \sqrt{(\varphi - \pi)^2/4 + r^2} \quad (11.8)$$

Note that $\tan \phi/2 \simeq -2/(\varphi - \pi)$. So with this much simplified Hamiltonian, we manage to capture the physics of the current operator around the avoided crossing. We have missed a factor of i such that σ_y has been replaced by σ_x , but as we only care about the magnitude of the off-diagonal elements and not their phase, this is OK. In the next section, we expand this model to the case of long junctions.

11.1.2 Long-junction regime

As we have seen, the Andreev spectrum of a Josephson nanowire can be much more complicated than that of a short weak link. Moreover, while we have theory for the energy spectrum of Josephson nanowires, we don't have a theory of the full microscopic Hamiltonian.¹ As such, we can't compute the full current operator $J_A = \frac{\partial H_A}{\partial \Phi}$, and we can't calculate the dispersive shifts.

In our work on quasiparticle spin detection [Hays et al. 2020], we developed a phenomenological model based on the avoided crossing arguments of the last section. We begin with a model of the Andreev level energies, and then use this to calculate a current operator J_A . Finally, we outline a calculation of $p\Phi_{zpf}$, which acts as a scale factor on the dispersive shift.

Model of the Andreev levels

In Chapter 8, we found that, for $E \ll \Delta$, the Andreev spectrum of a disorder-free, long weak link is given by

$$E_n = \pm \frac{\Delta \hbar v_F / L}{2(\Delta + \hbar v_F / L)} (\varphi - \pi(2n + 1)) \quad (11.9)$$

¹This is not to say it can't be calculated, it just hasn't been done yet.

We also saw that the due to spin-orbit coupling, the Fermi velocity can become spin- and momentum-dependent, such that some Andreev levels are built of slow-moving charge carriers with Fermi velocity v_1 and some are built of charge carriers with fast velocity v_2 . The slopes of the linearly dispersing Andreev levels are thus modified. Labeling these slopes m_1 and m_2 , we constructed the phenomenological Hamiltonian to treat the two-doublet situation necessary for our realization of the Andreev spin qubit. We label the four linearly-dispersing states as $|\uparrow_+\rangle$ (slope m_2), $|\uparrow_-\rangle$ (slope $-m_1$), $|\downarrow_+\rangle$ (slope m_1), and $|\downarrow_-\rangle$ (slope $-m_2$). Then we include disorder between like spins via a phenomenological parameter r , such that the Hamiltonian is

$$H_A(\Phi) = \frac{1}{\Phi_0} \begin{bmatrix} +m_2(\Phi + \Phi_{\text{cross}}) & r & 0 & 0 \\ r & -m_1(\Phi + \Phi_{\text{cross}}) & 0 & 0 \\ 0 & 0 & +m_1(\Phi - \Phi_{\text{cross}}) & r \\ 0 & 0 & r & -m_2(\Phi - \Phi_{\text{cross}}) \end{bmatrix} \quad (11.10)$$

Here Φ_{cross} is the flux at which the levels cross. between states of like spin. Note that we have ignored an overall offset of the levels within the gap such that the levels cross at zero energy. Diagonalizing this Hamiltonian gives the four Andreev levels $|\downarrow_q\rangle, |\uparrow_q\rangle, |\uparrow_a\rangle$ and $|\downarrow_a\rangle$ and the transition frequencies between them $f_{s,s'}$. Note that these transition frequencies over-constrain the model; i.e. the fourth $f_{s,s'}$ follows when the other three are known. The measured values $f_{s,s'}$ thus completely determine the phenomenological parameters that define the Hamiltonian. By fitting the spectrum [Fig. 11.4], we find $m_2 = h \times 22.6$ GHz, $m_1 = h \times 21.4$ GHz, $\Phi_{\text{cross}} = 0.055\Phi_0$, and $r = h \times 7.6$ GHz. Note that $\pm\Phi_{\text{cross}}$ is also the flux point where the frequencies of the spin-conserving transitions are minimum.

Model of the junction/resonator coupling

As we have discussed, the junction and the resonator are coupled because a fraction p of the resonator flux $\Phi_{\text{zpf}}(a + a^\dagger)$ drops over the junction. Above, we explained this coupling by performing an expansion to first-order in Φ_{zpf} , but now let's take it one more order out:

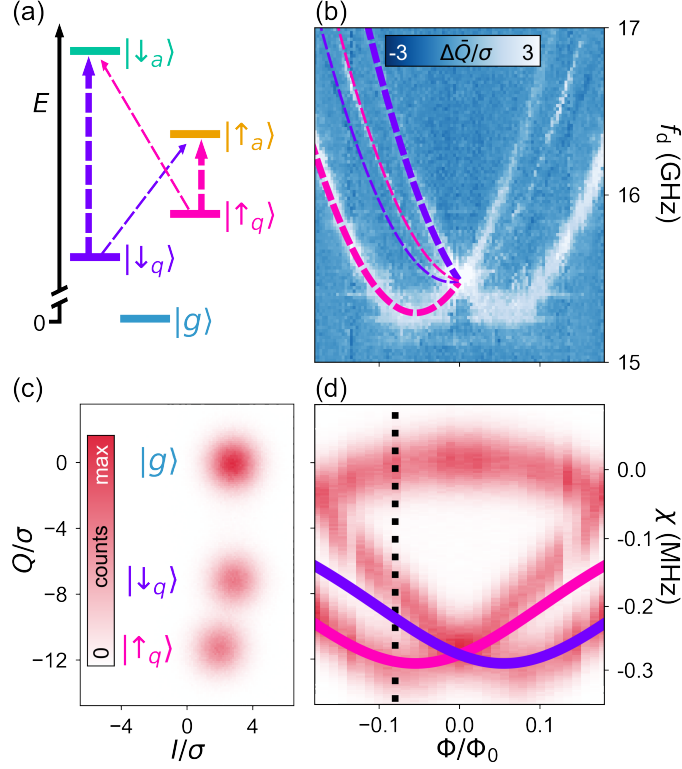


Figure 11.4: Dispersive readout and spectroscopy of a trapped quasiparticle | (a) Level structure and transitions out of the lower doublet for $\Phi < 0$. (b) Measured histogram of Γ/σ , where σ is the standard deviation of one distribution. The data cluster into three distributions, corresponding to $|g\rangle$, $|\downarrow_q\rangle$, and $|\uparrow_q\rangle$. (c) Drive-probe spectroscopy of the nanowire reveals the four transitions depicted in (a), with fits to a simple model plotted for $\Phi < 0$. (d) The distributions shown in (b) shift with Φ as the detuning between the quasiparticle transitions and the resonator varies, from which the absolute dispersive shift (right axis) can be determined. Dashed line indicates Φ for data in (b), and colored curves are predictions based on the extracted model parameters in (c) with only one additional free parameter (see text), which captures the scale and shape of the behavior.

$$\begin{aligned}
H &= \hbar\omega_r a^\dagger a + H_A(\Phi + p\Phi_{\text{zpf}}(a + a^\dagger)) \\
&\approx \hbar\omega_r a^\dagger a + H_A(\Phi) + \frac{dH_A}{d\Phi} p\Phi_{\text{zpf}}(a + a^\dagger) + \frac{1}{2} \frac{d^2 H_A}{d\Phi^2} (p\Phi_{\text{zpf}})^2 (a + a^\dagger)^2 + \dots \quad (11.11) \\
&\approx \hbar\omega_r a^\dagger a + H_A(\Phi) + J_A p\Phi_{\text{zpf}}(a + a^\dagger) + \mathcal{C}_A (p\Phi_{\text{zpf}})^2 a^\dagger a + \dots
\end{aligned}$$

where in the last step we have performed a rotating wave approximation. We thus find that the resonator flux couples to the junction current operator $J_A = \frac{dH_A}{d\Phi}$ at first order in $p\Phi_{\text{zpf}}$ and to the inverse inductance operator $\mathcal{C}_A = \frac{d^2 H_A}{d\Phi^2}$ at second order. We now consider

only the first-order coupling, and compute J_A from our model H_A :

$$J_A = \frac{dH_A}{d\Phi} = \frac{1}{\Phi_0} \begin{bmatrix} +m_1 & 0 & 0 & 0 \\ 0 & -m_2 & 0 & 0 \\ 0 & 0 & +m_2 & 0 \\ 0 & 0 & 0 & -m_1 \end{bmatrix} \quad (11.12)$$

The dispersive shifts χ_s of the two qubits states $|\downarrow_q\rangle, |\uparrow_q\rangle$ can then be computed at second order in perturbation theory [Manucharyan 2012]

$$\chi_s = -\frac{(p \Phi_{\text{zpf}})^2}{2\pi\hbar^2} \sum_{s'} \frac{2f_{ss'} |\langle s'_a | J_A | s_q \rangle|^2}{f_{ss'}^2 - f_r^2} \quad (11.13)$$

In the basis of the linearly-dispersing levels, J_A is diagonal while H_A is not. However, the only off-diagonal elements in H_A are between states of the same spin. As such, J_A remains block-diagonal in spin when written in the energy eigenbasis (which we do not do explicitly here). The matrix elements connecting different spins $\langle \bar{s}_a | J_A | s_q \rangle$ are thus zero and only the inter-doublet spin-conserving transitions contribute to the dispersive shift:

$$\chi_{\downarrow} \cong -\frac{(p \Phi_{\text{zpf}})^2}{2\pi\hbar^2} \frac{2f_{\downarrow\downarrow}}{f_{\downarrow\downarrow}^2 - f_r^2} |\langle \downarrow_a | J_A | \downarrow_q \rangle|^2 \quad \chi_{\uparrow} \cong -\frac{(p \Phi_{\text{zpf}})^2}{2\pi\hbar^2} \frac{2f_{\uparrow\uparrow}}{f_{\uparrow\uparrow}^2 - f_r^2} |\langle \uparrow_a | J_A | \uparrow_q \rangle|^2 \quad (11.14)$$

As discussed in the previous section, the parameters defining H_A (and therefore J) were inferred from the measured spectrum [Fig. 11.4(c)]. This allowed us to calculate the Φ -dependent matrix elements $\langle s_a | J_A | s_q \rangle$, and therefore the Φ -dependence of χ_s . We found that a value of $p\Phi_{\text{zpf}}/\Phi_0 = 1.70 \times 10^{-3}$, which is within 10% of an independent calculation (see Chapter 10), matched the data well in the vicinity of Φ_{cross} . The coupling strength $g_{c,s} = \frac{p\Phi_{\text{zpf}}}{\hbar} |\langle s_a | J_A | s_q \rangle|$ is plotted in Fig. 11.5. As expected, the coupling is peaked around Φ_{cross} where the mixing between the levels is strongest.

Finally, to translate the predicted χ_s to the resonator response, we used the scattering

formula for a resonator measured in reflection [Axline 2018]:

$$S_s = \frac{\omega_{\text{ro}} - (\omega_r + \chi_s) + i(\kappa_c - \kappa_i)/2}{\omega_{\text{ro}} - (\omega_r + \chi_s) - i(\kappa_c + \kappa_i)/2} \quad (11.15)$$

where $\omega_{\text{ro}} = 2\pi \times 9188.47$ MHz is the readout frequency. After multiplying by a constant complex scale factor to account for the amplitude and phase of our signal $\Gamma_s = Ae^{i\phi}S_s$, taking the imaginary part gave Q_s as plotted in Fig. 11.4(d), and again in Fig. 11.5(b). Additionally in Fig. 11.5(b), we plot the expected Φ -dependence of the distributions assuming $g_{c,s}$ remains constant at the maximum value of $2\pi \times 37.4$ MHz (dotted lines). In this case, the dispersive shift has much less Φ -dependence than what is measured. This illustrates the necessity of using the Φ -dependent $g_{c,s}$ as calculated from our model of J_A .

We now return to the inverse inductance \mathcal{C}_A . In the original expansion, we saw that the resonator and junction were coupled at first order in J_A and second order in \mathcal{C}_A . However, because the current coupling is via the off-diagonal elements $\langle s_a | J_A | s_q \rangle$, the dispersive shift is second order in $p\Phi_{\text{zpf}}$. On the other hand, the inverse inductance may induce frequency shifts through its diagonal elements: $\frac{(p\Phi_{\text{zpf}})^2}{\hbar} \langle s_q | \mathcal{C}_A | s_q \rangle$. Thus, both coupling terms contribute frequency shifts at second order in $p\Phi_{\text{zpf}}$. Although within our simple model $\mathcal{C}_A = 0$, in reality the full junction Hamiltonian is needed to calculate both J_A and \mathcal{C}_A . It is worth noting that in the short junction case where we do have theory, the value of the inverse inductance computed from $\langle g | \mathcal{C}_A | g \rangle$ can be much smaller than what one might expect from the Φ -dispersion of ϵ_A . Moreover, while we anticipate that the dispersive shift due to \mathcal{C}_A around $\Phi = 0$ should be negative, the shift around $\Phi = -0.5\Phi_0$ should be positive and of similar magnitude. In contrast, the shifts due to the current coupling should always be negative so long as $f_{s,s'} > f_r$. We only observe negative frequency shifts over the entire Φ range [Fig. 11.6], which we interpret as the current coupling being dominant. In general, a more advanced theory should be applied to understand the full flux dependence and dispersive shifts. Around the time of this writing, such a theory was developed and experimentally validated [Metzger et al. 2021].

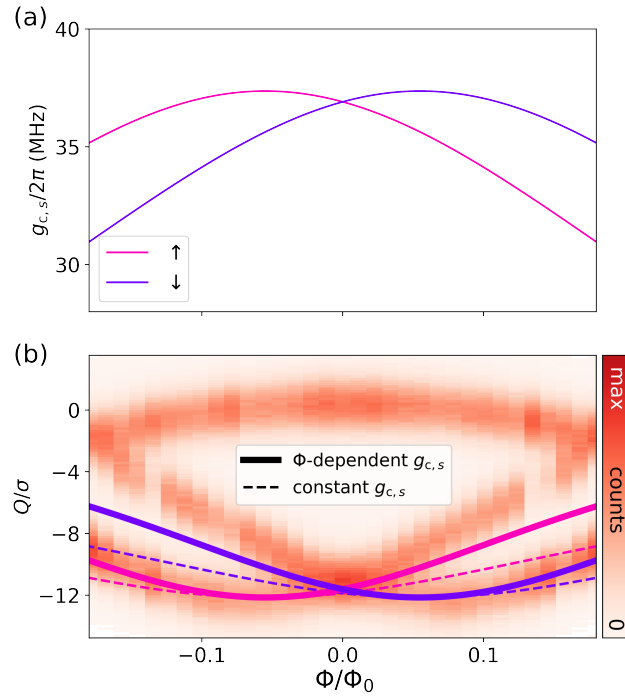


Figure 11.5: Φ -dependence of g_c | (a) Extracted coupling strengths $g_{c,s}$ for the two inter-doublet spin conserving transitions. The peaks coincide with the minimum frequency of the transitions ($\Phi = \pm\Phi_{\text{cross}}$) because this is where the mixing between current and energy eigenstates is strongest (see Supplementary Information). (b) Same data as shown in Fig. 11.4(d). Solid lines are the predicted $\chi_{s,1}$ as in the main text, and dashed lines are the $\chi_{s,1}$ if $g_{c,s}$ is assumed to be constant at its maximum value.

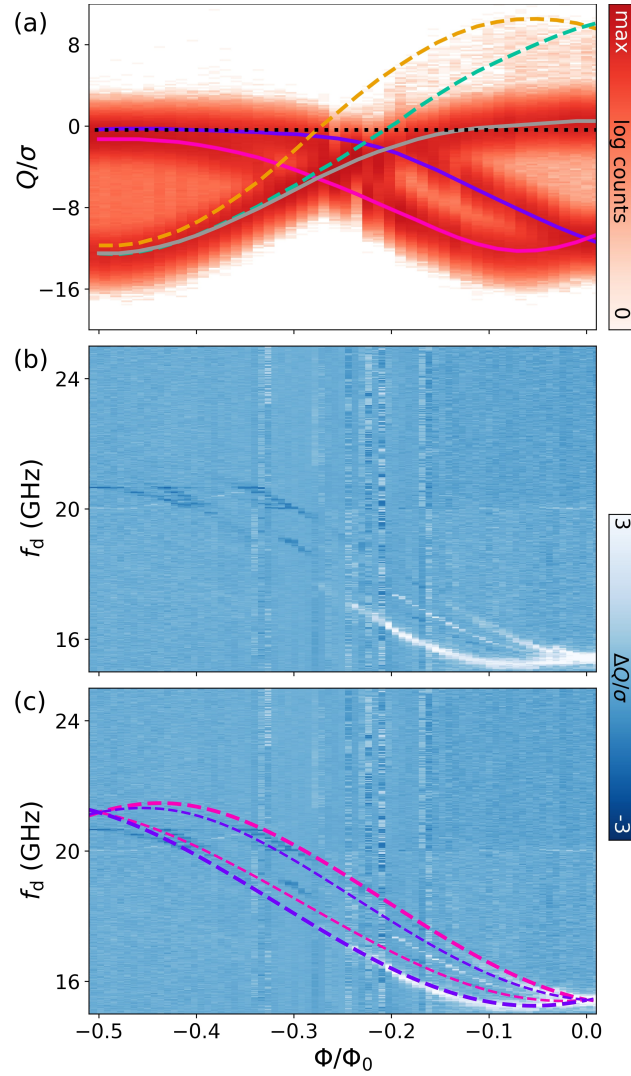


Figure 11.6: Spectroscopy and dispersive shifts over a full half flux quantum | (a) Φ -dependence of Q over a full half flux quantum. The $|\downarrow_q\rangle$ and $|\uparrow_q\rangle$ distributions (traced with purple and pink splines respectively) remain below the bare resonator Q (black dotted line) over the full Φ range, indicating negative dispersive shifts which are inconsistent with χ resulting from coupling to the inverse inductance operator. The dispersive shift of $|g\rangle$ (traced with the gray spline) is likely due to a pair transition with frequency above our measurement bandwidth. We also observe a small number of counts around $\Phi = 0$ at positive Q , indicating a residual quasiparticle population in $|\uparrow_a\rangle$ and $|\downarrow_a\rangle$. Assuming the observed dispersive shift of $|g\rangle$ is due only to the properties of the lower doublet, the dispersive shift of a quasiparticle in the upper doublet should be given by $\chi_{s,a} = -\chi_{s,q} + \chi_g$. Based on this formula and the plotted splines, we estimated the Φ -dependence of the $|\downarrow_a\rangle$ and $|\uparrow_a\rangle$ distributions (dashed, teal, and yellow). The predictions track roughly with the residual counts in the vicinity of $\Phi = 0$ before crossing the bare resonator Q . (b) Spectroscopy over the same flux range. We attribute the sign change in the measured $\Delta\bar{Q}$ to the crossings of χ_{s_1} with χ_{s_2} indicated in (a).

Dispersive shifts in the presence of resonator crossings

Mainly to give a flavor of how the dispersive shifts can vary qualitatively, we present some spectroscopy and dispersive shift data in the presence of resonator crossings [Fig. 11.7]. This data was taken on a different device (6YD1122). In two-tone spectroscopy, we observe two bundles of single-particle transitions, a pair transition coming down to ~ 5 GHz at $\Phi = \Phi_0/2$, and some other pair-like transitions at higher frequency that I believe are due to mystery levels (see Chapter 14). Where the pair transition crosses the resonator (frequency ~ 9 GHz), we observe divergences in χ which we fit to a Jaynes-Cummings model. Other features, likely associated with single-particle states, are observed at $\Phi = \Phi_0/2$.

11.2 Extended spectroscopy

11.2.1 Comparing spin-flipping/-conserving single particle transitions

In section 11.1.2 and in Ref. [Hays et al. 2020] in general, we explored a gate-bias point where the spin-conserving single particle transitions were much brighter than the spin-flipping ones. However, we did not find this to be a generic feature of all gate-bias points [Fig. 11.8]. Indeed, in Ref. [Hays et al. 2021] it was critical that all transitions be bright. We now understand that this has to do with a broken mirror symmetry. When the nanowire has a mirror symmetry, we do not expect spin-flipping single particle transitions. When this symmetry is broken, so long as spin and orbital degrees of freedom are suitably entangled, all transitions will be bright. In fact, it is even possible for the spin-flipping transitions to be brighter, as in Fig. 11.8(c)]. Near half flux, fainter features are also visible. The faint feature at $\chi \sim -3$ MHz has qualitative properties characteristic of spin-orbit split levels.

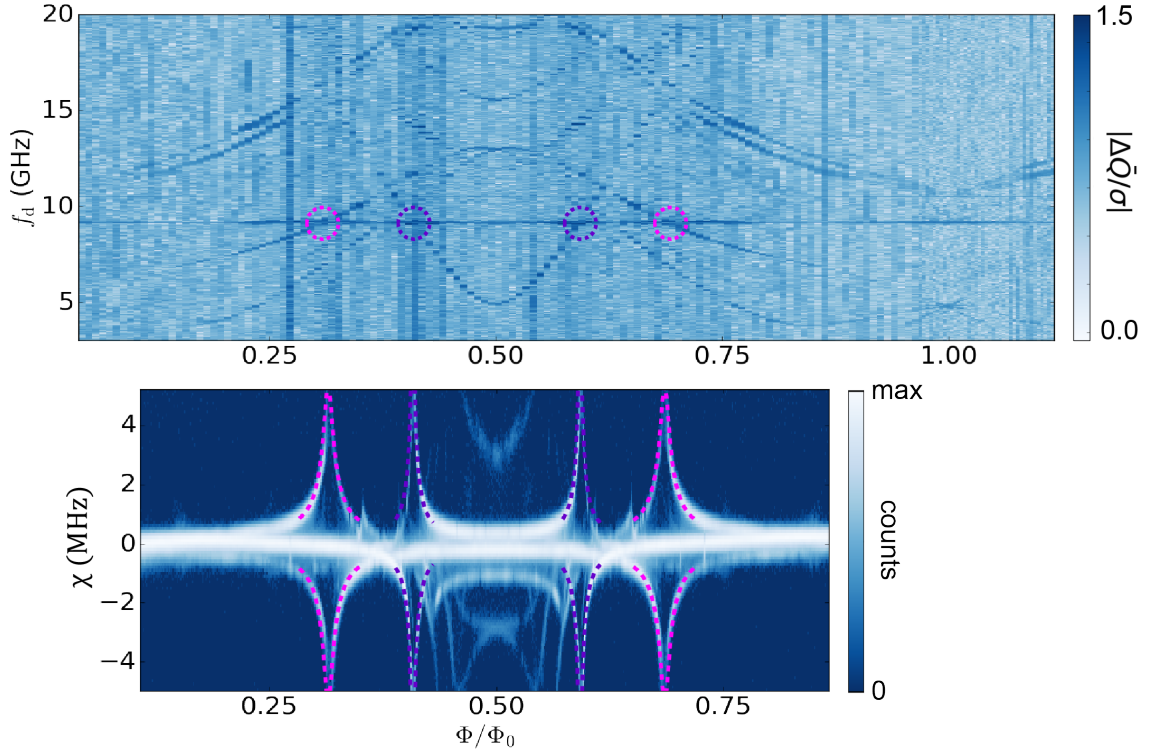


Figure 11.7: Spectroscopy and dispersive shifts in the presence of resonator crossings | Upper panel: two-tone spectroscopy versus Φ of device 6YD1122 at $V_c = 0.953$ V. Two bundles of single-particle transitions are observed, a pair transition that dips down to ~ 5 GHz at $\Phi = \Phi_0/2$, and higher-frequency pair-like transitions that likely involve mystery levels. Crossings with the resonator mode (flat line around 9 GHz) are marked in purple (pair transition) and pink (brightest single-particle transition). Lower panel: dispersive shift χ over a portion of the same Φ range. The strongest divergences are observed where the brightest single-particle transition and the pair transition cross the resonator. Fitting these divergences using a Jaynes-Cummings model using an estimate of \bar{n} as well as the measured Φ -dependence of the transitions give $g_c/2\pi = 25$ MHz for the single-particle transition at the crossing point and $g_c/2\pi = 35$ MHz for the pair transition.

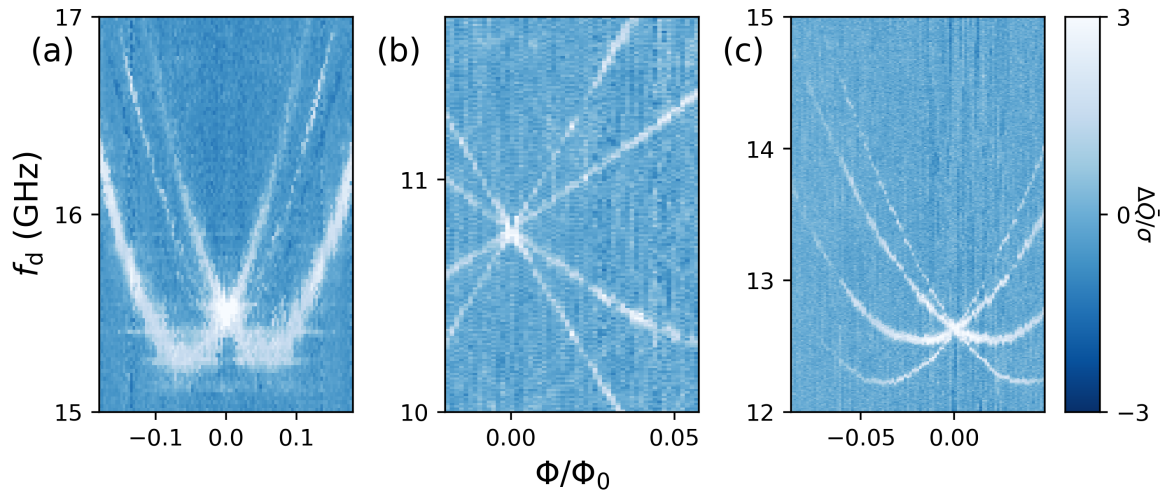


Figure 11.8: Comparing transitions brightness | Spectroscopy of single-particle transitions at several gate-voltage bias points. (a) $V_c = -1.36$ V, $V_p = 0.9$ V (b) $V_c = 23$ mV, $V_p = 0$ mV (c) $V_c = -214$ mV, $V_p = -30$ mV

What is the difference between these gate bias points? One possible explanation is that the gate is adjusting the extent to which spin and motional degrees of freedom are entangled. For instance, maximal entanglement would be achieved in the model of Fig. 8.5 if the chemical potential was tuned to the avoided crossing between the two sub-bands. While this may indeed be what's happening, as of yet we haven't done a systematic study of spin-flipping transition brightness versus voltage.

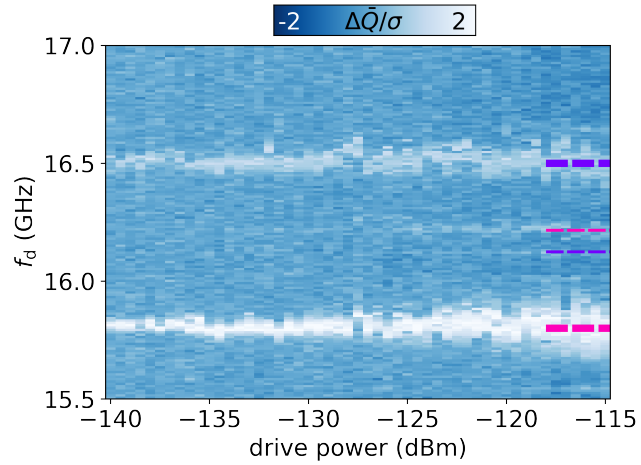


Figure 11.9: Brightness of the four inter-doublet transitions of 11.8(a) as a function of estimated drive power at the device | At low powers, only the spin-conserving transitions are visible, but as the power is increased the spin-flipping transitions also appear. Note that the spin-flipping transitions at the maximum power (-115 dBm) are still substantially dimmer than the spin-preserving transitions at the lowest power (-140 dBm).

11.2.2 Zeeman splitting of single-particle transitions

To perform a measurement of the Andreev levels in a Zeeman field, we used the same coil that we used to apply Φ . We simply measured the spectrum at $\Phi \simeq 414\Phi_0$. Converting this flux to a magnetic field using the device loop area of $2250 \mu\text{m}^2$ gives $380 \mu\text{T}$. In this way, we could measure the effect of a Zeeman field applied perpendicular to the plane of the device [Fig. 11.10]. We modeled the spectrum using the same approach as described in 11.1.2, but with an additional Zeeman-like term such that the spin-up states were shifted by $+E_Z$ and the spin-down states were shifted by $-E_Z$. Note that within this model, only the spin-flipping transitions are affected by E_Z . We found that $E_Z \approx h \times 35 \text{ MHz}$ qualitatively described the data, which corresponds to a shift in the $|\downarrow_q\rangle/|\uparrow_q\rangle$ degeneracy point to $\varphi = 2\pi \times 0.013$. For a more sophisticated treatment of the effects of magnetic field on the spectrum of Josephson nanowires, see Tosi et al. 2019.

We were unable to perform a more systematic investigation with magnetic field because, at these large coil currents ($\sim 30 \text{ mA}$), the spectrum wasn't very stable. It was pointed out by Cristian Urbina and Hugues Pothier that this was likely due to vortex dynamics in the resonator.

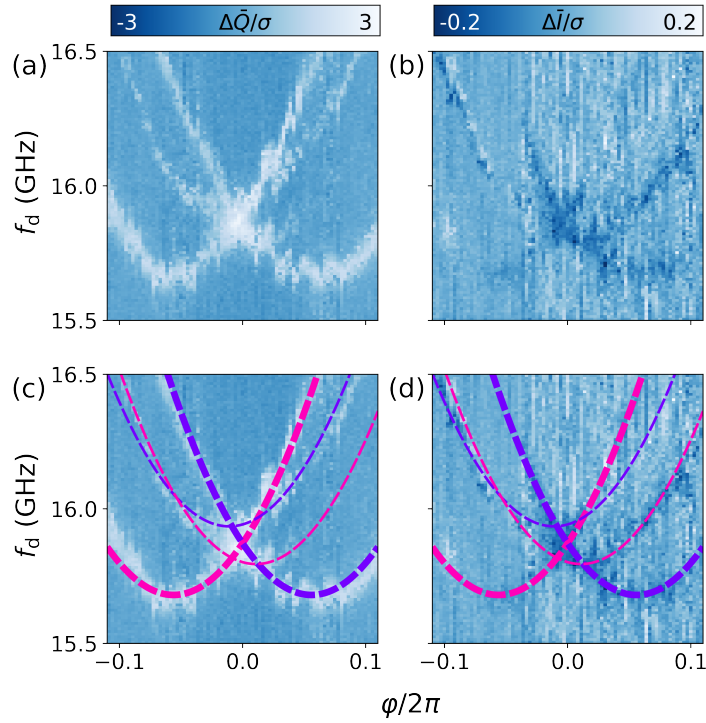


Figure 11.10: Spectroscopy at $B_{\perp} = 380 \mu\text{T}$ | Here we plot both I (a) and Q (b) to present information in both quadratures. The observed instabilities varied with time, and occurred when operating our flux coil at high current. The same data is plotted in (c)/(d), but with overlaid fits. We describe the data by the model described in 11.1.2 but we include an additional Zeeman-like term.

11.2.3 Other observations

+/- pattern of single-particle transitions

A feature that we occasionally observed was that, when all four inter-doublet transitions were bright, the transitions out of $|\uparrow_q\rangle$ (the first and third lowest-frequency) manifested as positive changes in \bar{Q} , while the transitions out of $|\downarrow_q\rangle$ (the second and fourth lowest-frequency) manifested as negative changes. Several examples of this can be seen in Fig. 11.11. We never explored this in detail, but a potential explanation is sketched out in panel (d). If we're constantly driving population out of one spin state which then decays back to both, the net result will be population flow from the initial spin state to the other spin state. For $|\downarrow_q\rangle$, this means a negative change in $\Delta\bar{Q}$ ($|\uparrow_q\rangle$ is below $|\downarrow_q\rangle$ in the IQ -plane), and vice versa for $|\uparrow_q\rangle$. This spin-mixing decay would be consistent with the observation

that all four transitions are bright. I don't think I've ever noticed a situation where only the spin-preserving transitions are visible, but one has negative $\Delta\bar{Q}$ and the other positive.

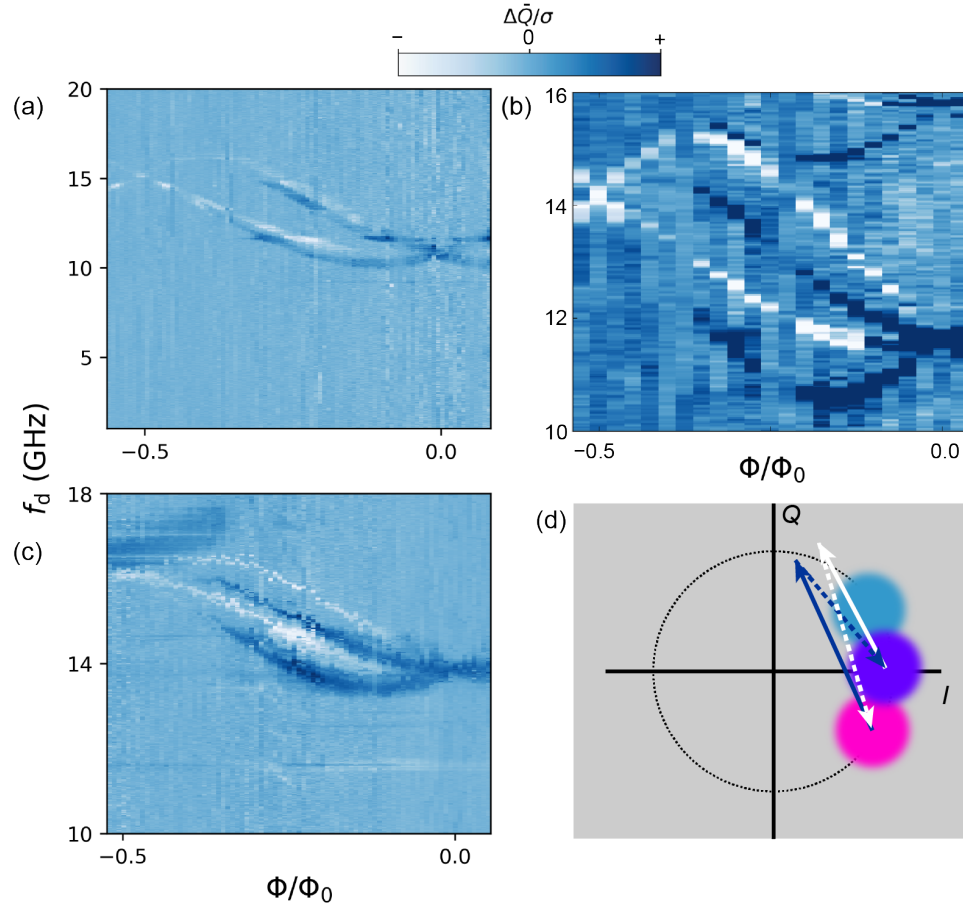


Figure 11.11: $+/-$ pattern in spectroscopy | (a-c) We occasionally observed that the four inter-doublet transitions had alternating $+/-$ signs of $\Delta\bar{Q}$. (d) A potential explanation: population driven out of $|\uparrow_q\rangle$ ($|\downarrow_q\rangle$) decays back partially to $|\downarrow_q\rangle$ ($|\uparrow_q\rangle$), resulting in positive (negative) $\Delta\bar{Q}$.

Miscellaneous transition spectra

As we saw in the spectroscopy of the Andreev levels versus gate voltage [Fig. 11.1], things can get quite messy. We can have nice clean spectra where we see a single bundle of single-particle transitions and a pair transition as in panel (a), (though the pair transition might actually be a two-photon process here). But things can vary a lot. We can have two sets of single-particle transitions close in frequency [panel (b)]. The dispersion of the single-particle bundles can vary strongly, and we can have a mess of pair transitions [panel (c)].

Panel (d) shows a bundle of single-particle transitions where the spin-flipping transitions are completely suppressed, and the $|\uparrow_q\rangle \leftrightarrow |\uparrow_a\rangle$ transition dips down to very low frequencies. In panel (e) we have some funny features flanking the pair transition above/below. Panel (f) shows a pair transition accompanied by a multi-photon feature, and a *hint* of a low-frequency feature that is symmetric about zero flux (marked by white circles). Hopefully, one day we can have a more detailed understanding of all of this variety.

References

- Axline, C. J., “Building blocks for modular circuit qed quantum computing”, PhD thesis (Yale University, 2018).
- Blais, A., R.-S. Huang, A. Wallraff, S. M. Girvin, and R. J. Schoelkopf, “Cavity quantum electrodynamics for superconducting electrical circuits: an architecture for quantum computation”, *Phys. Rev. A* **69**, 062320 (2004).
- Hays, M., V. Fatemi, K. Serniak, D. Bouman, S. Diamond, G. de Lange, P. Krogstrup, J. Nygård, A. Geresdi, and M. Devoret, “Continuous monitoring of a trapped superconducting spin”, *Nature Physics*, 1–5 (2020).
- Hays, M., V. Fatemi, D. Bouman, J. Cerrillo, S. Diamond, K. Serniak, T. Connolly, P. Krogstrup, J. Nygård, A. L. Yeyati, A. Geresdi, and M. H. Devoret, “Coherent manipulation of an andreev spin qubit”, *Science* **373**, 430–433 (2021).
- Manucharyan, V. E., “Superinductance.”, PhD thesis (Yale University, 2012).
- Metzger, C., S. Park, L. Tosi, C. Janvier, A. A. Reynoso, M. F. Goffman, C. Urbina, A. Levy Yeyati, and H. Pothier, “Circuit-qed with phase-biased josephson weak links”, *Phys. Rev. Research* **3**, 013036 (2021).
- Park, S. and A. L. Yeyati, “Andreev spin qubits in multichannel rashba nanowires”, *Phys. Rev. B* **96**, 125416 (2017).
- Tosi, L., C. Metzger, M. Goffman, C. Urbina, H. Pothier, S. Park, A. L. Yeyati, J. Nygård, and P. Krogstrup, “Spin-orbit splitting of Andreev states revealed by microwave spectroscopy”, *Phys. Rev. X* **9**, 011010 (2019).

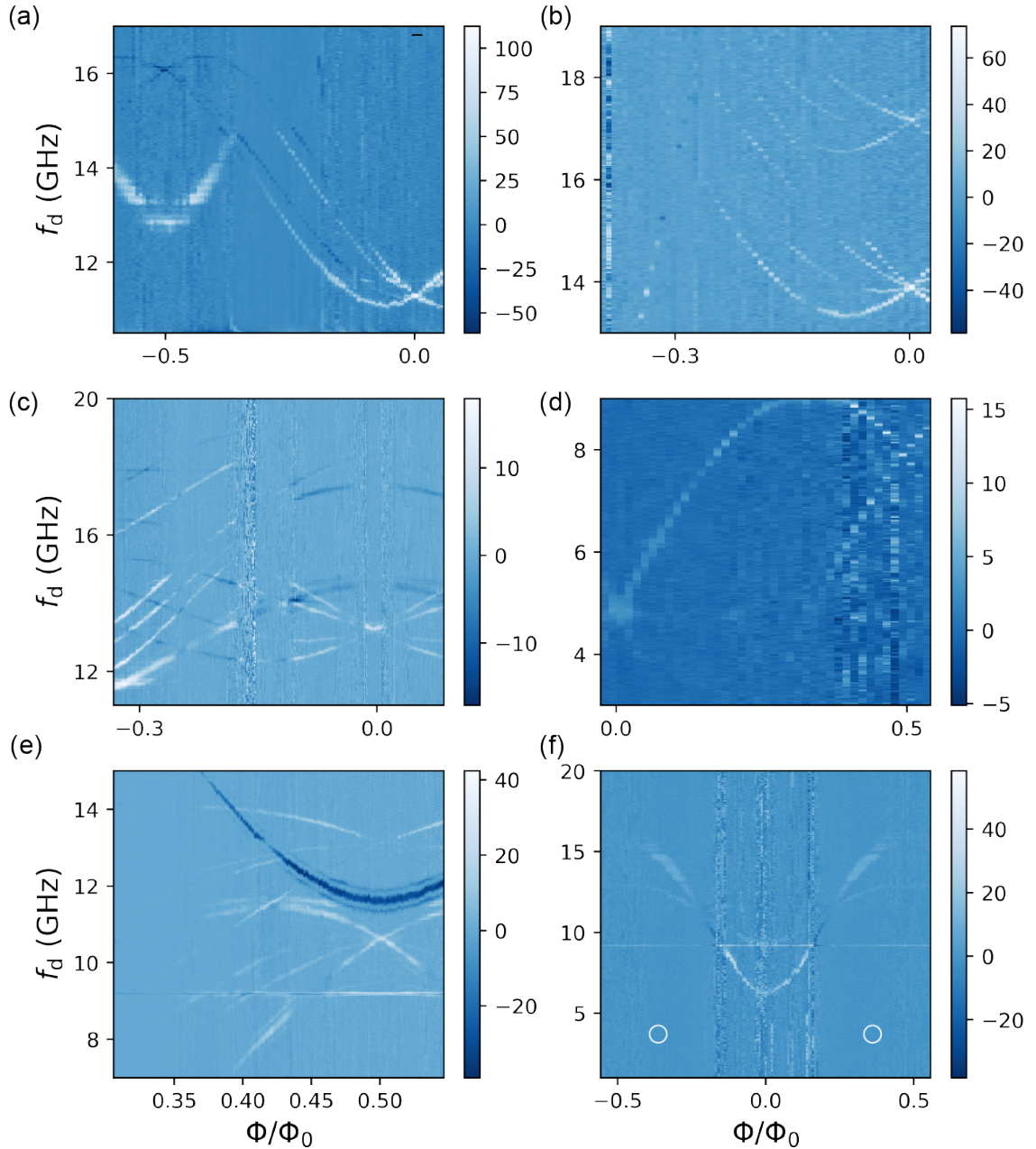


Figure 11.12: Miscellaneous transition spectra | Color is un-normalized $\Delta\bar{Q}$, sorry Michel!

Wallraff, A., D. I. Schuster, A. Blais, L. Frunzio, R.-S. Huang, J. Majer, S. Kumar, S. M. Girvin, and R. J. Schoelkopf, “Strong coupling of a single photon to a superconducting qubit using circuit quantum electrodynamics”, *Nature* **431**, 162–167 (2004).

Zazunov, A., V. Shumeiko, E. Bratus, J. Lantz, and G. Wendin, “Andreev level qubit”, *Phys. Rev. Lett.* **90**, 087003 (2003).

12

Raman transitions of the quasiparticle spin

In this chapter, we first present the theory of Raman transitions in the context of Andreev levels in Josephson nanowires. We then present detailed spectroscopy of Raman transitions, before discussing the measurement and simulation of quasiparticle spin manipulation. Special thanks to Javier Cerrillo for his help with the Raman Rabi simulations.

12.1 Theory of Raman transitions

In this section, we have set $\hbar = 1$.

Setting up the Λ system

To begin with, let's suppose there are only three Andreev levels of interest: $|\downarrow_q\rangle$, $|\uparrow_q\rangle$ and $|\uparrow_a\rangle$ [Fig. 12.1(a)]. The undriven Hamiltonian is given by

$$H_A = E_{\downarrow,q}|\downarrow_q\rangle\langle\downarrow_q| + E_{\uparrow,q}|\uparrow_q\rangle\langle\uparrow_q| + E_{\uparrow,a}|\uparrow_a\rangle\langle\uparrow_a| \quad (12.1)$$

Our goal is to drive transitions between $|\downarrow_q\rangle$ and $|\uparrow_q\rangle$ using $|\uparrow_a\rangle$ as an auxiliary level. We apply two drives [Fig. 12.1(a)] with frequencies and amplitudes given by

$$\text{Drive 1: } \omega_{\downarrow} = \omega_{\downarrow\uparrow} + \Delta_R + \delta/2 \quad A_{\downarrow} \quad (12.2)$$

$$\text{Drive 2: } \omega_{\uparrow} = \omega_{\uparrow\uparrow} + \Delta_R - \delta/2 \quad A_{\uparrow}$$

You can think of Δ_R as the detuning of the virtual level from $|\uparrow_a\rangle$, and δ as the detuning of the drives from the virtual level (we will want $\delta \sim 0$). These drives result in the two terms necessary to induce a Raman process:

$$\frac{\Omega_{\downarrow}}{2} e^{i\omega_{\downarrow}t} |\uparrow_a\rangle\langle\downarrow_q| + \frac{\Omega_{\uparrow}}{2} e^{i\omega_{\uparrow}t} |\uparrow_a\rangle\langle\uparrow_q| + \text{H.c.} \quad (12.3)$$

where the Rabi rates are $\Omega_{\downarrow} = A_{\downarrow}M_{\downarrow\uparrow}$, $\Omega_{\uparrow} = A_{\uparrow}M_{\uparrow\uparrow}$ with M_{ij} the drive matrix elements. It is convenient to move into the rotating frame of the two drives. We'll use the interaction representation $H \rightarrow e^{iH_r\hbar} (H_A - H_R) e^{-iH_r\hbar}$ where the rotation-generating Hamiltonian is

$$H_r = H_A + \delta/2 |\downarrow_q\rangle\langle\downarrow_q| - \delta/2 |\uparrow_q\rangle\langle\uparrow_q| - \Delta_R |\uparrow_a\rangle\langle\uparrow_a| \quad (12.4)$$

The Hamiltonian then becomes

$$\begin{aligned} H = & -\delta/2 |\downarrow_q\rangle\langle\downarrow_q| + \delta/2 |\uparrow_q\rangle\langle\uparrow_q| + \Delta_R |\uparrow_a\rangle\langle\uparrow_a| \\ & + \left(\frac{\Omega_{\downarrow}}{2} |\uparrow_a\rangle\langle\downarrow_q| + \frac{\Omega_{\uparrow}}{2} |\uparrow_a\rangle\langle\uparrow_q| + \text{H.c.} \right) \end{aligned} \quad (12.5)$$

This is the classic Λ system Hamiltonian: we have the energies of the three uncoupled Andreev levels in the rotating frame, and we have terms coupling the lower two levels to the upper one. However, there is no direct coupling between the lower two levels.

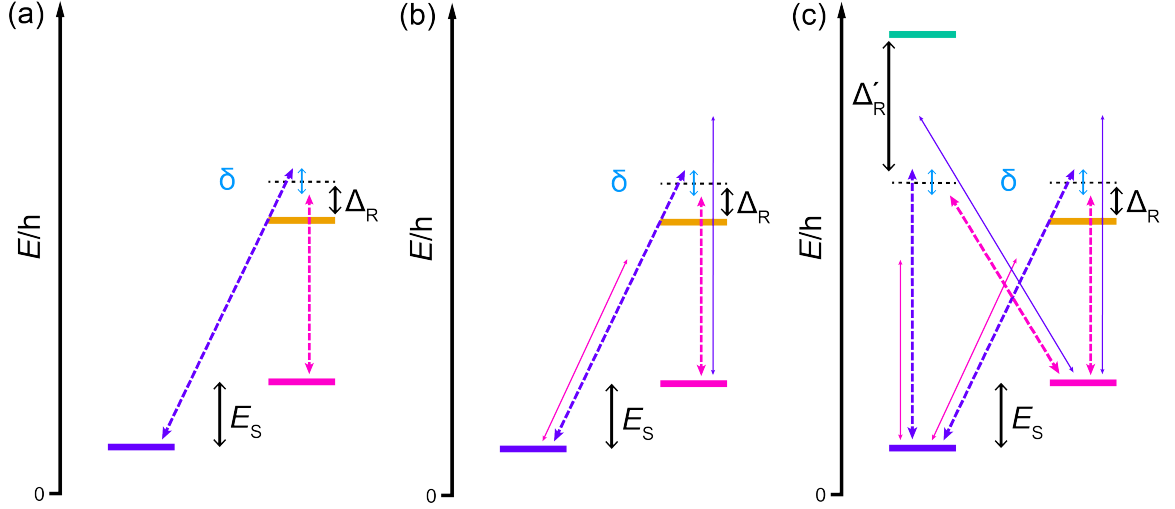


Figure 12.1: Building up the Hamiltonian under the action of the Raman drives | (a) The three levels and transitions of our desired Λ system. (b) The two drives can also couple to the opposite transition, producing Stark shifts (thin solid arrows). (c) In reality, the second level of the upper doublet $|\downarrow_a\rangle$ will always be present. This results in a secondary Raman process with the same δ , but a different value for the large detuning Δ'_R . Including the Stark shifts, there are thus a total of eight Hamiltonian terms that depend on the drive amplitudes.

Adiabatic elimination of $|\uparrow_a\rangle$

To gain some intuition for how the Hamiltonian 12.5 drives transitions between $|\downarrow_q\rangle$ and $|\uparrow_q\rangle$, it's helpful to adiabatically eliminate¹ $|\uparrow_a\rangle$. We solve the Schrodinger equation for the time derivative of the $|\uparrow_a\rangle$ amplitude and demand that it is zero:

$$0 = i \frac{d}{dt} \langle \uparrow_a | \psi \rangle = + \frac{\Omega_{\downarrow}}{2} \langle \downarrow_q | \psi \rangle + \frac{\Omega_{\uparrow}}{2} \langle \uparrow_q | \psi \rangle + \Delta_R \langle \uparrow_a | \psi \rangle \quad (12.6)$$

where $|\psi\rangle$ is the full quantum state. We then solve for $\langle \uparrow_a | \psi \rangle$, plug it into the equations for $\frac{d}{dt} \langle \downarrow_q | \psi \rangle$ and $\frac{d}{dt} \langle \uparrow_q | \psi \rangle$, and arrive at a reduced Hamiltonian which acts in the qubit Hilbert space spanned by $|\downarrow_q\rangle, |\uparrow_q\rangle$:

$$H = \frac{\delta_{\text{eff}}}{2} \sigma_z + \frac{\Omega_{\text{eff}}}{2} \sigma_x \quad \delta_{\text{eff}} = \delta + \frac{\Omega_{\uparrow}^2}{4\Delta_R} - \frac{\Omega_{\downarrow}^2}{4\Delta_R}, \quad \Omega_{\text{eff}} = \frac{\Omega_{\uparrow}\Omega_{\downarrow}}{2\Delta_R} \quad (12.7)$$

where we have dropped a constant offset. This is just the Rabi Hamiltonian for a driven

¹This procedure is only valid for $\Omega_{\uparrow}, \Omega_{\downarrow} \ll \Delta_R$ such that $|\uparrow_a\rangle$ remains depopulated, which was not always true for the experiments presented in this thesis.

qubit! The Rabi rate Ω_{eff} scales with the product of the two drive strengths, but drops off with the detuning Δ_R from the auxiliary level $|\uparrow_a\rangle$. The effective detuning of the Raman qubit δ_{eff} is due both to the original detuning δ of the drives from the virtual level, but also to the Stark shifts $\Omega_i^2/4\Delta_R$. As with a typical qubit, we will only have full oscillations when $\delta_{\text{eff}} = 0$. For $\delta = 0$, we thus find that we need equal drive strengths $\Omega_{\uparrow} = \Omega_{\downarrow}$ for full oscillations between $|\downarrow_q\rangle$ and $|\uparrow_q\rangle$.

Stark shift corrections

We have seen how the drives Eqn. 12.2 allow us to coherently manipulate the $|\downarrow_q\rangle/|\uparrow_q\rangle$ manifold. However, when we went from Eqn. 12.2 to Eqn. 12.3, we made an assumption: we assumed that drive 1 only coupled to the $|\downarrow_q\rangle \leftrightarrow |\uparrow_a\rangle$ transition, and that drive 2 only coupled to the $|\uparrow_q\rangle \leftrightarrow |\uparrow_a\rangle$ transition. There is no reason for this to be true; drive 1 will also couple to $|\uparrow_q\rangle \leftrightarrow |\uparrow_a\rangle$ and drive 2 to $|\downarrow_q\rangle \leftrightarrow |\uparrow_a\rangle$ as shown in Fig. 12.1(b). As these terms are far off resonance, we can take them into account by including them as Stark shifts in the Hamiltonian. They will modify the effective detuning as

$$\delta_{\text{eff}} \rightarrow \delta_{\text{eff}} + \frac{(A_{\downarrow}M_{\uparrow\uparrow})^2}{4(\Delta_R - E_s)} + \frac{(A_{\uparrow}M_{\downarrow\uparrow})^2}{4(\Delta_R + E_s)} \quad (12.8)$$

Note how the pairing of the drive amplitudes and matrix elements has been swapped. We now have four drive-dependent terms in the Hamiltonian: the two desired inter-doublet couplings and the two Stark shift terms.

What about $|\downarrow_a\rangle$?

Throughout this section so far, we have ignored $|\downarrow_a\rangle$, which we know has to be present in the system. How will this affect the Raman process? As shown in Fig. 12.1(c), it results in a secondary Raman process with the same small detuning δ , but a different value for the large detuning Δ'_R . This modifies the effective Rabi rate

$$\Omega_{\text{eff}} \rightarrow \frac{A_{\downarrow}A_{\uparrow}}{2} \left(\frac{M_{\downarrow\uparrow}M_{\uparrow\uparrow}}{\Delta_R} + \frac{M_{\downarrow\downarrow}M_{\uparrow\downarrow}}{\Delta'_R} \right) \quad (12.9)$$

The first term is exactly what we had in Eqn. 12.7, just split up into the drive amplitudes

and matrix elements now. The second term comes from the second Raman process. In our case, $\Delta_R < 0$ and $\Delta'_R > 0$. As such, the two Raman processes destructively interfere to reduce the overall Rabi rate. In this experiment, it was roughly a $\sim 20\%$ effect. As with the primary Raman process, there are also cross terms that lead to Stark shifts. Thus in total, there were a total of eight drive-dependent Hamiltonian terms we had to worry about.

But from an experimental point of view, it was only really necessary to consider all eight terms when we wanted to understand the structure of the coherent oscillations in detail (discussed below). When we first set out to drive Raman transitions, the main idea was straightforward: locate $|\downarrow_q\rangle \leftrightarrow |\uparrow_a\rangle$ and $|\downarrow_q\rangle \leftrightarrow |\uparrow_a\rangle$ in two-tone spectroscopy, then apply two simultaneous drives with carrier frequencies equally detuned from the measured resonances. Below, we sketch out how the experiment proceeded, starting with a tune up of the device.

12.2 Tuning up the device

As always, we possessed three *in-situ* control knobs of the nanowire Andreev levels: the loop flux Φ , a main gate voltage V_c acting on the nanowire weak link, and an additional gate voltage V_p applied to two more gates positioned on either side of the main gate. Upon cooling down the device, we observed Φ and gate voltage dependence of the readout resonance around $V_c, V_p = 0$, indicating that conduction channels in the nanowire link were transmitting. With $\Phi = -0.13\Phi_0$ and $V_p = 0$, we swept V_c while performing two-tone spectroscopy [Fig. 12.2(a)]. We observed several dispersing transitions, with a local maximum at $V_c = -71.0$ mV.

Parking V_c at the local maximum to mitigate the effects of electrostatic noise on the Andreev level coherence (see below for further data and discussion), we then performed two-tone spectroscopy while sweeping Φ [Fig. 12.2(b)]. Four flux-dependent resonances were observed, which cross at $\Phi = 0$. This is characteristic of inter-doublet transitions of a quasiparticle between spin-orbit split Andreev levels [Tosi et al. 2019]. In conjunction with the population transfer measurements shown in Fig. 12.4(a), this characteristic spectrum allowed us to identify the two lowest-frequency transitions as $|\uparrow_q\rangle \leftrightarrow |\uparrow_a\rangle$ and $|\downarrow_q\rangle \leftrightarrow |\uparrow_a\rangle$.

At certain Φ bias points, some of the transitions are not visible, or become significantly dimmer. For example, the $|\uparrow_q\rangle \leftrightarrow |\uparrow_a\rangle$ transition is barely visible at $\Phi \simeq -0.13\Phi_0$. This drop in signal occurs because the quasiparticle population of the relevant level of the lower doublet (either $|\downarrow_q\rangle$ or $|\uparrow_q\rangle$) decreases, often below 0.01. We attribute these population drops to evacuation of the quasiparticle into cold, dot-like levels in the nanowire that are brought into resonance with the Andreev doublets as Φ , V_c , and V_p are varied. This phenomenon is discussed in more detail in Chapter 14. While these features are not completely understood, we found they could easily be avoided with an appropriate choice of bias conditions. The effects of these population drops can be observed in Figs. 12.2, 12.3 and 12.5.

Having identified the transitions that defined the Λ system, we searched for a local maxima of the transitions in *both* gate voltages (not just V_c) in order to mitigate electrostatic noise. We found such a bias point at $V_c = -71.9$ mV and $V_p = 4.0$ mV (see Fig. 12.3 for Φ -dependence at these gate voltages).

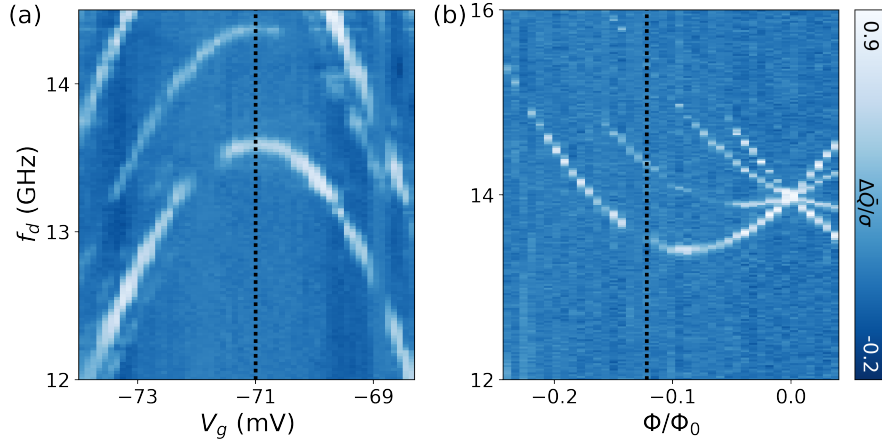


Figure 12.2: Gate and flux dependence of the inter-doublet transitions | (a) A local maximum (“sweet spot”) is observed in both $|\uparrow_q\rangle \leftrightarrow |\uparrow_a\rangle$ and $|\downarrow_q\rangle \leftrightarrow |\uparrow_a\rangle$ at $V_c = -71.0$ mV (black dotted line). (b) Flux dependence of the four inter-doublet transitions at $V_c = -71.0$ mV, $V_p = 0.0$ mV. Black dotted line indicates Φ bias for data shown in (a).

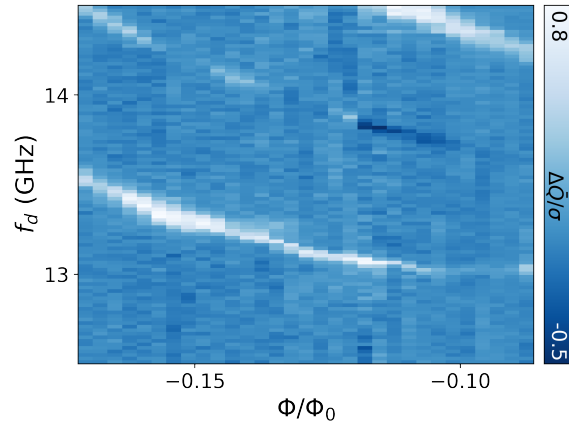


Figure 12.3: Flux dependence at the main working point | Flux dependence of $|\uparrow_q\rangle \leftrightarrow |\uparrow_a\rangle$ and $|\downarrow_q\rangle \leftrightarrow |\uparrow_a\rangle$ at the main working point ($V_c = -71.9$ mV, $V_p = 4.0$ mV).

12.3 Searching for Raman transitions

Having characterized the Λ system, we then investigated two-photon Raman transitions of the trapped quasiparticle at $\Phi = -0.10\Phi_0$. We first give a summary of these measurements, then present further details below.

After initializing the quasiparticle in $|\uparrow_q\rangle$ via post-selection, we applied two simultaneous Gaussian pulses with variable respective carrier frequencies f_\uparrow and f_\downarrow and then measured the final qubit spin state [Fig. 12.4(b)]. Along a line given by $f_\downarrow = f_\uparrow + 609$ MHz, we observe increased $|\downarrow_q\rangle$ population that we attribute to the onset of a Raman process. As expected for Raman transitions, the slope of this line is equal to one, since a shift of one drive frequency must be compensated by an equal shift of the other. The discrepancy between the spin splitting $E_s = 684$ MHz and the 609 MHz offset was due to an uncontrolled shift of the Andreev spectrum that occurred in between the measurements shown in Fig. 12.4(a) and Fig. 12.4(b).

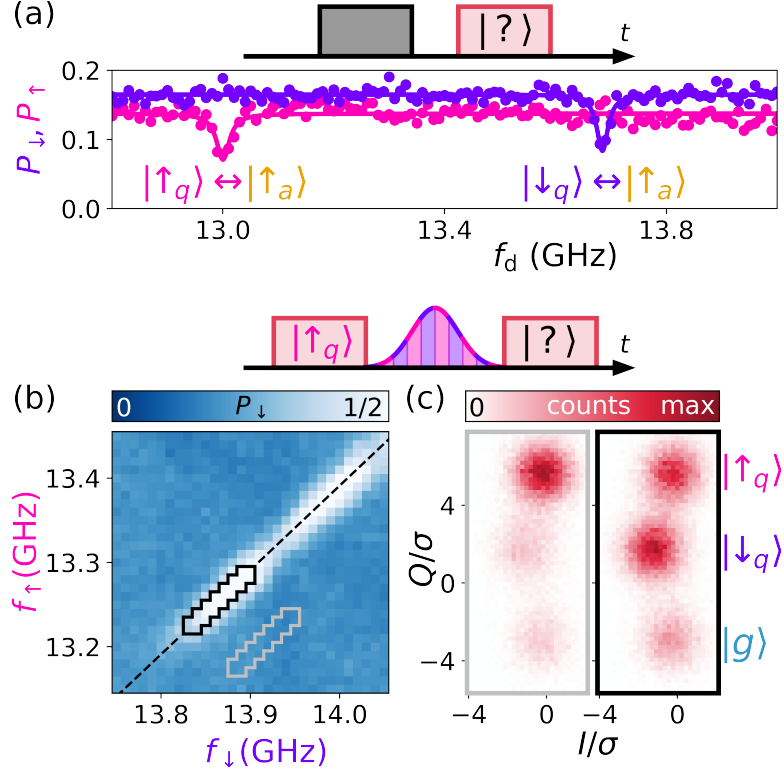


Figure 12.4: Raman transitions of a trapped quasiparticle | (a) In a two-tone measurement, the Josephson nanowire was first driven by a saturation pulse (gray) of variable carrier frequency f_d before the quasiparticle state was determined with a readout pulse (maroon). A dip is observed in P_{\uparrow} corresponding to the $|\uparrow_q\rangle \leftrightarrow |\uparrow_a\rangle$ transition and in P_{\downarrow} corresponding to the $|\downarrow_q\rangle \leftrightarrow |\uparrow_a\rangle$ transition. (b) The quasiparticle was first prepared in $|\uparrow_q\rangle$ via an initial readout pulse and post-selection. Simultaneous Gaussian pulses (100 ns standard deviation) of variable frequency f_s were then applied, followed by a final readout pulse. The observed peak in the final $|\downarrow_q\rangle$ population lies along $f_{\downarrow} = f_{\uparrow} + 609$ MHz (black dashed line). (c) Full Γ histograms of the final readout pulse for the two subsets of measurements enclosed by the gray and black solid lines in (b). Data in the region enclosed by the gray line shows little population transfer from the post-selected $|\uparrow_q\rangle$ (left panel), while data in the region enclosed by the black shows significant population transfer to $|\downarrow_q\rangle$ (right panel).

To further illustrate the dynamics of the quasiparticle under the Raman transitions, we histogram Γ for data points off/on resonance with the Raman process [Fig. 12.4(c)]. Off resonance, the quasiparticle was found predominantly in $|\uparrow_q\rangle$, as expected from post-selection on the initial readout pulse. On resonance, there was significant population transfer to $|\downarrow_q\rangle$ as desired, as well as a small population transfer to $|\downarrow_g\rangle$. This is due to drive-induced quasiparticle evaporation, which we had to account for in our simulation of coherent spin dynamics, as is discussed in the next section.

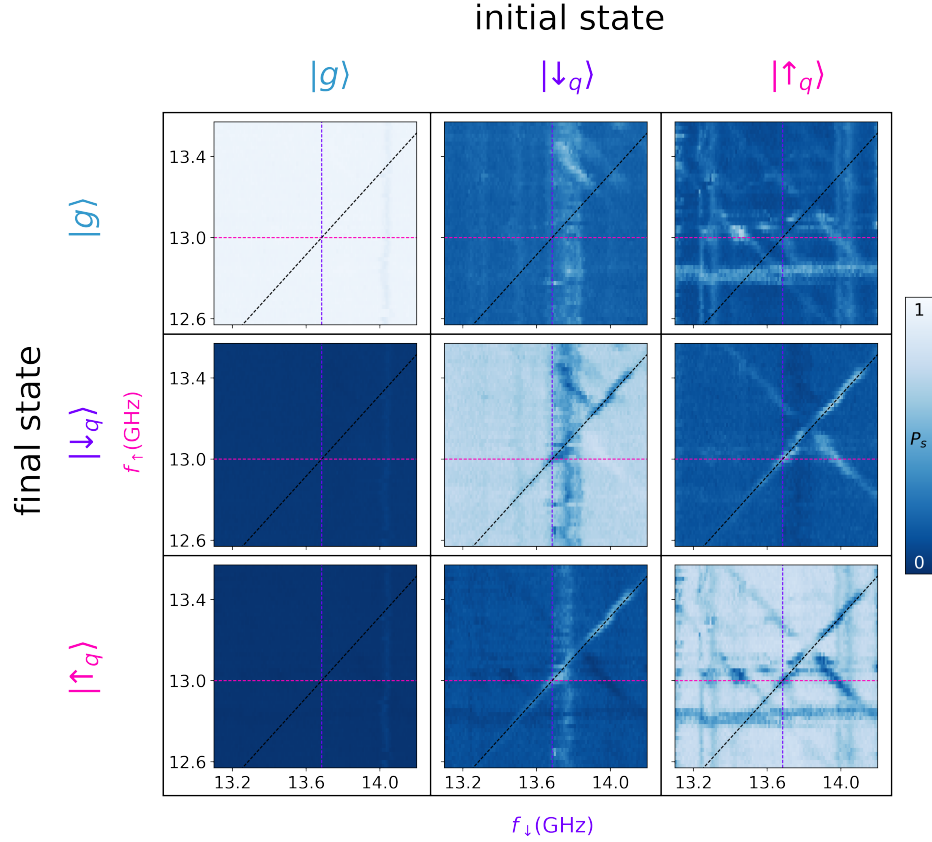


Figure 12.5: All transition probabilities under the action of simultaneous drive pulses of variable carrier frequencies | Measured transition frequencies of $|\uparrow_q\rangle \leftrightarrow |\uparrow_a\rangle$ and $|\downarrow_q\rangle \leftrightarrow |\uparrow_a\rangle$ are indicated by pink and purple dashed lines, respectively. Black dashed lines have a slope of one, and run through the crossing point of the two transitions.

First though, a bit more detail on our Raman spectroscopy measurements. In Fig. 12.5, we present the data for any post-selected initial state (not just $|\uparrow_q\rangle$), and over a wider-frequency range than shown above. We note that the drive powers used in this measurement were 30 dB larger than in the two-tone spectroscopy measurement of Fig. 12.4(a). The $|\downarrow_q\rangle \leftrightarrow |\uparrow_a\rangle$ transition is visible (though broadened) just above its low-power value, while the $|\uparrow_q\rangle \leftrightarrow |\uparrow_a\rangle$ transition is no longer visible. Other transitions that are constant in one drive frequency or the other are observed, perhaps due to evaporation of the quasiparticle into the same dot-like levels as discussed above. Several multi-photon transitions are observed that lie along $f_\uparrow = -f_\downarrow + c$. The -1 slope indicates that the two drive frequencies are adding to reach a highly-excited state of the system, perhaps even exciting the quasi-

particle above the superconducting gap. Finally, the desired two-photon Raman process $|\downarrow_q\rangle \leftrightarrow |\uparrow_q\rangle$ occurs along the black dashed line, which has slope 1 and intersects with the crossing point of the two single-photon transitions of the Λ system (unlike the data shown in Fig. 12.4(b) above). This measurement was taken between the measurements displayed in Fig. 12.4(b) and 12.4(a). We thus conclude that there was an uncontrolled shift of the Andreev levels between the measurement shown Fig. 12.5 and Fig. 12.4(b), as we referenced above. Such jumps were not uncommon in this experiment, and occurred on a timescale of days to weeks.

12.4 Coherent spin dynamics

Using an experiment similar to that shown in Fig. 12.5, we chose drive frequencies such that the desired Raman process $|\downarrow_q\rangle \leftrightarrow |\uparrow_q\rangle$ was being driven, but the drives were maximally detuned from undesired processes. We then varied the amplitudes A_\downarrow, A_\uparrow to induce coherent oscillations of the quasiparticle spin [Fig. 12.6(a)]. To better understand these coherent dynamics, we performed a simulation of our system using QuTiP [Johansson, Nation, and Nori 2013] [Fig. 12.6(b)]. Here we present transition probabilities out of the two spin states under the action of these variable amplitude drive pulses, both measured and simulated (measurements where the system started in $|g\rangle$ showed no features).

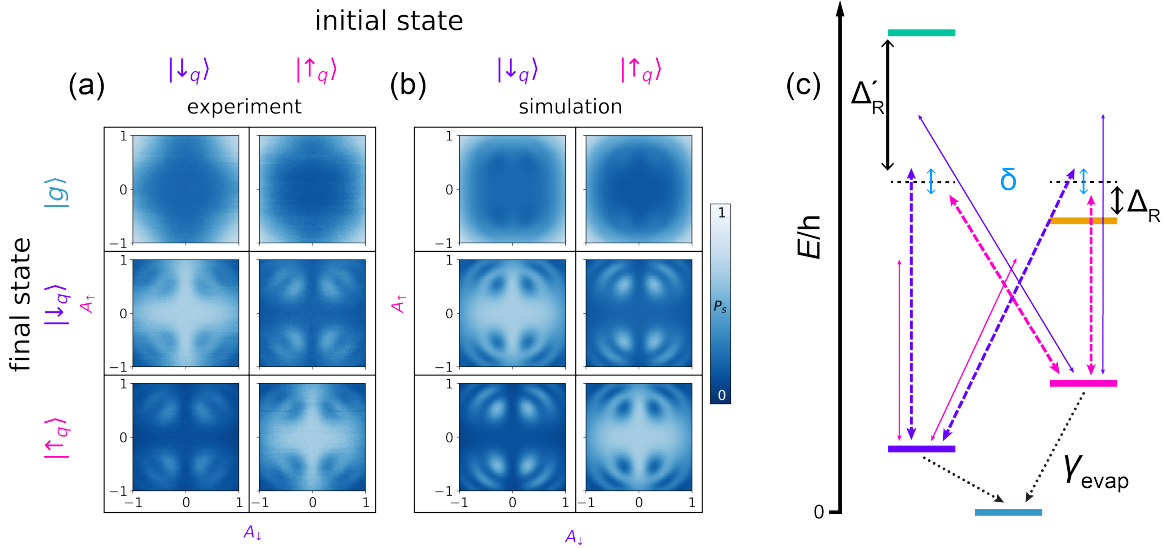


Figure 12.6: Coherent Λ -Rabi oscillations of the quasiparticle spin | (a) Measured final state probabilities after the application of simultaneous drive pulses, with the spin initialized in either $|\downarrow_q\rangle$ or $|\uparrow_q\rangle$. (b) Simulated probabilities. (c) Level diagram with simulation parameters.

The simulation of the coherent dynamics included all four Andreev levels $|\downarrow_q\rangle, |\uparrow_q\rangle, |\uparrow_a\rangle$, and $|\downarrow_a\rangle$ [Fig. 12.6(c)]. While there were only two drives applied in this experiment, because each drive could couple to each of the four inter-doublet transitions we needed to account for a total of eight Hamiltonian terms. Four of these terms produced two Raman

processes [dashed double-headed arrows in Fig. 12.6(c)], one of which was via $|\uparrow_a\rangle$ as desired, and the other was via $|\downarrow_a\rangle$. The $|\uparrow_a\rangle$ Raman process dominated the dynamics, as the detuning of the drives from $|\uparrow_a\rangle$ was $\Delta_R = -290$ MHz, as compared to the detuning to $|\downarrow_a\rangle$ which was $\Delta'_R = 1.36$ GHz. The other four Hamiltonian terms produced Stark shifts [thin solid double-headed arrows in Fig. 12.6(c)], which were necessary to include in order to properly capture the shape of the oscillations.

The fixed parameters in the simulation were the four inter-doublet transition frequencies, the measured dephasing rates of both doublets, the pulse length and shape (Gaussian, 40 ns standard deviation), and the detunings $\Delta_R = -290$ MHz, $\Delta'_R = 1.36$ GHz. We fit the simulation to the data using six free parameters: the four drive matrix elements associated with the four inter-doublet transitions ($M_{\downarrow\uparrow}$, $M_{\uparrow\uparrow}$, $M_{\downarrow\downarrow}$, $M_{\uparrow\downarrow}$), the detuning δ from the Raman resonance condition, and the ratio α of the f_{\uparrow} drive amplitude to the f_{\downarrow} drive amplitude. From the fit, we extract the below values and associated co-variance matrix:

$$\begin{array}{l}
\delta/(2\pi) = 5.5 \\
M_{\downarrow\uparrow}/(2\pi) = 232 \text{ MHz} \\
M_{\uparrow\uparrow}/(2\pi) = 255 \text{ MHz} \\
M_{\downarrow\downarrow}/(2\pi) = 280 \text{ MHz} \\
M_{\uparrow\downarrow}/(2\pi) = 80 \text{ MHz} \\
\alpha = 0.54
\end{array}
\quad C = \begin{pmatrix}
+0.02 & +0.01 & -0.09 & +0.2 & +0.2 & +0.0003 \\
+0.01 & +70 & -50 & -200 & +200 & +0.02 \\
-0.09 & -50 & +30 & +100 & -100 & -0.02 \\
+0.2 & -200 & +100 & +500 & -40 & -0.05 \\
+0.2 & +200 & -100 & -400 & +400 & +0.06 \\
+0.0003 & +0.02 & -0.02 & -0.05 & +0.06 & +0.00002
\end{pmatrix} \quad (12.10)$$

Note that the extracted values of the matrix elements include the drive amplitudes at the device, which we estimate to be ~ 400 nV across the junction.

Additionally, as can be seen in Fig. 12.6, we observed a drive-induced quasiparticle evaporation rate; the $|g\rangle$ population grows as the drive amplitudes are increased. In simulation, we found that this quasiparticle evaporation was captured by including two dissipators on the lower doublet of the form $\sqrt{\gamma_{\text{evap}}}(|A_{\downarrow}|^2 + |A_{\uparrow}|^2 + |A_{\downarrow}||A_{\uparrow}|)|g\rangle\langle\downarrow_q|$, $\sqrt{\gamma_{\text{evap}}}(|A_{\downarrow}|^2 + |A_{\uparrow}|^2 + |A_{\downarrow}||A_{\uparrow}|)|g\rangle\langle\uparrow_q|$, with $\gamma_{\text{evap}}/(2\pi) = 1.2 \pm 0.1$ MHz as extracted from the $|g\rangle$ population data. While this is certainly an over-simplified model (no frequency depen-

dence, no spin dependence, etc.), the scaling of the rate with the drive amplitudes indicates that the evaporation is likely due to multi-photon transitions of the trapped quasiparticle to excited states either in the dot-like levels previously discussed or into the continuum above the superconducting energy gap of the leads. This differs with previous results on drive-induced quasiparticle evaporation where a linear scaling of the rate with power was observed [Levenson-Falk et al. 2014], most likely because the Andreev levels studied in this work exist at lower energy. These results are also consistent with our observation that the undesired transitions seen in Fig. 12.6 only occur at high powers.

Finally, we included readout errors in the simulation by extracting the transition probabilities between the outcomes of the first and second readout pulses for the zero-amplitude experimental data and then applying the resultant transfer matrix to the simulated probabilities for all drive amplitudes. While this did not result in a qualitative change of the data, it was important for replication of the experimental contrast. Note that this is why there are some Raman features visible in the simulated $|g\rangle$ data: the rate at which the quasiparticle spontaneously evacuates the junction during readout is slightly spin-dependent. Although we were unable to measure the upper doublet population directly because the dispersive shift of these states was too small at this bias point, the simulation indicates that it was below 20%.

References

- Johansson, J. R., P. D. Nation, and F. Nori, “Qutip 2: a Pndreev framework for the dynamics of open quantum systems”, *Computer Physics Communications* **184**, 1234–1240 (2013).
- Levenson-Falk, E., F. Kos, R. Vijay, L. Glazman, and I. Siddiqi, “Single-quasiparticle trapping in aluminum nanobridge Josephson junctions”, *Physical review letters* **112**, 047002 (2014).
- Tosi, L., C. Metzger, M. Goffman, C. Urbina, H. Pothier, S. Park, A. L. Yeyati, J. Nygård, and P. Krogstrup, “Spin-orbit splitting of Andreev states revealed by microwave spectroscopy”, *Phys. Rev. X* **9**, 011010 (2019).

13

Interactions of Andreev levels with the environment

Interactions between a quantum system and its environment will cause the system to decohere. We can separate this decoherence into two kinds of processes relative to the energy eigenstates of the system:

1. **Transitions:** The environment can induce transitions between the eigenstates.
2. **Dephasing:** The environment can dephase superpositions of the eigenstates.

In this Chapter, we will first discuss environment-induced transitions of Andreev levels in the context of both the Andreev pair qubit as well as long-junction physics. We will then investigate dephasing of pair states, single-quasiparticle states, and spin states of an individual quasiparticle.

13.1 Environment-induced transitions

For Andreev levels, environment-induced transitions can be further broken down into parity-conserving processes, which can occur via phonon/ photon exchange with the environment, and parity-switching processes, which require the exchange of quasiparticles.

In general, there are two kinds of measurements we can perform to investigate environment-induced transitions. One approach is to apply a microwave pulse to move

the system to an excited state, which we can then watch decay back to the steady-state of the system. The second approach is to repeatedly measure the system and monitor its **quantum jumps**: every so often, the system will spontaneously transition from one eigenstate to another due to interactions with the environment.

As a first example, we will present our investigation of parity dynamics in the Andreev pair qubit experiment. We will also discuss a tool that we used throughout this thesis to investigate quantum jumps called a **hidden Markov model**. We will then move onto our investigations of other environment-induced transitions, moving back and forth between quantum jump measurements and pulsed measurements as we go.

13.1.1 Parity dynamics and hidden Markov models

We originally probed parity dynamics in the context of the Andreev pair qubit [Fig. 13.1]. By continuously monitoring the resonator response to the readout tone, we captured quantum jumps between $|g\rangle$, $|e\rangle$ and the two spin states.¹ Qualitatively, we found that while the system moved quickly between $|g\rangle$ and $|e\rangle$, it remained in the odd manifold on much longer timescales.

As with all quantum jump analysis presented in this work, we used a hidden Markov model algorithm to analyze the trace. This analysis assumes that the system possesses three states, and that each state $|i\rangle$ results in values of Γ with different (but potentially overlapping) probability distributions $P(\Gamma|i)$. Importantly, $P(\Gamma|i)$ does not need to be known *a priori*. By analyzing $\Gamma(t)$, the algorithm yields the most probable $P(\Gamma|i)$, state assignments at each t , and transition rates γ_{ji} from $|i\rangle$ to $|j\rangle$. In this context, the analysis gave us the rates between $|g\rangle$, $|e\rangle$, and the spin states [Fig. 13.2(a)].

However, the hidden Markov model analysis makes an assumption: the underlying processes governing the jumps are Poissonian. To verify this, we would always compare the probability distribution of dwell times between jumps of the system to theory. A histogram of the dwell times between any two states should follow an exponential decay $\frac{1}{\bar{\tau}}e^{-\tau/\bar{\tau}}$ where τ is the dwell time and $\bar{\tau}$ is the average dwell time. We instead histogrammed the dwell times weighted by their length and compare to $\frac{\tau}{\bar{\tau}}e^{-\tau/\bar{\tau}}$ [Fig. 13.2(b)] [Vool et al.

¹Note that in the context of the pair qubit, the two spin states have the same dispersive shift.

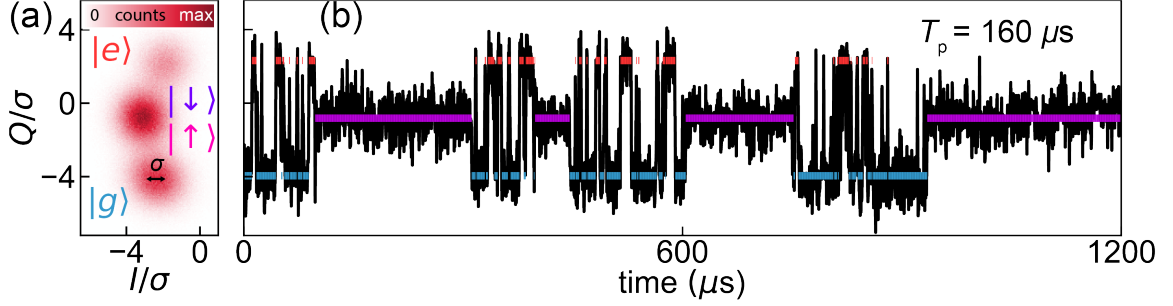


Figure 13.1: Quantum jumps between the many-body configurations of a single Andreev doublet | (a) Histogram of the I and Q quadratures of the resonator readout tone ($f_{\text{pair}} = 8.5$ GHz, $\Phi = \Phi_0/2$). Each count corresponds to an integration period of 480 ns and the total number of counts is 9.6×10^5 . The (I, Q) -pairs cluster into three Gaussian distributions corresponding to the many-body configurations of the Andreev levels. Data are rescaled by the standard deviation σ of the $|g\rangle$ distribution. (b) Time evolution of I/σ for a sample of the data in (a). The state assignments shown by the blue, purple, and red bars result from a maximum-likelihood estimation to a hidden Markov model. This also yields the parity lifetime of the doublet $T_p = 160 \mu\text{s}$. As was noted in Chapter 3, this data was taken with a small detuning ~ 500 MHz between f_{pair} and f_r , resulting in off-resonant driving of f_{pair} by the readout tone. The parity dynamics may also have been affected [Janvier 2016].

2014]. This weighting increases the visibility of low-frequency fluctuations of the transition rates. The fidelity of the data to the theory is computed as

$$F = \frac{\sum_i \sqrt{M_i T_i}}{\sum_i M_i} \quad (13.1)$$

where M_i are the measured bin values and T_i the theoretical. For this data, the fidelities of all six histograms are 0.97 or above, verifying that the system follows Poisson statistics and that the use of a hidden Markov model is valid. Throughout our exploration of Andreev levels in Josephson nanowires, we never observed jump traces that were significantly non-Poissonian.

If we want to talk about the dynamics between the even and odd manifolds, it is a bit cumbersome to have to quote all four parity-switching rates. Typically, we use the **parity lifetime** as a summary of the dynamics between the even and odd manifolds. We define it as follows: the parity decay rate $1/T_p$ is the average rate of population transfer from the odd manifold to the even manifold, plus the average rate of population transfer from the

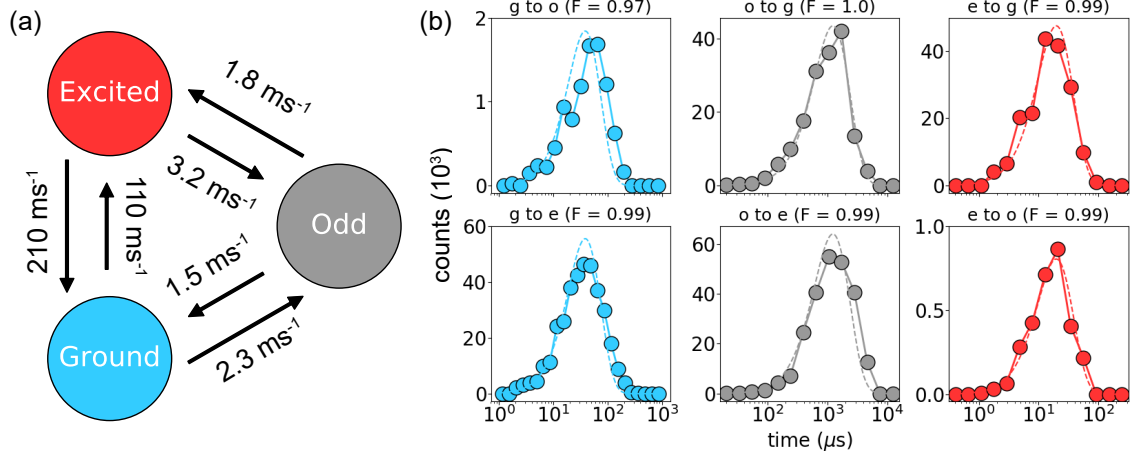


Figure 13.2: Transition rates and dwell times of the Andreev pair qubit | (a) The six transition rates between $|g\rangle$, $|e\rangle$, and the odd manifold extracted from the data in Fig. 13.1 with a hidden Markov model algorithm. (b) Histograms of dwell times between jumps of the Andreev levels, weighted by the dwell time. The dashed lines give the predicted distributions assuming the processes are all Poissonian. The fidelity F of the measured histograms to a Poisson process is shown above each plot.

even manifold to the odd manifold.² Separating the odd manifold into the two spin states $|\uparrow\rangle$ and $|\downarrow\rangle$, the rate from odd to even is given by $\gamma_{\text{odd, even}} = P_{\downarrow}(\gamma_{\downarrow, g} + \gamma_{\downarrow, e}) + P_{\uparrow}(\gamma_{\uparrow, g} + \gamma_{\uparrow, e})$ where P_i is the probability for the state to be occupied. Because we cannot distinguish between $|\downarrow\rangle$ and $|\uparrow\rangle$, we assume $P_{\downarrow} = P_{\uparrow} = 0.5$, $\gamma_{\downarrow, g} = \gamma_{\uparrow, g} = \gamma_{o, g}$, and $\gamma_{\downarrow, e} = \gamma_{\uparrow, e} = \gamma_{o, e}$. With these simplifications, we have $\gamma_{\text{odd, even}} = \gamma_{o, g} + \gamma_{o, e}$. Similarly, we assume that $\gamma_{g, \downarrow} = \gamma_{g, \uparrow} = \gamma_{g, o}/2$ and $\gamma_{e, \downarrow} = \gamma_{e, \uparrow} = \gamma_{e, o}/2$, where the factor of $1/2$ comes from the spin degeneracy. This gives $\gamma_{\text{even, odd}} = P_g \gamma_{g, o} + P_e \gamma_{e, o}$, and the final expression for the parity lifetime becomes

$$\frac{1}{T_p} = \gamma_{\text{odd, even}} + \gamma_{\text{even, odd}} = \gamma_{og} + \gamma_{oe} + P_g \gamma_{go} + P_e \gamma_{eo} \quad (13.2)$$

where the probabilities to be in $|g\rangle$ and $|e\rangle$ are given by $P_g = \gamma_{eg}/(\gamma_{ge} + \gamma_{eg})$ and $P_e = \gamma_{ge}/(\gamma_{ge} + \gamma_{eg})$. Plugging in the rates extracted with the hidden Markov model yields $160 \pm 10 \mu\text{s}$.

From the quantum jumps measurement, we could also extract the pair lifetime from the rates between $|g\rangle$ and $|e\rangle$. However, these measurements were a bit spoiled: due to

²This is approximately double the average parity switching rate; we define the parity lifetime in this way to mirror the definition of T_1 for a two-level system

the relatively weak coupling $g_c/2\pi = 23$ MHz in this original experiment, we had to operate the system with f_{pair} quite close to the resonator at a detuning of only ~ 500 MHz. The readout tone was thus off-resonantly driving f_{pair} , and inducing the observed large excited state population. In later experiments, we were able to increase the coupling and so enter the QND regime typical of cQED. These problems should not have affected the parity switching rates.³

13.1.2 Pair decay

While we never performed a systematic study of pair transition lifetimes, it always seemed to be in the range of $5 - 20 \mu\text{s}$. This is similar to what was measured in atomic point contacts [Janvier et al. 2015]. In our paper on the Andreev pair qubit, we found a lifetime of $13 \mu\text{s}$, which was measured at $\Phi = \Phi_0/2$. Due to the electrostatic instabilities in that device, we were unable to measure the Φ -dependence of the lifetime (though we certainly could have in later devices; I just never got around to it). What is causing this energy decay? It doesn't seem like it can be photons. In the pair qubit paper, the closest known microwave transition was the readout mode. This should only have induced a Purcell decay of $\simeq 170 \mu\text{s}$. The most likely culprit is phonons; they are often to blame for energy loss in conventional quantum dots. This is just speculation though. More work needs to be done on this front.

13.1.3 Inter-doublet quasiparticle decay

Upon entering the long-junction regime of Josephson nanowires, we had access to much richer dynamics. However, even when more doublets were present, we found that the unperturbed nanowire was still most likely to be in $|g\rangle$, $|\downarrow_q\rangle$, or $|\uparrow_q\rangle$.⁴ This made sense; within a particular parity manifold, the nanowire was predominantly in the lowest energy states. A natural question for the odd manifold was then, given that a single trapped quasiparticle

³We have seen some effects on the parity switching rates at higher readout power, see Ref. [Janvier 2016] for a systematic study of such effects in atomic point contacts. While we don't understand exactly what's happening here, this is a common theme in cQED. Bad things happen when you crank up the power too much.

⁴By this point, we had cranked up g_c so that we did not need to tune the Andreev transitions close to the resonator to achieve the necessary dispersive shifts. We thus did not observe heightened $|e\rangle$ population as in Fig. 13.1(a), or similar effects with the upper doublet.

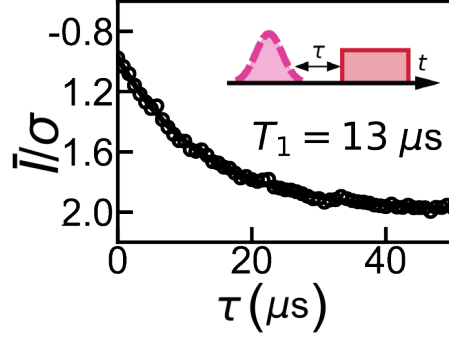


Figure 13.3: Measurement of the pair transition lifetime | A π -pulse resonant with a pair transition at $f_{\text{pair}} = 6.84$ GHz was first applied, then we waited a variable delay τ before measuring the resonator response. An exponential fit yielded a pair transition lifetime of $13 \mu\text{s}$.

likes to relax to the lowest doublet, how fast does this decay take place? To probe this, we excited quasiparticles from the lower doublet to the upper doublet, then watched them fall back down.

As an example, we present the effect of driving with Gaussian pulses the two transitions available to a quasiparticle initially in $|\uparrow_q\rangle$ [pink dashed arrows in Fig. 13.4(a, e)]. Two new distributions were revealed, attributable to $|\uparrow_a\rangle$ and $|\downarrow_a\rangle$ [Fig. 13.4(b, f)]. Because χ for the upper doublet was approximately negative that of the lower doublet over this flux range [Fig. 11.6], these distributions were located at positive Q . By varying the amplitude A of the $|\uparrow_q\rangle \leftrightarrow |\uparrow_a\rangle$ pulse, we induced Rabi oscillations of the quasiparticle population between the two doublets [Fig. 13.4(c)]. While coherent manipulation of quasiparticle pairs had been demonstrated in the past [Janvier et al. 2015; Hays et al. 2018], this data represented the first coherent manipulation of an individual quasiparticle in a superconductor.

With an understanding of the upper doublet distributions in hand, we measured the decay of a quasiparticle back down to the lower doublet. Following a $|\uparrow_q\rangle$ to $|\uparrow_a\rangle$ π -pulse, we found that the quasiparticle decayed preferentially to $|\uparrow_q\rangle$ [Fig. 13.4(d)] with a timescale of $T_{aq,\uparrow} = 2.8 \pm 0.1 \mu\text{s}$, whereas after a saturation pulse on the $|\uparrow_q\rangle \leftrightarrow |\downarrow_a\rangle$ transition, the quasiparticle decayed preferentially to $|\downarrow_q\rangle$ with a timescale $T_{aq,\downarrow} = 3.2 \pm 0.1 \mu\text{s}$ [short-time behavior in Fig. 13.4(g)]. We thus observed that the spontaneous inter-doublet decay was spin-conserving, though we do not believe it was limited by J_A -mediated Purcell decay (see next paragraph). Following the spin-flipping $|\uparrow_q\rangle \leftrightarrow |\downarrow_a\rangle$ pulse, the initial spin-conserving

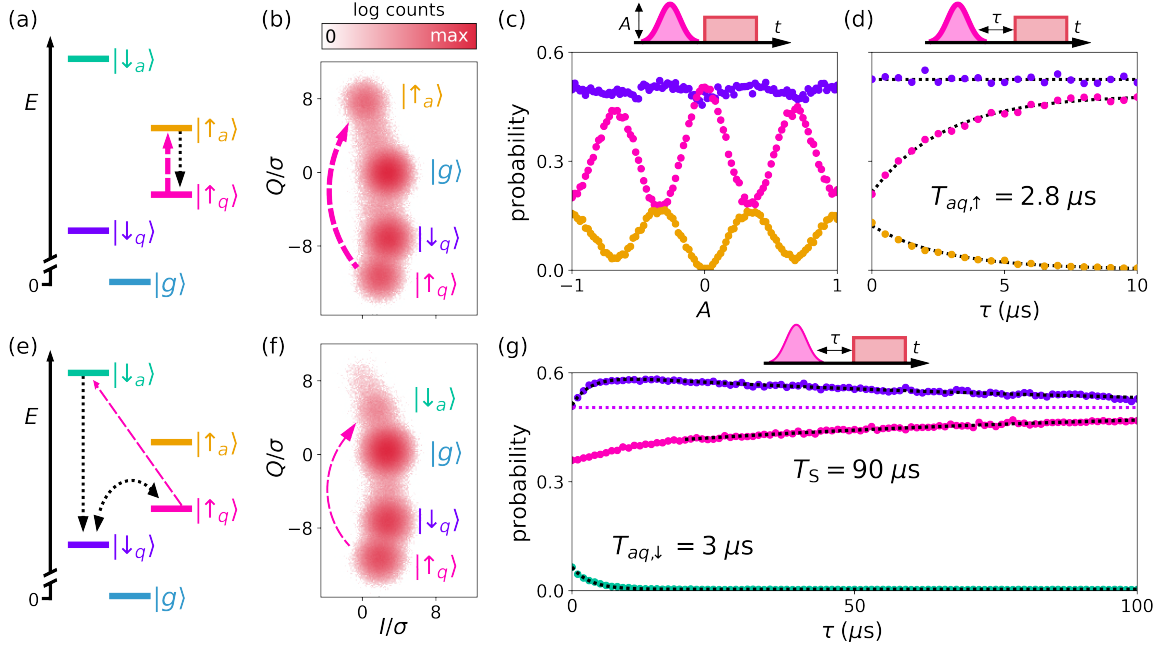


Figure 13.4: Driven dynamics of a quasiparticle initially in $|\uparrow_q\rangle$ ($\Phi = 0.085\Phi_0$) | The quasiparticle was excited into either $|\uparrow_a\rangle$ ((a) through (d)) or $|\downarrow_a\rangle$ ((e) through (g)) using Gaussian pulses on the transitions depicted by the pink arrows in (a)/(e). Following each pulse, the distributions corresponding to $|\uparrow_a\rangle/|\downarrow_a\rangle$ were visible in the Γ histogram ((b)/(f)). In (c), (d) and (g), we plot occupation probabilities for the states of interest as pulse sequence parameters are varied. Probabilities are computed as the number of counts within 2σ of the distribution centers, normalized by the steady-state counts. Fits to theory are denoted by dotted black curves. (c) Varying the normalized amplitude A of the $|\uparrow_q\rangle \leftrightarrow |\uparrow_a\rangle$ pulse resulted in coherent oscillations of the quasiparticle within the \uparrow manifold. (d) Varying the delay τ between the $|\uparrow_q\rangle \leftrightarrow |\uparrow_a\rangle$ pulse and the readout pulse revealed exponential decay of the quasiparticle back to $|\uparrow_q\rangle$ with timescale $T_{aq,\uparrow}$ (black arrow in (a)). (g) Following a $|\uparrow_q\rangle \leftrightarrow |\downarrow_a\rangle$ pulse, an initial exponential decay to $|\downarrow_q\rangle$ with timescale $T_{aq,\downarrow}$ (single-headed black arrow in (e)) resulted in equal and opposite deviation of the $|\downarrow_q\rangle$ and $|\uparrow_q\rangle$ populations from their equilibrium value (magenta dotted line). This spin polarization then exponentially decayed with timescale T_s (double-headed black arrow in (e)).

relaxation resulted in an average spin polarization of the quasiparticle in the lower doublet, which then decayed on a timescale $T_s = 90 \pm 10 \mu\text{s}$ [Fig. 13.4(g)]. We attribute the slight bi-exponential behavior of $|\downarrow_q\rangle$ to spin relaxation within the upper doublet before decay to the lower doublet, and thus only fit to the long-time behavior of $|\downarrow_q\rangle$. Such inter-doublet spin-flipping pulses followed by spin-conserving decay could thus be used to initialize the spin state of a trapped quasiparticle, with a fidelity limited by the rate of $|\uparrow_q\rangle \rightarrow |\downarrow_a\rangle$ population transfer compared to T_s .

As the spin-conserving nature of inter-doublet quasiparticle decay dynamics mirrored

that of the drive/resonator coupling to the Andreev levels, a natural hypothesis was that the coupling to the environment was also via the current operator. This would just be typical Purcell decay; the current operator could couple the Andreev levels to the microwave environment. As in the pair qubit case discussed at the beginning of this Chapter, the closest microwave mode was the readout. We can thus calculate the expected Purcell decay rate as $\approx (\kappa_c + \kappa_i) \frac{g_c^2}{(2\pi f_{\uparrow\uparrow} - 2\pi f_r)^2} = \frac{1}{4.3 \text{ ms}}$. This is roughly three orders of magnitude higher than the observed decay rate. As such, another bath must be at work. Phonons? Again, no hard evidence.

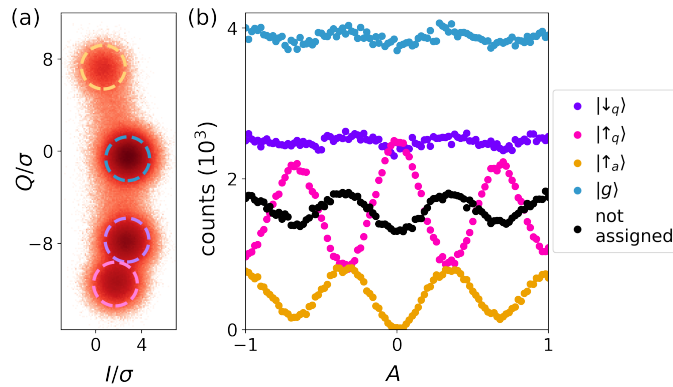


Figure 13.5: Analysis of the driven dynamics | (a) Histogram of all measurement shots taken during the experiment Fig. 13.4(c). Shots inside the dashed circles (radius 2σ) were assigned to the corresponding state. Shots outside these regions were left unassigned. Note that here we also include $|g\rangle$ for illustration. (b) At each value of the normalized pulse amplitude A , we count the number of points inside each of the four depicted circles in (a). The number of unassigned counts is also plotted.

Further details

The Gaussian pulses used in the experiments depicted in Fig. 13.4(b-d) had standard deviations of 20 ns, while the pulses used in the experiments depicted in Fig. 13.4(f,g) had 250 ns standard deviations due to the larger total energy required to induce spin-flipping transitions. To compute the probabilities plotted in Fig. 13.4(c,d,g), we first counted the number of shots within 2σ of the distribution centers. Shots outside of these regions were left unassigned. Fig. 13.5 illustrates this for the measurement depicted in Fig. 13.4(c), additionally including counts assigned to the $|g\rangle$ population as well as the unassigned counts. For Fig. 13.4(c,d,g), we then normalized by the steady-state (undriven) counts for the primary states

of interest ($|\downarrow_q\rangle$, $|\uparrow_q\rangle$ and $|\uparrow_a\rangle$ for the Fig. 13.4(c) measurement). Due to decay from $|\uparrow_a\rangle$ to $|\uparrow_q\rangle$ during measurement, some shots were mistakenly assigned to $|g\rangle$ and $|\downarrow_q\rangle$ or were unassigned because their mid-flight capture resulted in a value of Γ that was not associated with any one state distribution. This resulted in small oscillations in the apparent populations of these states, large oscillations of the number of shots not assigned to any state [Fig. 13.5], and also what appears to be an unequal probability change between states $|\uparrow_a\rangle$ and $|\uparrow_q\rangle$ in Fig. 13.4(c). The magnitude of these unintended oscillations decreased with shorter integration time, which is consistent with our interpretation; however, the discrimination power also suffered. Such decay during measurement also explains the observed $|\downarrow_a\rangle$ population in Fig. 13.4(f), as well as the unequal population deviations at $\tau = 0$ observed in Fig. 13.4(d,g).

A simultaneous fit of the form $P_{\downarrow,q} = c_{\downarrow,q}$, $P_{\uparrow,q} = -a_{\uparrow,q}e^{-\tau/T_{aq,\uparrow}} + c_{\uparrow,q}$, $P_{\uparrow,a} = a_{\uparrow,a}e^{-\tau/T_{aq,\uparrow}}$ was applied to the three curves of Fig. 13.4(d). Because the data were not normalized, the only shared parameter between the three curves was $T_{aq,\uparrow}$. Similarly, the three curves of Fig. 13.4(d) were simultaneously fit with $P_{\downarrow,q} = -a_{\downarrow,aq}e^{-\tau/T_{aq,\downarrow}} + a_{\downarrow,s}e^{-\tau/T_s} + c_{\downarrow,q}$, $P_{\uparrow,q} = -a_{\uparrow,s}e^{-\tau/T_s} + c_{\uparrow,q}$, $P_{\downarrow,a} = a_{\downarrow,a}e^{-\tau/T_{aq,\downarrow}}$. Here the shared parameters were $T_{aq,\uparrow}$ and T_s . We only fit to the $|\uparrow_q\rangle$ data for greater than $20 \mu\text{s}$ due to the observed bi-exponential decay. We attribute this to spin-mixing within the upper doublet before decay to the lower doublet. However, we were unable to accurately measure these dynamics due to the large overlap between the $|\uparrow_a\rangle$ and $|\downarrow_a\rangle$ distributions and the relative weakness of the effect (the quasiparticle decays to the lower doublet before much spin mixing can occur).

13.1.4 Spin flips

Given that, in the long-junction regime of a Josephson nanowire, we found the system to be predominantly in $|g\rangle$, $|\downarrow_q\rangle$, and $|\uparrow_q\rangle$, we then wanted to understand the dynamics between these states. In particular, we wanted to understand the spin dynamics; this had never been measured before.

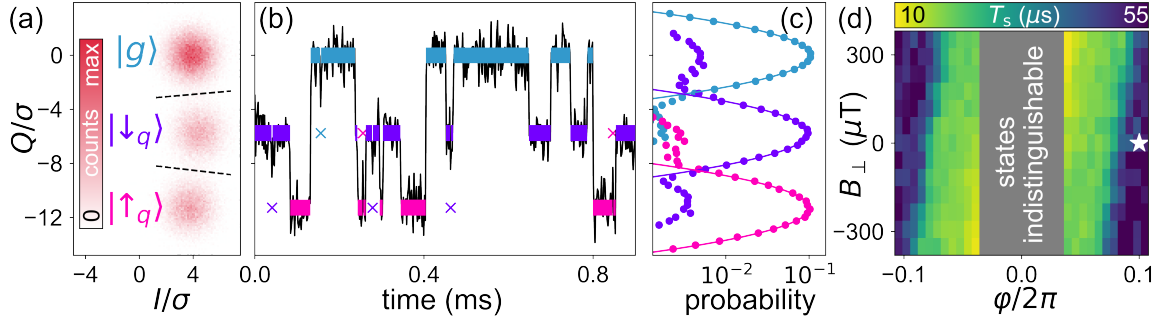


Figure 13.6: Quantum non-demolition readout of the quasiparticle spin ($\Phi = 0.100\Phi_0$) | (a) The system state was assigned to be $|g\rangle$, $|\downarrow_q\rangle$, or $|\uparrow_q\rangle$ based on thresholds indicated by the black dashed lines. (b) $Q(t)$ reveals quantum jumps between the three states. Colored bars indicate state assignments, with isolated points indicated by crosses and colored by the most likely state. (c) Histogram of Q conditioned on the state assignment of the previous measurement (indicated by color). Solid lines are Gaussian fits. (d) By analyzing $\Gamma(t)$ using a hidden Markov model, the spin lifetime T_s was determined as a function of both φ and a magnetic field B_\perp applied perpendicular to the chip substrate. The star indicates the bias for data in (a), (b), and (c).

As in the case of the pair qubit, we probed these dynamics by continuously monitoring the response of the resonator to the readout tone [Fig. 13.6]. In this experiment, as it was the first time the spin state of a quasiparticle had been probed, we also wanted to know how well we could detect the spin state. Instead of exclusively using a hidden Markov analysis,⁵ we performed state assignment using the thresholds indicated by the black dashed lines in Fig. 13.1.4(a). For perfectly QND measurement, consecutive shots should always yield the same result, which means that transitions should never be observed. To compare to this ideal, we histogrammed Q conditioned on the state assignment of the previous shot [Fig. (c)]. We observed that consecutive shots found the same state $|i\rangle$ with high probability $P_{i,i}$, with occasional transitions and miss-assignments resulting in the observed peaks at the other distribution centers. We quantify these effects with the quantum non-demolition metric [Touzard et al. 2019] $\mathcal{F} = (P_{\downarrow,\downarrow} + P_{\uparrow,\uparrow})/2 = 92.2 \pm 0.1\%$.

Besides the spin detection fidelity, we were also interested in the spin lifetime. We determined the spin lifetime T_s as a function of both $\varphi \cong 2\pi \frac{\Phi}{\Phi_0} \text{mod}(2\pi)$ and a magnetic field B_\perp applied perpendicular to the chip substrate [Fig. 13.1.4(d)] using a hidden Markov model algorithm [see Fig. 13.9 for all rates]. At $B_\perp = 0 \mu\text{T}$, we observed that T_s increased

⁵For state detection, we usually want to know how well we can determine the state given a single shot (an IQ -pair)

with $|\varphi|$ symmetrically about $\varphi = 0$. Note that at $\varphi/2\pi = 0.085$, $T_s = 42 \pm 2 \mu\text{s}$ as compared to $90 \pm 10 \mu\text{s}$ obtained in the free-decay measurement [Fig. 13.4(g)], perhaps due to drive-induced saturation of the environment. The dependence of T_s on φ is correlated with the energy splitting between $|\downarrow_q\rangle$ and $|\uparrow_q\rangle$, which goes to 0 at $\varphi = 0$ [Fig. 13.7]. Applying a positive (negative) B_\perp resulted in a positive (negative) shift of the φ -dependence. This can be explained by a Zeeman-like shift of the Andreev levels, consistent with the observed spectrum at $B_\perp = 380 \mu\text{T}$ [Fig. 13.10] and expected for a magnetic field applied parallel to the spin-orbit field [Reynoso et al. 2012; Tosi et al. 2019].

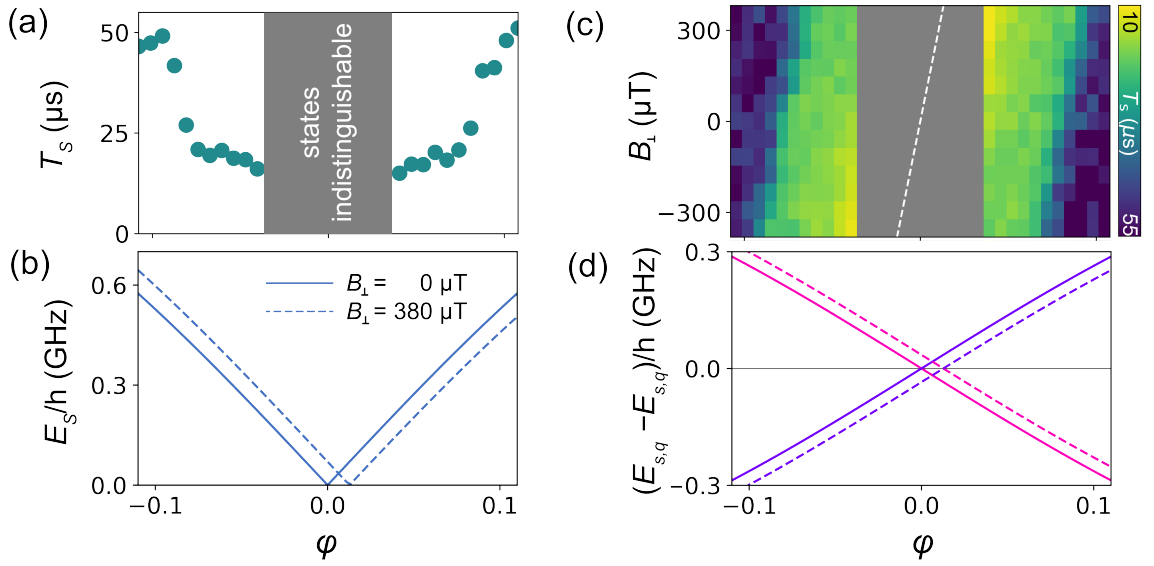


Figure 13.7: Comparison of E_s and T_s | (a) Zero-field cut of data presented in Fig. 13.6(d). (b) Spin splitting extracted from spectroscopy at $B_\perp = 0 \mu\text{T}$ and $B_\perp = 380 \mu\text{T}$ [Fig. 13.10]. (c) Same data as presented in Fig. 13.6(d). (d) Calculated energies of $|\downarrow_q\rangle$ and $|\uparrow_q\rangle$ based on panel (b), referenced to their average. At $B_\perp = 380 \mu\text{T}$, $|\downarrow_q\rangle$ is shifted down and $|\uparrow_q\rangle$ is shifted up. Their crossing point thus shifts right, along with the full E_s curve as depicted in (b). The interpolated value of the crossing point shift with field is depicted by the white dashed line in (c), which tracks with the behavior of the T_s .

In an attempt to understand the source of the quasiparticle spin flips, we compared our system to electrostatically-confined semiconductor quantum dots [Hanson et al. 2007]. In any spin-flip process, two quantities must be conserved: angular momentum and energy. There are two possible culprits for the angular momentum exchange:

1. It could be the nuclei of the nanowire (hyperfine interaction); all the isotopes of our nanowires have nonzero nuclear spin. The only naturally-occurring isotope of ar-

senic is ^{75}As , which has a nuclear spin of $3/2$, while indium has two naturally occurring isotopes ^{113}In and ^{115}In both with a spin of $9/2$.

2. It could be an interaction between spin and phonons mediated by spin-orbit coupling.

We will go into more detail on this below.

For energy exchange, it can only be phonons. Because the nuclear magnetic moment is so much smaller than that of the electron, if the E_s isn't approximately zero then the nuclei will be unable to absorb the energy associated with the electron spin flip.

Here we make an attempt to describe the spin flips we observe using a simple spin-orbit coupling + phonon model. The basic idea is the following: phonons can create an electric field \mathbf{E} due to the piezoelectric effect.⁶ If, due to spin-orbit coupling, the "spin" is actually a hybridized state of spin and orbital degrees of freedom, then an electric field can induce a transition. The Andreev levels of our Josephson nanowires are certainly hybridized states, as discussed in Chapter 8.

To estimate the scaling of such an effect in our system, we first need to consider the structure of the phonon modes. For the sub-GHz frequency range that we're interested in, the only phonons of interest are the "extensional" phonons, which are basically just vibrations in the longitudinal direction [Mariager et al. 2010]. Assuming these phonons can leak into the niobium titanium nitride leads fairly easily, we're left with a simple 1D problem $\omega_{\text{ph}} = c_{\text{ph}}/k_{\text{ph}}$. Note that this means the phonon density of states will be constant. Fermi's golden rule tells us that the rate from $|\downarrow_q\rangle$ to $|\uparrow_q\rangle$ should be given by

$$\begin{aligned}\Gamma_{\uparrow,\downarrow} &= \frac{2\pi}{\hbar} \sum_{N,N'} |\langle \uparrow, N' | \mathbf{E} | \downarrow, N \rangle|^2 p(N) \\ &= \frac{2\pi}{\hbar} |\langle \uparrow_q | \mathbf{E} / |\mathbf{E}| | \downarrow_q \rangle|^2 E_{\text{zpf}}^2 (\bar{N} + 1)\end{aligned}\tag{13.3}$$

and $\Gamma_{\downarrow,\uparrow} = \Gamma_{\uparrow,\downarrow} e^{-E_s/k_B T}$. Note that we normalize the strength of the electric field in the

⁶Electric fields can also be created by so-called "deformation potential" phonons, though these typically dominate at larger energy scales (approximately 35 GHz for indium arsenide [Hanson et al. 2007]).

spin-flip matrix element, and then each phonon contributes an additional factor of E_{zpf} .

Let's just focus on the scaling with energy. The zero-point fluctuations of the phonon-induced electric field are given by the zero-point fluctuations of the displacement times a piezoelectric constant. So using our knowledge of the quantum harmonic oscillator, we have $E_{\text{zpf}}^2 \propto 1/E_s$ (the phonons must have the same energy as the spin). We will also get some scaling from the population of the phonon mode \bar{N} , which is just the Bose-Einstein distribution. Finally, the electric field matrix element $\langle \uparrow_q | \mathbf{E} / |\mathbf{E}| | \downarrow_q \rangle$ will have some energy dependence. We've actually calculated this using a tight-binding model; see the supplement of our work on spin manipulation. Putting this all together, we plot the normalized spin-flip rate in Fig. 13.8. The phonon portion of the rate $(\bar{N} + 1)(1 + e^{-E_s/k_B T})E_s$ (purple curve) decreases as we move away from $\Phi = 0$, just like the data [Fig. 13.7]. But this is cancelled out by the matrix element $|\langle \uparrow_q | \mathbf{E} / |\mathbf{E}| | \downarrow_q \rangle|^2$ (pink curve), such that their product, which gives the total rate $\Gamma_s = \Gamma_{\downarrow, \uparrow} + \Gamma_{\uparrow, \downarrow}$ (green curve) ends up increasing away from $\Phi = 0$. This is not consistent with the data. An additional mystery (clue?) is that increasing the temperature did not affect T_s until approximately 150 mK [Fig. 13.11], and even then the increase was Φ -independent. This indicates that whatever bath is causing the Φ -dependent spin flip rate is not well-coupled to the rest of the device. Nuclei? Perhaps.

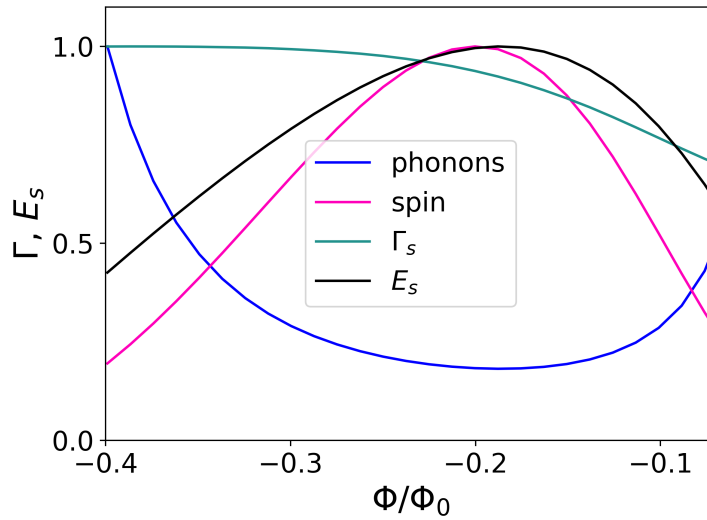


Figure 13.8: Estimated Φ dependence of spin-orbit induced spin flips | All curves are normalized to their maximum value. The spin splitting E_s (black curve) and spin-flip electric-field matrix element $|\langle \uparrow_q | \mathbf{E} / |\mathbf{E}| | \downarrow_q \rangle|^2$ (pink curve) are calculated using a tight-binding model of the Josephson nanowire (see the supplement of our spin manipulation work). The scaling of the phonon portion of the spin flip rate $(\bar{N} + 1)(1 + e^{-E_s/k_B T})E_s$ is shown in purple. Green is the estimated spin flip rate Γ_s , and is the product of the pink and purple curves. The scaling is relatively weak, but the spin-flip matrix element wins out in the calculation such that Γ_s increases as we move away from $\Phi = 0$, unlike the data [Fig. 13.7].

Dependence of all transition rates on temperature and magnetic field

Not only did our analysis give us the spin flip rates, it also gave us the all the parity switching rates. As discussed above, we found strong dependence of the spin-flip rates on φ correlated with the energy splitting between $|\downarrow_q\rangle$ and $|\uparrow_q\rangle$. As described in Chapter 11, the B_\perp -dependence is consistent with a Zeeman-like shift E_Z of the Andreev energies. We found that $E_Z \approx h \times 35$ MHz qualitatively described the data, which corresponds to a shift in the $|\downarrow_q\rangle/|\uparrow_q\rangle$ degeneracy point to $\varphi = 2\pi \times 0.013$, consistent with the B_\perp/φ slope observed in the spin-flipping rates [white dashed lines in the $\gamma_{s,\bar{s}}$ plots of Fig. 13.9].

The two rates corresponding to quasiparticles entering the junction were almost entirely unaffected by both φ and B_\perp . Curiously, the rates corresponding to the inverse process (quasiparticles leaving the junction) were generally higher and exhibited some weak features. In particular, the φ -dependence of $\gamma_{g,s}$ at $B_\perp = 0$ exhibits a peak for the higher energy spin state [Fig. 13.9]. Applying a positive (negative) B_\perp resulted in a negative (positive) shift of the φ -dependence, opposite that of the spin-flip rates. This is consistent with the higher-energy spin state coming into resonance with a cold mode through which the quasiparticle can be evacuated. See Chapter 14 for more discussion and data associated with such unknown fermionic modes.

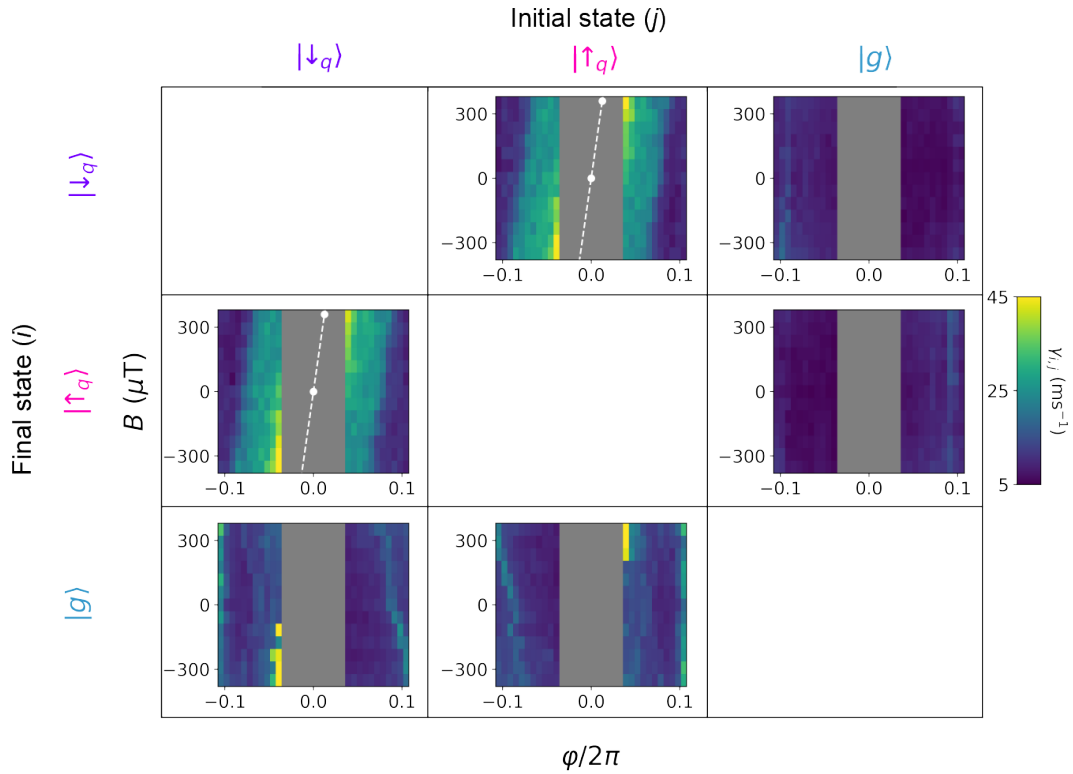


Figure 13.9: All transition rates versus φ and B_{\perp} | The six extracted transition rates $\gamma_{i,j}$ between $|g\rangle$, $|\downarrow_q\rangle$, and $|\uparrow_q\rangle$ as a function of φ and B_{\perp} at the base temperature of the fridge $T = 35$ mK. White dashed lines in the spin-flip rate panels are an estimate of the B_{\perp} dependence of the $|\downarrow_q\rangle/|\uparrow_q\rangle$ degeneracy point (see Fig. 13.10).

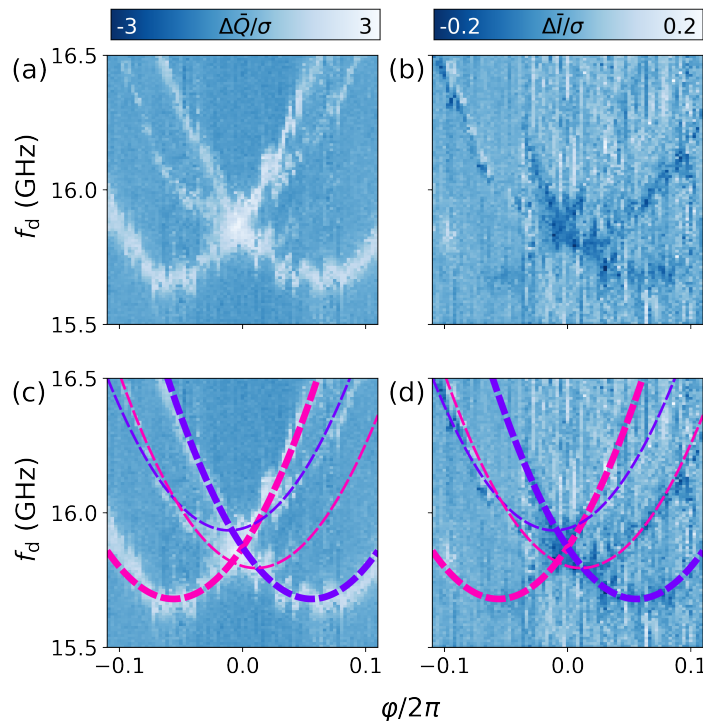


Figure 13.10: Spectroscopy at $B_{\perp} = 380 \mu T$ | Here we plot both I (a) and Q (b) to present information in both quadratures. The observed instabilities varied with time, and occurred when operating our flux coil at high current. The same data is plotted in (c)/(d), but with overlaid fits. We describe the data by the model described in Chapter 11, but we include

We also investigated the dependence of the rates on the temperature of the mixing chamber T [Fig. 13.11]. Surprisingly, we observed the spin-flipping rates were unaffected by increasing T until ~ 150 mK. Moreover, the temperature dependence of the spin-flip rates was purely additive to the low-temperature behavior and did not itself depend on φ . This suggests that the mechanism resulting in the low-temperature φ -dependence is not the same as the mechanism that kicks in at higher temperatures. Similarly, the parity-switching rates were unaffected by increasing T until ~ 150 mK. These rates should be related to the fraction of broken Cooper pairs in the circuit, which has been shown in other contexts to be temperature independent below a similar temperature scale due to non-equilibrium quasiparticles present at low temperatures [Martinis, Ansmann, and Aumentado 2009; Barends et al. 2011; Catelani et al. 2011; Serniak et al. 2018]. Thus, this data is consistent with the known phenomenology of non-equilibrium quasiparticles in superconducting circuits.

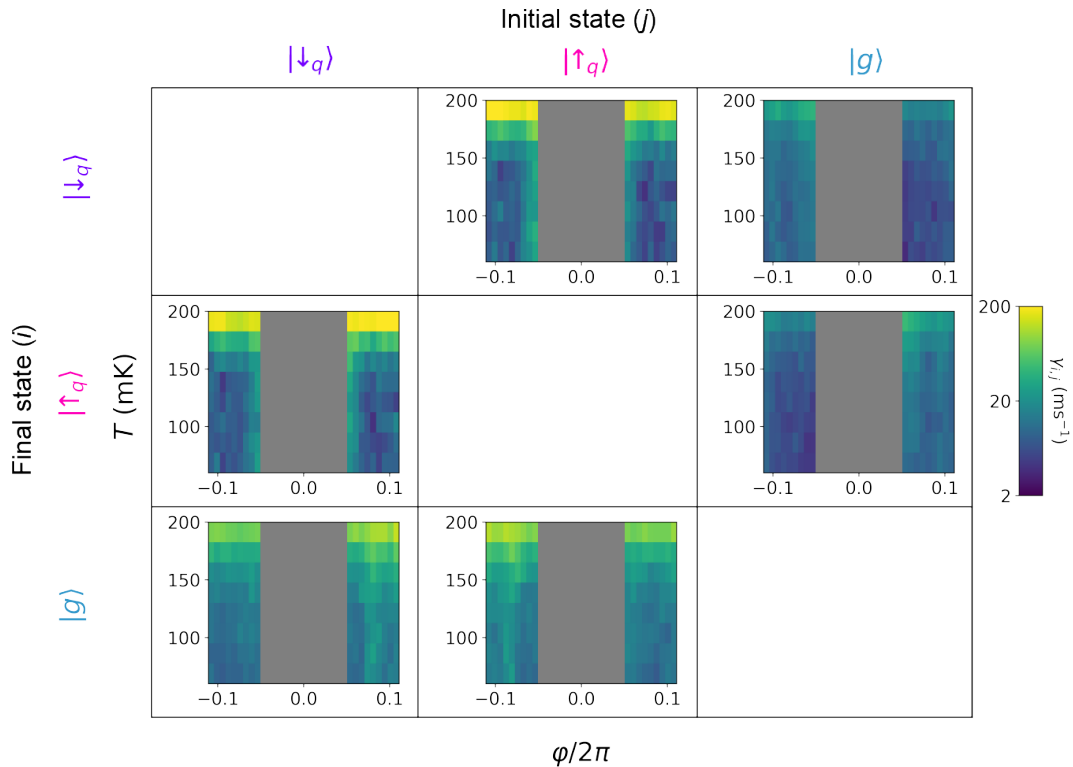


Figure 13.11: All transition rates versus φ and T | The six extracted transition rates $\gamma_{i,j}$ between $|g\rangle$, $|\downarrow_q\rangle$, and $|\uparrow_q\rangle$ as a function of φ and mixing chamber temperature T at $B = 0$ mT.

13.2 Dephasing

For the most part, we found that dephasing of the Andreev levels was due to flux noise and electrostatic noise. This is a common theme in coherent quantum systems; if you can tune the system energy with a bias knob, that usually means that the environment can too. In this work, the one exception we found to this rule was the Andreev spin qubit. Instead, as we will explain in this section, the Andreev spin qubit T_2 was limited by an unknown source of dephasing that coupled specifically to spin; this was the most interesting result to come out of our investigations of Andreev level dephasing. We will thus frame our discussion around the Andreev spin qubit coherence, and will naturally touch on the coherence of inter-doublet and pair transitions as we go.

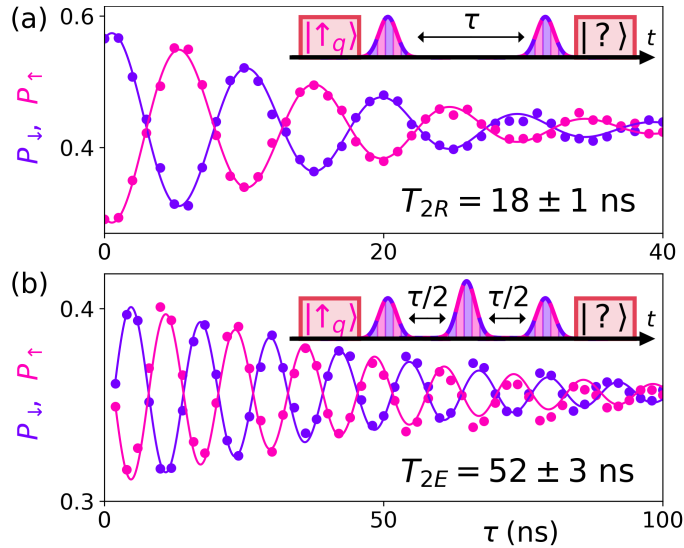


Figure 13.12: Coherence decay of the quasiparticle spin | Bias settings were $V_c = -59.1$ mV, $V_p = -33.3$ mV, $\Phi = -0.115\Phi_0$. (a) A Ramsey experiment reveals $T_{2R} = 18 \pm 1$ ns. (b) A Hahn-echo experiment reveals $T_{2E} = 52 \pm 3$ ns. Oscillations were introduced in both cases by adding a τ -dependent phase to the final Raman pulse.

13.2.1 The Andreev spin qubit

As discussed in detail in Chapter 12, we used Raman transitions to manipulate the quasiparticle spin, thus realizing the Andreev spin qubit. With this ability in hand, we then characterized the coherence lifetime of this qubit. A Ramsey measurement [Fig. 13.12(a)] revealed spin coherence decay with a timescale $T_{2R} = 18 \pm 1$ ns, while a Hahn-echo pulse

sequence [Fig. 13.12(b)] resulted in a slightly longer timescale $T_{2E} = 52 \pm 3$ ns. Both measurements were well-described by a decay envelope $\exp[-(\tau/T_2)^{1+\alpha}]$ with $\alpha = 0.3 \pm 0.1$, indicative of broadband noise $1/f^\alpha$ [Martinis et al. 2003]. We note, however, that the observed ratio of $T_{2E}/T_{2R} = 2.9$ would predict a different exponent $\alpha = 0.8 \pm 0.1$, though still broadband compared to $1/f$ where $T_{2E}/T_{2R} \rightarrow \infty$. The observed oscillations in P_\uparrow, P_\downarrow are centered about a lower value in Fig. 13.12(b) as compared to 13.12(a), which we attribute to additional quasiparticle de-trapping caused by the echo pulse (see Chapter 12). Both the observed Ramsey and Hahn-echo coherence times are comparable to that of spin-orbit qubits, perhaps the closest cousins of the Andreev spin qubit [Nadj-Perge et al. 2010; Petersson et al. 2012; Van den Berg et al. 2013]. However, because here the quasiparticle was trapped in Andreev levels, we possessed a different experimental lens with which to investigate the effects of the environment on the spin coherence.

13.2.2 Comparing to inter-doublet transitions

As the Andreev levels of a Josephson nanowire are tunable via both electrostatic voltages and Φ , we first suspected charge or flux noise as the source limiting the Andreev spin qubit coherence. However, we found that neither T_{2R} nor T_{2E} varied with V_c, V_p or Φ .

We then took a step back, and started investigating the T_2 of interdoublet transitions. They were much easier to measure (no need to tune up Raman), so a more thorough study was easier. Unlike the spin T_2 , we found that the inter-doublet T_2 did vary with V_c . Specifically, it was maximum at **sweet spots**, which are bias point where the transition of interest has a local minimum or maximum in the bias knob. At sweet spots, the transition is first-order insensitive to noise in the bias.

An example of a sweet spot is shown in Fig. 13.13(a) for two inter-doublet transitions; we indeed observed that the T_2 of the $|\uparrow_q\rangle \leftrightarrow |\uparrow_a\rangle$ transition had a maximum at the sweet spot. Away from this sweet spot, first-order electrostatic noise contributed to dephasing, causing T_2 to drop. We model this behavior using the relation for exponential coherence decay $\frac{1}{T_2} = (2\pi V_{\text{rms}} \frac{df}{dV_c})^2 + \Gamma_0$, where $V_{\text{rms}} = 0.24 \pm 0.01$ mV is the fitted value for the effective root-mean-square voltage noise and $\Gamma_0 = 0.012 \pm 0.001$ ns⁻¹ is a V_c -independent dephasing rate [Martinis, Ansmann, and Aumentado 2009]. We note that the T_2 at the sweet

spot is given by Γ_0 , as we found that second-order noise coupling to $\frac{d^2 f}{dV_c^2}$ was negligible [Houck et al. 2009].

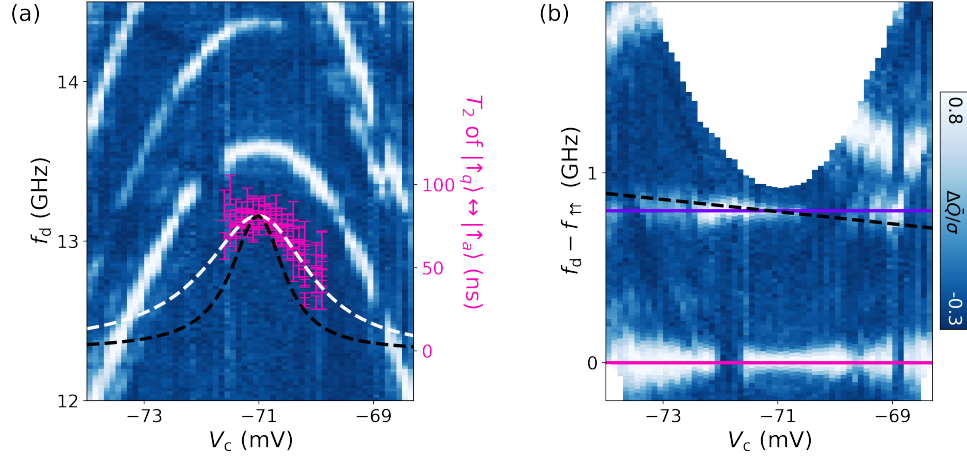


Figure 13.13: Extracting a lower-bound on the electrostatic-noise-induced dephasing time of the quasiparticle spin | (a) Two-tone spectroscopy and inter-doublet T_{2E} versus V_c . A local maximum is observed in both transitions at $V_c = -71.0$ mV. Measurements of the coherence time of $|\uparrow_q\rangle \leftrightarrow |\uparrow_a\rangle$ are shown in pink (right axis). White dashed line is a fit to the T_2 data assuming first-order noise in V_c plus a constant dephasing rate. Black dashed line corresponds to the expected T_2 given this same constant dephasing rate, but *twice* the V_c noise. (b) Same data as shown in (a), but with the fitted frequency of the $|\uparrow_q\rangle \leftrightarrow |\uparrow_a\rangle$ transition subtracted from f_d for each V_c bias. Both the purple and pink lines have no slope, and lie along the average values of the two transitions. The black dashed line is an upper bound on the slope of the $|\downarrow_q\rangle \leftrightarrow |\uparrow_a\rangle$ transition.

Why didn't this gate noise affect the Andreev spin qubit coherence? The answer is that we observed an immeasurably small dependence of the spin splitting E_s on V_c . We extracted E_s/h versus V_c by taking the difference between the frequencies of the $|\downarrow_q\rangle \leftrightarrow |\uparrow_a\rangle$ and $|\uparrow_q\rangle \leftrightarrow |\uparrow_a\rangle$ transitions. We visualize this in Fig. 13.13(b) by plotting the same two-tone data as shown in Fig. 13.13(a), but with the fitted value of the $|\uparrow_q\rangle \leftrightarrow |\uparrow_a\rangle$ transition $f_{\uparrow\uparrow}$ subtracted from the drive frequency f_d at every V_c bias. The $|\uparrow_q\rangle \leftrightarrow |\uparrow_a\rangle$ transition thus lies along $f_d - f_{\uparrow\uparrow} = 0$ (pink horizontal line), while the V_c dependence of the E_s/h is given by the behavior of $f_{\downarrow\uparrow}$ (purple horizontal line). We observe that E_s/h has no discernible slope with V_c , consistent with the lack of a spin T_2 dependence on V_c . The spin T_2 was limited by something else.

Suppose this unknown source of dephasing disappeared. What would we expect the spin T_2 to be? We determined a lower bound on the V_c -induced spin T_2 as follows: using

an upper bound on the E_s/h slope $\frac{dE_s/h}{dV_c} < 32$ MHz/mV [black dashed line in Fig. 13.13(b)] and *twice* the extracted value of V_{rms} as an upper bound on the electrostatic noise [black dashed line in Fig. 13.13(a)], we found a lower bound $4.2 \mu\text{s}$. This is quite extraordinary; we can have this nice control knob V_c over the Andreev levels, but at the same time it doesn't cause much dephasing.

13.2.3 Comparing to pair transitions

What limits the Andreev spin qubit coherence? Similarly, what limits the coherence of the inter-doublet transitions at the sweet spot? While these questions are not yet fully answered, we gained one more clue by comparing the coherence of pair transitions and inter-doublet transitions at several gate bias points [Tab. 13.1]. We found that the pair transition coherence times were systematically an order of magnitude longer than inter-doublet transition coherence times. To first order, perturbations that couple to spin (such as a Zeeman field) result in equal and opposite energy shifts of the two doublet. As such, these perturbations do not change the frequency of the doublet pair transition, and therefore do not cause dephasing. However, spin-specific perturbations do induce dephasing of both inter-doublet transitions and the Andreev spin qubit. We thus conclude that the coherence lifetime of the Andreev spin qubit is limited by a spin-specific noise source such as hyperfine interactions with the spinful nuclei of indium and arsenic (though nuclear baths are typically lower frequency than the measured ratio $T_{2E}/T_{2R} = 2.9$ would indicate [Malinowski et al. 2017]), phonon-induced fluctuations of the nanowire spin-orbit coupling, or noisy paramagnetic impurities on the surface of the nanowire [Hanson et al. 2007].

Transition	V_c (mV)	V_p (mV)	T_{2E} (ns)
$ \uparrow_q\rangle \leftrightarrow \uparrow_a\rangle$	-166.3	-127.6	39 ± 8
pair	-164.9	-127.6	257 ± 9
$ \downarrow_q\rangle \leftrightarrow \uparrow_a\rangle$	144.5	24.9	9 ± 1
pair	116.2	23.8	420 ± 20
$ \uparrow_q\rangle \leftrightarrow \uparrow_a\rangle$	32.7	-4.7	11 ± 3
pair	30.0	-4.7	490 ± 10

Table 13.1: Coherence lifetimes of various Andreev transitions.

References

- Barends, R., J. Wenner, M. Lenander, Y. Chen, R. C. Bialczak, J. Kelly, E. Lucero, P. O'Malley, M. Mariantoni, D. Sank, et al., "Minimizing quasiparticle generation from stray infrared light in superconducting quantum circuits", *Appl. Phys. Lett.* **99**, 113507 (2011).
- Catelani, G., R. J. Schoelkopf, M. H. Devoret, and L. I. Glazman, "Relaxation and frequency shifts induced by quasiparticles in superconducting qubits", *Phys. Rev. B* **84**, 064517 (2011).
- Hanson, R., L. P. Kouwenhoven, J. R. Petta, S. Tarucha, and L. M. K. Vandersypen, "Spins in few-electron quantum dots", *Rev. Mod. Phys.* **79**, 1217–1265 (2007).
- Hays, M., G. de Lange, K. Serniak, D. van Woerkom, D. Bouman, P. Krogstrup, J. Nygård, A. Geresdi, and M. Devoret, "Direct microwave measurement of Andreev-bound-state dynamics in a semiconductor-nanowire Josephson junction", *Phys. Rev. Lett.* **121**, 047001 (2018).
- Houck, A. A., J. Koch, M. H. Devoret, S. M. Girvin, and R. J. Schoelkopf, "Life after charge noise: recent results with transmon qubits", *Quantum Information Processing* **8**, 105–115 (2009).
- Janvier, C., L. Tosi, L. Bretheau, Ç. Ö. Girit, M. Stern, P. Bertet, P. Joyez, D. Vion, D. Esteve, M. F. Goffman, H. Pothier, and C. Urbina, "Coherent manipulation of Andreev states in superconducting atomic contacts", *Science* **349**, 1199–1202 (2015).
- Janvier, C., "Coherent manipulation of Andreev bound states in an atomic contact", PhD thesis (2016).
- Malinowski, F. K., F. Martins, P. D. Nissen, E. Barnes, Ł. Cywiński, M. S. Rudner, S. Fallahi, G. C. Gardner, M. J. Manfra, C. M. Marcus, et al., "Notch filtering the nuclear environment of a spin qubit", *Nature nanotechnology* **12**, 16 (2017).
- Mariager, S. O., D. Khakhulin, H. T. Lemke, K. S. Kjær, L. Guerin, L. Nuccio, C. B. Sørensen, M. M. Nielsen, and R. Feidenhansl, "Direct observation of acoustic oscillations in InAs nanowires", *Nano Letters* **10**, 2461–2465 (2010).

- Martinis, J. M., M. Ansmann, and J. Aumentado, “Energy decay in superconducting Josephson-junction qubits from nonequilibrium quasiparticle excitations”, *Phys. Rev. Lett.* **103**, 097002 (2009).
- Martinis, J. M., S. Nam, J. Aumentado, K. Lang, and C. Urbina, “Decoherence of a superconducting qubit due to bias noise”, *Physical Review B* **67**, 094510 (2003).
- Nadj-Perge, S., S. Frolov, E. Bakkers, and L. P. Kouwenhoven, “Spin-orbit qubit in a semiconductor nanowire”, *Nature* **468**, 1084–1087 (2010).
- Petersson, K. D., L. W. McFaul, M. D. Schroer, M. Jung, J. M. Taylor, A. A. Houck, and J. R. Petta, “Circuit quantum electrodynamics with a spin qubit”, *Nature* **490**, 380–383 (2012).
- Reynoso, A. A., G. Usaj, C. A. Balseiro, D. Feinberg, and M. Avignon, “Spin-orbit-induced chirality of Andreev states in Josephson junctions”, *Phys. Rev. B* **86**, 214519 (2012).
- Serniak, K., M. Hays, G. De Lange, S. Diamond, S. Shankar, L. Burkhardt, L. Frunzio, M. Houzet, and M. Devoret, “Hot nonequilibrium quasiparticles in transmon qubits”, *Phys. Rev. Lett.* **121**, 157701 (2018).
- Tosi, L., C. Metzger, M. Goffman, C. Urbina, H. Pothier, S. Park, A. L. Yeyati, J. Nygård, and P. Krogstrup, “Spin-orbit splitting of Andreev states revealed by microwave spectroscopy”, *Phys. Rev. X* **9**, 011010 (2019).
- Touzard, S., A. Kou, N. Frattini, V. Sivak, S. Puri, A. Grimm, L. Frunzio, S. Shankar, and M. Devoret, “Gated conditional displacement readout of superconducting qubits”, *Phys. Rev. Lett.* **122**, 080502 (2019).
- Van den Berg, J., S. Nadj-Perge, V. Pribiag, S. Plissard, E. Bakkers, S. Frolov, and L. Kouwenhoven, “Fast spin-orbit qubit in an indium antimonide nanowire”, *Physical review letters* **110**, 066806 (2013).
- Vool, U., I. M. Pop, K. Sliwa, B. Abdo, C. Wang, T. Brecht, Y. Y. Gao, S. Shankar, M. Hatridge, G. Catelani, et al., “Non-poissonian quantum jumps of a fluxonium qubit due to quasiparticle excitations”, *Physical review letters* **113**, 247001 (2014).

14

Unexplained observations

14.1 Quasiparticle interaction with unknown sub-gap states

In several devices, we have observed signatures of unknown fermionic modes that are coupled to the Andreev levels of the Josephson nanowire. We refer to these modes as “mystery levels.” Personally, I think a near-perfect understanding of such modes will be critical if a Majorana-based topological computer is ever to be realized. The mystery levels can exchange quasiparticles with the Andreev levels, which, in the context of parity-based Majorana qubits, will result in decoherence. Much like a thorough understanding of the microwave environment is necessary for successful implementation of superconducting qubits, a thorough understanding of the fermionic environment will be necessary for Majorana qubits.

The main “mystery” associated with the mystery levels is their physical location. As we show below, the energies of these levels do not disperse much with Φ . However, they could still be localized to the weak link. For instance, they could belong to a channel with weak coupling to the left/right leads such that they do not disperse with Φ , and thus are more similar to the states of a conventional quantum dot. Or, they could inhabit other dot-like regions elsewhere in the nanowire. For instance, there are known to be imperfections at the ends of the nanowire. Though as the ends of the nanowire are many coherence lengths away from the weak link, this seems unlikely to be the source of the mystery levels. While

the data presented below certainly proves the existence of these mystery levels, it does little to answer this question of physical location. That must be left to future work.

The data presented in this section was taken on device 6YD1122 (weak link length of a 200 nm). We also observed signatures of mystery levels in device 6YD1111 (the device used in [Hays et al. 2020; Hays et al. 2021]), primarily in the form of bias points with low odd-manifold population.

Spectroscopy

We first noticed the mystery levels in spectroscopy [Fig. 14.1]. In addition to a pair transition (frequency f_{pair}), we observed several transitions with frequency $f_{\text{pair}}/2 + c$ with c some constant. Additionally, there were two dimmer transitions with frequency $-f_{\text{pair}}/2 + c$. These transitions can all be described by assuming the existence of four additional levels with energies $E/h = 9.8$ GHz, 10.3 GHz, 13.9 GHz, 12.9 GHz as shown in panel (c). The transitions can then be attributed to either pair transitions where one quasiparticle is driven into the Andreev doublet and one into a mystery level, or single-particle transitions where a quasiparticle is driven from the Andreev doublet to one of the mystery levels. For some unknown reason, we only observed the single-particle transitions for the two higher-energy mystery levels.

To verify this interpretation, we checked how the Andreev doublet population was affected when the mystery level transitions were driven. In Fig. 14.2, we present the effect of driving a doublet/mystery level pair transition. With the doublet/mystery level in the ground state [panel (a)], driving the pair transition populates the mystery level and one level of the doublet. We thus expect population flow from $|g\rangle$ to the odd-parity (spin) states, which is what we observe in panel (c). However, if the doublet starts off in the odd-parity manifold, we would expect population flow from the odd-parity manifold to $|e\rangle$ [panel (b)]. However, we observed no increase of the $|e\rangle$ population. For some reason, the transition shown in panel (b) was blocked. This could be explained by an interaction energy E_c between the quasiparticles. In this simplistic model, the odd parity manifold would still have energy E_A , but $|g\rangle$ would have energy E_c and $|e\rangle$ would have energy $2E_A + E_c$. This would be consistent with the observed pairs of parity-breaking transitions [Fig.

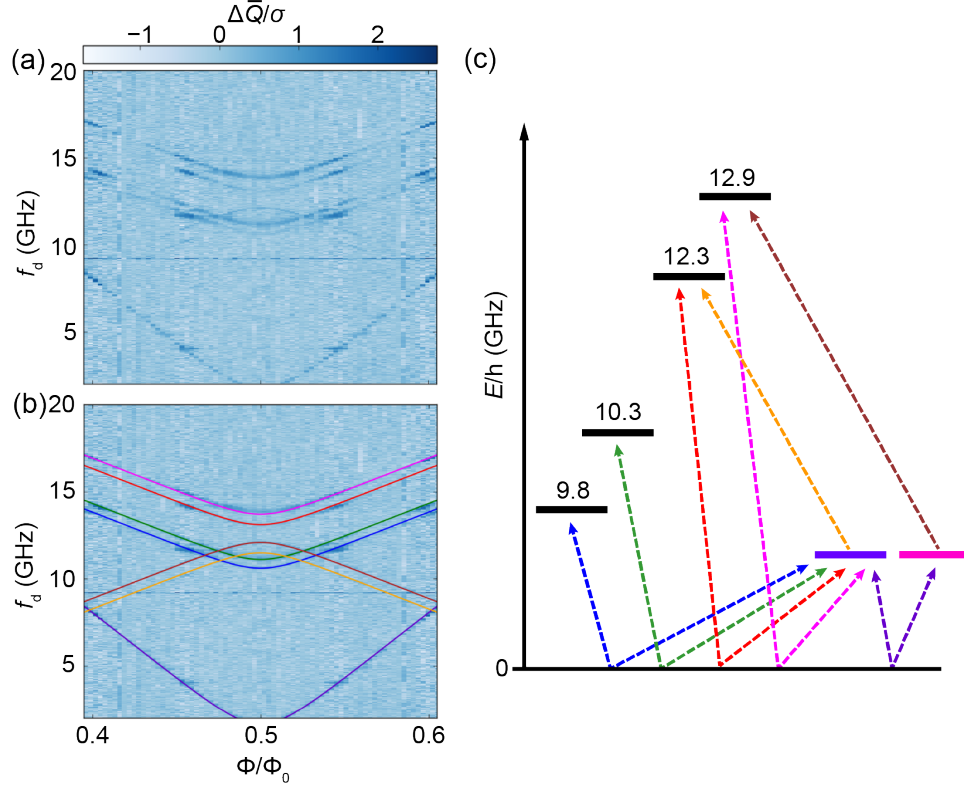


Figure 14.1: Spectroscopy of the mystery levels | (a) Two-tone spectroscopy of an Andreev doublet and four mystery levels. (b) After extracting the frequency f_{pair} of the pair transition (lowest-frequency transition), the other six transitions can be explained according to the level diagram/transitions depicted in (c). The pair transition curve is a naive fit to the short junction formula, which gives $\Delta/h = 12.8$ GHz and $\tau = 0.996$.

14.1(a)] spaced by ~ 500 MHz. We would only need two mystery levels with frequencies $(9.8 + 10.3)/2$ GHz, $(12.3 + 12.9)/2$ GHz, and $E_c = 500/2$ MHz.

Is this a reasonable charging energy? If the normal region of the weak link was completely de-coupled from the superconducting leads, then we would expect $E_c \sim \frac{(2e)^2}{2h(15\epsilon_0)(200 \text{ nm})} = 3$ THz, where 15 is the dielectric constant of indium arsenide. On the other hand, a short weak link has $E_c = 0$. In between these regimes, the charging energy is scaled roughly by the percentage of time spent on the dot, squared. In the double-barrier model, for instance, one would need to consider the coupling to the leads, the time of flight across the junction, and the superconducting gap. One could imagine fitting the spectrum to extract these parameters, but the double-barrier model is under-constrained for this data set [Fig. 14.1(a)] since we don't have data around $\Phi = 0$.

Another issue is that if the split transitions were due to charging effects, then we would expect the higher-frequency transition in each pair to be associated with population flow from the odd manifold to $|e\rangle$, which is not what we observe [Fig. 14.2(c)]. We note that we have observed this blocking phenomenon [Fig. 14.2(b)] only once; perhaps it was a one-off. Also, note that the splitting could not be explained by spin-orbit effects. Such splitting must depend on Φ and, in particular, must go to zero at $\Phi = \Phi_0/2$.

Finally, we also found that we could achieve partial coherent manipulation between $|g\rangle$ and the odd manifold by driving this transition [Fig. 14.2(d)]. Oscillations were observed upon varying the amplitude of a 10 ns square pulse, albeit with very low contrast.

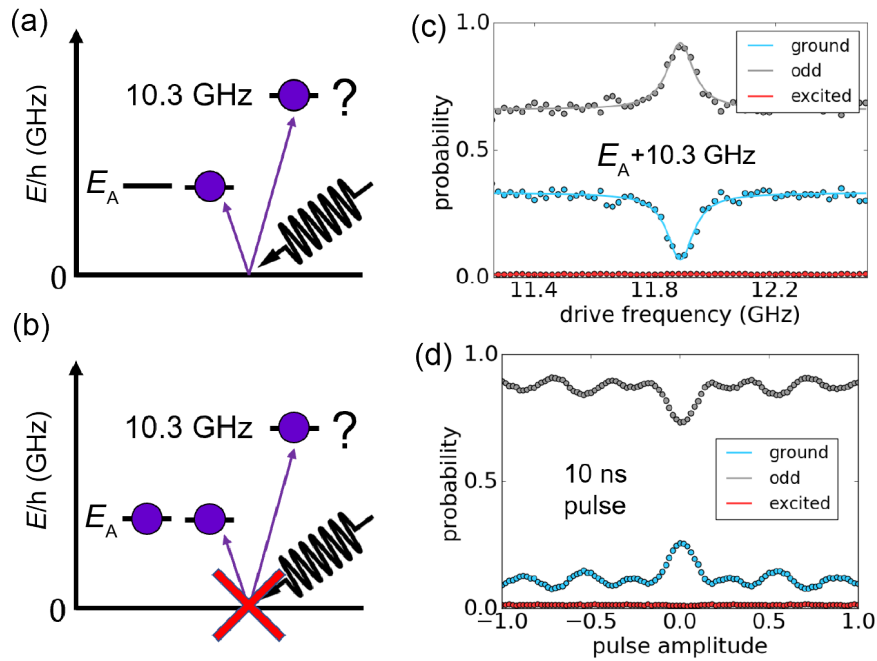


Figure 14.2: Driving a pair transition with a mystery level | (a) Driving a pair transition involving a doublet level and a mystery level with energy $h \times 10.3 \text{ GHz}$ results in population flow from $|g\rangle$ to the odd manifold (c). However, we would also expect population flow from the odd manifold to $|e\rangle$ as depicted in (b), but this is not observed. (d) Driving the pair transition using a 10 ns square pulse of variable amplitude resulted in weak oscillations.

Steady-state parity fluctuations

While the blocking phenomenon described above may have been a one time observation, the effect of the mystery levels on steady-state parity was certainly not. We observed gate- and flux-dependent fluctuations of the parity at many bias points over several devices. We present one example in Fig. 14.3.

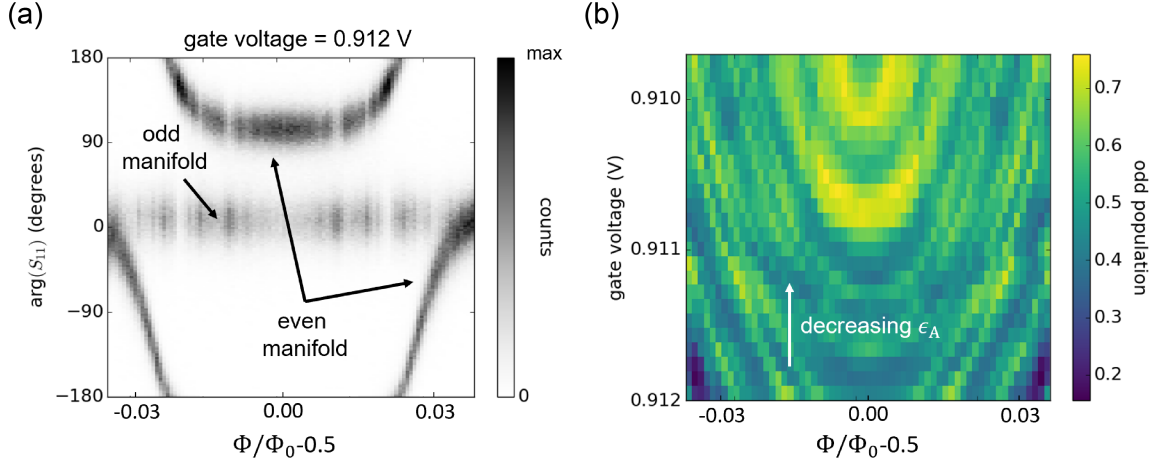


Figure 14.3: Parity fluctuations due to mystery levels | (a) Histogram of the phase of the resonator reflection coefficient versus Φ . A doublet pair transition is tuned close to the resonator frequency, such that we can distinguish the two parity manifolds. Fluctuations of the parity are observed that are symmetric about $\Phi = \Phi_0/2$. (b) Odd state population with V_c and Φ . In a separate spectroscopy measurement, we found that the doublet energy ϵ_A increased in frequency with decreasing V_c , as indicated by the white arrow. The dips in population can be explained by the doublet coming into resonance with various mystery levels, which gobble up the quasiparticles occupying the doublet.

First, we biased the device such that a pair transition was slightly above the resonator at $\Phi = \Phi_0/2$. In panel (a), we histogram the readout phase as a function of Φ . We observe fluctuations in the average parity that are symmetric about half flux. In panel (b), we show the same experiment, repeated as V_c was varied. The odd state population was computed as the counts around zero phase [see panel (a)]. We find that the parity fluctuations follow parabolic bands in Φ/V_c .

These results can be explained by the presence of the mystery levels. Let's suppose the mystery levels are cold, such that when the doublet is tuned into resonance with one of them, it gobbles up the doublet's quasiparticle: odd manifold $\rightarrow |g\rangle$. Now imagine the flux parabola of the Andreev doublet (locally a parabola anyway) being tuned past this mystery

level with the gate. Then, what we observe in panel (b) is exactly what we expect. Each dark parabola corresponds to the doublet energy being tuned past a particular mystery level. However, this explanation does not explain why the odd manifold population can be above 0.5.

14.2 Temperature dependence of quasiparticle parity jumps

In our investigation of the Andreev pair qubit [Hays et al. 2018], we found that the odd manifold had larger population than the even manifold at higher temperatures [Fig. 14.4]. While both the odd→even and even→odd jump rates increased with temperature, we found that even→odd rates had a stronger dependence, and thus the odd manifold had higher population. We did not take data between 50 mK and 150 mK because the rates seemed stable up until 150 mK, and we were dealing with electrostatic instabilities in this sample that made measurements difficult.

We hypothesized that this could be due to a charging effect. Suppose the ground state has energy E_c , the odd manifold energy E_A , and the excited state energy $2E_A + E_c$. Then, it is possible that the odd manifold would have higher population at intermediate temperature scales. Such a charging energy might be expected if the coupling to the leads was weak such that the Andreev levels were more dot-like. However, preliminary theory suggested that it would be difficult to have a situation where charging energy is high, but also observe as large a Φ -dispersion as we did.

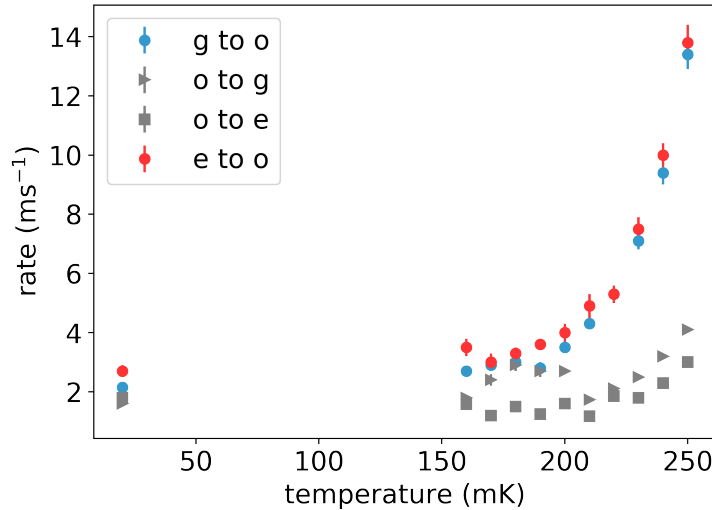


Figure 14.4: Temperature-induced increase of odd manifold population | A hidden Markov model algorithm was used to extract the rates between the even and odd manifold states as a function of the mixing chamber temperature. At higher temperatures, the rates from even to odd are higher than those from odd to even, corresponding to an increase in the odd manifold population.

References

- Hays, M., V. Fatemi, K. Serniak, D. Bouman, S. Diamond, G. de Lange, P. Krogstrup, J. Nygård, A. Geresdi, and M. Devoret, “Continuous monitoring of a trapped superconducting spin”, *Nature Physics*, 1–5 (2020).
- Hays, M., G. de Lange, K. Serniak, D. van Woerkom, D. Bouman, P. Krogstrup, J. Nygård, A. Geresdi, and M. Devoret, “Direct microwave measurement of Andreev-bound-state dynamics in a semiconductor-nanowire Josephson junction”, *Phys. Rev. Lett.* **121**, 047001 (2018).
- Hays, M., V. Fatemi, D. Bouman, J. Cerrillo, S. Diamond, K. Serniak, T. Connolly, P. Krogstrup, J. Nygård, A. L. Yeyati, A. Geresdi, and M. H. Devoret, “Coherent manipulation of an andreev spin qubit”, *Science* **373**, 430–433 (2021).